Supramolecular Self-Assembled Nanoparticle for Organelle Targeting in Cancer

A Thesis Submitted to Partial Fulfillment of the Degree of

Doctor of Philosophy

By

Chandramouli Ghosh

ID: 2014-3292

Research Supervisor

Dr. Sudipta Basu

Indian Institute of Technology, Gandhinagar

Associate Professor

Co-Guide

Dr. Nirmalya Ballav

Associate Professor

Indian Institute of Science Education & Research, Pune

Indian Institute of Science Education and Research, Pune

Dedicated To

My Family

Father & Mother

Certificate

This is to certify that the work incorporated in this entitled "**Supramolecular self-assembled nanoparticle for organelle targeting in cancer.**" submitted by **Chandramouli Ghosh** carried out by candidate at Indian Institute of Science Education and Research (IISER), Pune, under my supervision. The work presented here or any part of it has not been included in any other thesis submitted previously for the award of any degree or diploma from any other university or institution.

Date: 07/01/2019

Sudipta Basu

Dr. Sudipta Basu
(Research Supervisor)
Associate Professor
IIT Gandhinagar
India.

Nirmalya B 7/1/2019

Dr. Nirmalya Ballav
(Co-Guide)
Associate Professor
IISER Pune

निर्मल्य बल्लव / Nirmalya Ballav
सहयोगी प्राध्यापक, रसायनशास्त्र / Associate Professor, Chemistry
भारतीय विज्ञान शिक्षा एवं अनुसंधान संस्थान
Indian Institute of Science Education & Research
पुणे / Pune - 411 008, India

Declaration

I hereby declare that the thesis entitled "**Supramolecular self-assembled nanoparticle for organelle targeting in cancer.**" submitted for Doctor of Philosophy in chemistry at Indian Institute of Science Education and Research (IISER), Pune, has not been submitted by me to any other university or institution. This work presented here was carried out at the Indian Institute of Science Education and Research (IISER) Pune under the supervision of Dr. Sudipta Basu and co-guide Dr. Nirmalya Ballav. This written submission of thesis represents my ideas in my own words and where others' ideas have been included; I have adequately cited and referenced the original sources. I also declare that I have adhered to all principles of academic honesty and integrity and have not misrepresented or fabricated or falsified any idea/data/fact/source in my submission. I understand that violation of the above will be cause for disciplinary action by the Institute and can also evoke penal action from the sources which have thus not been properly cited or from whom proper permission has not been taken when needed.

Date: 07.01.2018

Chandramouli Ghosh
ID-2014-3292
(Senior Research Fellow)
Department of Chemistry
IISER, Pune- 411008
India.

Acknowledgement

I would like to take the opportunity to express my deep sense of gratitude to my respected faculty advisor Dr. Sudipta Basu & Co-guide Dr. Nirmalya Ballav for their careful guidance, support and encouragement throughout my research career.

I would like to thank Dr. Manas Kumar Santra and Dr. Arnab Mukherjee for being my research advisory committee (RAC) members and providing me valuable comments during RAC meetings. A special mention of Dr. K.N.Ganesh (our former director), Dr. M. Jayakanan and Dr. H. Chakrapani who had given us the privilege to work in the biology laboratory.

I express my sincere thanks to all lab-mates (Aditi, Aman, Sohan ,Shalini Abhik, Sandeep,, Ankur, Deepali, Nikunj, Kamil,) for their suggestion for betterment of my performance in every aspect. A special thanks to Piyush More and Meenu Kuman for teaching me the biological experiments. I also want to thank Dhrubojyoti Dutta for his valuable suggestions during my research work. I also want to thank Poulomi Sengupta (NCL Pune) and Mukul (IISER Pune) for helping me in biological experiments.

I am also thankful to my collaborator Dr. Manas Kumar Santra (NCCS Pune) & Neha Gupta for the biology (both from Chemistry and Biology department) and lab-technitians for helping me throughout in their own special ways. I would like to thank CSIR-UGC for funding and providing a high quality research atmosphere. I also want to thank Tushar and all other people from the administrative department at IISER Pune.

I also want to thank my friends for the wonderful time I have spent in IISER Pune.

Finally I would like to thank my father & mother (Samarendra Nath Ghosh & Tapati Ghosh) & my best friend Moulika Bhattacharyya for their huge support.

Chandramouli Ghosh

IISER Pune (SRF Ph.D.)

Supramolecular Self-Assembled Nanoparticle for Organelle Targeting in Cancer

Abstract

Cancer is one of the leading causes of morbidity and mortality worldwide. To understand the characteristics of cancer cells, the hallmarks of cancer are outlined by Hanahan and Weinberg. Resisting cell death, sustaining proliferative signaling and deregulation of cellular energetics are the imperative hallmarks of cancer which are tightly governed by important sub-cellular organelles such as nucleus, mitochondrion and endoplasmic reticulum(ER). Thus specific targeting of the organelles in cancer cells is interesting strategy for future cancer therapy. However, organelle targeting in cellular milieu is highly challenging task. To address this, we have developed self-assembled glycosylated chalcone boronic acid derivatives to target anti-apoptotic Bcl-2 in mitochondria and showed their anticancer activity. ER is involved in protein synthesis/folding and dis-regulation in that mechanism leads to ER-stress. Moreover, ER membrane wraps around another important organelle, nucleus and forms double membrane nuclear envelop leading to ER-nuclear cross-talk. Hence, we hypothesize that simultaneous targeting of ER and nuclear DNA in cancer cells would lead to improved anti-cancer efficacy. To achieve this, we have developed triazine based small molecule which supramolecularly self-assembled into spherical nanoparticle which can induce ER-stress and DNA damage in cancer cells. Interestingly, the ER-targeting self-assembled nanoparticle induced autophagy in cancer cells, leading to combination therapy with autophagy inhibitor for improved therapeutic efficacy. Subsequently, we have engineered lipidic nanoparticle for specific targeting of ER-resident chaperon GRP94 to induce ER stress as interesting strategy in cancer therapy. These ER localizing GRP94 targeting nanoparticle induced improved anti-cancer effect in cancer cells. Finally, we have engineered lipidic nanoparticle to target proteasome which is having cross-talk with ER stress through unfolded protein response (UPR) for disruption of ubiquitin proteasome system (UPS) as novel strategy for cancer treatment. These lipidic proteasome targeted nanoparticles inhibited sub-cellular protein degradation machinery to trigger cancer cell death. We anticipate that, here presented unique approaches will extend the concept of supramolecular self-assembly of small molecules and lipidic nanoparticles to target multiple sub-cellular organelles simultaneously for improved therapeutic effect in anti-cancer therapy in future.

Table of Contents

Synopsis

Cancer is one of the leading causes of morbidity and mortality worldwide. To understand the characteristics of cancer cells, the hallmarks of cancer are outlined by Hanahan and Weinberg. Resisting cell death and deregulation of cellular energetics are the two imperative hallmarks of cancer which are tightly governed by important sub-cellular organelles such as mitochondrion, nucleus & endoplasmic reticulum. Organelle targeting has emerged as novel, alternative targets for next generation cancer therapy. However, there are three major challenges in targeting organelles ***(a) selective targeting of major organelles such as nucleus, mitochondria and endoplasmic reticulum in cellular milieu, (b) specific targeting of these organelles in cancer tissues keeping organelles in healthy cells intact and (c) overcome drug resistance.*** (*Chapter 1*). We have addressed these challenges by merging organic synthesis, chemical biology and nanotechnology based platforms in this thesis (Scheme 1).

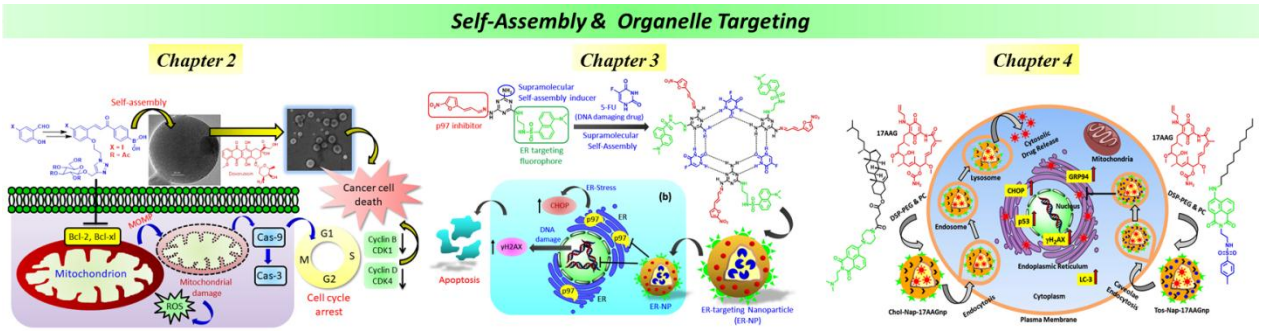

Scheme 1: Targeting Organelle in cancer cells using chemical biology and nanotechnology platforms.

In *Chapter 2*, we have developed supramolecular self-assembly of glycosylated chalcone boronic acid in water and showed anticancer effect. Chalcone and boronic acids are important privileged structures in myriads of natural and synthetic products having diverse biological activities. However, their therapeutic window is highly narrow due to their hydrophobic nature affecting unpredictable biodistribution. To address this, we herein have synthesized a novel hybrid glycosylated chalcone−boronic acid library. Cell viability, flow cytometry, confocal microscopy, and gel electrophoresis assays demonstrated that one of the library members induces cell cycle arrest in the G2/M phase through the activation of p21 and decrease levels of cyclin B1 and CDK1. In addition, it also induces apoptosis, primarily due to the inhibition of Bcl-2/ Bcl-xl and the augmentation of BAX to prompt mitochondrial damage and reactive oxygen species generation. Most interestingly, the lead cytotoxic

glycosylated chalcone−boronic acid self-assembled in water into a spherical nanodrug that can further entrap another anticancer drug (doxorubicin) to show remarkably improved efficacy in breast cancer cells. This novel lead compound has prospective as a vector-free nanodrug for combination cancer therapy.

In ***Chapter 3***, we have developed supramolecular self-assembled nanoparticle for selective targeting of endoplasmic reticulum in cancer cells. The endoplasmic reticulum (ER) is one of the most important organelles controlling myriads of cellular functions including protein folding/misfolding/unfolding, calcium ion homeostasis and lipid biosynthesis. Subsequently, due to its functional dysregulation in cancer cells, it has emerged as interesting target for anti-cancer therapy. However, specific targeting of ER in cancer cells remains a major challenge due to the lack of ER-selective chemical tools. Furthermore, for performing multiple cellular functions ER is dependent on nucleus through complicated cross-talk. Herein, we have engineered a supramolecular self-assembled hexameric rosette structure from two small molecules: tri-substituted triazine and 5-fluorouracil (5FU). This rosette structure consists of ER-targeting moiety with fluorescence tag, ER-stress inducer and nuclear DNA damaging drug simultaneously, which further self-assembled into ER-targeting spherical nano-scale particle (ER-NP). These ER-NPs internalized into HeLa cervical cancer cells by macropinocytosis and specifically localized into ER to induce ER stress and DNA damage leading to cell death through apoptosis. Interestingly, ER-NPs initiated autophagy, inhibited by a combination of ER-NP and chloroquine (CQ) to augment cancer cell death. This work has potential to exploit the concept of supramolecular self-assembly into developing novel nano-scale material for specific sub-cellular targeting of multiple organelles for future anti-cancer therapy.

In ***Chapter 4***, finally, we have developed lipidic nanoparticle which can selectively target endoplasmic reticulum in cellular milieu and exerts endoplasmic reticulum stress. So, we have synthesized green fluorescent sulfonamide based napthalimide conjugate and prepared lipicid nanoparticle with encapsulation of ER stress inducer 17AAG. These ER specific nanoparticles can selectively accumulate into ER and induce cell death through ER stress. Interestingly, these lipidic ER specific nanoparticles do not accumulate any other organelle such as lysosome and mitochondria. These lipidic nanoparticles selectively accumulate in ER and induced ER stress which has been detected by overexpression of ER stress marker CHOP. Interestingly, lipidic ER-NP initiated autophagy, inhibited by a combination of lipidic

ER-NP and chloroquine (CQ) to augment cancer cell death. We envision that the here presented unique approaches can be translated into clinics in future as platform technologies to inhibit multiple diverse targets concurrently to improve the therapeutic efficacy, reduce the off-target toxicity, overcome drug resistance and finally, offer a better quality of life to the cancer patients.

List of Publication

1. **Ghosh, C.**; Gupta, N.; More, P.; Sengupta, P.; Mallick, A.; Santra, M. K.; Basu, S.; Engineering and In Vitro Evaluation of Acid Labile Cholesterol Tethered MG132 Nanoparticle for Targeting Ubiquitin-Proteasome System in Cancer. *ChemistrySelect* **2016**, *1*, 5099-5106.

2. **Ghosh, C.**; Gupta, N.; Mallick, A.; Santra, M. K.; Basu, S. Self-assembled glycosylated chalcone–boronic acid nanodrug exhibits anticancer activity through mitochondrial impairment. *ACS Applied Bio Materials* **2018**, *1*, 347-355.

3. **Ghosh, C.**; Nandi, A.; Basu, S. Supramolecular Self-assembly of Triazine-Based Small Molecule Targeting Endoplasmic Reticulum in Cancer Cells. *Nanoscale* **2019**, *11*, 3326-3335.

4. **Ghosh, C.**; Nandi, A.; Basu, S. Nanoparticle Mediated ER Stress in Cancer Cells through Unfolded Protein Response. *Manuscript under* revision. **.**

Chapter 1

Introduction

1.1 Cancer

Cancer is one of the leading causes of death, accounting for 8.2 million deaths worldwide in 2012.[1] Over the past several decades, remarkable breakthroughs have been made in advancing our understanding of how cancer originates and develops, which has in turn led to better methods for both diagnosis and treatment.[2] Although the overall mortality of cancer is showing a declining trend for the first time in five decades, it still remains at a high rate of 20.2%.[3] According to International Union Against Cancer (UICC) 2017 report, over 7 million people die from cancer and more than 11 million cases are diagnosed worldwide per year. Tobacco kills more than 5 million people, of whom 1.5 million die of lung cancer. Also, more than 160,000 cases of childhood cancer are diagnosed and at least 90,000 children die of cancer. In 2020, if current trends continue, new cases of cancer will increase to 16 million per year and more than 10 million people will die annually. According to World Health Organization (WHO), globally, nearly 1 in 6 deaths is caused by cancer.[4]

Cancer is defined as abnormal growth of cells which tends to proliferate in an uncontrolled manner. In normal tissues, number of cells in tissue is determined by the balance between the cell division and cell death, whereas in cancer this ratio is altered and leads to formation of tumor. (Figure 1) [5] Cancer can develop in any part of body and there are more than 200 different types of cancer can be grouped based on the type of the cell they start growing in.[6-7] Cancer starts from DNA damage of the cells and it is called mutation. This damage happens when cells duplicate prior to the cell division, make mistakes. Although this damage can be repaired before cell division, but some time it may be ignored and transfer to daughter cells. If this mutated gene accumulated in cells it may affect the regulation of cell cycle of the cells, which leads to faster cell division w.r.t normal cells and result is the formation of tumor. Chemical compounds (carcinogens) have an obvious role of forming gene mutations and cancer cells. In addition, smoking involves several carcinogenic chemical compounds that lead to lung cancer.[8] Interestingly, environmental chemical substances with carcinogenic properties influence directly or indirectly the cytoplasm and nucleus of cells, and lead to genetic disorders and gene mutations.[9] Viruses, bacteria and radiation are other carcinogenesis factors, comprising about 7% of all cancers.[10] In general, cancer disrupts cellular relations and results in the dysfunction of vital genes. This disruption is affective in the cell cycle, and leads to abnormal proliferation. [11-12]

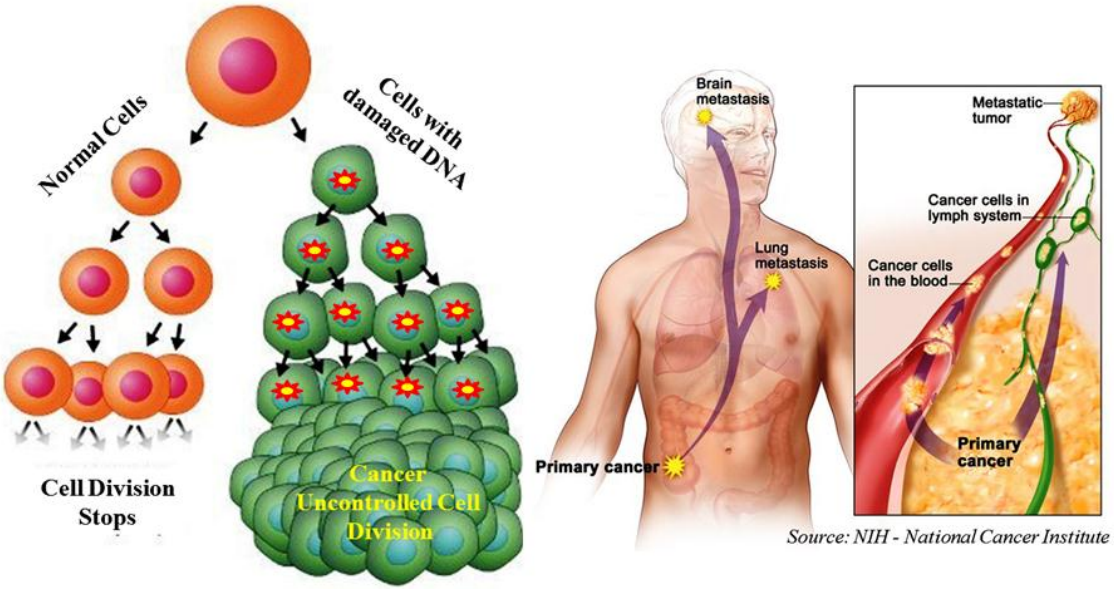

Figure 1: What is cancer & how cancer is different from normal cells. (Image taken from Google)

1.2 Therapeutic Targeting of the Hallmarks of Cancer:

To understand the complexities in the characteristics of cancer cell, in the year 2000, D. Hanahan and R. Weinberg outlined the hallmarks of cancer, namely, sustaining proliferative signaling, evading growth suppressors, resisting cell death, enabling replicative immortality, induction of angiogenesis and activating invasion and metastasis.[13] Later, after a decade, they added another two enabling characteristics, i.e., genome instability/mutation and tumor-promoting inflammation and two other emerging hallmarks, namely, deregulating cellular function and avoiding immune destruction (Figure 2).[14] Out of these ten hallmarks, resisting cell death and deregulation of cellular energetics are the two imperative hallmarks of cancer which are tightly governed by major sub-cellular organelles such as nucleus, mitochondrion and endoplasmic reticulum.

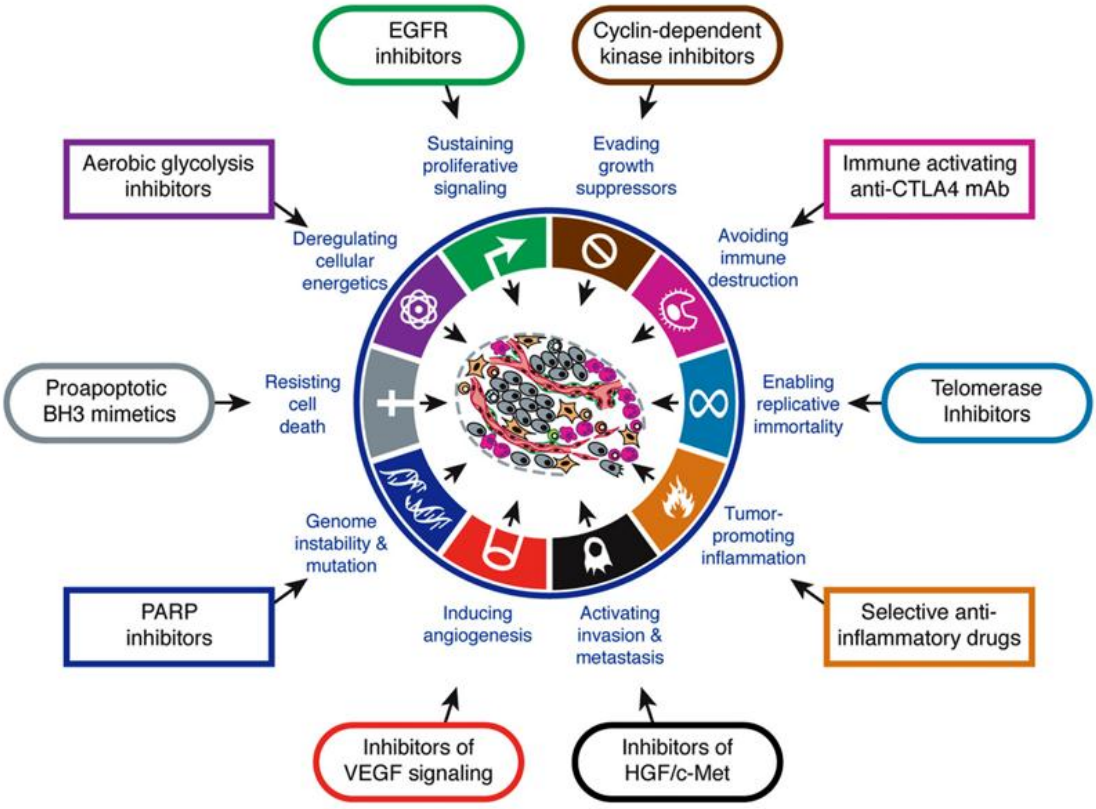

Figure 2: Hallmarks of cancer (adapted from Hanahann et al. *Cell* **2011**, *144*, 646-674)

1.3 Organelle Targeting in Cancer Therapy:

Cellular signaling pathways are complex networks which are highly interconnected with each other. There are large number of intracellular signaling pathways receive information from different growth factors at the cell surface through the receptor proteins which are embedded in the plasma membrane and integrate these information to regulate diverse biological processes including protein synthesis, cell growth, differentiation, cell architecture and polarity, motility, and programmed cell death (apoptosis). Thus targeted drug delivery is essential for several diseases like cancer, which is characterized by groups of cells exhibiting properties of uncontrolled and undifferentiated growth, invasion, and sometimes metastasis, i.e., spread of cancer to other tissues with the aid of connective tissues like blood and lymph. Subcellular delivery involves delivering a drug in its active form to its target site of action inside the cell. So an attractive strategy to increase the therapeutic index of a drug is to specifically deliver the therapeutic molecule in its active form, not only into target tissue, nor even to target cells, but more importantly, into the targeted organelle, i.e., to its intracellular therapeutic active site (Figure 3).[15-17]

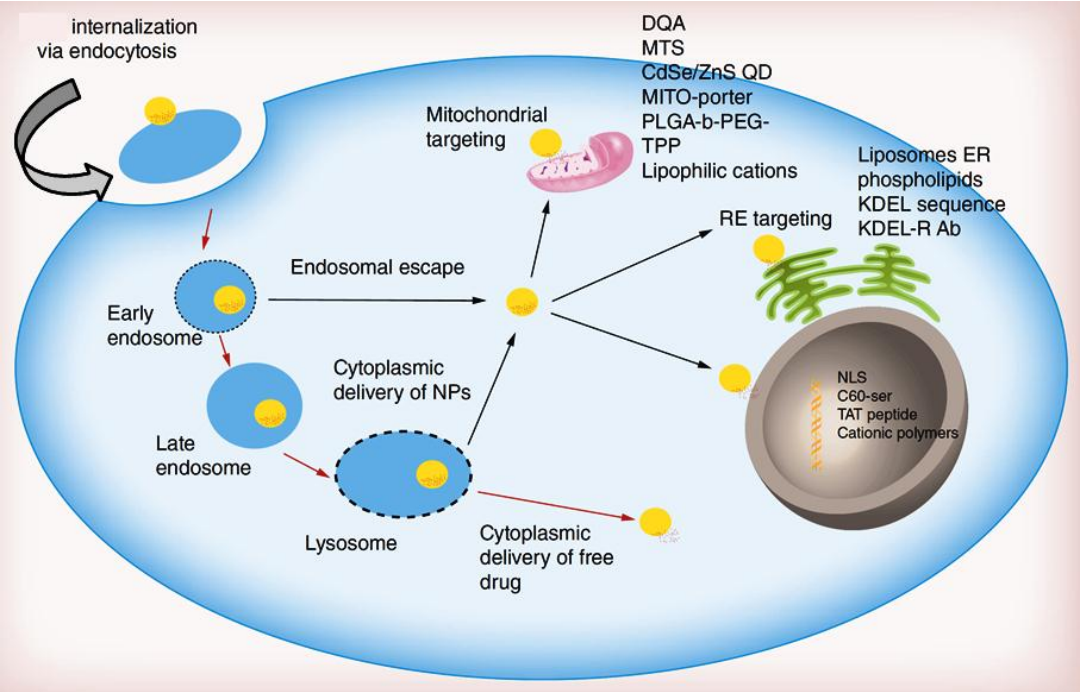

Figure 3: Cytosolic delivery and targeting of the nucleus, the mitochondrion and the endoplasmic reticulum. (*Nanomedicine* **2015**, *10*, 1923–1940.)

1.3. a. Role of Nucleus in Cancer:

The nucleus is the control center of the eukaryotic cell which governs cell physiology by controlling replication and transcription processes. The sequestering of genetic material within the nucleus of the eukaryotic cell provides the nucleus with a powerful mechanism for the regulation of gene expression and other cellular processes through selective translocation of proteins between the nucleus and cytoplasm. In fact, the nucleus is responsible for all diseases derived from mutation of gene such as cancer, heart dysfunction, muscular dystrophy and neurodegenerative disease. There are various drugs which act on DNA to prevent replication and transcription of a variety of important genes (Figure 4). However, a therapeutic molecule, even if delivered inside the target cell, often fails to reach its subcellular target. For instance, only 0.1% of free plasmids from cytosol were able to translocate into the nucleus by crossing the nuclear membrane.[18] Additionally, proliferating cells causing disease (such as in tumors) acquire genetic changes which may make them resistant to a particular drug, resulting in the production of new daughter cells that are also drug-resistant.

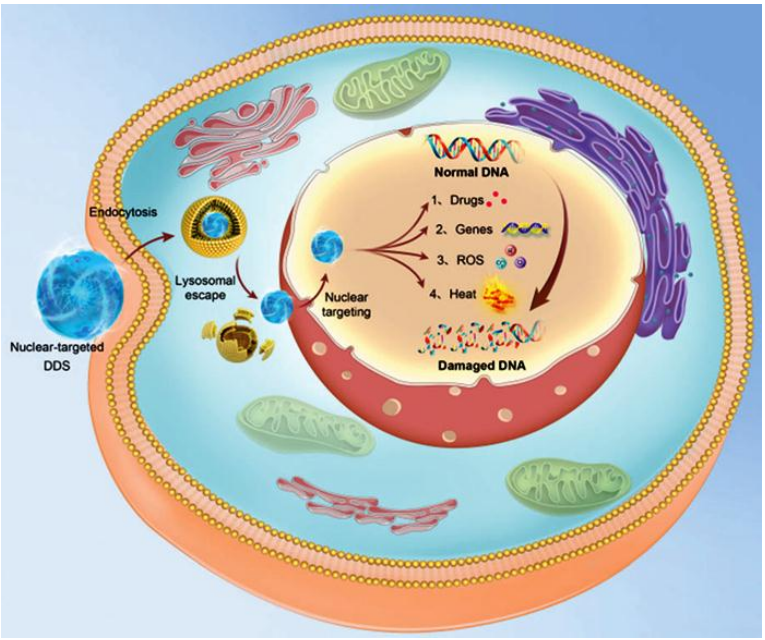

Figure 4: Schematic illustration of cell nucleus-targeting nanotherapeutics for enhanced tumor treatments. (*Chem. Soc. Rev.* **2018**, *47*, 6930-6946).

1.3.b. Targeting Nucleus:

The nuclear membrane is difficult to penetrate.[19-20] Indeed, the small pore size of the nuclear membrane (≈ 10 nm) prevents the passage of molecules larger than 40 kDa even when the pores are dilated.[21] Consequently, large molecules must be actively transported beyond the membrane by proteins. The functionalization of nanoparticles with nuclear localization signals (NLS), which are characterized by basic amino acid residues, implies the recognition of the NLS by its cytoplasmic receptors, such as importins. Subsequently, the NLS peptide binds the nuclear-pore complex and the cargo is released into the nucleus via translocation through the pores.[22] Particles modified with the KKKRKV peptide from the Simian virus 40 large tumor antigene, or peptide KRPAATKKAGQAKKKKL from nucleoplasmin (an enzyme involved in nucleosome assembly) accumulated in much larger amounts in the nuclear membrane than did unmodified controls.[23-27] The HIV-1 TAT peptide is a well-known nuclear membrane translocator, which when applied on the surface of nanoparticles enables them to elude endosomal sequestration and to accumulate in the nucleus.[28] Notably, doxorubicin exerted stronger anticancer activity when it was encapsulated in mesoporous silica particles whose surface was modified with the TAT peptide.[27] In other nuclear targeting strategies, a positive charge was applied to the particle surface. Cationic polymers such as

PEI and poly (l-tartaramidoamine) increased the targeting of particles to the nucleus due to its ability to permeabilize the nuclear envelope a process that favors proper delivery of plasmid DNA payloads to the nuclei of target cells.[29-30]

1.3.c. Role of Mitochondria in Cancer:

Mitochondria is a membrane bound organelle found in eukaryotic cells, which is responsible for synthesis of adenosine triphosphate (ATP) to the cell by the process of oxidative phosphorylation, and hence it is known as the powerhouse of the cell. Mitochondrial dysfunction has been linked to many of the hallmarks of cancer cells including their limitless proliferative potential, impaired apoptosis, insensitivity to anti-growth signals, enhanced anabolism and decreased autophagy.[31] Mitochondria are involved in apoptotic cell death, adenosine triphosphate synthesis, production of reactive oxygen species and calcium metabolism. Consequently, mitochondrial dysfunction has been associated with a variety of disorders (cancer, neurodegenerative diseases, cardiovascular disease and diabetes)[32] and they have been extensively studied as therapeutic intracellular targets. Moreover, mitochondrial biogenesis and turnover, fission and fusion dynamics, cell death, oxidative stress, metabolism and bioenergetics, signaling and mitochondrial DNA can contribute immensely in each steps of tumorigenesis.[33-35] As a result, mitochondrion has emerged as one of the unconventional, alternative targets for next-generation cancer therapy

1.3.d. Targeting Mitochondria:

Mitochondrial-targeted nanoscale systems are emerging as prime pharmacological strategies in the treatment of cancer. Since mitochondria play a major role in executing apoptosis-mediated cell death, thus targeting mitochondria to initiate apoptosis is likely to be promising treatment strategy for curbing cancer. Curbing the mitochondrial ROS production by delivery of antioxidants to the mitochondria, activating mitochondrial membrane permeability, targeting Bcl-2 proteins to inhibit or down-regulate anti-apoptotic action, delivering therapeutic genes for the expression of pro-apoptotic proteins including Bax, Bak are few of the effective mitochondrial targeted treatment strategies in cancer.[36] Considerable efforts are being undertaken to discover molecules that target mitochondria (Figure 5).[37] Mitochondrial targeting is achieved by various delocalized lipophilic cations such as small molecule ligands, mitochondria-penetrating-peptides (MPP), cationic ‘bolalipid’- based vesicles, mitochondrial protein import machineries and molecules targeting mitochondrial inner/outer membranes.

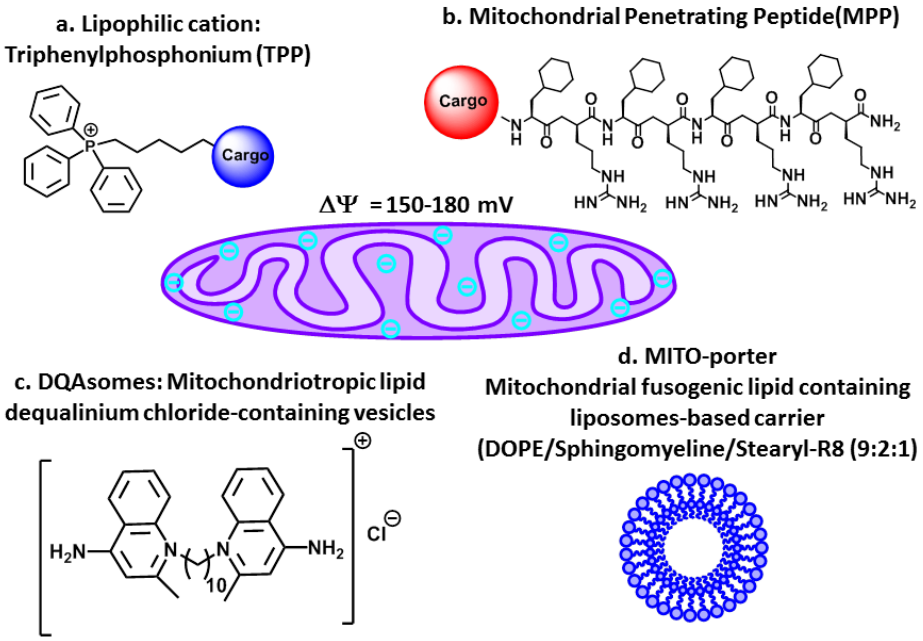

Figure 5: Summary of current strategies for mitochondrial targeting. (*Adv. Drug Deliv. Rev* **2014**, *66*, 26–41.)

Sufficient lipophilicity combined with delocalized positive charge is a pre-requisite for mitochondriotropic molecules. One of the most important lipophilic cation triphenylphosphonium (TPP) has demonstrated selective accumulation in the mitochondria upon intracellular delivery.[38] Mitochondria maintain a constant membrane potential of about −180 to −200 mV across their lipid bilayer by using channel pumps and oxidative phophorylation pathways.[39] This high negative membrane potential is not present in any other cellular organelle, which offers a unique chemical opportunity for selective accumulation of lipophilic cations to the mitochondria. On the other hand Mitochondria-targeted peptides were proposed as the alternative to delocalized lipophilic cations for delivering bioactive compounds to mitochondria. Among these are peptides based on natural amino acid sequences targeting mitochondria and synthetic peptides, typically carrying hydrophobic (phenylalanine, tyrosine, isoleucine) and positively charged (arginine, lysine) amino acids. Another example of targeting mitochondria is mitochondrial-targeting nano-preparation, MITO-Porter, developed by Harashima group holds promise as an efficacious system for the delivery of both large and small bioactive molecules into mitochondria.[40] MITO-Porter is a liposome based nanocarrier composed of DOPE/sphingmyelin/Strearyl-R8 (9:2:1) that delivers its macromolecular cargo to the mitochondrial interior via membrane fusion.[41] Dequalinium is a dicationic amphiphilic compound that self-assembles and forms vesicle-like

aggregates referred to as dequalinium liposomes or DQAsomes.[42] These vesicles translocate into cells via endocytosis and fuse with the mitochondrial outer membrane. DQAsomes have been evaluated to determine their potential to serve as a mitochondriotropic, non-viral transfection vector for delivery of mitochondrial DNA to the mitochondrial membrane. [43]

1.3.e. Role Endoplasmic Reticulum in Cancer:

The endoplasmic reticulum (ER) is a specialized organelle that orchestrates the synthesis, folding and transport of at least one-third of the proteins in eukaryotic cells. It regulates protein homeostasis, termed proteostasis, a process that monitors the biogenesis, folding, assembly, trafficking and degradation of all proteins destined for organelles and the extracellular space. Many different perturbations can alter the function of this organelle, leading to the accumulation of unfolded or misfolded proteins inside the ER, a cellular condition referred to as ER stress. ER stress initiates a series of adaptive mechanisms that together are known as the unfolded protein response (UPR) (Figure 6).[44]

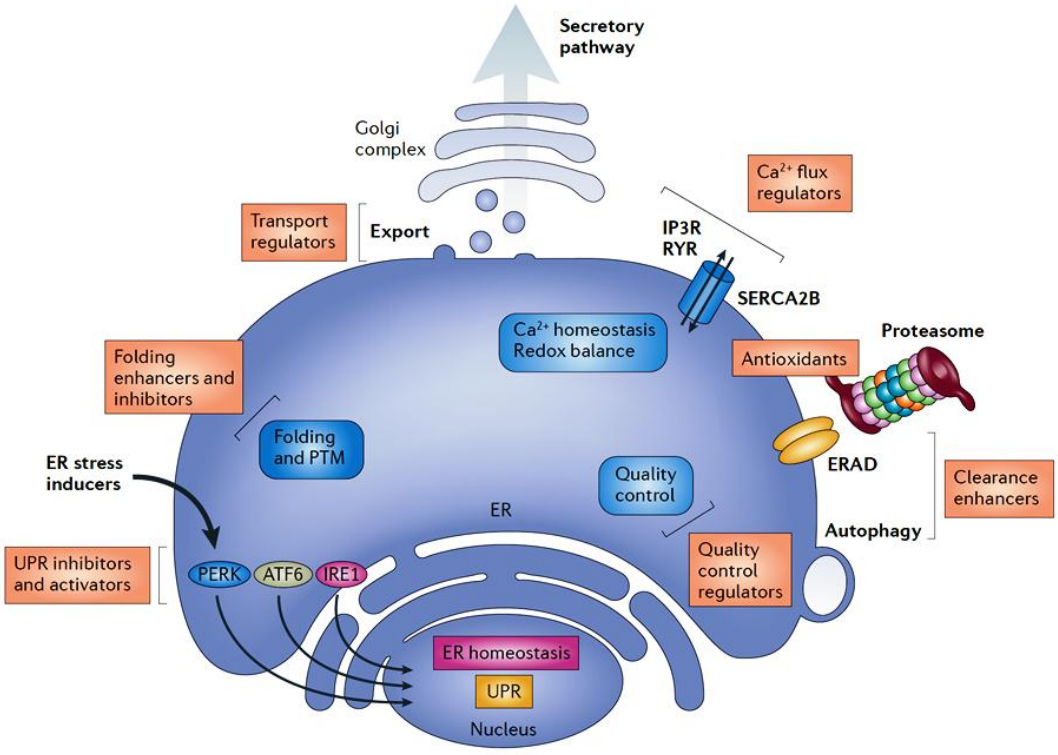

Figure 6: Sites of action of therapeutic molecules to target ER proteostasis. (*Nat. Rev.* **2014**, *12*, 703-714)

Activation of the UPR affects many aspects of the secretory pathway to restore protein-folding homeostasis. Conversely, if cell damage is sufficiently severe, UPR signaling results in cell death by apoptosis.[45]

1.3.f. Targeting Endoplasmic Reticulum:

Cellular health depends on the normal function of the endoplasmic reticulum (ER) to fold, assemble, and modify critical proteins to maintain viability. When the ER cannot process proteins effectively, a condition known as ER stress ensues. When this stress is excessive or prolonged, cell death via apoptotic pathways is triggered. Interestingly, most major diseases have been shown to be intimately linked to ER stress, including diabetes, stroke, neurodegeneration, and many cancers. Thus, controlling ER stress presents a significant strategy for drug development for these diseases. Physiologically, protein trafficking to the ER is mediated by the KDEL sequence and its receptor (KDEL-R) expressed on this organelle. This sequence is an ER localization signal and was used to improve the intracellular targeting of these organelles,[46] Delie and coworkers developed anti-KDEL functionalized polymeric nanoparticles loaded with paclitaxel for the treatment of prostate cancer[47] and Pollock et al. demonstrated lipidic nanoparticle of various phospholipid compositions can selectively go to ER. They showed that the liposomal system composed of phosphatidyl ethanolamine: phosphatidyl choline: phosphatidyl inositol: phosphatidyl serine (1.5:1.5:1:1) trafficked directly to the ER, fused with the ER membrane, to deliver hydrophobic drugs.[48]

1.4. Fundamentals of Organelle Targeting in Cancer by Nanotechnology:

Nanomedicine, the application of nanotechnology to medicine, is anticipated to help us move toward the selectively targeting organelle in cancer cells. After several decades of technological developments, drug-delivery systems based on engineered nanoparticles have started to show great promise.[49-50] As shown in Figure 7, the nanoparticles used for drug delivery can be readily fabricated from either soft (organic and polymeric) or hard (inorganic) materials, with their sizes being controlled typically in the range of 1–100 nm and compositions/ structures being engineered to load anticancer drugs in a variety of configurations.[51] The physicochemical properties of the nanoparticles can also be finely tuned by tailoring their chemical compositions, sizes, shapes, structures, morphologies, and surface properties. A number of such delivery systems have been approved for cancer therapy in the

clinics, with many more currently under clinical trials or preclinical evaluations. Nanoparticle-based therapeutics is poised to significantly improve the treatment outcomes for oncological diseases, promising to reshape the landscape of the pharmaceutical industry.[52]

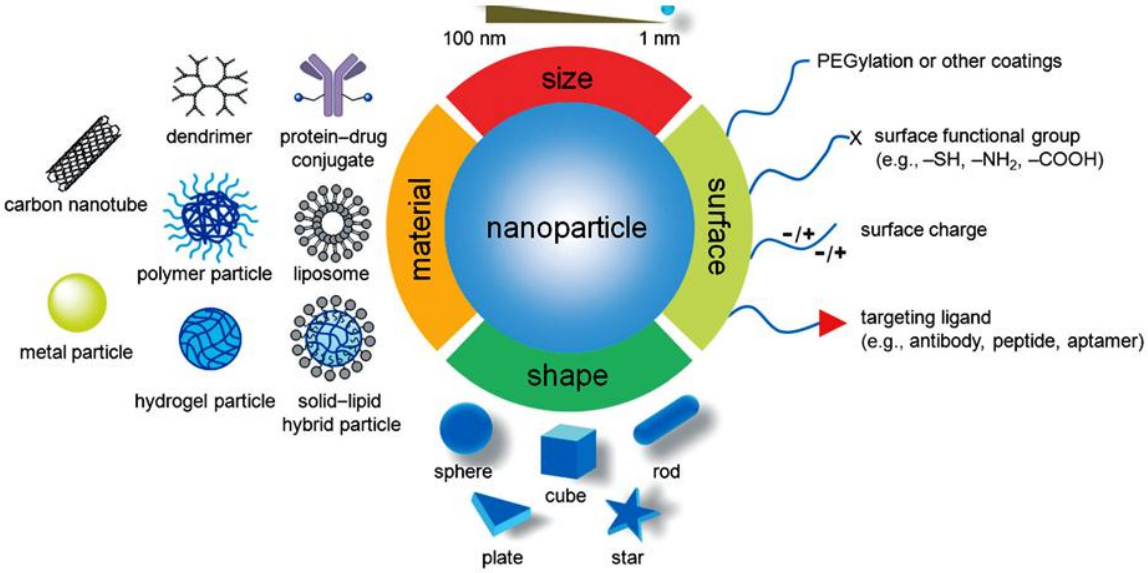

Figure 7: Characteristics of nanoparticles in a nut shell (adapted from Xia et al. *Angew. Chem. Int. Ed*. **2014**, *53*, 12320-12364.)

The major organelles such as Nucleus, Mitochondria and Endoplasmic Reticulum are ubiquitous in the healthy as well as cancer cells. Hence, selective sub-cellular targeting of these organelles in cancer cells, keeping them unperturbed in healthy cells, could be of central importance for the development of cancer therapeutics and therefore demanding nanotechnology-based toolkits.[53] Nanotechnology based platforms have revolutionized cancer therapeutics in last decade. Several nanovectors including liposomes, polymeric nanoparticles, nanocell, layer-by-layer nanoparticles, graphene oxide, gel-liposome and carbon nanotubes (Figure 7) have been demonstrated to deliver small molecule drugs, nucleic acids (genes and siRNAs) and therapeutic proteins successfully into tumor tissues through passive [enhanced permeability and retention (EPR) effect] and active targeting (cancer biomarker driven) (Figure 8).[54-55]

1.4.a. Passive Targeting: To effectively deliver drugs to the targeted site, the delivery system must remain in the bloodstream for a considerable time without being eliminated by means of metabolism and phagocytosis. The delivery vehicles are usually grabbed in the blood circulation by body's defense mechanism, the reticulo-endothelial system (RES) present in spleen and liver. Passive targeting involves designing drug carrier systems to evade reticulo-endothelial system. Fast growing tumor cells require recruitment of new vessels for oxygen and nutrient supply. That results in growth factor imbalance and leads to highly disorganized tumor vessels contributing to passive targeting. Unique microenvironment surrounding tumor cells differs from normal cells, also contributes to the passive targeting. Hyperproliferating tumor cells show high metabolic rate utilizing the energy obtained through glycolysis, resulting in acidic environment. Delivery vehicles are designed to remain stable at physiological pH (pH = 7.4) and to release the drugs at acidic pH. Cancer cells even express unique biological macromolecules such as matrix metalloproteinases, which can be used in passive targeting. Fast growing vascularization, leakiness and defective lymphatic drainage contribute to the passive targeting. Molecular weight, size, surface properties of the vector play role in passive targeting.[56-57]

1.4.b. Enhanced Permeability and Retention (EPR) Effect: It is an effective strategy to selectively deliver nanosize anticancer drugs/drug carriers to the tumor tissue. This effect was first noticed by Maeda and coworkers in studying the inflammation induced by microbial infections.[58] The nanovectors having size < 200 nm were found to be most effective in cancer therapy and diagnosis. This due to their preferential accumulation into tumor tissues through the unique leaky vasculature compared to the tight endothelial junctions of the healthy tissues. This mechanism is termed as enhanced permeability and retention (EPR) effect (Figure 8) and is the basis for selectively targeting tumor tissues via passive targeting.[59] Recent research focuses on delivery of polymer conjugates, micellar or liposomal drugs of anticancer agents via this mechanism and along with active targeting, the EPR effect is becoming an attractive strategy for such drug designs.[60]

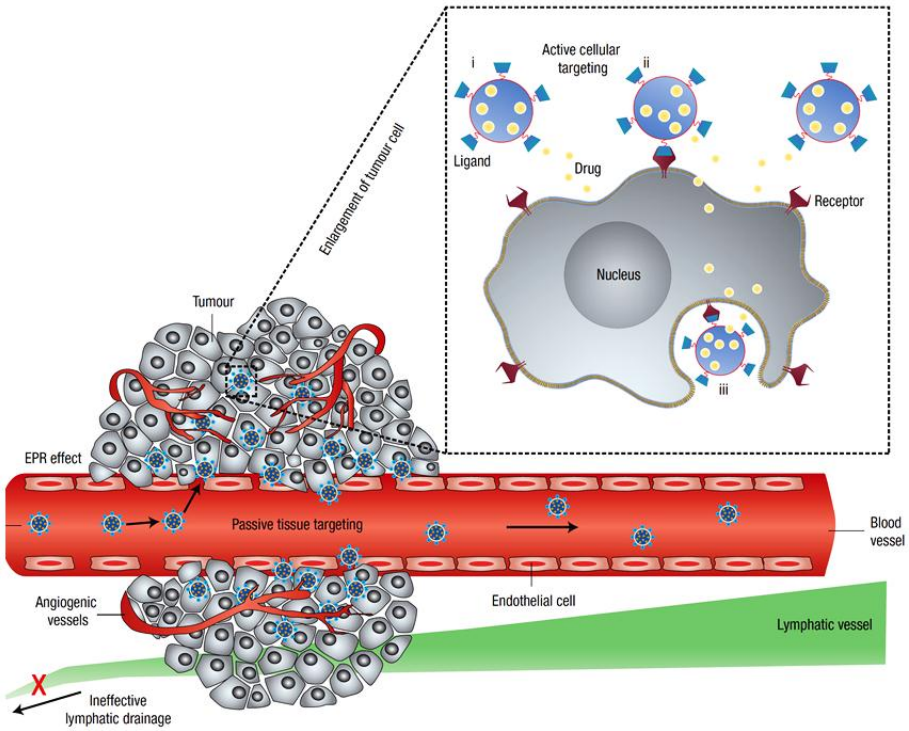

Figure 8: Schematic representation of passive and active targeting (adapted from Peer et al. *Nat. Nanotechnol.*, **2007**, *2*, 751-760)

1.4.c. Active Targeting: Active targeting involves attaching specific ligands to the drug delivery vehicle which will interact with their complementary receptors over-expressed on specific tumor tissues. Active targeting makes use of specific surface exposed receptor and ligand interaction to deliver the drug at specific site. The conjugated ligands can be antibodies, peptides or glycans. However, capacity of delivering drug at particular concentration is compromised in active targeting. Most of the cancer cells express specific molecular markers, which are not expressed by normal cells, serve as site for active targeting. The target cell, usually, accumulate the drug through receptor-mediated endocytosis. Endocytosed drug carriers are then transported to endosomes and lysosomes, where these are processed to release the drug by lysosomal enzymes. Since resistance inducing proteins such as P-glycoprotein cannot pump out nanoparticle-associated drug or drug-polymer conjugates that have entered the cell *via* the endocytic mechanism, active targeting mechanisms provide an alternative way to combat multi-drug resistance.[61-63]

1.5. Aim of Thesis:

Organelle targeting has emerged as novel, alternative targets for next generation cancer therapy. However, there are three major challenges in targeting organelles ***(a) selective targeting of major organelles such as nucleus, mitochondria and endoplasmic reticulum in sub-cellular milieu, (b) specific targeting of these organelles in cancer tissues keeping organelles in healthy cells intact.*** To address these, we have developed self-assembled glycosylated chalcone boronic acid which exhibits anticancer activity through mitochondrial impairment (***Chapter 2***). To target endoplasmic reticulum we have developed triazine based p97 inhibitor containing chimeric molecule which self-assembled with DNA damaging drug 5 Fluoro-uracil to form nanoparticle, that can simultaneously target nucleus and endoplasmic reticulum in cancer cells (***Chapter 3***). Finally, we have developed lipidic nanoparticle which can selectively target endoplasmic reticulum in cellular milieu and exerts endoplasmic reticulum stress. Herein we developed green fluorescent sulfonamide based napthalimide conjugate and prepared lipidic nanoparticle with encapsulation of ER stress inducer 17AAG. These ER specific nanoparticles can selectively accumulate into ER and induce cell death through ER stress (***Chapter 4***). We envision that, here presented unique approaches can be translated into clinics in future as platform technologies to inhibit multiple diverse organelles concurrently to improve the therapeutic efficacy for cancer treatment.

1.6. Reference:

1. Globocan 2012, IARC 2013.

2. Steichen, S. D.; Caldorera-Moore, M.; Peppas, N. A. A review of current nanoparticle and targeting moieties for the delivery of cancer therapeutics. *Eur. J. Pharm. Sci.* **2013**, *48*, 416-427.

3. Latest world cancer statistics, IARC 2013.

4. Siegel, R. L.; Miller, K. D.; Jemal, A. Cancer Statistics. *CA. Cancer J. Clin.* **2017**, *67*, 7–30.

5. WHO. WHO | Cancer http://www.who.int/cancer/en/.

6. Let's beat cancer sooner, Cancer Research UK, http://www.cancerresearchuk.org/about-cancer/what-is-cancer/how-cancer-starts/types-of-cancer.

7. National Institutes of Health (US); NIH Curriculum Supplement Series [Internet]. Understanding Cancer. https://www.ncbi.nlm.nih.gov/books/NBK20362/.

8. Aizawa. K.; Liu. C.; Tang. S.; et al. Tobacco carcinogen induces both lung cancer and nonalcoholic steatohepatitis and hepatocellular carcinomas in ferrets which can be attenuated by lycopene supplementation. *Int. J. Cancer* **2016**, *139*, 1171-1181.

9. Poon, S. L.; McPherson, J. R.; Tan, P.; Teh, B. T.; Rozen, S. G. Mutation signatures of carcinogen exposure: genome-wide detection and new opportunities for cancer prevention. *Genome Med.* **2014**, *6*, 24.

10. Parkin, D. M. The global health burden of infection-associated cancers in the year 2002. *Int. J. Cancer.* **2006**, *118*, 3030-3044.

11. Seto. M.; Honma. K.; Nakagawa. M. Diversity of genome profiles in malignant lymphoma. *Cancer Sci*. **2010,** *101*, 573-578.

12. Cigudosa, J. C.; Parsa, N. Z.; Louie, D. C.; et al. Cytogenetic analysis of 363 consecutively ascertained diffuse large B-cell lymphomas. *Genes Chromosom. Cancer* **1999**, *25*, 123-133.

13. Hanahan, D.; Weinberg, R. The Hallmarks of Cancer. *Cell* **2000**, *100*, 57–70.

14. Hanahan, D.; Weinberg, R. A. Review Hallmarks of Cancer: The Next Generation. *Cell* **2011**, *144*, 646–674.

15. Peer, D.; Karp, J. M.; S. Hong, S.; Farokhzad, O. C.; Margalit, R.; Langer, R. Nanocarriers as an emerging platform for cancer therapy. *Nat. Nanotechnol.* **2007**, *2*, 751–760.

16. Wilhelm, S.; Tavares, A. J.; Dai, Q.; Ohta, S.; Audet, J.; Dvorak, H. F.; Chan, W.C. Analysis of nanoparticle delivery to tumours. *Nat. Rev. Mater.* **2016**, *1*, 16014.

17. Liu, J.; Li, M.; Luo, Z.; Dai, L.; Guo, X.; Cai, K. *Nano Today* **2017**, *15*, 56–90.

18. Pollard, H.; Remy, J. S.; Loussouarn, G.; Demolombe, S.; Behr, J. P.; Escande, D. Polyethylenimine but not cationic lipids promotes transgene delivery to the nucleus in mammalian cells. *J. Biol. Chem.* **1998**, *273*, 7507–7511.

19. Asati, A.; Santra, S.; Kaittanis, C.; Perez, J. M. Surface-chargedependent cell localization and cytotoxicity of cerium oxide nanoparticles. *ACS Nano* **2010**, *4*, 5321–5331.

20. Tkachenko, A. G.; Xie, H.; Coleman, D.; Glomm, W.; Ryan, J., Anderson, M. F.; Franzen, S.; Feldheim, D. L.; Multifunctional gold nanoparticle-peptide complexes for nuclear targeting. *J. Am. Chem. Soc.* **2003**, *125*, 4700–4701.

21. Suntharalingam, M.; Wente, S. R. Peering through the pore: nuclear pore complex structure, assembly, and function. *Dev. Cell* **2003**, *4*, 775–789.

22. Cook, A.; Bono, F.; Jinek, M.; Conti, E. Structural biology of nucleocytoplasmic transport. *Annu. Rev. Biochem.* **2007**, *76*, 647–671.

23. Kubitscheck, U.; Grünwald, D.; Hoekstra, A.; Rohleder, D.; Kues, T.; Siebrasse, J. P.; Peters, R. Nuclear transport of single molecules dwell times at the nuclear pore complex. *J. Cell Biol.* ***2005***, *168*, 233–243.

24. Biswas, S.; Dodwadkar, N. S.; Deshpande, P. P.; Torchilin, V. P. Liposomes loaded with paclitaxel and modified with novel triphenylphosphonium-PEG-PE conjugate possess low

toxicity, target mitochondria and demonstrate enhanced antitumor effects *in vitro* and *in vivo*. *J. Control Release* **2012**, *159*, 393–402.

25. Liu, J. N.; Bu, W.; Pan, L. M.; Zhang, S.; Chen, F.; Zhou, L.; Peng, W.; Shi, J. Simultaneous nuclear imaging and intranuclear drug delivery by nuclear-targeted multifunctional upconversion nanoprobes. *Biomaterials* **2012**, *33*, 7282-7290.

26. Pan, L.; He, Q.; Liu, J.; Chen, Y.; Ma, M.; Zhang, L.; Shi, J. Nuclear-targeted drug delivery of TAT peptide-conjugated monodisperse mesoporous silica nanoparticles. *J. Am. Chem. Soc.* **2012**, *134*, 5722–5725.

27. Eguchi, A.; Furusawa, H.; Yamamoto, A.; Akuta, T.; Hasegawa, M.; Okahata, Y.; Nakanishi, M. Optimization of nuclear localization signal for nuclear transport of DNAencapsulating particles. *J. Control. Release* **2005**, *104*, 507–519.

28. Ziegler, A, Seelig, J. High affinity of the cell-penetrating peptide HIV-1 Tat-PTD for DNA. *Biochemistry* **2007**, *46*, 8138–8145.

29. Grandinetti, G.; Reineke, T. M. Exploring the mechanism of plasmid DNA nuclear internalization with polymer-based vehicles. *Mol. Pharmaceutics* **2012**, *9*, 2256–2267.

30. Grandinetti, G.; Smith, A. E.; Reineke, T. M. Membrane and nuclear permeabilization by polymeric pDNA vehicles: efficient method for gene delivery or mechanism of cytotoxicity? *Mol. Pharmaceutics* **2012**, *9*, 523–538.

31. Modica-Napolitano, J. S.; Singh, K. K. Mitochondrial dysfunction in cancer. *Mitochondrion* **2004**, *4*, 755-762.

32. Dias, N.; Bailly, C. Drugs targeting mitochondrial functions to control tumor cell growth. *Biochem. Pharmacol.* **2005**, *70*, 1–12.

33.Vyas, S.; Zaganjor, E.; Haigis, M. C. Mitochondria and Cancer. *Cell* **2016**, *166*, 555–566.

34. Wallace, D. C. Mitochondria and Cancer. *Nat. Rev. Cancer* **2012**, *12*, 685–698.

35. Fulda, S.; Galluzzi, L.; Kroemer, G. Targeting Mitochondria for Cancer Therapy. *Nat. Rev. Drug Discov.* **2010**, *9*, 447–464.

36. Li, X.; Marani, M.; Yu, J.; Nan, B.; Roth, J. A.; Kagawa, S.; Fang, B.; Denner, L.; Marcelli, M. Adenovirus-mediated Bax overexpression for the induction of therapeutic apoptosis in prostate cancer. *Cancer. Res* **2001**, *61*, 186-191.

37. Weissig, V.; Boddapati, S. V.; D'Souza, G. G. M. Cheng, S. M.; Targeting of low-molecular weight drugs to mammalian mitochondria. *Drug Design Reviews-Online*, **2004**, *1*, 15-28.

38. Ross, M. F.; Kelso, G. F.; Blaikie, F. H.; James, A. M.; Cocheme, H. M.; Filipovska, A.; Da Ros, T.; Hurd, T. R.; Smith, R. A. J. Murphy, M. P. Lipophilic triphenylphosphonium cations as tools in mitochondrial bioenergetics and free radical biology. *Biochemistry (Moscow)* **2005**, *70*, 222-230.

39. Chen, L. B. Mitochondrial membrane potential in living cells, *Annu. Rev. Cell Biol.* **1988**, *4*, 155–181.

40. Yasuzaki, Y., Yamada, Y.; Harashima, H., Mitochondrial matrix delivery using MITO-Porter, a liposome-based carrier that specifies fusion with mitochondrial membranes. *Biochem. Biophys. Res. Commun.* **2010**, *397*, 181-186.

41. Yamada, Y.; Akita, H.; Kamiya, H.; Kogure, K.; Yamamoto, T.; Shinohara, Y.; Yamashita, K.; Kobayashi, H.; Kikuchi, H.; Harashima, H. MITO-Porter: a liposome-based carrier system for delivery of macromolecules into mitochondria via membrane fusion. *Biochim. Biophys. Acta*, **2008**, *1778*, 423-432.

42. Weissig, V., Lizano, C.; Torchilin, V. P. Selective DNA release from DQAsome/DNA complexes at mitochondria-like membranes. *Drug Delivery*, **2000**, *7*, 1-5.

43. D'souza, G. G.; Rammohan, R.; Cheng, S. M.; Torchilin, V. P.; Weissig, V. DQAsome-mediated delivery of plasmid DNA toward mitochondria in living cells. *J. Control. Release* **2003**, *92*, 189-197.

44. Hetz, C.; Chevet, E.; Harding, H. P. Targeting the unfolded protein response in disease. *Nat. Rev. Drug Discov.* **2013**, *12*, 703-719.

45. Maly, D. J.; Papa, F. R. Druggable sensors of the unfolded protein response. *Nat. Chem. Bio.* **2014**, *10*, 892-901.

46. Capitani, M.; Sallese, M. The KDEL receptor: new functions for an old protein. *Febs. Lett.* **2009**, *583*, 3863–3871.

47. Delie, F.; Petignat, P.; Cohen, M. GRP78-targeted nanotherapy against castrate-resistant prostate cancer cells expressing membrane GRP78. *Target Oncol.* ***2013***, *8*, 225–230.

48. Pollock, S.; Antrobus, R.; Newton, L.; Kampa, B.; Rossa, J.; Latham, S.; Nichita, N. B.; Dwek, R. A.; Zitzmann, N. Uptake and trafficking of liposomes to the endoplasmic reticulum. *FASEB J.* **2010**, *24*, 1866–1878.

49. Whitesides, G. M. The 'right' size in nanobiotechnology. *Nat. Biotechnol*. **2003**, *21*, 1161 – 1165.

50. LaVan, D. A.; McGuire, T.; Langer, R. Small-scale systems for in vivo drug delivery. *Nat. Biotechnol.* **2003**, *21*, 1184 – 1191.

51. Lobatto, M. E.; Fuster, V.; Fayad, Z. A.; Mulder, W. J. M. Perspectives and opportunities for nanomedicine in the management of atherosclerosis. *Nat. Rev. Drug Dis*. **2011**, *10*, 835 – 852.

52. Wang, A. Z.; Langer, R.; Farokhzad, O. C. Nanoparticle delivery of cancer drugs. *Annu. Rev. Med*. **2012**, *63*, 185 – 198.

53. Pathak, R. K.; Kolishetti, N.; Dhar, S. Targeted Nanoparticles in Mitochondrial Medicine. *Wiley Interdiscip. Rev. Nanomed. Nanobiotechnol.* **2015**, *7*, 315–329.

54. Ferrari, M. Cancer Nanotechnology: Opportunities and Challenges. *Nat. Rev. Cancer* **2005**, *5*, 161–171.

55. Peer, D.; Karp, J. M.; Hong, S.; Farokhzad, O. C.; Margalit, R.; Langer, R. Nanocarriers as an Emerging Platform for Cancer Therapy. *Nat. Nanotechnol.* **2007**, *2*, 751–760.

56. Sun, T.; Zhang, Y. S.; Pang, B.; Hyun, D. C.; Yang, M.; Xia, Y. Engineered Nanoparticles for Drug Delivery in Cancer Therapy. *Angew. Chem. Int. Ed.* **2014**, *53*, 12320–12364.

57. Jiang, W.; Huang, Y.; An, Y.; Kim, B. Y. S. Remodeling Tumor Vasculature to Enhance Delivery of Intermediate-Sized Nanoparticles. *ACS Nano* **2015**, *9*, 8689–8696.

58. Matsumura, Y.; Maeda, H. A New Concept for Macromolecular Therapeutics in Cancer Chemotherapy: Mechanism of Tumoritropic Accumulation of Proteins and the Antitumor Agent Smancs. *Cancer Res.* **1986**, *46*, 6387–6392.

59. Maeda, H.; Nakamura, H.; Fang, J. The EPR Effect for Macromolecular Drug Delivery to Solid Tumors: Improvement of Tumor Uptake, Lowering of Systemic Toxicity, and Distinct Tumor Imaging in Vivo. *Adv. Drug Deliv. Rev.* **2013**, *65*, 71–79.

60. Rajora, A.; Ravishankar, D.; Osborn, H.; Greco, F. Impact of the Enhanced Permeability and Retention (EPR) Effect and Cathepsins Levels on the Activity of Polymer-Drug Conjugates. *Polymers* **2014**, *6*, 2186–2220.

61. Wang, M.; Thanou, M. Targeting Nanoparticles to Cancer. *Pharmacol. Res.* **2010**, *62*, 90–99.

62. Bazak, R.; Houri, M.; El Achy, S.; Kamel, S.; Refaat, T. Cancer Active Targeting by Nanoparticles: A Comprehensive Review of Literature. *J. Cancer Res. Clin. Oncol.* **2015**, *141*, 769–784.

63. Byrne, J. D.; Betancourt, T.; Brannon-Peppas, L. Active Targeting Schemes for Nanoparticle Systems in Cancer Therapeutics. *Adv. Drug Deliv. Rev.* **2008**, *60*, 1615–1626.

Chapter 2

Self-Assembled Glycosylated-Chalcone-Boronic-Acid Nano-Drug Exhibits Anticancer Activity through Mitochondrial Impairment

This Chapter has been published as:

Ghosh, C.; Gupta, N.; Mallick, A.; Santra, K. M.; Basu, S. *ACS Appl. Bio Mater.* **2018**, *1*, 347−355.

DOI: 10.1021/acsabm.8b00089

2.1. Introduction:

Breast cancer is one of the most commonly detected cancers and a major cause of death among women in the world.[1] Breast surgery, radiotherapy, hormone therapy, and chemotherapy are mainly employed as conventional strategy for treating breast cancer.[2] In a chemotherapy regimen, small-molecule anticancer drugs (paclitaxel, doxorubicin, and cisplatin) have been successfully used in clinics for breast cancer.[3−8] However, treatment with highly cytotoxic drugs involves toxicity that leads to a painful life for patients. Moreover, prolonged exposure to chemotherapeutic drugs resulted in drug resistance.[9−12] As a result, the development of novel biomaterials with anticancer activity is highly necessary for next-generation breast-cancer therapeutics. Small molecules have long been explored as attractive materials to understand cellular mechanisms, leading to the development of blockbuster drugs for cancer therapy.[13−17] Natural (compound 1, Scheme 1a) as well as synthetic chalcones have emerged as one of the interesting privileged structures with diverse biological activities including antimalarial, anti-inflammatory, and anticancer activities.[18−22] Similarly, the boronic acid functional group also attracted much attention due to its ability to interact with biological targets for development of chemical sensors, probes, and drugs.[23−26] Bortezomib (compound 2, Scheme 1a), a peptide-based boronic acid proteasome inhibitor, is already being used in clinics for the treatment of multiple myeloma.[27−30] Hence, fusing these two different chemotypes into a new molecular entity (compound 3, Scheme 1a) for enhanced biological effect has gained lots of interest.[31,32] However, a major limitation for bioactive chalcone and boronic acids is poor water solubility, leading to erratic biodistribution, side effects, and a small therapeutic window.[22,33−36] To overcome these limitations, several nanoplatforms have been explored for the improvement of their pharmacokinetics.[37−40] Nevertheless, most of the nanovectors cause unwanted toxicity through biodegradation and metabolism.[41] Hence, a new concept of direct conjugation of hydrophobic drugs with hydrophilic small molecules (peptides or polyethylene glycol oligomers) leading to selfassembled nanoscale structures emerged as an interesting strategy.[42−46] However, the vector component remains essential to triggering self-assembly into drug-loaded nanoscale platforms. Therefore, vector-less self-assembled pure nanodrugs consisting exclusively of anticancer compounds could become the future of cancer chemotherapy.[47−50] In this work, we report the synthesis of a glycosylated chalcone−boronic acid library through aldol condensation and Cu (II)-mediated click chemistry as key steps. One of the library members was found to induce cell cycle arrest at the G2/M phase by down-regulating cyclin B/CDK1

and activating p21. In addition, it also facilitates the mitochondrial damage through the inhibition of Bcl-2 and Bcl-xl along with the augmentation of Bax, leading to reactive oxygen species (ROS) formation (Scheme 1c). Interestingly, the cytotoxic lead compound (along with other library members) selfassembled into sub-200 nm spherical particles in water, which can entrap a Food and Drug Administration approved drug for the treatment of breast cancer (doxorubicin) to augment breast cancer cell death. This novel glycosylated chalcone−boronic acid derivative can act as a potential vector-free nanodrug for future breast cancer therapy.

2.2. Results & Discussion:

2.2.1. Synthesis of Glycosylated Chalcone−Boronic Acid Library:

Glycosylated chalcone−boronic acids were synthesized in three steps using aldol condensation and Cu (II)-mediated click chemistry (Scheme 1b). First, 5-halo-2-hydroxybenzaldehydes (10a−d) were reacted with 2 azidoethylmethanesulfonate (6) in the presence of cesium carbonate as a base at room temperature for 24 h to obtain 2-(2-azidoethoxy)-5-benzaldehydes (11a−d) in 40−48% yield. 2- Azidoethylmethanesulfonate (6) was synthesized starting from 2-bromoethan-1-ol (4) in an overall 91% yield after two steps.[51] 2-(2-Azidoethoxy)-5-benzaldehydes (11a−d) were further reacted with (4-acetylphenyl) boronic acid (12) in the presence of potassium hydroxide (KOH) by aldol condensation for 12 h to afford azido chalcone−boronic acids (13a−d) in a 31−40% yield. The lower yield in the alkylation of phenolic OH and aldol condensation were attributed to the lower conversion of starting materials into products as well as the decomposition of compounds into silica gel column chromatography.[52] Moreover, the aldol condensation of (4-acetylphenyl) boronic acid (12) was not reported before, and compounds 13a−d were found to be difficult to isolate due to their inherent low stability. Finally, all chalcone−boronic acids were glycosylated by propargyl alcohol modified acetyl protected or deprotected glucose (compounds 8 or 9, respectively) using copper sulfate (CuSO4) in a water/tBuOH (1:1) mixture at room temperature for 24 h to synthesize glycosylated chalcone−boronic-acids (14a−h) in 78−91% yield (Table 1). We used CuSO4 as a catalyst for the click chemistry to avoid any unwanted byproducts generated while using Cu (I) catalysts.[51,53] Moreover, the final compounds (14a−h) were dialyzed to remove any trace of CuSO4 before performing any biological studies. The protected or deprotected propargyl alcohol-modified glucoses (8 or 9) were synthesized from penta-acetyl-protected glucose (7) in 65% and 84% yield,

respectively.[54,55] All of the intermediates and final compounds were characterized by combination of nuclear magnetic resonance (NMR; ^{1}H, ^{13}C, and ^{11}B), Fourier transform infrared (FTIR), and high-resolution mass spectrometry (HRMS); (Figures S1−S85).

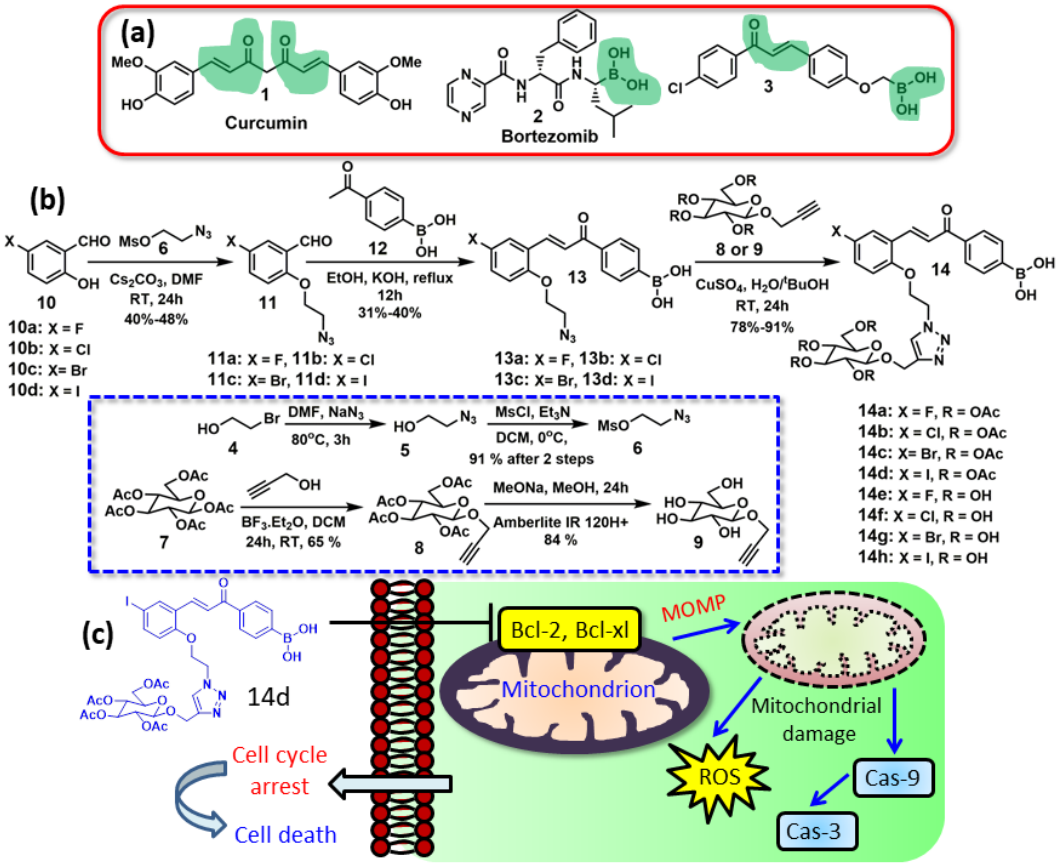

Scheme 1. (a) Structures of natural products having chalocone and boronic acid moieties with diverse biological activity, (b) Synthetic scheme of glycosylated-chalcone-boronic acid library and (c) Mechanism of action of compound 14d in damaging mitochondria in MCF7 cells.

Table 1. Compounds Synthesized in Scheme 1

compounds	X	compounds	X	R
10a	F	**14a**	F	Ac
10b	Cl	**14b**	Cl	Ac
10c	Br	**14c**	Br	Ac
10d	I	**14d**	I	Ac
11a	F	**14e**	F	H
11b	Cl	**14f**	Cl	H
11c	Br	**14g**	Br	H
11d	I	**14h**	I	H
13a	F			
13b	Cl			
13c	Br			
13d	I			

Table 1: List of Synthesized Compounds.

2.2.2 Cytotoxicity of Glycosylated-Chalcone-Boronic Acid Library:

To evaluate the cytotoxicity effect of the glycosylated chalcone−boronic acid derivatives, MCF7 cells were incubated with all of the library members (14a−h) in varying concentrations. At 48 h, cell-growth inhibition was determined using methylthiazolyldiphenyl-tetrazolium bromide (MTT) reagent. Intriguingly, compounds 14b−d showed dose-dependent cell-growth inhibition with having IC50 (50% growth inhibition) values of 33.5, 46.3, and 21.8 μM, respectively (Figure 1a). However, compounds 14b−d showed nearly 92.3 ± 1.5%, 85.5 ± 5.3%, and 84.1 ± 5.5% cell growth inhibition at 100 μM concentration. In contrast, compound 14a showed only 33.0 ± 9.5% cell growth inhibition. The rest of the library members (compounds 14e−h) inhibited only 5.5 ± 1.3%, 25.8 ± 4.7%, 18.5 ± 1.6%, and 36.3 ± 7.9% cell growth, respectively, having a negligible cytotoxic effect with IC50 > 100 μM (Figure 1b). To evaluate the toxicity profile of the protected glycosylated chalcone−boronic acids in noncancerous cells, we treated MCF10A human epithelial mammary gland cells with compounds 14a−d in different concentrations. At 48 h, cell viability assay showed that, even in a 100 μM concentration, 14a−d induced 78.9 ± 2.6%, 66.9 ± 1.1%, 63.9 ± 0.9%, and 96.1 ± 1.4% cell viability, respectively (Figure 2). From this MTT assay, we deduced that the most cytotoxic compound, 14d, is not at all toxic to the noncancerous mammary gland cells. We selected compound 14d for further understanding of the growth-suppressive effect due to its lowest IC50 value.

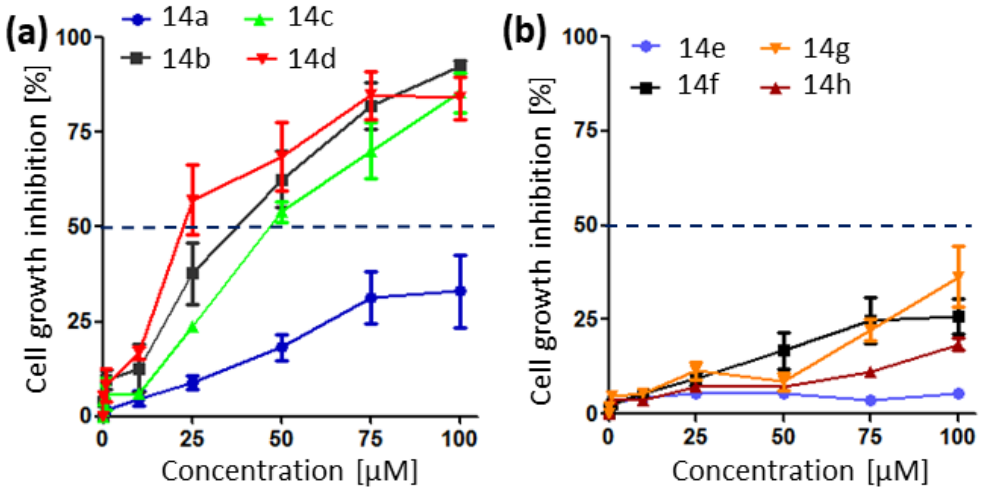

Figure 1. Concentration dependent cell growth inhibition assay of glycosylated-chalocone-boronic acids in MCF7 cells at 48 h post incubation. (a). Compound 14a to 14d, (b). Compound 14e to 14h.

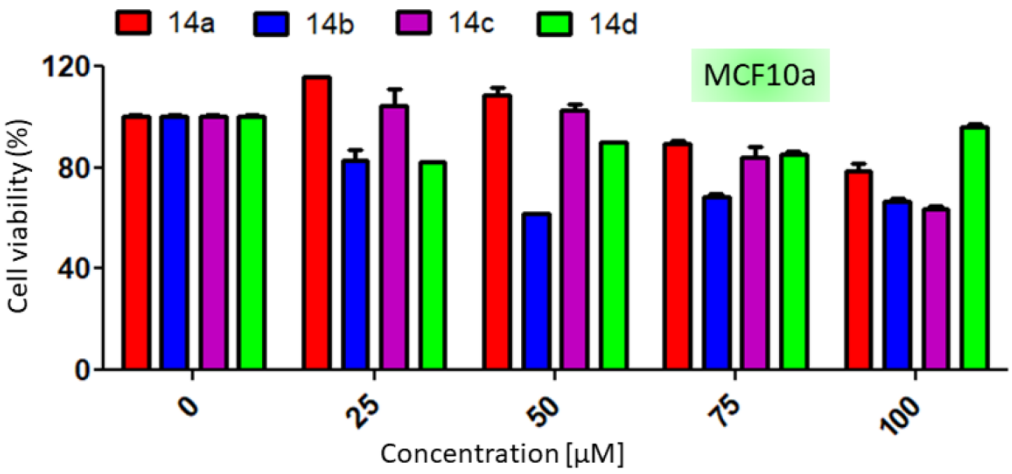

Figure 2: Dose dependent cell viability assay of compound 14a-d in non-cancerous human epithelial breast cells at 48 h post-incubation.

2.2.3. Cell Cycle Arrest and Apoptosis.

We further wanted to understand the mechanism of growth inhibition by compound 14d in breast cancer cells. To this end, we examined the cell cycle profile of MCF7 cells following treatment of compound 14d. MCF7 cells were treated with 20 µM of compound 14d for 24 h, and a profile of different phases of cell cycle was analyzed by flow cytometry using propidium iodide (PI). Results revealed that cells were specifically arrested at the G2/M phase of the cell cycle following treatment of compound 14d (Figure 3a). For example, vehicle treated cells have 34% G2/M, whereas 14d-treated cells have 54% G2/M, indicating that approximately 50% of G2/M population increased following treatment with 14d. To understand how 14d facilitated the G2/M-phase arrest, we checked the levels of cyclin B and CDK1, which are associated with the G2/M phase. Immunoblotting data revealed that levels of cyclin B and CDK1 (cyclin-dependent kinase 1) were significantly declined by a factor of 3.2 and 1.3, respectively, following incubation with 14d (Figures 3b and 4a,b). We further checked the expression of CDK inhibitor p21, which was increased remarkably after treatment with 14d (Figures 3b and 4c). Collectively, our results suggest that 14d potentially arrests the cells at G2/M due to decreased levels of mitotic cyclin/CDK and an increased level of p21.

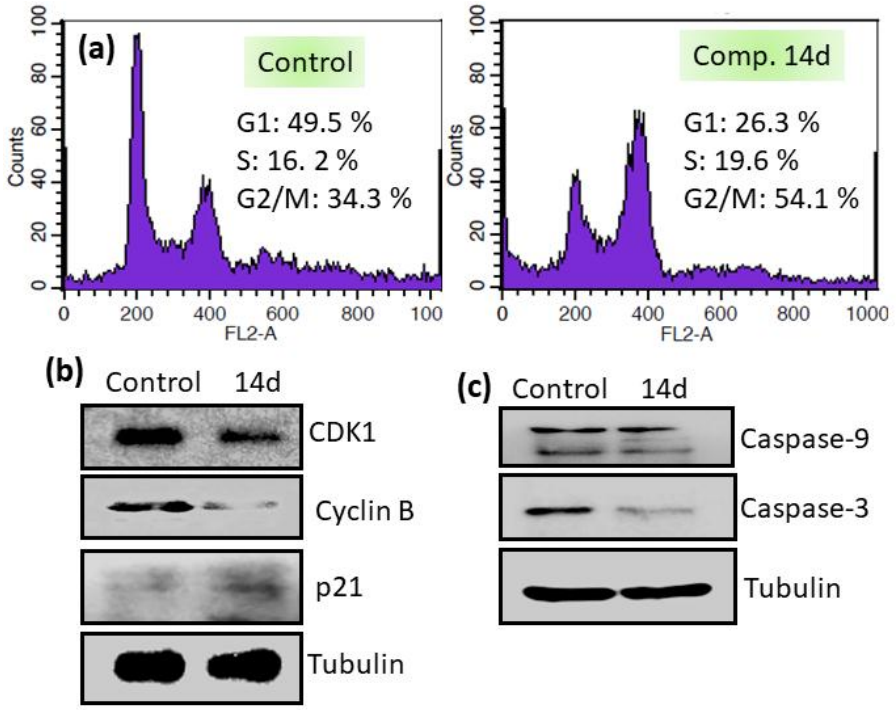

Figure 3. (a) Flow cytometry analysis showing cell cycle arrest induced by compound 14d in MCF7 cells at 24 h post-incubation. (b, c) Western blot analysis of to show the expression of CDK1, cyclin B, p21, Caspase-9 and caspase-3 in MCF7 cells after treatment with compound 14d for 24 h.

Furthermore, we checked whether 14d induces apoptosis to inhibit the growth of cancer cells. Hence, the expression levels of initiator caspase-9 and activator caspase-3 were evaluated by immunoblotting in the absence and presence of 20 μM of 14d for 24 h. Immunoblotting data revealed that total levels of caspase 9 and caspase 3 decreased (Figure 3c). Protein quantification (Figure 4d,e) evidently showed that 14d reduced the level of caspase-9 and -3 by a factor of 1.6 and 2.2, respectively, compared to vehicle (DMSO)-treated cells. The immunoblotting data demonstrated that 14d induced death through the induction of apoptosis and cell cycle arrest.

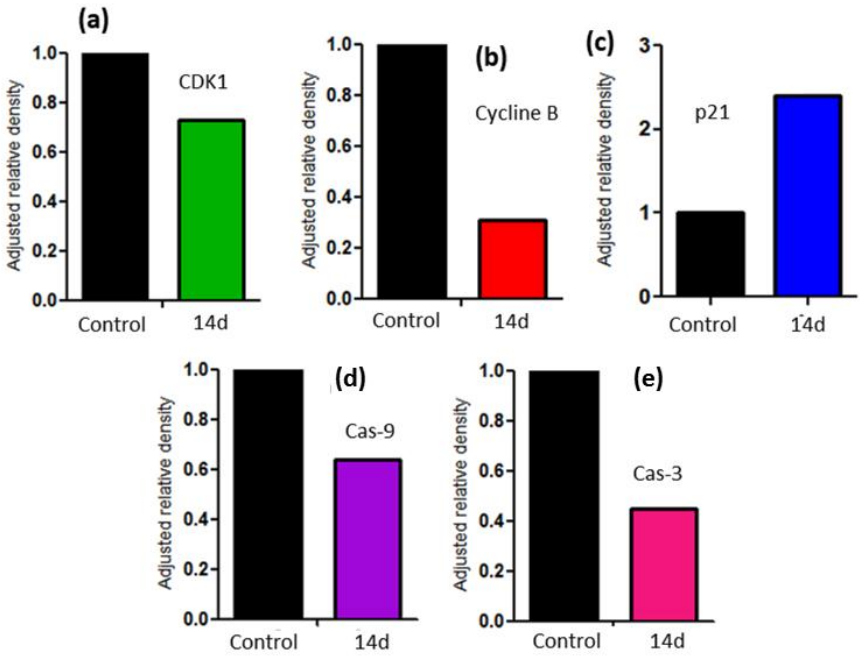

Figure 4: Quantification of (a) CDK1, (b) Cyclin, (c) p21, (d) Caspase-9 and (e) Caspase-3 from western blot after treatment of MCF7 cells with compound 14d for 24 h.

2.2.4. Mitochondrial Damage and Reactive Oxygen Species Generation.

The induction of apoptosis through an intrinsic pathway is associated with disruption of mitochondrial membrane (MOMP).[56,57] MOMP can be estimated by cyanine-based JC1 dye, which shows characteristic fluorescence emission shift from green (~525 nm) to red (~590 nm) by changing from monomeric form (in cytosol) to aggregated form (inside mitochondria).[58] MCF7 cells were treated with 20 µM of 14d for 24 h. Cell were then incubated with JC1 dye for 20 min followed by confocal laser scanning microscopy (CLSM). Fluorescence confocal microscopy images demonstrated that 14d treatment resulted in increased levels of green fluorescence and decreased levels of red fluorescence (Figure 5a). An increased level of fluorescent JC1-monomer compared to the level of red-fluorescent JC1-aggregate was observed, which clearly confirmed that mitochondrial outer membrane was permeabilized, leading to the disaggregation of JC1 dye from mitochondria to cytosol.

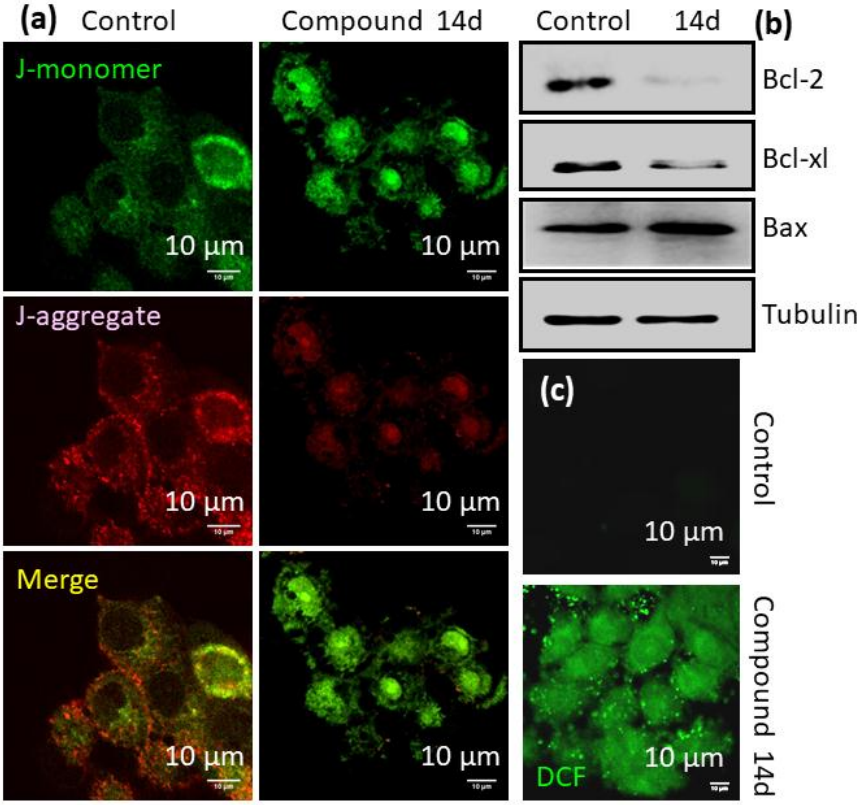

Figure 5: Mitochondrial damage induced by compound 14d. (a) Confocal microscopy images of MCF7 cells after treatment with compound 14d for 24 h followed by treatment with JC1 dye. Scale bar = 10 µm. (b) Western blot analysis of anti-apoptotic Bcl-2, Bcl-xl and pro-apoptotic Bax in MCF7 cells after treatment with compound 14d for 24 h. (c) Confocal microscopy images.

Instead, vehicle (DMSO) incubated cells displayed a comparable amount of J-monomer (green) and a higher level of J-aggregate (red), indicating undamaged mitochondria in MCF7 cells. Further quantification from CLSM also validated that 14d amplified green and red fluorescence signals by a factor of 1.8 in comparison with control cells (Figure 6d). This JC1 assay confirmed that 14d induced cell death in MCF7 cells by mitochondrial damage. MOMP is cascaded through the down-regulation of antiapoptotic B-cell CLL/lymphoma 2 family proteins (Bcl-2 and Bcl-xl) with the simultaneous up-regulation of pro-apoptotic Bcl-2-associated-X-protein (Bax), leading to the pore formation on mitochondrial membrane.[59–61] For the evaluation of the mechanism of MOMP, MCF7 cells were treated with 14d for 24 h, and the expression of Bcl-2, Bcl-xl and Bax was measured through Western blot. From the blot images (Figure 5b) and protein quantification (Figure 6 a, b, c), it was observed that 14d significantly reduced the expression of Bcl-2 and Bcl-xl by 12.5- and 2-fold, respectively,

compared to the control cells. However, 14d increased the expression of pro-apoptotic Bax by 1.9-fold (Figures 5b and 6c). This Western blot analysis revealed that 14d induced mitochondrial damage by inhibiting Bcl-2 and Bcl-xl and up-regulating Bax in MCF7 cells.

Mitochondrial damage through MOMP leads to the ROS generation, which was evaluated through dichlorodihydrofluorescein diacetate (H2DCFDA) assay.[56-62] MCF7 cells were incubated with 14d and treated with nonfluorescent H2DCFDA. The subcellular generation of green fluorescent dichlorofluorescein (DCF) from H2DCFDA upon reaction with ROS was observed by microscopy. The fluorescence images in Figure 5c clearly showed that the treatment of 14d resulted in a significantly increased level of ROS compared to that of non-treated cells. Fluorescence measurement data revealed that 14d increased ROS by a factor of 25 compared to vehicle-treated control cells (Figure 6e). This H2DCFDA assay exhibited that compound 14d mediated mitochondrial damage generated ROS in MCF7 cells.

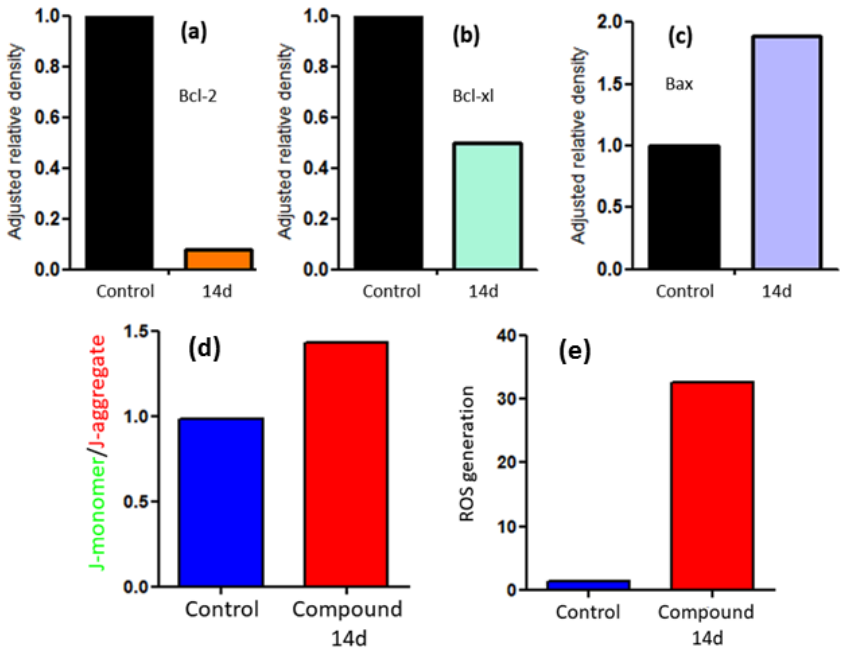

Figure 6: Quantification of (a) Bcl-2, (b) Bcl-xl, (c) Bax, (d) J-monomer/J-aggregate & (e) ROS from western blot after treatment of MCF7 cells with compound 14d for 24 h.

2.2.5 Self-Assembly into Nano-Drug:

We hypothesized that the glycosylation of chalcone−boronic acid would improve the water solubility and self-assembly into pure nanoscale drug for better biodistribution and tumor-tissue accumulation by passive targeting.[63] The self-assembly of 14d in water was evaluated. To our surprise, dynamic light scattering (DLS) and the Tyndall effect showed that 14d self-assembled into 158 nm particles (Figures 7a). Further characterization of the shape, size, and morphology by copy (FESEM), atomic force microscopy (AFM), and transmission electron microscopy (TEM); [Figure 7b−d] unequivocally confirmed that 14d self-assembled into spherical sub-200 nm particles in water. We also observed the self-assembly of all of the library members by electron microscopy. FESEM images confirmed that all of the glycosylated chalcone-boronic acids (14a−h) self-assembled into spherical nanoscale particles (Figures 8 & 9). We further evaluated the critical aggregation constant (CAC) of all of the library members by using a pyrene encapsulation assay through the monitoring of the change in I3 and I1 values in the and hydrophilic environment, respectively.[64] It was observed that acetate protected glycosylated chalcone-boronic acids self-assembled in the range of CAC = 0.21−0.26 mg/mL (Figure 10). However, deprotected glycosylated chalcone− boronic acids showed much less CAC (0.073−0.13 mg/mL; Figure 11). These CAC values demonstrated that unprotected glycosylated chalcone-boronic acids self-assembled much rapidly compared with the protected analogues. Ideally, being more hydrophilic in nature, the unprotected glycosylated chalcone-boronic acids should show higher CAC values compared with protected glycosylated chalcone-boronic acids. We anticipate that the free OH groups on glucose moiety in unprotected chalcone-boronic acids form strong intra- and intermolecular H bonding with boronic acid [B(OH)2] moiety, leading to supra-molecular network-like structures.[37,38] This supra molecular structure might increase the overall hydrophobicity of the unprotected compounds to show lower CAC values. Nevertheless, this kind of intra- and intermolecular H bonding is much weaker in acetyl-protected chalcone-boronic acids, leading to higher CAC values. However, the exact reason for this reverse CAC phenomena is currently not known and under investigation. These light scattering and electron-microscopy data confirmed that all of the library members self-assembled into nanoscale particles in water.

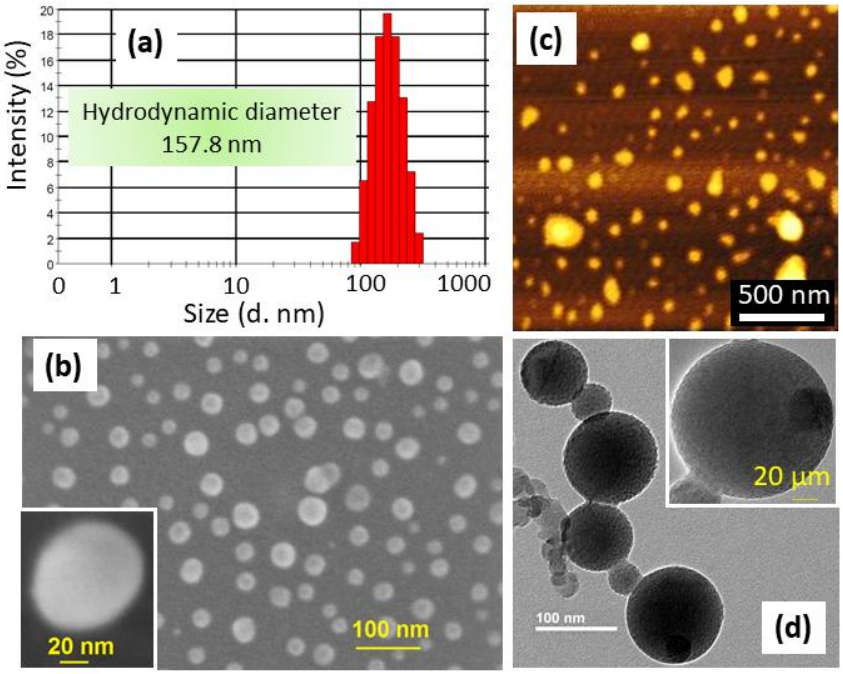

Figure 7: Self-assembly of compound 14d in water was characterized by (a) Dynamic light scattering (DLS), (b) FESEM, (c) AFM and (d) TEM.

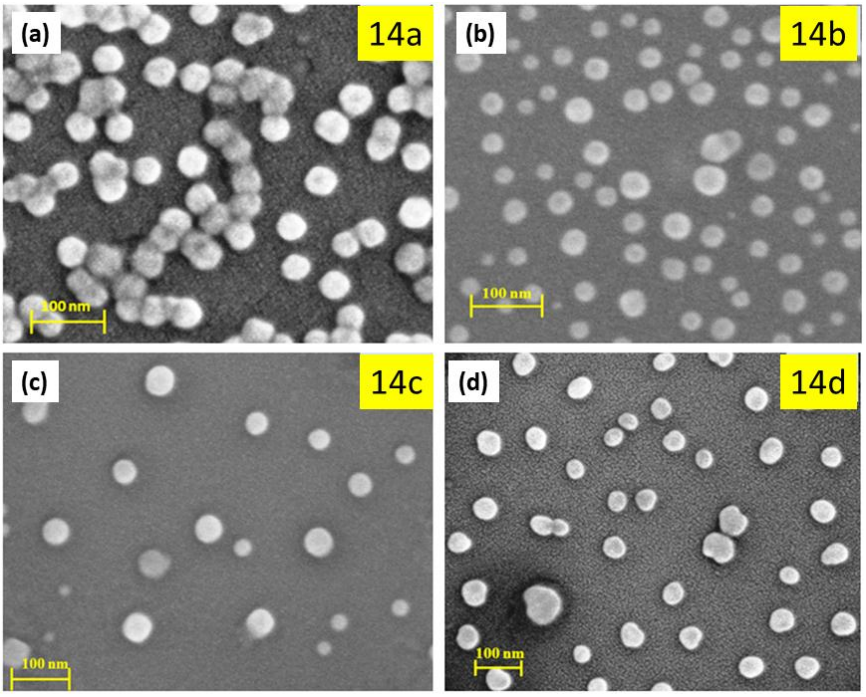

Figure 8: (a-d) FESEM images of nanoparticles from self-assembly of compound 14a, 14b, 14c and 14d respectively in water.

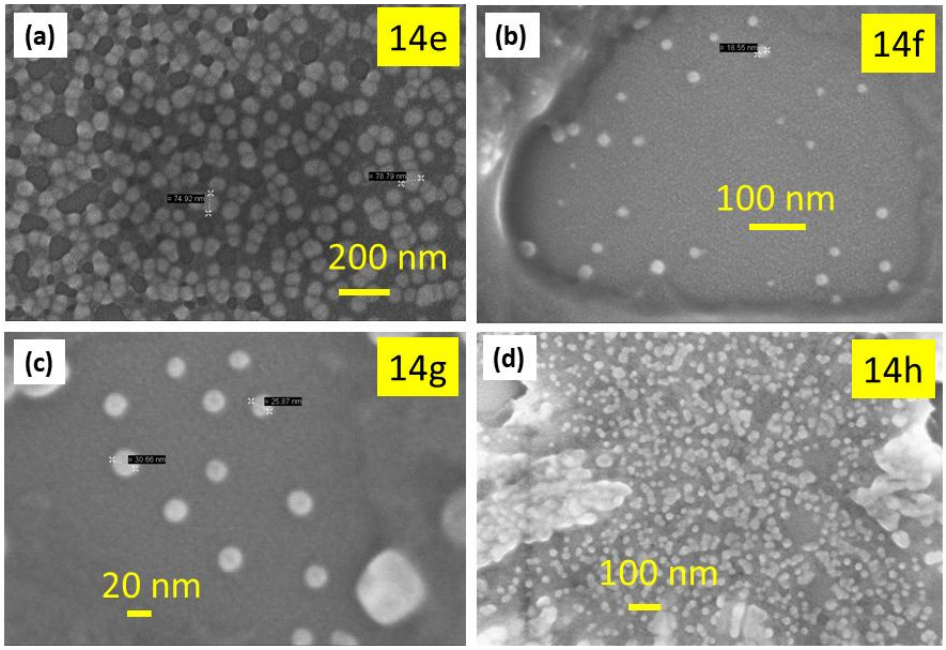

Figure 9: (a-d) FESEM images of nanoparticles from self-assembly of compound 14e, 14f, 14g and 14h respectively in water.

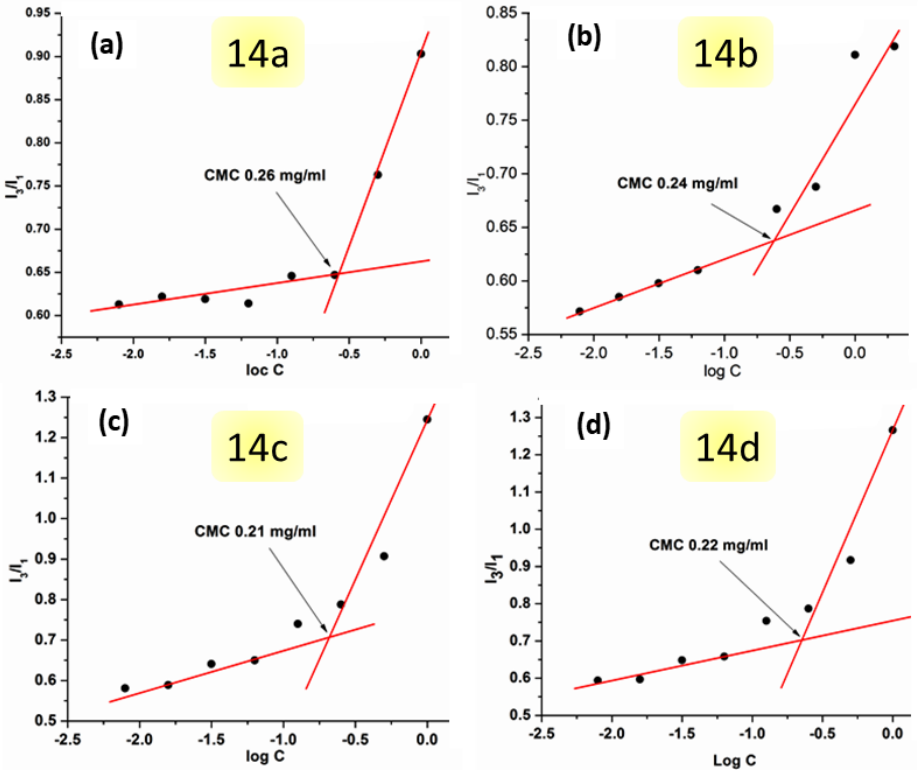

Figure 10. (a-d) Determination of critical aggregation concentration (CAC) of self-assembled nanoparticle from compound 14a, 14b, 14c and 14d by pyrene encapsulation method.

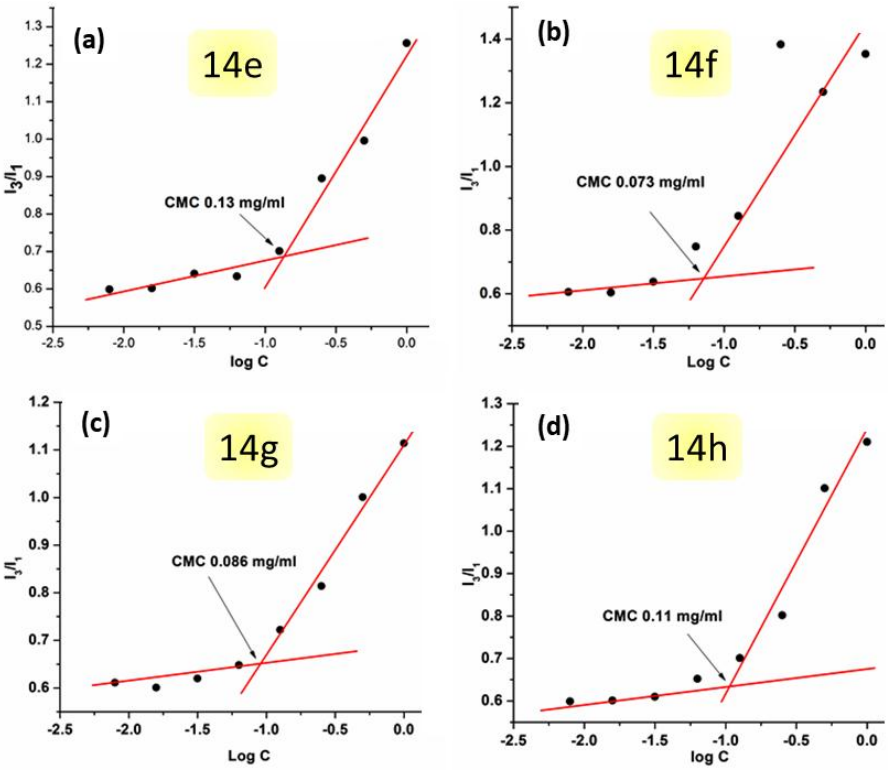

Fiqure 11: (a-d) Determination of critical aggregation concentration (CAC) of self-assembled nanoparticle from compound 14e, 14f, 14g and 14h by pyrene encapsulation method.

2.2.6. Doxorubicin-Encapsulated Nano-Drug:

To explore the potential of our pure nanodrug in combination drug delivery, the Food and Drug Association approved anticancer drug doxorubicin (Dox) was encapsulated into self-assembled nanoparticle generated from 14d. The size and shape of doxorubicin-entrapped nanoparticle (14d-Dox-NP) were characterized by FESEM and confocal microscopy. FESEM images (Figure 12a) showed that 14d-Dox-NP self-assembled into spherical sub-200 nm particles. Further visualization of red fluorescence in CLSM images (Figure 13a) confirmed the presence of doxorubicin into the self-assembled nanoparticles. Moreover, a significant increase (5-fold) in the fluorescence anisotropy of encapsulated doxorubicin in 14d-Dox-NP compared to the free doxorubicin also validated the successful encapsulation of doxorubicin in self-assembled nanoparticle (Figure 13b). To be successful in delivering the drugs into tumor tissues, the nanoparticles should be able to release its payload a acidic environment (mimicking lysosomal compartment).[65] Hence, we evaluated the release of doxorubicin from the nanoparticle at acidic milieu (pH = 5.5) in a timedependent manner using the dialysis method.[66] It was observed that nearly 55.2 ± 1.1% of doxorubicin was released after 96 h

from 14d-Dox-NPs (Figure 12b). As a control, 14d- Dox NPs were also incubated in pH = 7.4 buffer (physiological condition), and the release of doxorubicin was evaluated at different time points. Interestingly, only 14.3 ± 1.3% of doxorubicin was released, even after 96 h, from the self-assembled nanoparticles (Figure 12b). From these microscopy (electron and fluorescence), anisotropy, and release profiles, it was evident that self-assembled compound 14d can entrap the anticancer drug doxorubicin and release it in a tumor environment slowly. Finally, doxorubicin-loaded pure nanodrug was assessed in killing cancer cells. MCF7 breast cancer cells were incubated with 14d-Dox-NPs, and viable cells were measured after 48 h. The MTT data (Figure 12c) confirmed that 14d-Dox-NP showed much improved efficacy with much lower IC_{50} = 1.59 µM, whereas free doxorubicin showed IC_{50} = 5.8 µM and 14 showed IC_{50} = 23.6 µM. This MTT experiment confirmed that doxorubicin-encapsulated self-assembled nanodrug engineered from 14d can kill breast cancer cells more efficiently compared to free drug. However, to fully realize the potential of this nanodrug in clinics, in vivo experiments in murine breast cancer model need to be performed in the future.

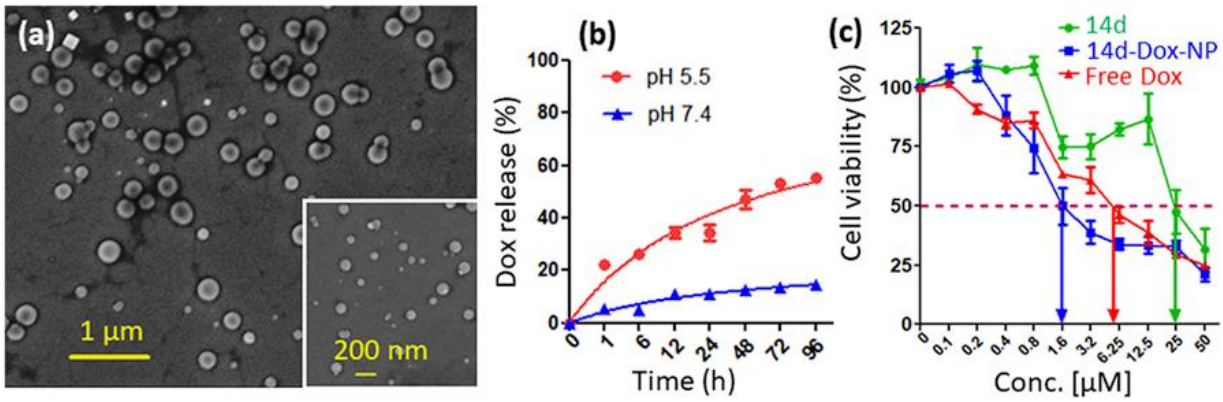

Figure 12: (a) FESEM images of doxorubicin entrapped self-assembled nano-drug from compound 14d. (b) Concentration dependent cell viability assay of doxorubicin loaded self-assembled nano-drug from compound 14d in MCF7 cells after 48 h post incubation.

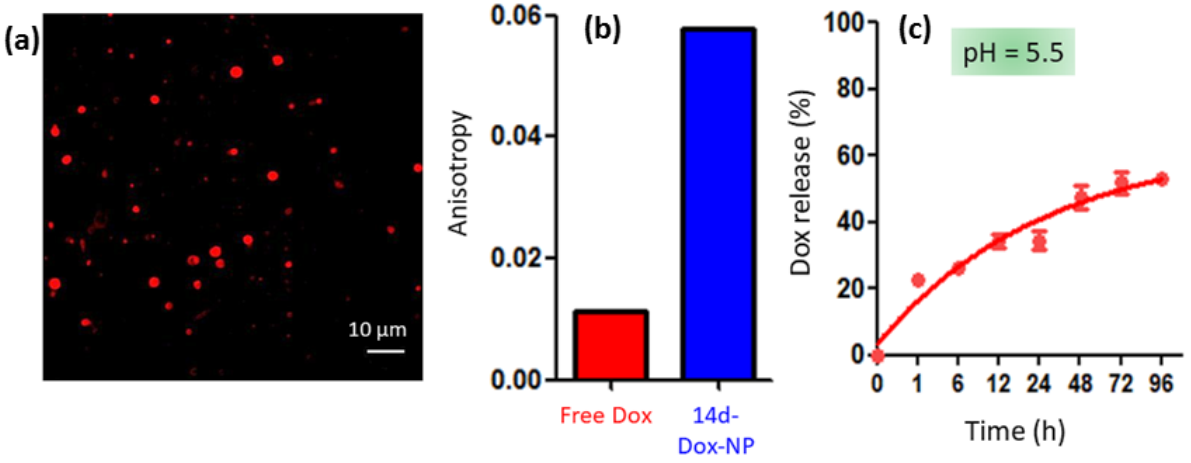

Figure 13: (a) Confocal laser scanning microscopy (CLSM) of doxorubicin encapsulated self-assembled nanoparticle from compound 14d (14d-Dox-NP). (b). Quantification of fluorescence anisotropy of doxorubicin in water as well as in encapsulated into self-assembled nanoparticle from compound 14d. (c). Time dependent release of doxorubicin from doxorubicin encapsulated self-assembled nanoparticle from compound 14d (14d-Dox-NPs) at pH = 5.5.

2.3. Conclusion:

In conclusion, using aldol condensation and click chemistry, we have synthesized a small library of glycolsylated-chalocone-boronic acid derivatives. Cell viability, flow cytometry and western blot analysis revealed that one library member suppresses the growth of cancer cells by simultaneous induction of cell cycle arrest and apoptosis through altering the stability of molecular players associated with these processes. . This lead cytotoxic glycosylated-chalcone-boronic acid triggered mitochondrial damage by inhibiting anti-apoptotic Bcl-2/Bcl-xl and up-regulating pro-apoptotic Bax followed by cleavage of caspase-9/3. Interestingly, all the library members self-assembled in water into nano-scale spherical particle. The self-assembled nanodrug generated from lead molecule can encapsulate anti-cancer drug doxorubicin to show improved efficacy in breast cancer cells. We anticipate that this vector free self-assembled nano-drug could be translated into clinics in future for next-generation combination cancer therapy.

2.4. Materials & Methods:

2.4.1. Materials: Commercially available chemicals and solvents were used without further purification and distillation. Chemical reactions were carried out in inert gas (nitrogen gas) condition. Pre-coated silica gel aluminum sheets 60F254 are used for analytical thin-layer chromatography (TLC), was obtained from EMD Millipore Laboratories. Cell culture media (Dulbecco's modified Eagle's medium (DMEM)) and 3-(4,5- dimethylthiazol-2-yl)-2,5-diphenyltetrazolium bromide (MTT) were purchased from HiMedia. Sodium dodecyl sulfate (SDS), Hanks' balanced salts, N-(2 hydroxyethyl)piperazine-N′-ethanesulfonic acid sodium salt, propidium iodide, Lab Tek chamber slide 8 wells, 5,5′,6,6′-tetrachloro-1,1′,3,3′ tetraethylbenzimidazolylcarbocyanine iodide (JC 1 dye)and 2′,7′-dichlorofluoresceindiacetate (DCFH-DA) were obtained from Sigma-Aldrich. All of the primary and secondary antibodies were obtained from Cell Signaling Technology, Biolegend, and Abcam. Confocal laser scanning microscopy was performed by a Zeiss LSM 710 machine. Flow cytometry analysis was performed using a BD FACS Calibur flow cytometer. Each sample was done in triplicate

2.4.2. Experimental Procedure:

2.4.2.a. General procedure for synthesis of halogenated azo-ethers (11a-d):

5-halo-salicylaldehyde (1 equiv) and Cs_2CO_3 (1.3 equiv) were dissolved into 3 mL dry DMF at inert atmosphere condition. Followed by 2-azidoethyl methanesulfonate (3) was added drop wise and let it allowed to stir at room temperature for 20h. After the completion of the reaction, 10 ml water was added and 5 ml ethyl acetate. The organic layer was separated three times and combined organic layer was washed thrice with brine (10 ml three times). The collective organic layer was dried over Na_2SO_4 and evaporated. The crude was purified by column chromatography with 6% ethyl acetate/hexane.

2.4.2.b. General procedure for aldol condensation reaction to synthesize chalcone-boronic acids (13a-d):

2-(2-azidoethoxy)-5-halobenzaldehyde (1 equiv) and 4-acetylphenylboronic acid (1.2 equiv) were dissolved into ethanol. Ethanolic KOH (4 equiv) was added drop wise at 0 °C and the reaction mixture was allowed for starring for 20 h at room temperature. The reaction was monitored by thin layer chromatography (TLC). After completion, 10 mL water was added and the ethanol was evaporated from the reaction mixture. The reaction mixture was transferred into a beaker and ethyl acetate was added. The pH of the solution was adjusted by adding 1M HCl till pH 3-4. The reaction mixture was separated by ethyl acetate and organic

layer was washed by brine (5 mL X 2). The organic layer was dried over anhydrous Na_2SO_4, filtered and evaporated. The crude product was purified by column chromatography using 25% ethyl acetate/hexane as mobile phase.

2.4.2.c. General procedure of click reaction to synthesize glycosylated-chalcone-boronic acid (14a-h):

Compound 13 (1 equiv) and compound 8 or 9 (1 equiv) were dissolved into ^tBuOH: H_2O (1:1), followed by addition of $CuSO_4$ (0.2 equiv) and sodium ascorbate (0.5 equiv) and the reaction was stirred for 24 h at room temperature. After the completion of the reaction, ^tBuOH was evaporated from reaction mixture and organic layer was extracted from ethyl acetate/water. The organic layer was dried over anhydrous Na_2SO_4, filtered and evaporated under reduced pressure. The crude product was purified by 60-70% ethyl acetate/hexane by silica gel column chromatography.

2.4.3. Determination of size distribution of nanoparticles by dynamic light scattering (DLS):

The mean particle size of compound 14d is determined by dynamic light scattering (DLS) method using Zetasizer-Malvern instrument in aqueous medium in triplicate.[67]

2.4.4. Determination of shape of nanoparticles by Field-emission scanning electron microscopy (FESEM):

Eight microliters of compound 14d in aqueous solution was drop casted in a silicon coated chip and dried at room temperature under vacuum desiccators for 24h. The silicon wafer was gold coated (30−40 nm thickness) using Quorum, Q150T-E5 after complete evaporation of solvent. The images were taken using Carl Zeiss-Ultra plus (FE-SEM) instrument at voltage of 4.0 kV.[67]

2.4.5. Determination of shape of nanoparticles by Atomic force microscopy (AFM):

The aqueous solution of compound 14d drop casted on mica sheet and dried using high vacuum pump till complete removal of solvent. Size, shape, morphology and height of nanoparticles were measured using Nano-Wizard-AFM.[67]

2.4.6. Determination of size and shape of nanoparticles by TEM: The aqueous solution of 14d was drop casted on copper coated TEM grid. The sample was allowed to settle down and after one hour the solvent was removed. After removal of the excess solvent from TEM grid,

the grid was washed thrice. Finally fresh solution of 0.5% uranyl acetate was placed on the TEM grid. After 5 min, the uranyl acetate solution was removed and the sample was washed thrice with water. The sample was kept overnight for complete removal of water from TEM grid. The sample was imaged using TEM instrument.[67]

2.4.7. Determination of critical aggregation constant (CAC). Pyrene solution of 2×10^{5} M was prepared in acetone. Each of the compounds was taken in eight different concentrations (0.1, 0.5, 0.25, 0.125, 0.626, 0.03125, 0.0156, 0.0078 mg) and 50 µL of the pyrene stock solution was added. Pyrene was added such a way that the final concentration of pyrene should be 10^{6} µM. After acetone was evaporated and 1 mL of distilled water was added. The samples were sonicated and kept for 1 h to homogenization. In steady state fluorescence the sample was excited at 317 nm and emission was recorded at 371 nm (I_1) and at 383 nm (I_3). After this I_3/I_1 was calculated and a graph was plotted for I_3/I_1 vs log C. The intersecting point depicts the critical aggregation concentration (CAC) in each graph.

2.4.8. Determination of drug release from Dox-14d nanoparticle:

The release of doxorubicin from 14d-Dox-NPs was determined at lysosomal pH = 5.5 and physiological pH = 7.4 at different time points. The doxorubicin encapsulated 14d sample was taken 250 µL and placed in a 500 Da dialysis membrane both for pH= 5.5 and pH= 7.4. These bags were placed into 2mL of pH = 5.5 and pH = 7.4 solution at 25^{o}C. A 200 µL portion of the aliquot was collected from dialysis bag and recorded the absorbance at preplanned time intervals by UV-Vis spectroscopy. (λ_{max} = 498 nm).[67]

2.4.9. Determination of Cell viability (MTT Assay):

Five thousand MCF7 cells were placed in 96-wells plate and incubated overnight at 37^{o}C in 5% carbon dioxide environment. After attachment of cells, the cells were treated with varying concentration of 14d drug for 48h time. Next, 5mg/ml solution of MTT in water was added in individual wells and incubated for 4h at 37^{o}C. Finally, media was removed from 96-well plate and 100 µL DMSO was added. After keeping for 5 mins absorbance was recorded at 540 nm. The cell viability was calculated using absorbance values. [67]

2.4.10. Experimental procedure of Cell cycle analysis by FACS:

5×10^{5} MCF7 cells were seeded in a 6 well plate and kept overnight for attachment. 20 µM aqueous solutions of 14d was added into each plate and allowed to keep for 24h. After 24h

treatment of this drug, the media was removed and washed with chilled PBS. Next, the cells were detached with trypsin and plated down using centrifuge at 1000 rpm for 5mins. The supernatant was removed and the plated cells were fixed with 70% ethanol in water. After fixation 500 ml RNase-PI solution was added and analyzed the cells by flow cytometry. [67]

2.4.11. Experimental procedure of Western blot analysis:

MCF7 cells were seeded one day prior to the treatment. Next day, cells were incubated with either 0.1% DMSO (treated as control) or 20 μM compound 14d for 24 h. The cells were then harvested, washed with ice cold PBS buffer and lysed in lysis buffer (50 mM Tris pH7.4, 5 mM EDTA, 250 mM NaCl, 10 mM sodium fluoride, 0.5mM sodium orthovanadate and 0.5% Triton X100) on ice for 20 minutes. Lysates were then centrifuged at 13000xg for 20 minutes at 4 °C. The supernatants were collected and the protein concentration was estimated using Bradford method using bovine serum albumin as a standard. The protein samples were prepared in 1X Lamelli Buffer (250 mM Tris HCl pH 6.8, 10% SDS Glycerol 50%, β-mercaptoetanol 5%, Bromophenol blue 0.12%) and boiled for 5 minutes. The protein samples were then resolved in SDS-PAGE and transferred onto polyvinylidene fluoride membrane (Merck Millipore, Billerica, MA, USA). Skimmed milk (3%) in TBST was used for blocking the membrane for 1 h. The membrane was then washed and incubated with the respective primary antibodies [Cyclin A (sc-70896), Cyclin B (Sc-22776), Cyclin E (Sc-481), Cyclin D (sc-717), CDK1 (MA5-15824), CDK4 (sc-70832) and Tubulin (Sigma T5168)] at 4 °C for overnight. The membrane was then washed thrice with TBST and incubated with respective HRP conjugated secondary antibody [Goat anti-rabbit IgG-HRP (sc-2004), Goat anti-mouse IgG-HRP (sc-2005)]. Immunoblots were developed in Amersham Imager 600, GE using chemiluminescence substrate from Thermo Scientific.[67]

2.4.12. Determination of mitochondrial outer membrane permeabilization by JC1 assay:

Ten thousand MCF7 cells were seeded in a Lab Tek chamber and 20μM aqueous solution of 14d was treated for 24h. After the drug treatment, JC1 dye (10ug/ml) was added at 37^{o}C for half an hour. Similarly, a control experiment was performed. Finally, the cells were imaged using confocal microscopy [Emission= 535 nm green {JC1 monomeric} / 590 nm red {JC1 aggregate] and showed green/red emission.[68]

2.4.13. Determination of ROS Generation by DCFH-DA Assay: After treatment with compound 14d, the cells were then washed with chilled PBS and treated with DCFH-DA for 30 min. Finally, the cells were washed thrice with PBS (pH 7.4) and visualized by confocal microscopy.[68]

2.4.14. Spectroscopic characterization:

2-(2-azidoethoxy)-5-fluorobenzaldehyde (11a):

Yield: 42 %

1H NMR (CDCl3, 400MHz): δ = 10.70 (s, 1H), 7.564 (dd, *J* = 8.8, 2.4 Hz, 1H), 7.29 (m, 1H), 6.975 (dd, *J* = 8.8, 2.4 Hz, 1H), 4.271 (t, *J* = 4.8 Hz, 2H), 3.694 (t, *J* = 4.8 Hz, 2H).

13C NMR (CDCl3, 100MHz): δ = 188.4, 158.6, 156.5, 125.9, 122.6, 114.5, 114.2, 68.2, 50.3.

ESI-HRMS: Observed m/z for [M-N2+H]+ = 182.0630.

2-(2-azidoethoxy)-5-cholorobenzaldehyde (11b):

Yield: 45.0%

1H NMR (CDCl3, 400MHz): δ = 10.434 (s, 1H), 7.8115 (d, *J* = 2.8 Hz, 1H), 7.495(dd, *J* = 2.8 Hz, 1H), 6.931(d, *J* = 9.2 Hz, 1H), 4.253 (t, *J* = 4.8 Hz, 2H), 3.686 (t, *J* = 4.8 Hz, 2H).

13C NMR (CDCl3, 100MHz): δ =188.2, 158.9, 135.5, 128.4, 127.4, 126.0, 114.1, 68.0, 50.3.

ESI-HRMS: Observed m/z for [M+Na]+ = 248.0211.

2-(2-azidoethoxy)-5-bromobenzaldehyde (11c):

Yield: 40.4%

1H NMR (CDCl3, 400MHz): δ = 10.45 (s, 1H), 7.95(d, *J* = 2.8 Hz, 1H), 7.63 (dd, *J* = 8.8 Hz, 2.8 Hz, 1H), 6.877(d, *J* = 8.8 Hz, 1H), 4.248 (t, *J* = 4.8 Hz, 2H), 3.686 (t, *J* = 4.8 Hz, 2H).

13C NMR (CDCl3, 100MHz): δ = 188.0, 159.4, 138.4, 131.4, 126.4, 114.5, 67.9, 50.2.

ESI-HRMS: Observed m/z [M+Na]+ = 291.9697.

2-(2-azidoethoxy)-5-iodobenzaldehyde (11d):

Yield: 43.5%

1H NMR (CDCl3, 400MHz): δ = 10.37 (s, 1H), 8.12 (d, *J* = 2.4 Hz, 1H), 7.811(d, *J* = 8.8 Hz, 2.4 Hz, 1H), 6.763(d, *J* = 8.8 Hz, 1H), 4.240 (t, *J* = 4.8 Hz, 2H), 3.682 (t, *J* = 4.8 Hz, 2H);

13C NMR (CDCl3, 100MHz): δ = 188.2, 160.5, 144.5, 137.7, 127.19, 115.2, 68.1, 50.5.

ESI-HRMS: Observed m/z [M+Na]+ =339.9559.

(E) -4-(3-(2-(2azidoethoxy)-5-fluorophenyl) acryloyl) phenylboronic acid (13a):

Yield: 30.5%

1H NMR (MeOH-d4, 400MHz): δ = 8.20 (m, 3H), 7.818 (d, *J* = 16.0 Hz, 1H), 7.561 (dd, *J* = 8.8 Hz, 2.4 Hz, 1H), 7.125 (m, 1H), 7.076 (m, 1H), 6.898 (d, *J* = 8.8 Hz, 2H), 4.236 (t, *J* = 4.8 Hz, 2H), 3.720 (t, *J* = 4.8 Hz, 2H);

13C NMR (MeOH-d4, 100MHz): δ = 190.9, 163.9, 159.9, 157.5, 155.1, 138.8, 132.4, 130.9, 126.9, 125.0, 118.9, 118.6, 116.4, 115.9, 115.7, 115.2, 69.3, 51.4.

11B NMR (MeOH-d4, 128.32 MHz): δ = 18.627

ESI-HRMS: Observed m/z for [M-N2+H]+ = 328.1101

(E) -4-(3-(2-(2azidoethoxy)-5-chlorophenyl) acryloyl) phenylboronic acid (13b):

Yield: 29.7%

1H NMR (MeOH-d4, 400MHz): δ = 8.23 (d, *J* = 8.8 Hz, 2H), 7.984 (d, *J* = 16.00 Hz, 1H), 7.838 (d, *J* = 16.0 Hz, 1H), 7.775 (d, *J* = 2.4 Hz, 1H), 7.377 (dd, *J* = 8.8 Hz, 2.8 Hz, 1H), 7.082 (d, *J* = 8.8 Hz, 1H), 6.894 (d, *J* = 8.8 Hz, 1H), 4.265 (t, *J* = 4.8 Hz, 2H), 3.742 (t, *J* = 4.8 Hz, 2H).

13C NMR (MeOH-d4, 100MHz): δ = 190.7, 163.7, 157.3, 138.4, 132.2, 131.9, 130.6, 129.4, 127.3, 126.9, 125.0, 116.2, 114.9, 68.1, 51.2.

11B NMR (128.32MHz, MeOH-d4): δ= 18.4

ESI-HRMS: Observed m/z for [M-N2+H]+ = 366.0624.

(E) -4-(3-(2-(2-azidoethoxy)-5-bromophenyl) acryloyl) phenylboronic acid (13c):

Yield: 25.6%

1H NMR (MeOH-d4, 400MHz): δ = 8.015 (d, *J* = 8.8 Hz, 2H), 7.955 (d, *J* = 16.0 Hz, 1H), 7.881 (d, *J* = 2.4 Hz, 1H), 7.817 (d, *J* = 16.0 Hz, 1H), 7.486 (dd, *J* = 8.8 Hz, 2.4 Hz, 1H), 6.697 (d, *J* = 8.8 Hz, 1H), 6.894 (d, *J* = 8.8 Hz, 2H), 4.235 (t, *J* = 4.8 MHz, 2H).

13C NMR (MeOH-d4, 100MHz): δ = 190.8, 163.9, 157.9, 138.5, 135.1, 134.4, 132.6, 132.4, 131.9, 130.8, 127.5, 125.2, 116.4, 115.5, 114.6, 68.9, 51.3.

11B NMR (MeOH-d4, 128.32MHz): δ = 19.561

HR-MS: Observed m/z for [M-N2+H]+ = 456.0540, & [M-N2+H+2]+ = 458.0059.

(E) -4-(3-(2-(2-azidoethoxy)-5-iodophenyl) acryloyl) phenylboronic acid (13d):

Yield: 27.5%

1H NMR (MeOH-d4, 400MHz): δ = 8.046 (d, *J* = 2.4 Hz, 1H), 8.022 (d, *J* = 8.8 Hz, 2H), 7.930 (d, *J* = 16.0 Hz, 1H), 7.820 (d, *J* = 16.0 Hz, 1H), 7.681 (dd, *J* = 8.8 Hz, 2.4 Hz, 1H), 6.897 (dd, *J* = 8.8 Hz, 3H), 4.247 (t, *J* = 4.8 Hz, 2H), 3.742(t, *J* = 4.8 MHz, 2H).

13C NMR (MeOH-d4, 100MHz): δ = 190.9, 163.9, 158.7, 141.2, 138.8, 138.5, 132.4, 130.9, 127.9, 125.1, 116.4, 115.8, 84.2, 68.7, 51.3.

11B NMR (MeOH-d4, 128.32MHz): δ= 22.5.

HR-MS: Observed m/z for [M-N2+H]+= 436.0169.

Compound 14a:

Yield: 84%

1H NMR (CDCl3, 400MHz): δ = 7.963 (d, *J* = 8.8 Hz, 2H), 7.907 (d, *J* = 16.0 Hz, 1H), 7.799 (s, 1H), 7.472 (d, *J* = 16.0 Hz, 1H), 7.368 (dd, *J* = 8.8 Hz, 2.4 Hz, 1H), 7.018 (m, 1H), 6.958 (d, *J* = 8.8 Hz, 2H), 6.880 (dd, *J* = 8.8 Hz, 2.4 Hz, 1H), 5.135 (t, *J* = 9.2 Hz, 1H), 5.5055 (t, *J* = 9.2 Hz, 1H), 4.956 (m, 1H), 4.090 (m, 1H), 4.817 (t, *J* = 4.8 Hz, 2H), 4.771 (d, *J* = 8 Hz, 1H), 4.663 (d, *J* = 8.00 Hz, 1H), 4.429 (t, *J* = 4.8 Hz, 2H), 4.167(dd, *J* = 8.0 Hz, 4.4 Hz, 2H), 3.701 (m, 1H), 2.054 (s, 5H), 1.973 (s, 7H).

13C NMR(CDCl3, 100MHz): δ = 189.1, 171.0, 170.3, 169.7, 169.6, 161.4, 156.4, 152.9, 144.2, 139.4, 137.1, 131.4, 124.7, 118.0, 117.7, 115.8, 114.6, 114.5, 114.1, 113.9, 113.8, 100.0, 72.9, 71.9, 71.3, 68.5, 67.8, 62.6, 61.9, 50.9, 50.0.

ESI-HRMS: Observed m/z for [M-N2+H]+ = 714.2300, 715.2332 & [M-N2+Na]+ = 736.2119, 737.2151.

Compound 14b:

Yield: 85.6%

1H NMR (CDCl3, 400MHz): δ = 7.973 (d, *J* = 8.8 Hz, 2H), 7.0909 (d, *J* = 16.0 Hz, 1H), 7.790 (s, 1H), 7.624 (d, *J* = 2.4 Hz, 1H), 7.492 (d, *J* = 16.0 Hz, 1H), 7.280 (dd, *J* = 8.8 Hz, 2.4 Hz, 1H), 6.975 (d, *J* = 8.8 Hz, 2H), 6.791 (d, *J* = 8.8 Hz, 1H), 5.136 (t, *J* = 9.6 Hz, 1H), 5.043 (t, *J* = 9.6 Hz, 1H), 4.945 (m, 1H), 4.887 (d, *J* = 12.8 Hz, 1H), 4.829 (m, 2H), 4.768 (d, *J* = 12.8 Hz, 1H), 4.662 (m, 1H), 4.438 (t, *J* = 4.8 Hz, 2H), 4.235 (m, 1H), 4.169 (m, 2H), 3.71 (m, 2H), 2.055 (s, 3H), 1.97 (s, 9H).

13C NMR (CDCl3, 100MHz): δ = 189.3, 171.3, 170.8, 170.6, 169.9, 161.7, 155.5, 144.6, 137.1, 131.8, 131.7, 131.4, 130.7, 128.3, 127.6, 126.5, 125.0, 124.7, 116.2, 114.0, 100.3, 73.2, 72.2, 68.8, 67.7, 62.9, 62.2, 50.2.

ESI-HRMS: Observed m/z for [M+H]+ = 757.2225, 758.2155.

Compound 14c:

Yield: 86.8%

1H NMR (CDCl3, 400MHz): δ = 7.973 (d, *J* = 8.8 Hz, 2H), 7.904 (d, *J* = 16.0 Hz, 1H), 7.783 (s, 1H), 7.763 (d, *J* = 2.4 Hz, 1H), 7.480 (d, *J* = 16.0 Hz, 1H), 7.421 (dd, *J* = 8.8 Hz, 2.4 Hz, 1H), 6.976 (dd, *J* = 8.8 Hz, 1H), 6.740 (d, *J* = 8.8 Hz, 1H), 5.131 (t, *J* = 9.2 Hz, 1H), 5.039 (t, *J* = 9.6 Hz, 1H), 4.929 (m, 2H), 4.826 (m,1H), 4.762 (d, *J* = 12.8 Hz, 1H), 4.656 (d, *J* = 8.0 Hz, 1H), 4.436 (t, *J* = 4.9Hz, 1H), 4.17 (dd, *J* = 11.8 Hz, 3.4 Hz, 1H), 3.707 (m, 1H), 3.39 (t, *J* = 7.2 Hz, 2H), 2.41 (d, *J* = 8.1Hz,1H), 2.059 (s, 3H), 2.026 (s, 3H), 1.97 (s, 6H).

13C NMR (CDCl3, 100MHz): δ = 188.9, 171.0, 170.3, 169.7, 169.6, 161.5, 155.6, 144.3, 139.4, 136.7, 133.6, 131.5, 130.9, 130.4, 126.7, 124.6, 124.5, 115.8, 114.5, 104.0, 72.9, 71.9, 71.3, 68.5, 67.3, 62.6, 61.9, 49.8, 49.7.

ESI-HRMS: Observed m/z for [M-H]+ = 800.1658 and [M-H+2]+ = 802.1651.

Compound 14d:

Yield: 88.5%

1H NMR(CDCl3, 400MHz): δ = 7.970 (d, *J* = 8.8 Hz, 2H), 7.933 (s, 1H), 7.866 (d, *J* = 15.6 Hz, 1H), 7.610 (t, *J* = 8.8 Hz, 1H), 7.472 (d, *J* = 15.6 Hz, 1H), 6.968 (d, *J* = 8.8 Hz, 2H), 6.628 (d, *J* = 8.8 Hz, 1H), 5.134 (m, 1H), 5.054 (d, *J* = 5.5 Hz, 1H), 4.951 (t, *J* = 4.8 Hz, 2H), 4.825 (m, 2H), 4.761 (d, *J* = 12.8 Hz, 1H), 4.657 (d, *J* = 8.0 Hz, 1H), 4.429 (t, *J* = 4.8 Hz, 2H), 4.187 (m, 2H), 3.719 (d, *J* = 9.6 Hz, 1H), 2.507 (s, 4H), 1.976 (s, 8H).

13C NMR (CDCl3, 100MHz): δ = 189.0, 171.0, 170.4, 169.7, 169.6, 161.4, 156.4, 140.0, 139.4, 136.9, 136.7, 131.4, 127.1, 124.6, 124.3, 115.8, 114.5, 114.2, 100.0, 72.9, 71.9, 71.3, 68.5, 67.2, 62.6, 61.9, 50.9, 49.8.

ESI-HRMS: Observed m/z for [M-N2+H]+ = 822.1336, 823.1393, [M-N2+Na]+ = 844.1179, 845.1209.

Compound 14e:

Yield: 82%

1H NMR (DMSO-d6, 400MHz): δ = 8.216 (s, 1H), 8.076 (d, *J* = 8.8 Hz, 2H), 7.893 (d, *J* = 16.0 Hz, 1H), 7.797 (d, *J* = 16.0 Hz, 1H), 7.258 (m, 1H), 7.140 (m, 1H), 6.906 (d, *J* = 8.8 Hz, 2H), 6.832 (t, *J* = 8.8 Hz, 1H), 5.017 (br s, 1H), 4.915 (br s, 1H), 4.852 (m, 2H), 4.619 (d, *J* = 12.0 Hz, 1H), 4.511 (t, *J* = 5.2 Hz, 2H), 4.266 (d, *J* = 8.0 Hz, 1H), 4.030 (q, *J* = 7.2 Hz, 1H), 3.691 (d, *J* = 8.0 Hz, 1H), 3.465 (m, 1H), 3.119 (m, 2H), 3.021 (t, *J* = 5.2 Hz, 2H).

13C NMR (DMSO-d6, 100MHz): δ = 187.0, 162.1, 143.8, 135.6, 131.4, 131.2, 128.9, 124.6, 123.7, 117.7, 115.3, 115.0, 115.0, 102.1, 76.8, 76.6, 73.3, 70.0, 67.4, 61.4, 61.0, 59.0, 48.8.

11B NMR (DMSO-d6, 128.32 MHz): δ = 25.35.

ESI-HRMS: Observed m/z for [M-N2+H]+ = 546.1447, [M-N2+Na]+ = 568.1701, 569.1733.

Compound 14f:

Yield: 80%

1H NMR (DMSO-d6, 400MHz): δ = 8.199 (d, *J* = 8.8 Hz, 2H), 7.915 (d, *J* = 16.0 Hz, 1H), 7.757 (d, *J* = 16.0 Hz, 1H), 7.441 (dd, *J* = 8.8, 2.4 Hz, 1H), 7.265 (dd, *J* = 8.0, 2.4 Hz, 1H), 7.191 (d, *J* = 2.4 Hz, 1H), 7.017 (d, *J* = 8.8 Hz, 1H), 6.843 (d, *J* = 8.8 Hz, 2H), 5.042 (dd, *J* = 12.4 Hz, 2H), 4.937 (m, 2H), 4.849 (m, 2H), 4.729 (t, *J* = 4.8 Hz, 2H), 4.643 (d, *J* = 12.8 Hz, 1H), 4.380 (t, *J* = 5.6 Hz, 2H), 4.263 (dd, *J* = 4.8 Hz, 1H), 4.047 (s, 1H);

13C NMR (DMSO-d6, 100MHz): δ = 190.2, 163.3, 143.8, 131.5, 131.2, 131.1, 128.8, 128.3, 125.3, 124.8, 124.6, 124.1, 118.7, 115.3, 102.2, 76.9, 76.7, 73.3, 70.1, 70.0, 67.0, 61.4, 61.1, 48.7.

ESI-HRMS: Observed m/z for [M-N2+H]+ = 562.1596, [M-N2+Na]+ = 584.1412, 586.1394.

Compound 14g:

Yield: 79%

1H NMR (DMSO-d6, 400MHz): δ = 8.206 (s, 1H), 8.083 (d, *J* = 8.8 Hz, 2H), 7.907 (d, *J* = 16.0 Hz, 1H), 7.750 (d, *J* = 16.0 Hz, 1H), 7.556 (dd, *J* = 8.8, 2.4 Hz, 1H), 7.095 (d, *J* = 8.8 Hz, 1H), 6.90 (d, *J* = 8.8 Hz, 2H), 4.999 (m, 1H), 4.916 (m, 2H), 4.851 (t, *J* = 4.8 Hz, 2H), 4.613 (d, *J* = 12.4 Hz, 1H), 4.536 (t, *J* = 4.8 Hz, 2H), 4.263 (d, *J* = 8.0 Hz, 1H), 3.691 (m, 1H), 3.488 (m, 1H), 3.160 (d, *J* = 4.8 Hz, 1H), 3.114 (br s, 2H), 3.063 (br s, 1H), 2.958 (br s, 1H).

13C-NMR (DMSO-d6, 100MHz): δ = 187.0, 162.2, 160.5, 155.7, 143.8, 135.2, 133.8, 131.2, 130.6, 125.8, 124.6, 123.7, 115.3, 102.2, 76.8, 76.6, 73.3, 70.0, 67.1, 61.4, 61.0, 58.2, 48.7.

ESI-HRMS: Observed m/z for [M-N2+H]+ = 606.1093, 608.1071; [M-N2+Na]+ = 628.6466, 630.0880.

Compound 14h:

Yield: 77.5%

1H NMR (DMSO-d6, 400 MHz): δ = 8.28 (d, *J* = 2.4 Hz, 1H), 8.20 (s, 1H), 8.08 (d, *J* = 8.8 Hz, 2H), 7.88 (d, *J* = 15.6 Hz, 1H), 7.73 (d, *J* = 15.6 Hz, 1H), 7.69 (dd, *J* = 8.8, 2.4 Hz, 1H), 6.96 (d, *J* = 8.8 Hz, 1H), 6.90 (d, *J* = 8.8 Hz, 2H), 5.00 (d, *J* = 2.4 Hz, 1H), 4.92 (m, 2H), 4.85 (t, *J* = 4.8 Hz, 2H), 4.61 (d, *J* = 12.4 Hz, 1H), 4.512 (t, *J* = 4.8 Hz, 2H), 4.260 (d, *J* = 8.0 Hz, 1H), 4.095 (d, *J* = 2.4 Hz, 2H), 4.027 (m, 2H), 3.682 (m, 1H), 3.448 (br s, 1H), 3.120 (br s, 1H), 3.061 (br s, 1H), 2.95 (br s, 1H).

13C NMR (DMSO-d6, 100 MHz): δ = 187.5, 162.6, 156.4, 144.3, 140.2, 135.8, 131.7, 129.5, 126.6, 125.1, 124.0, 115.9, 115.8, 115.6, 102.7, 77.3, 73.8, 70.5, 67.4, 61.9, 61.5, 49.2, 49.0.

ESI-HRMS: Observed m/z for [M-N2+H]+ = 654.0956, [M-N2+Na]+ = 676.0775, 677.0807.

2.5. Appendices:

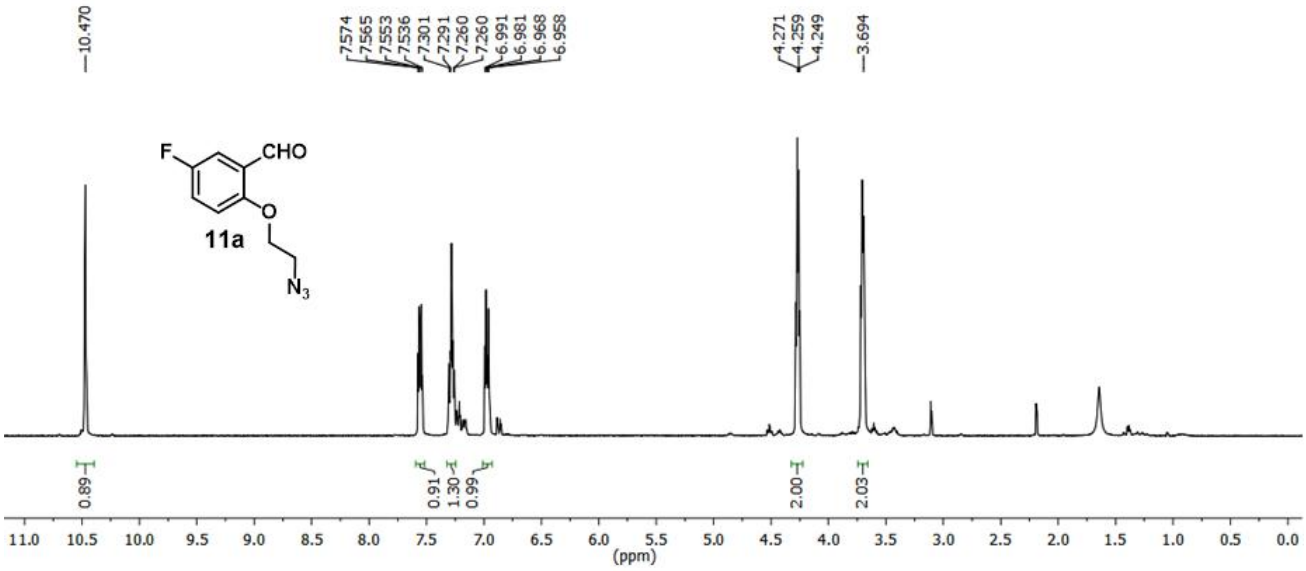

Fig. S1: ^{1}H NMR spectra of compound 11a.

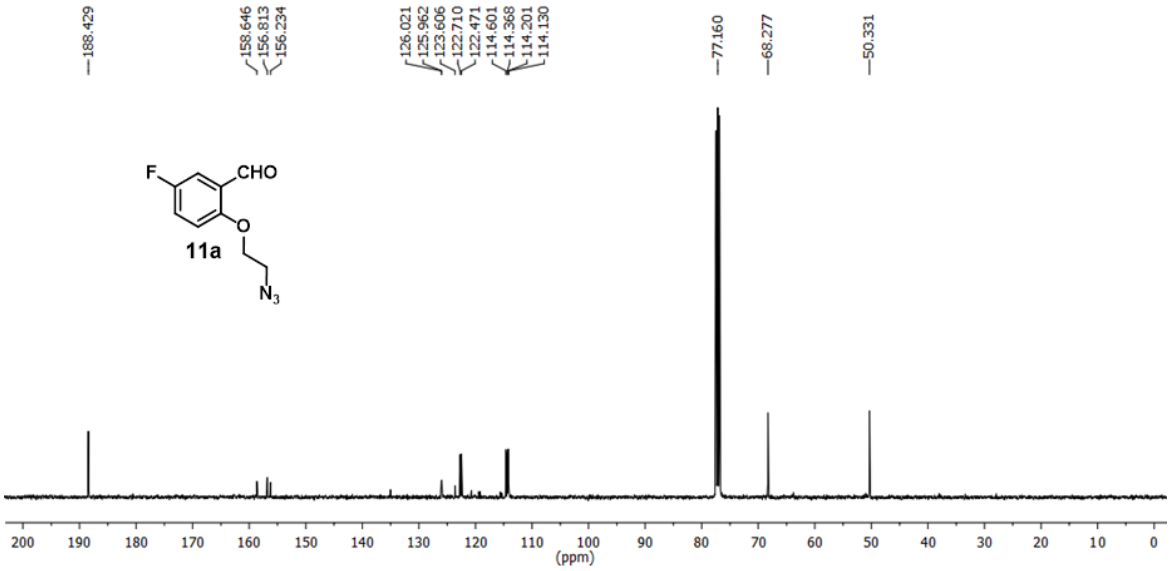

Fig. S2: ^{13}C NMR spectra of compound 11a.

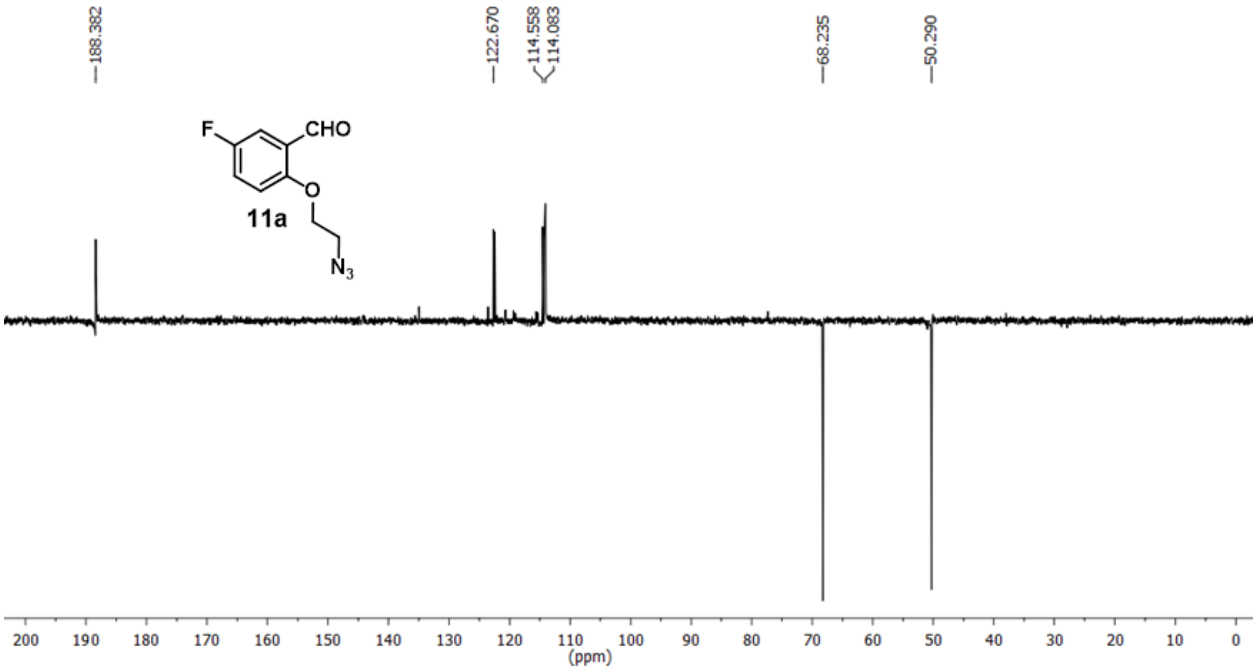

Fig. S3: ^{13}C DEPT spectra of compound 11a.

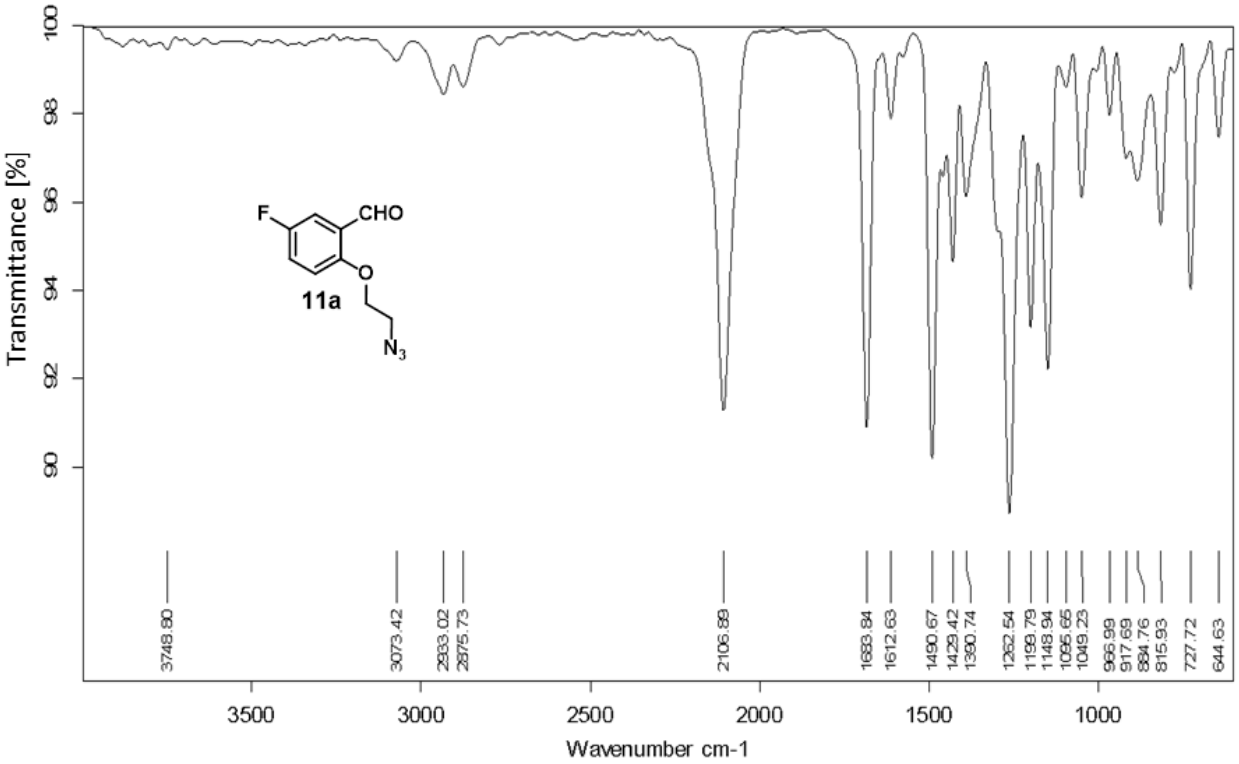

Fig. S4: FT-IR spectra of compound 11a.

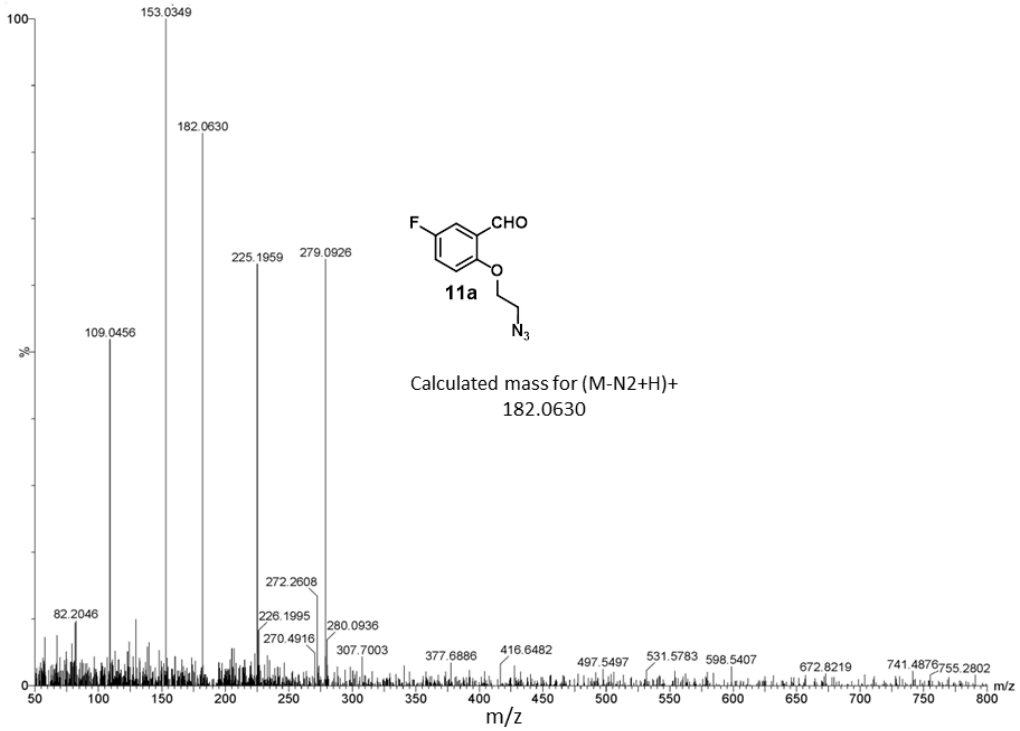

S5: HR-MS spectra of compound 11a.

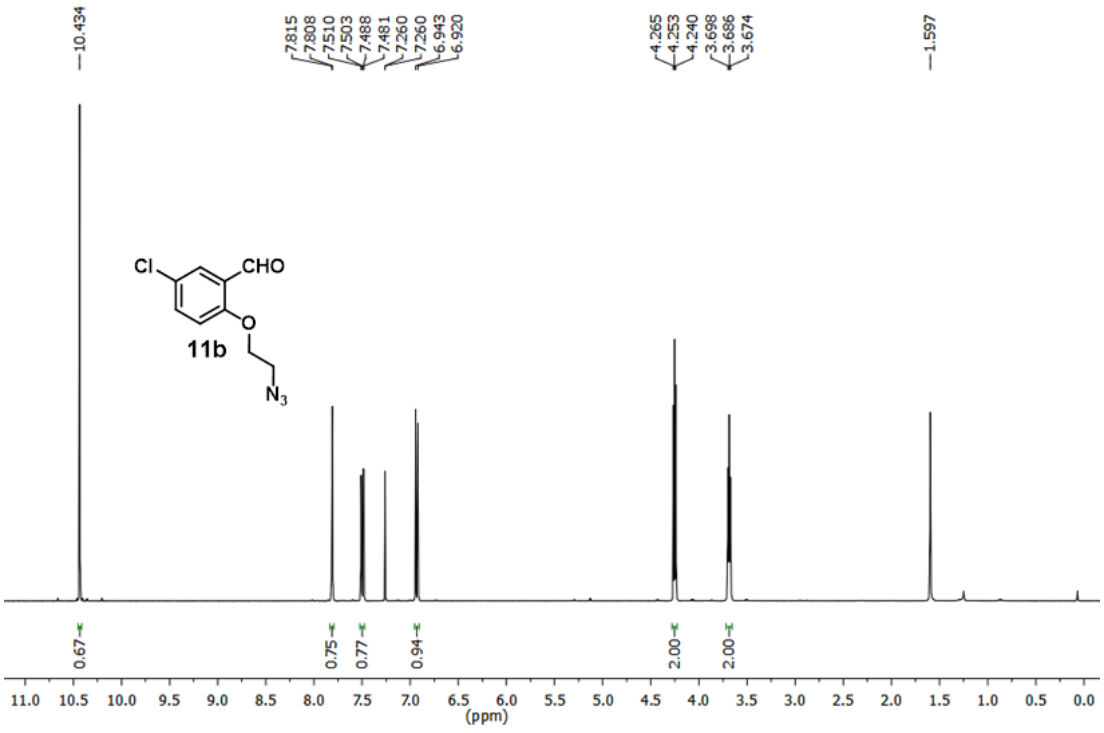

S6: ^{1}H NMR spectra of compound 11b.

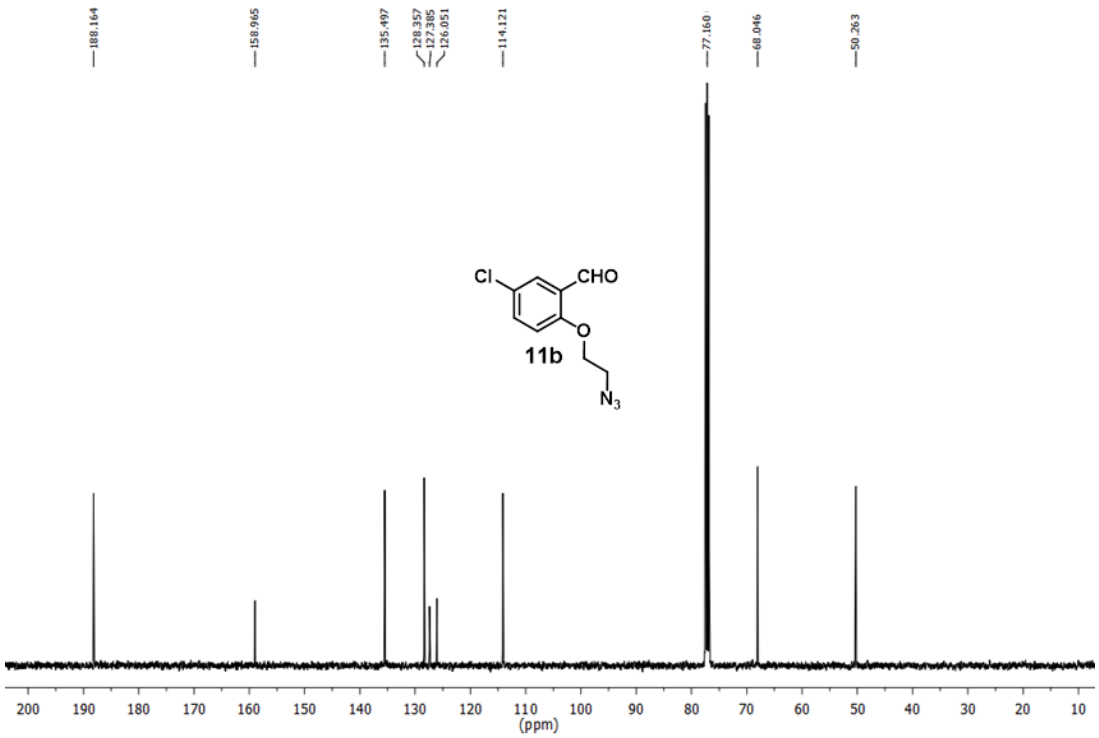

Fig.S7: ^{13}C NMR spectra of compound 11b.

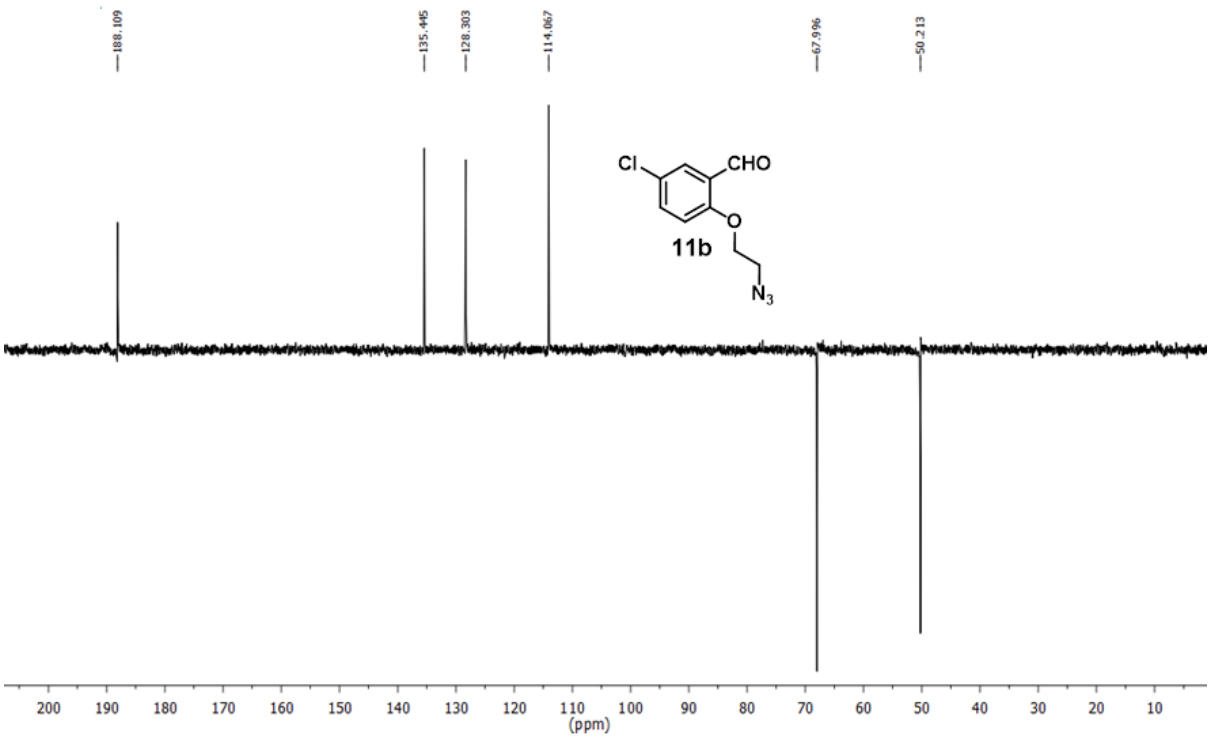

Fig. S8: ^{13}C DEPT spectra of compound 11b.

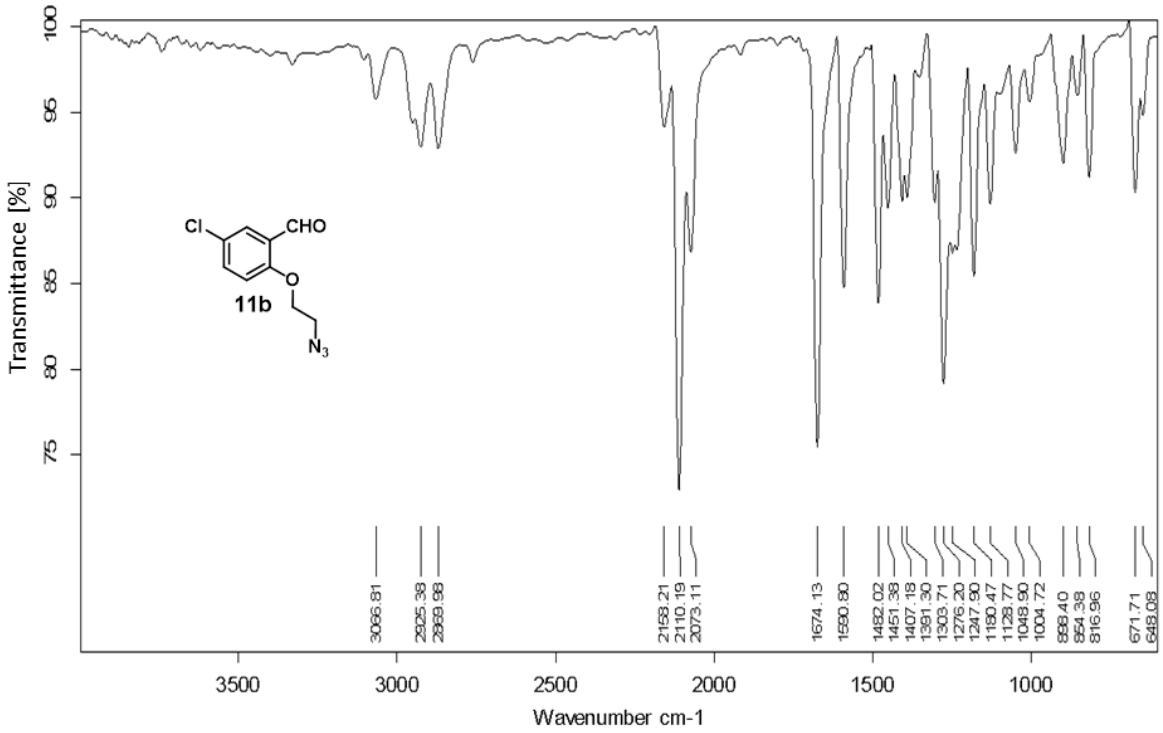

Fig. S9: FT-IR spectra of compound 11b.

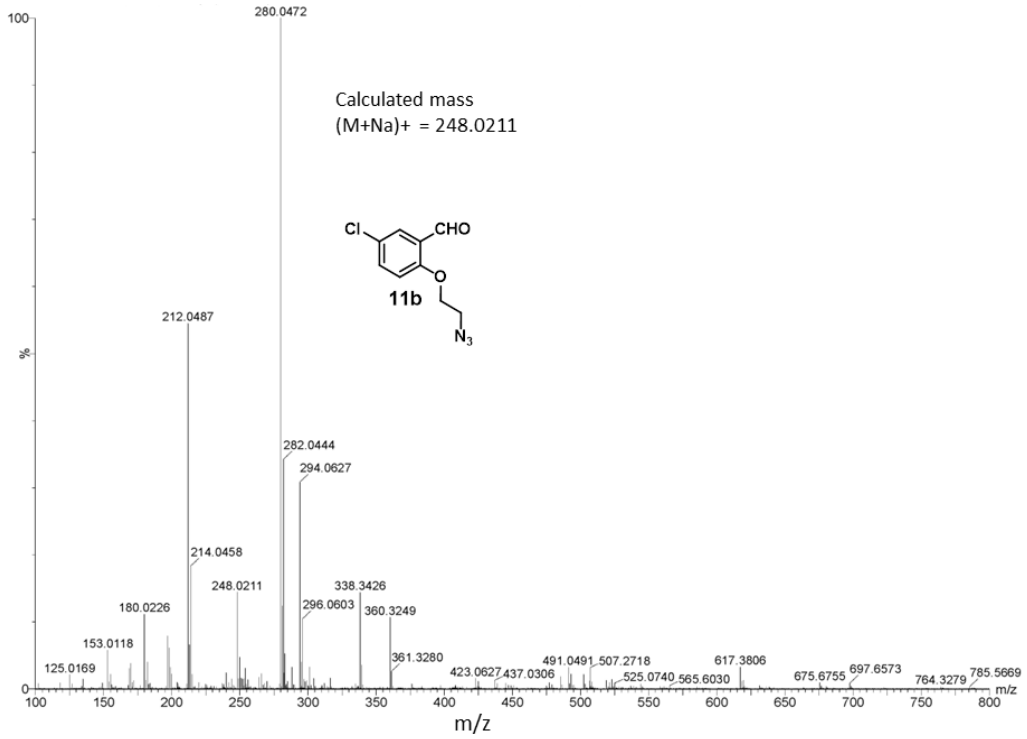

Fig. S10: HR-MS spectra of compound 11b.

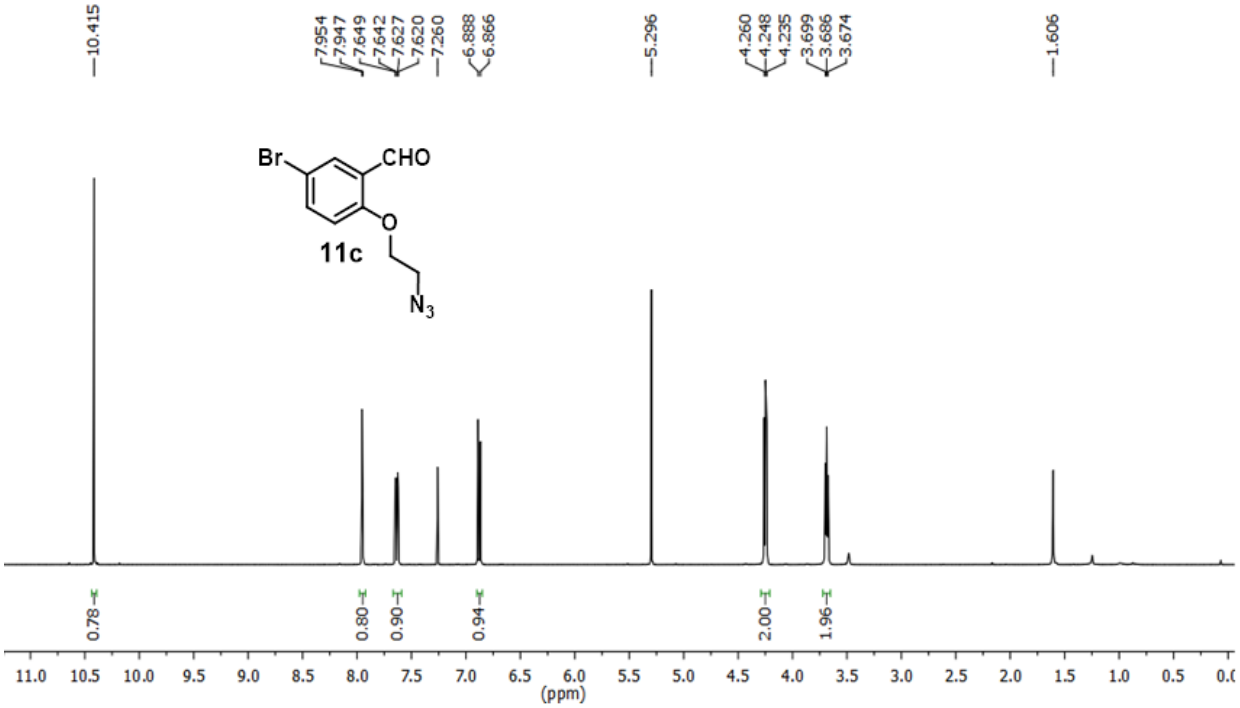

Fig. S11: ^{1}H NMR spectra of compound 11c.

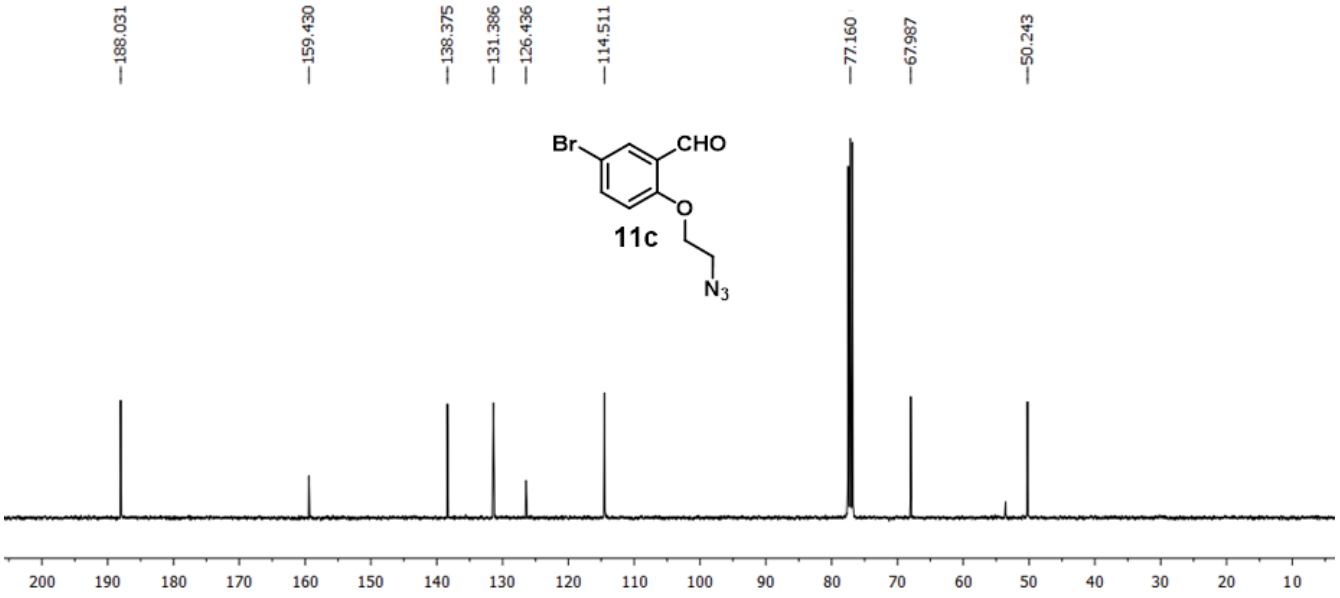

Fig. S12: ^{13}C NMR spectra of compound 11c.

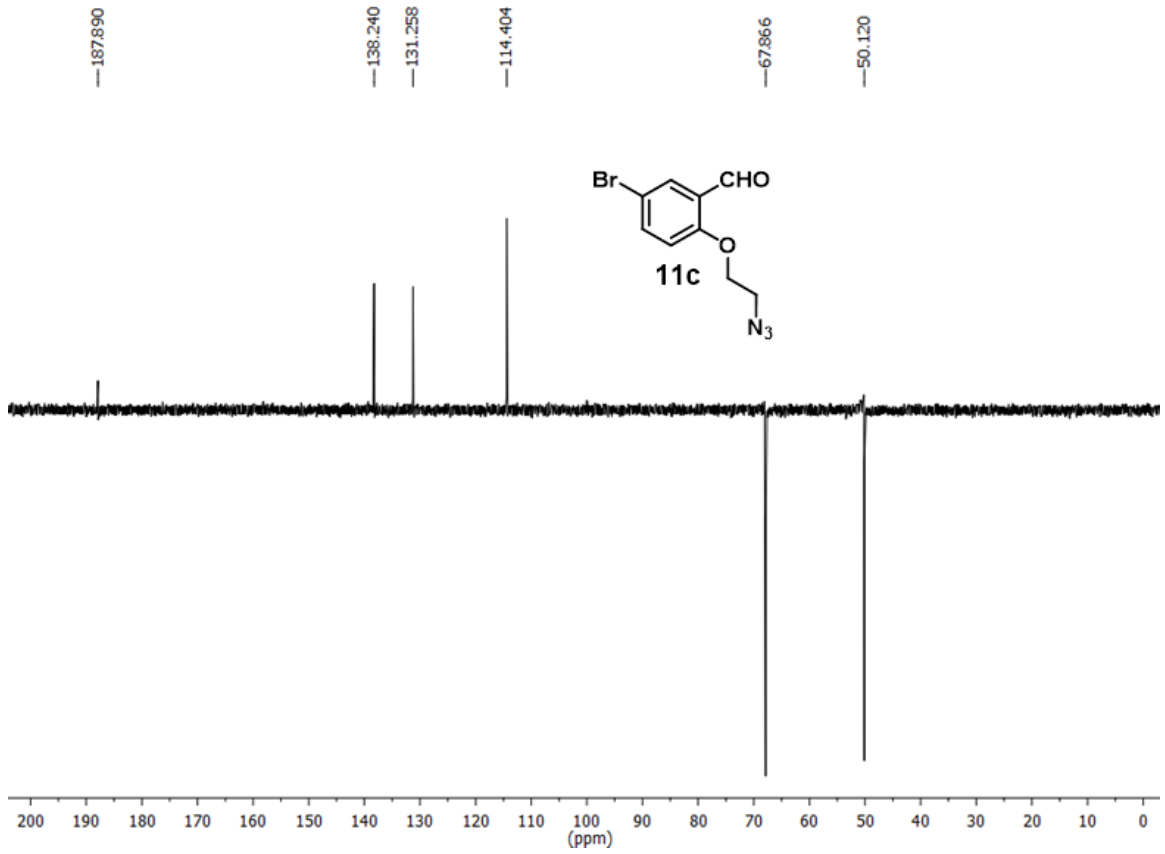

Fig. S13: ^{13}C DEPT spectra of compound 11c.

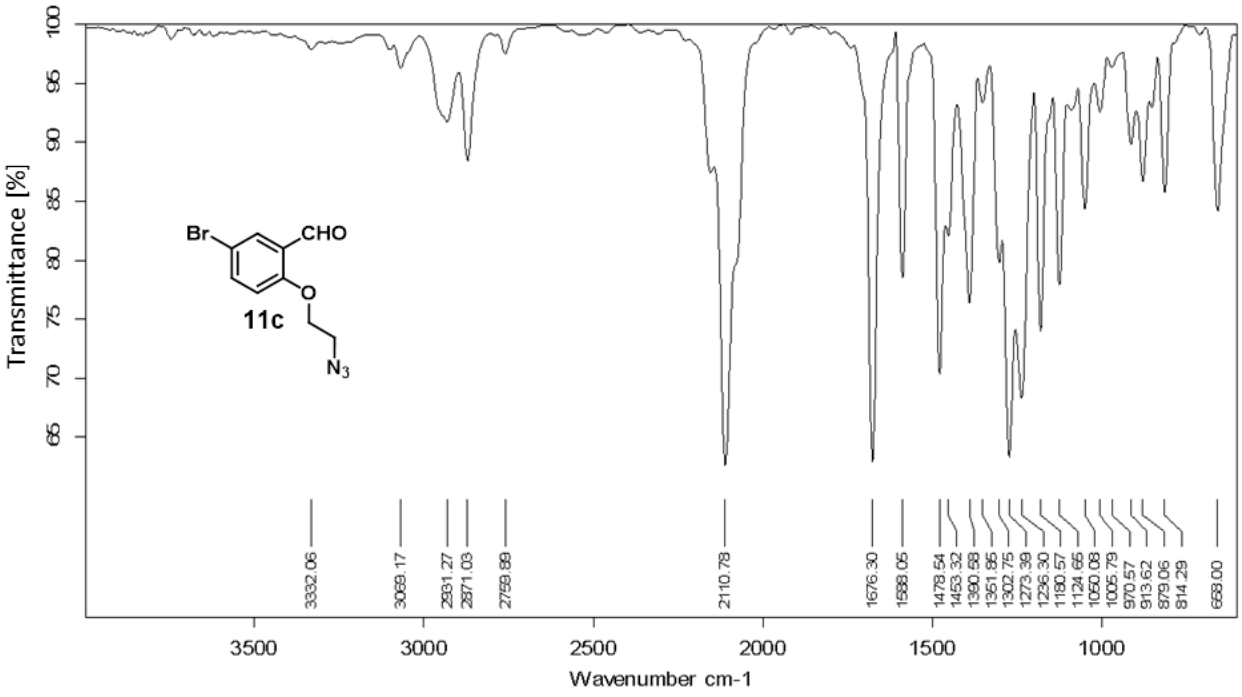

Fig. S14: FT-IR spectra compound 11c.

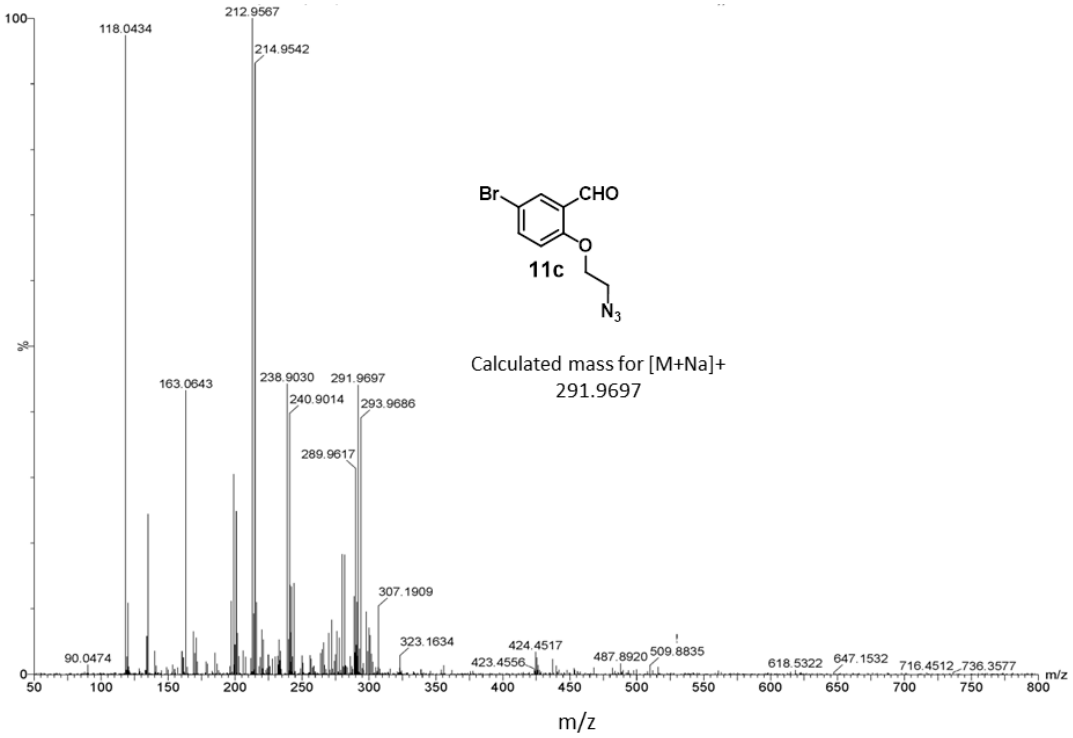

Fig. S15: HR-Ms spectra of compound 11c

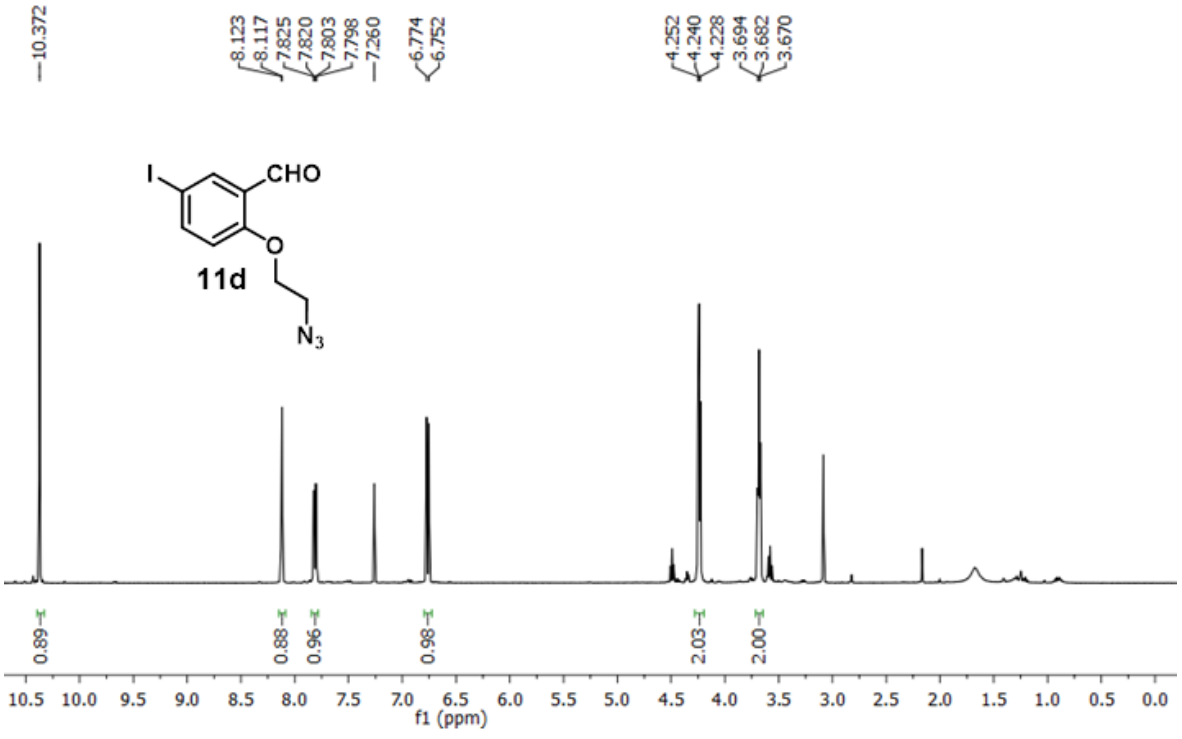

Fig. S16: ^{1}H NMR spectra of compound 11d.

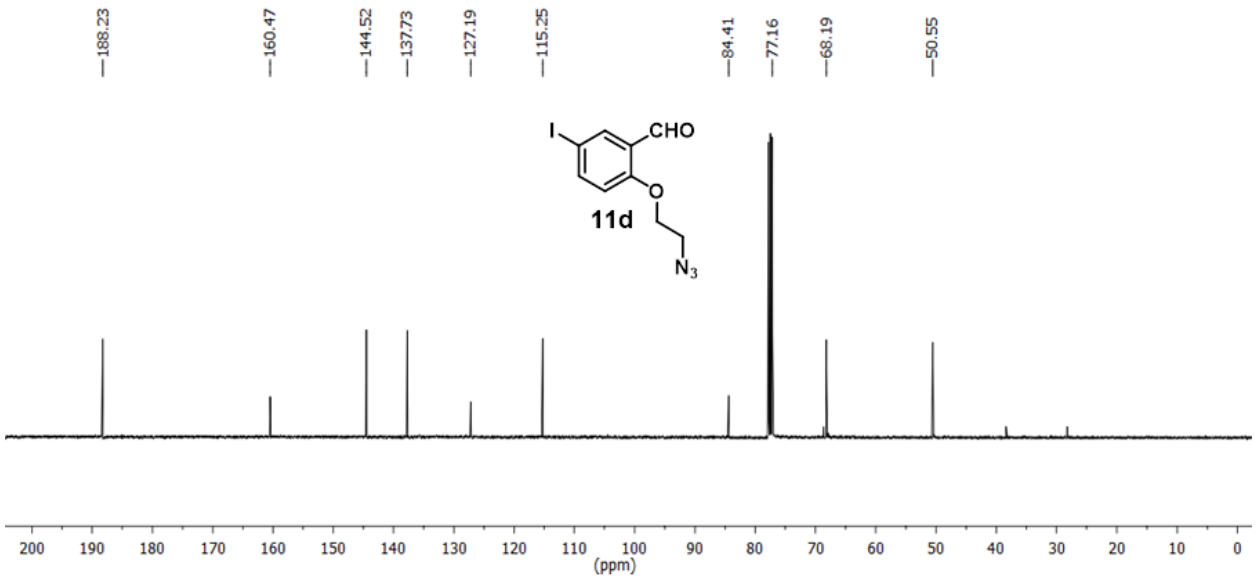

Fig. S17: ^{13}C NMR spectra of compound 11d.

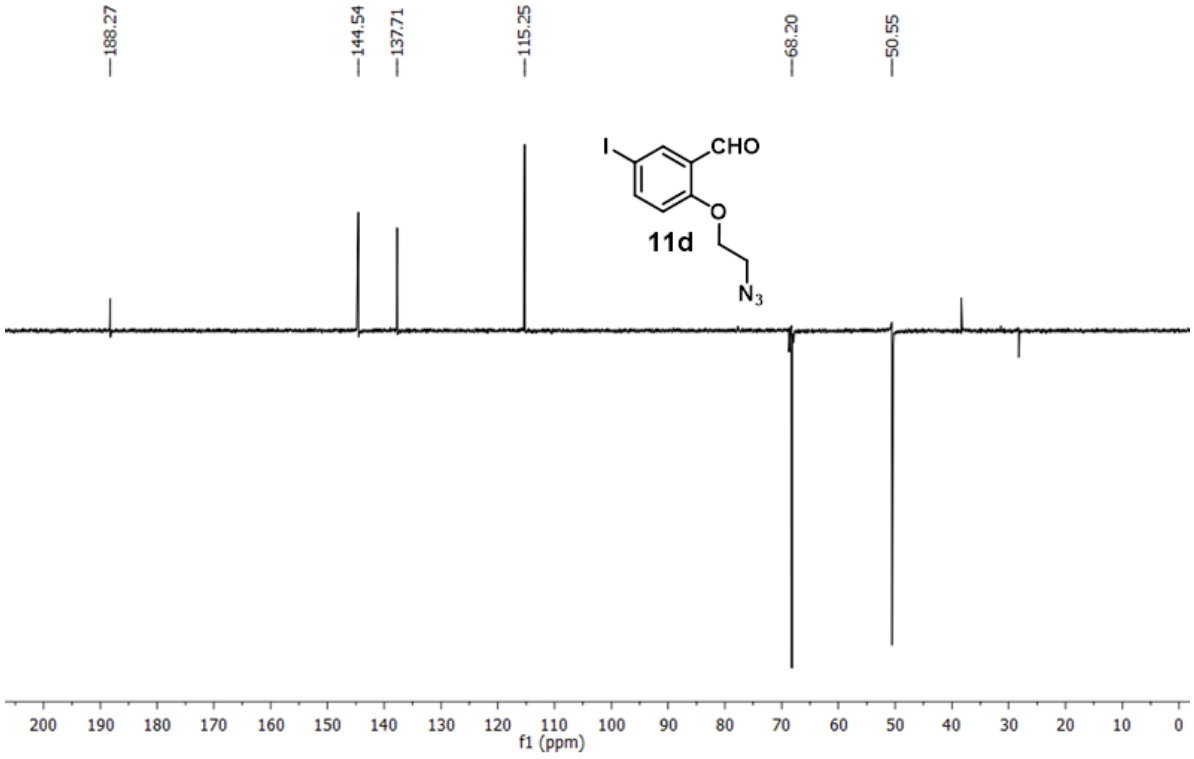

Fig. S18: ^{13}C DEPT spectra of compound 11d.

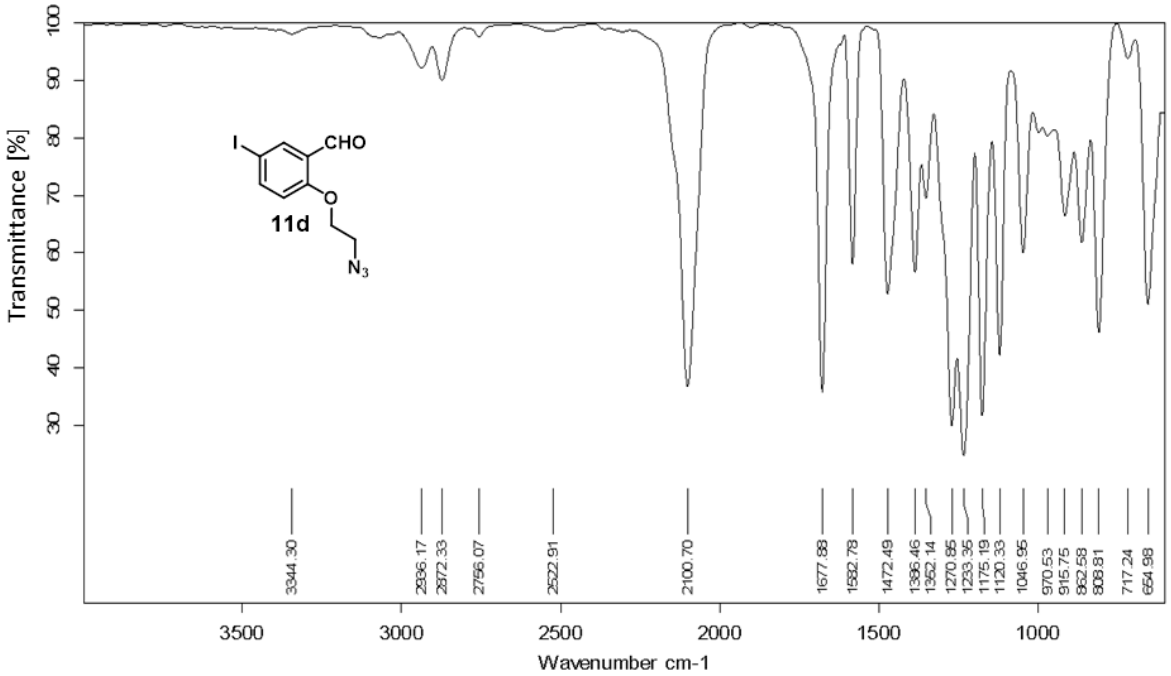

Fig. S19: FT-IR spectra of compound 11d.

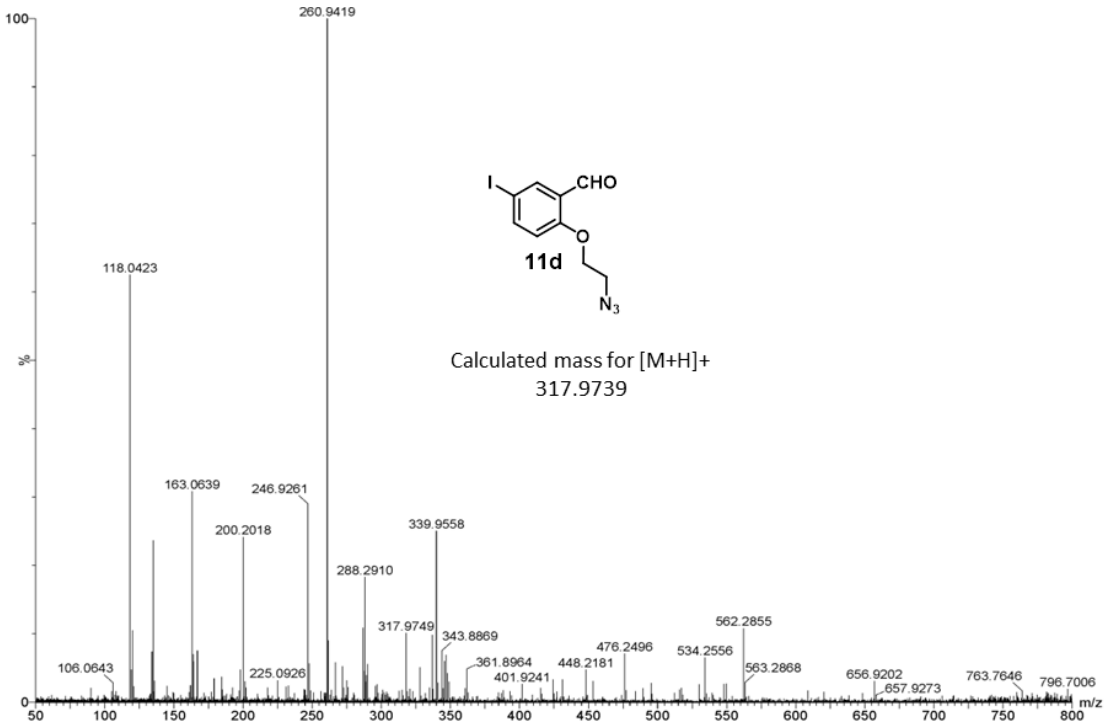

Fig. S20: HR-MS spectra of compound 11d.

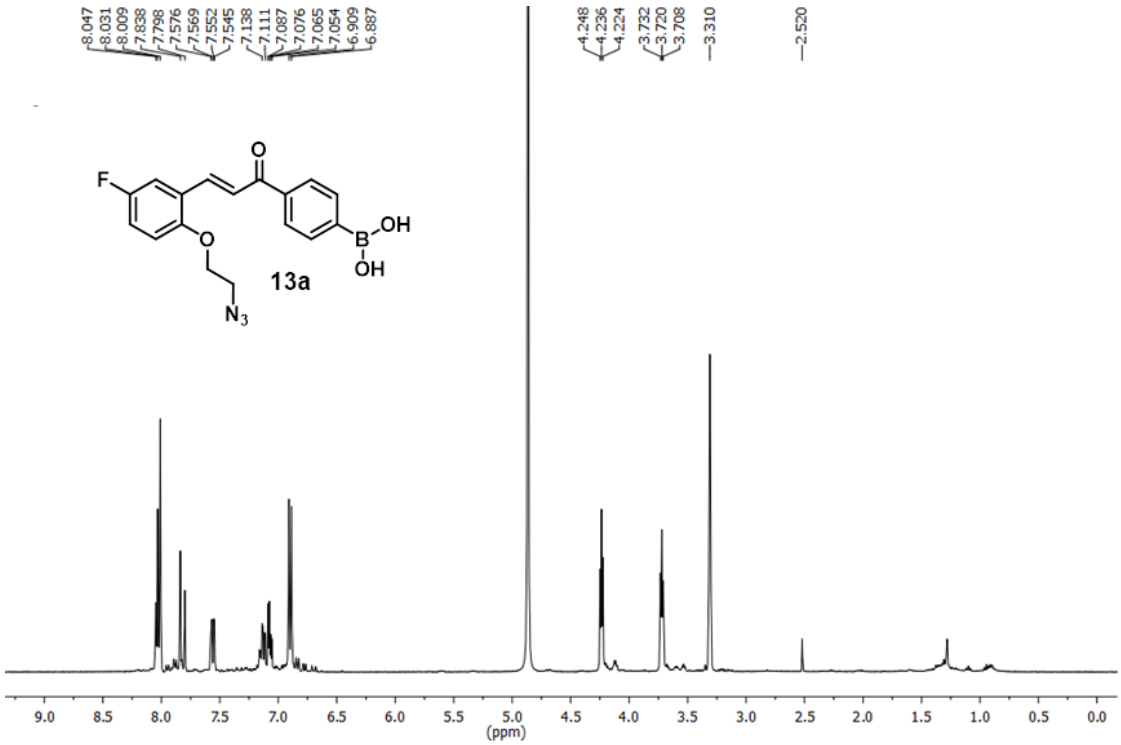

Fig. S21: ^{1}H NMR spectra of compound 13a.

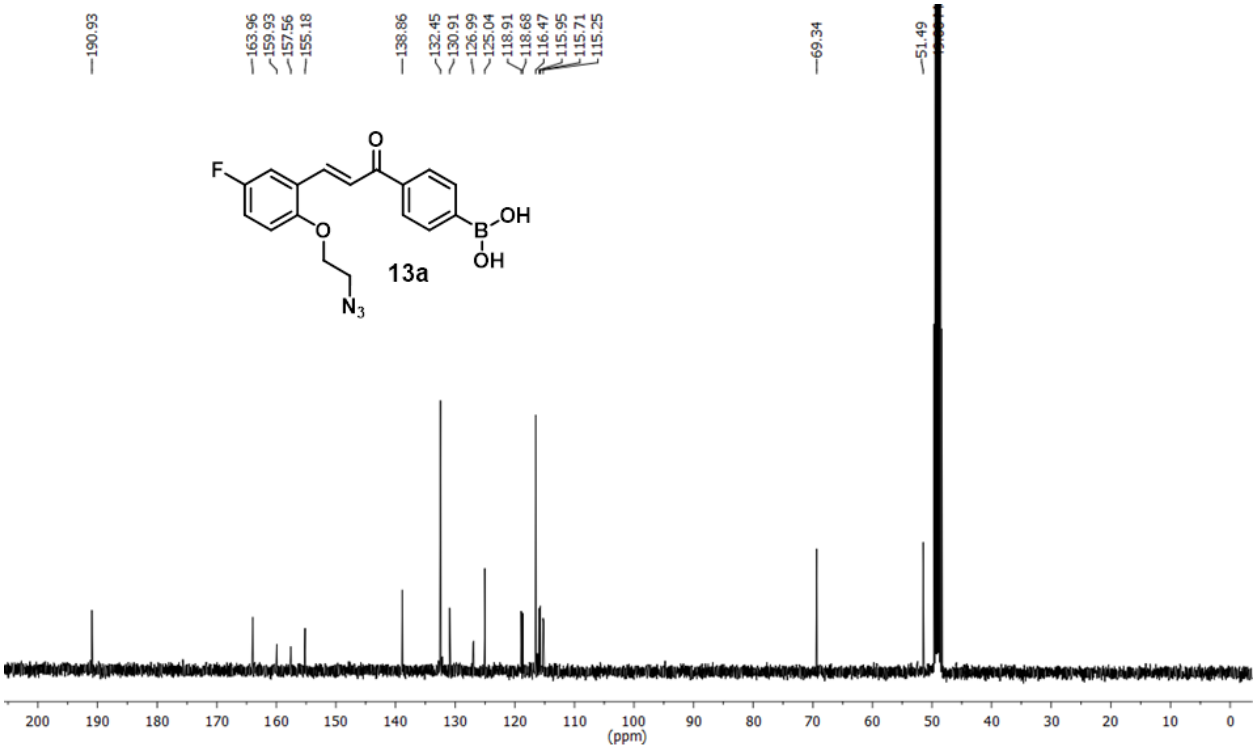

Fig. S22: ^{13}C NMR spectra of compound 13a.

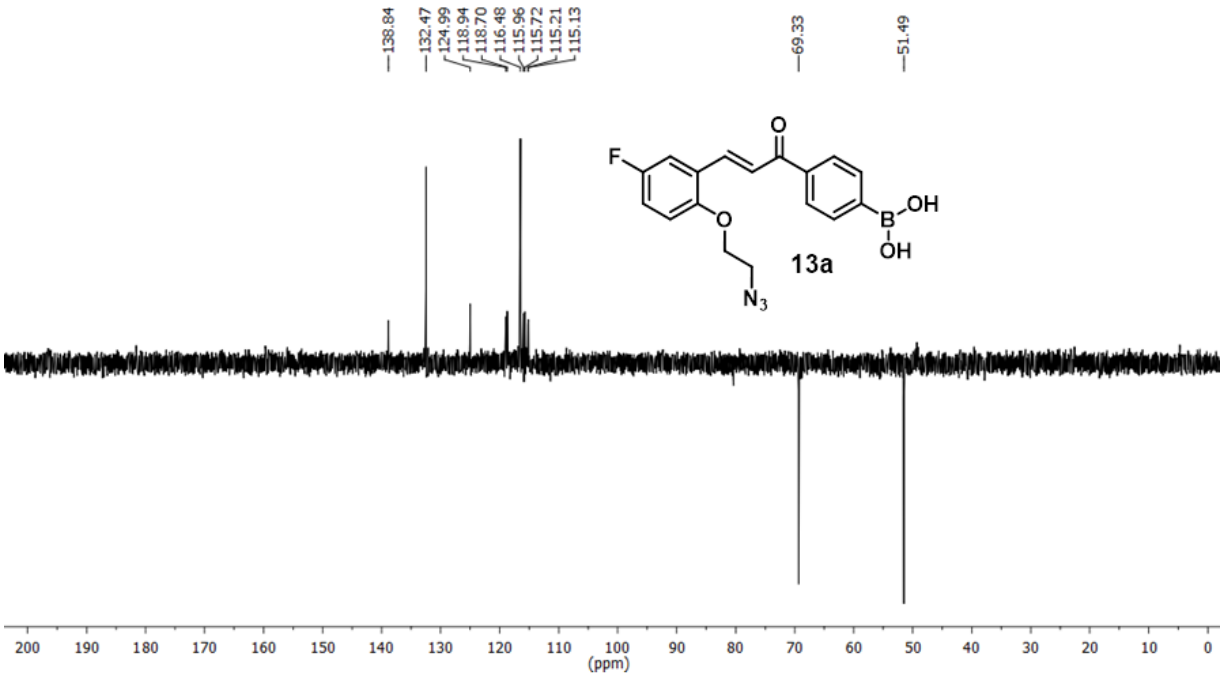

Fig. S23: 13C DEPT spectra of compound 13a.

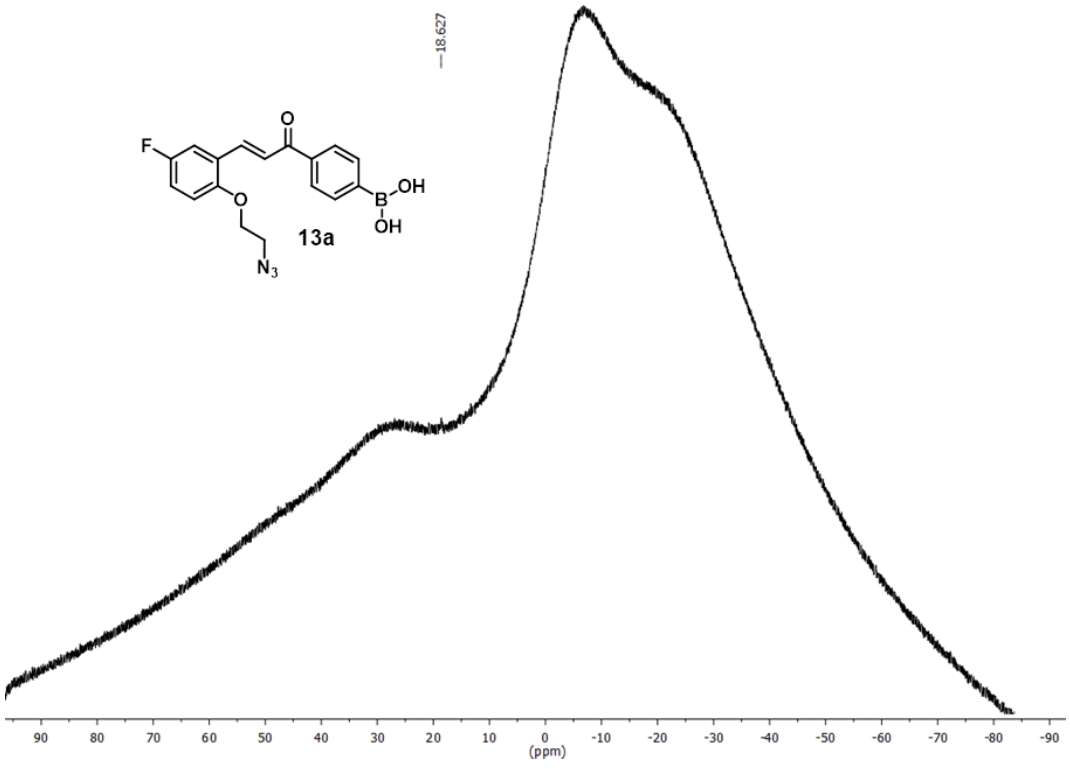

Fig. S24: 11B NMR spectra of compound 13a.

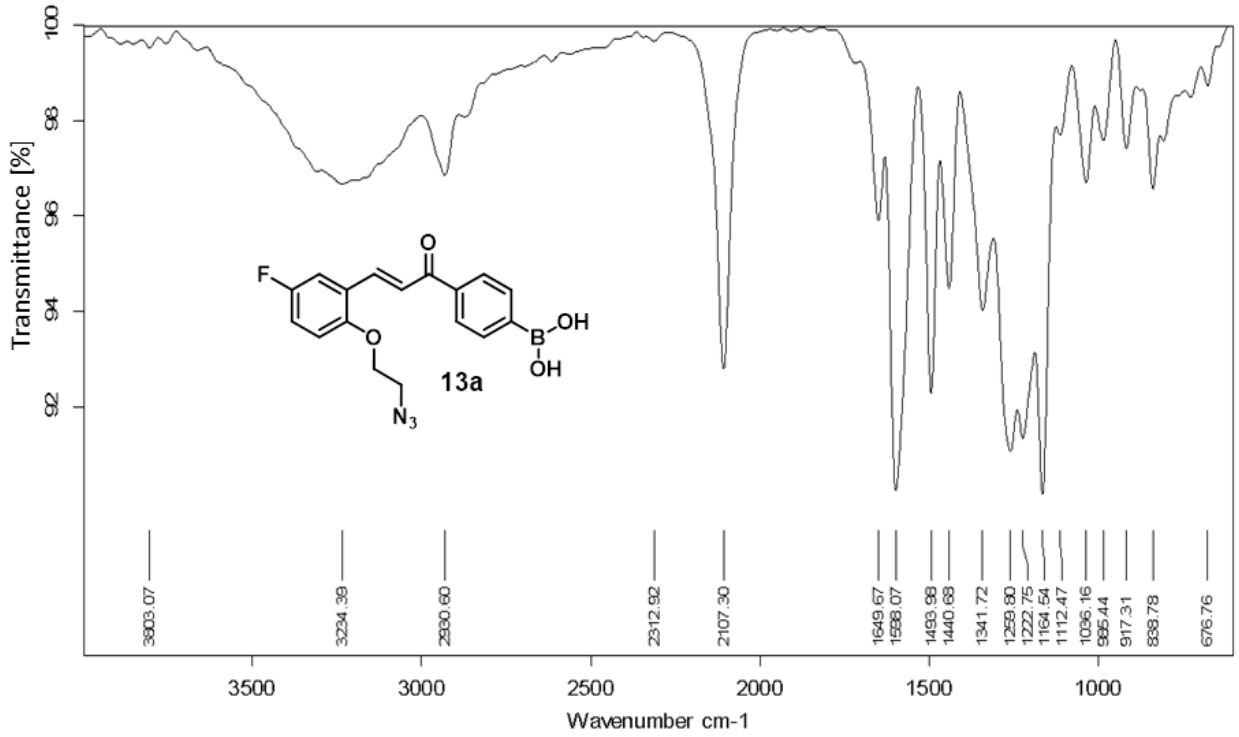

Fig. S25: FT-IR spectra of compound 13a.

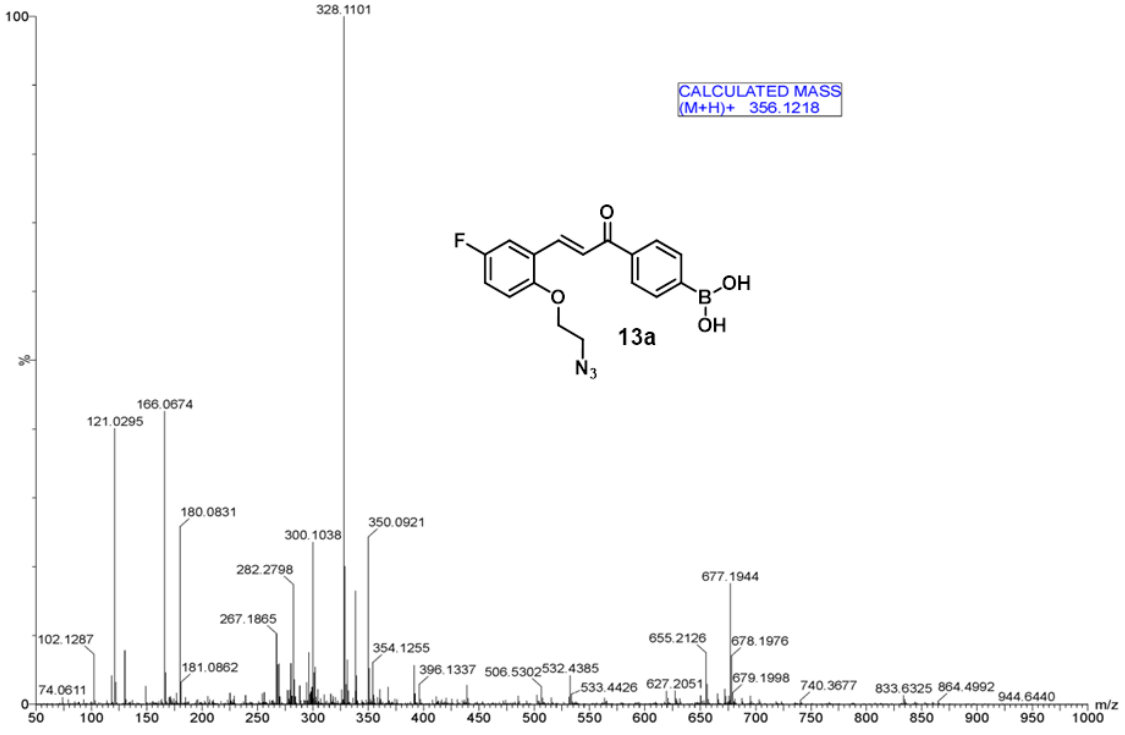

Fig. S26: HR-MS spectra of compound 13a.

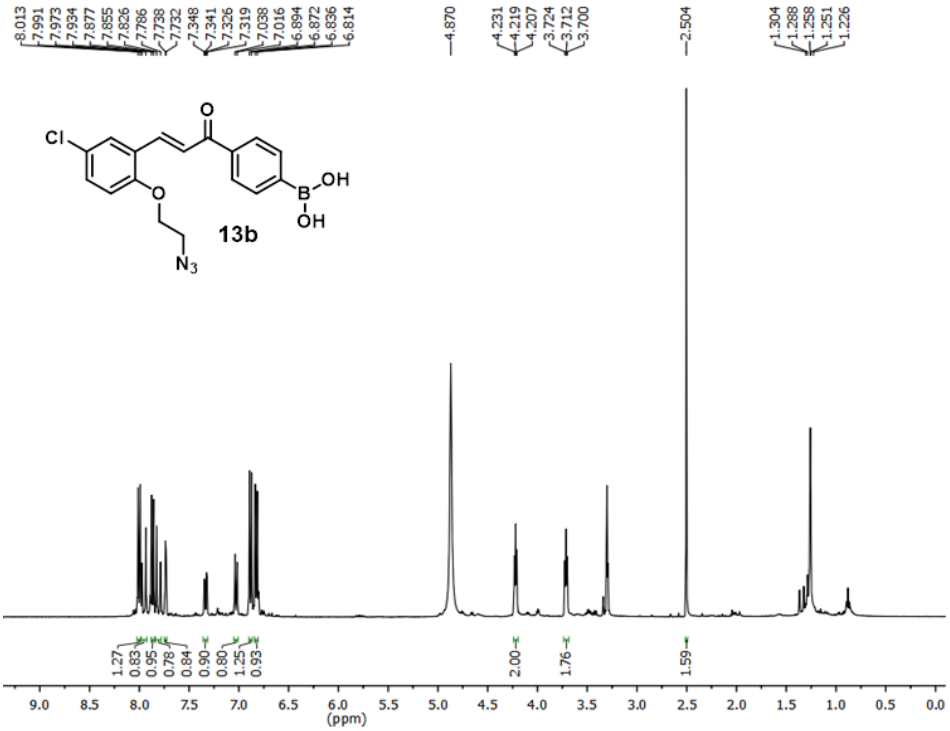

Fig. S27: 1H NMR spectra of compound 13b.

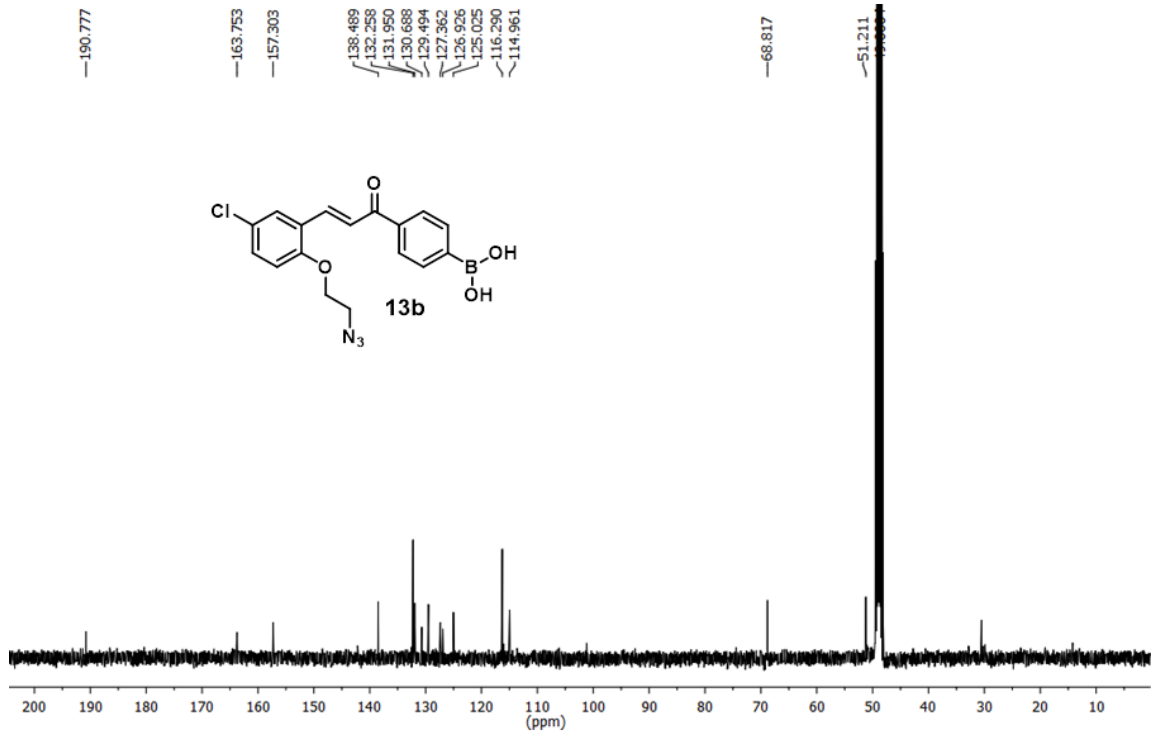

Fig. S28: 13C NMR spectra of compound 13b.

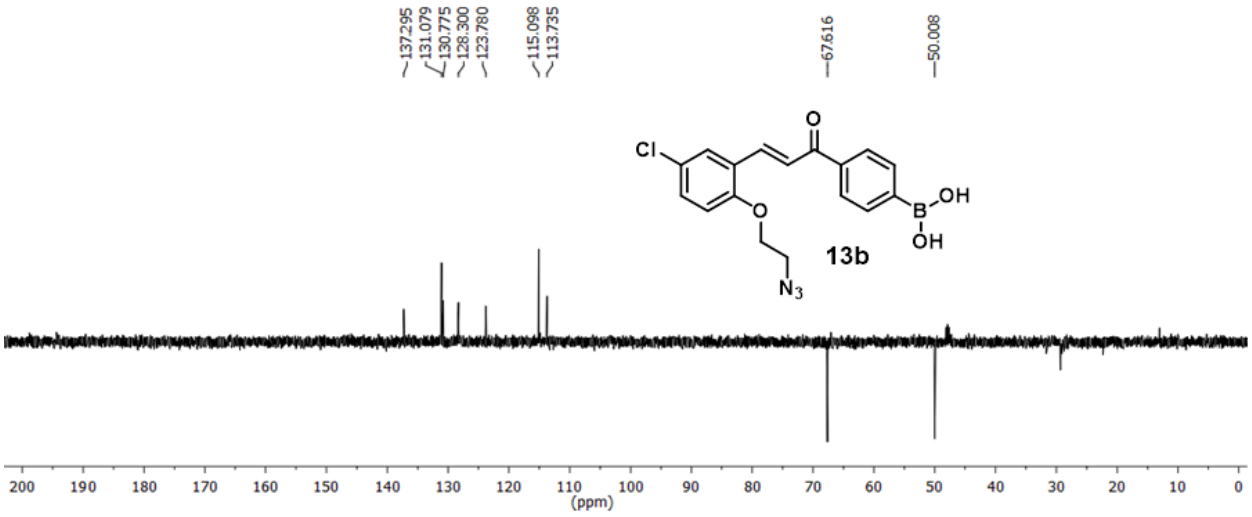

Fig. S29: 13C DEPT spectra of compound 13b.

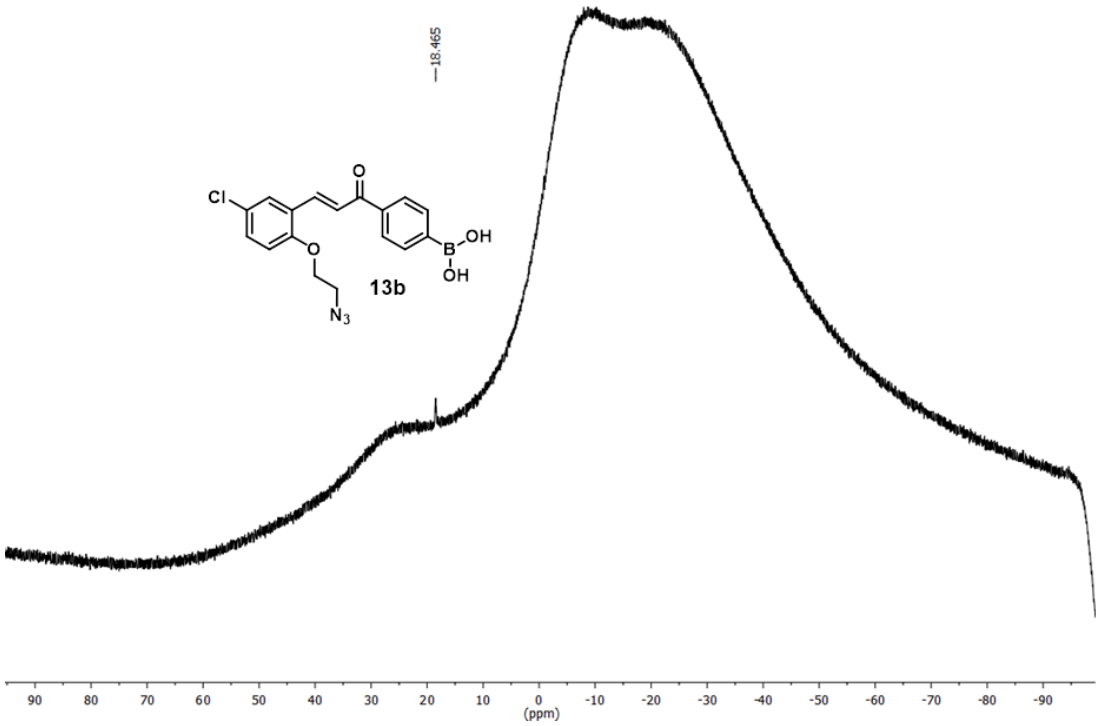

Fig. S30: 11B NMR spectra of compound 13b.

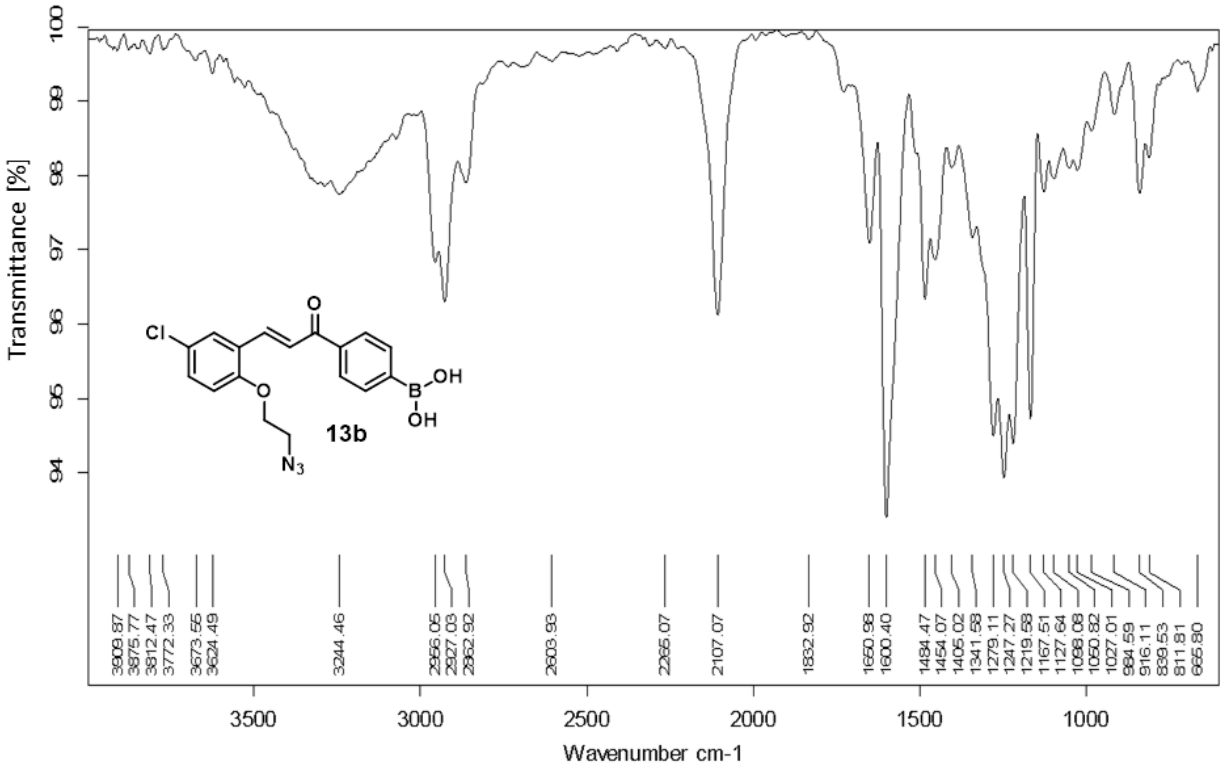

Fig. S31: HR-MS spectra of compound 13b.

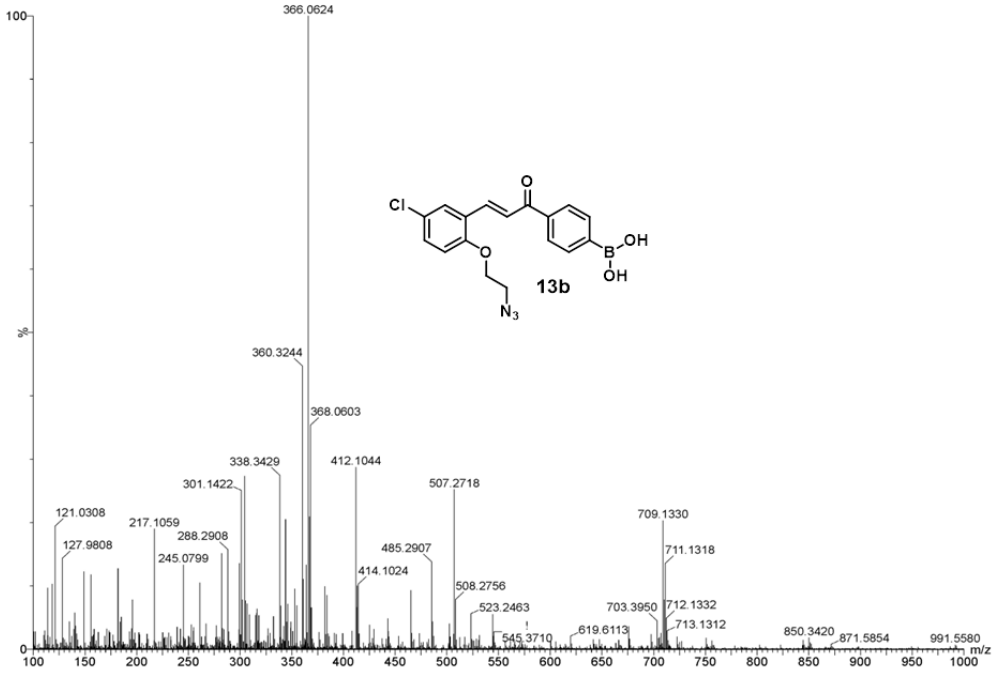

Fig. S32: HR-MS spectra of compound 13b.

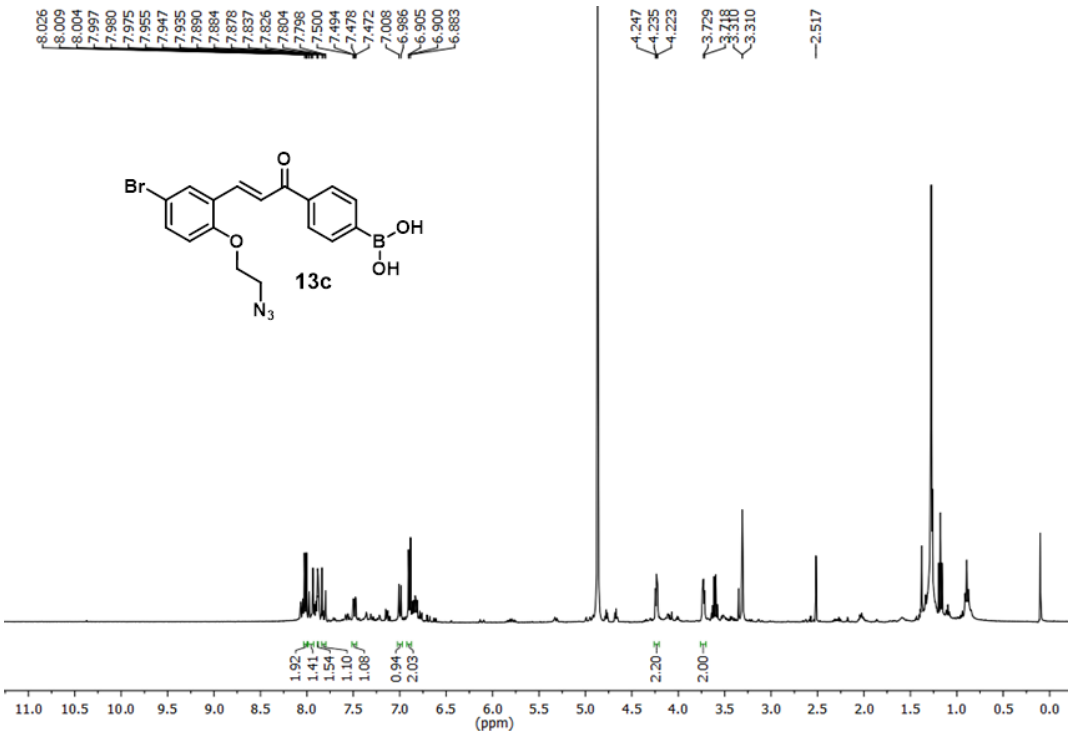

Fig. S33: 1H NMR spectra of compound 13c.

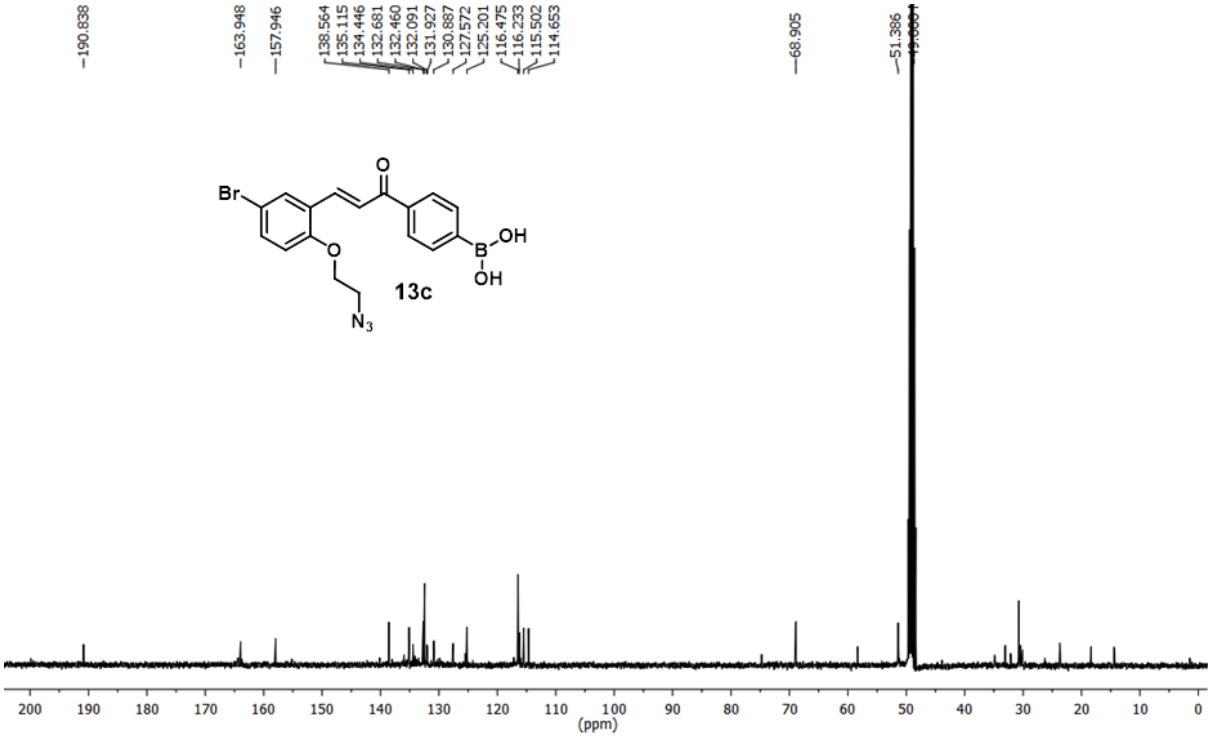

Fig. S34: 13C NMR spectra of compound 13c.

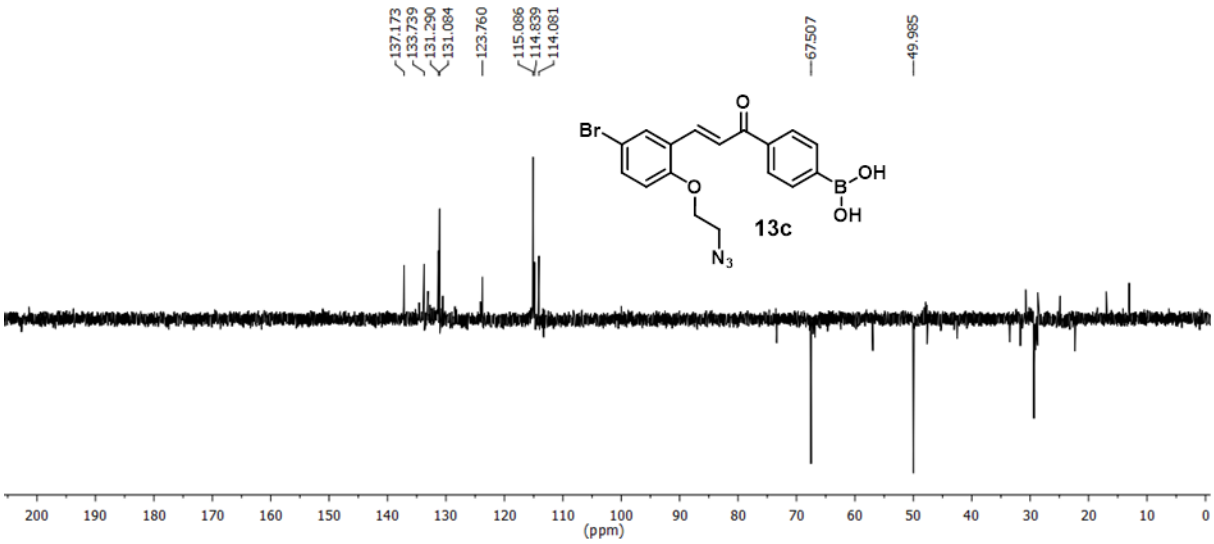

Fig. S35: 13C DEPT spectra of compound 13c.

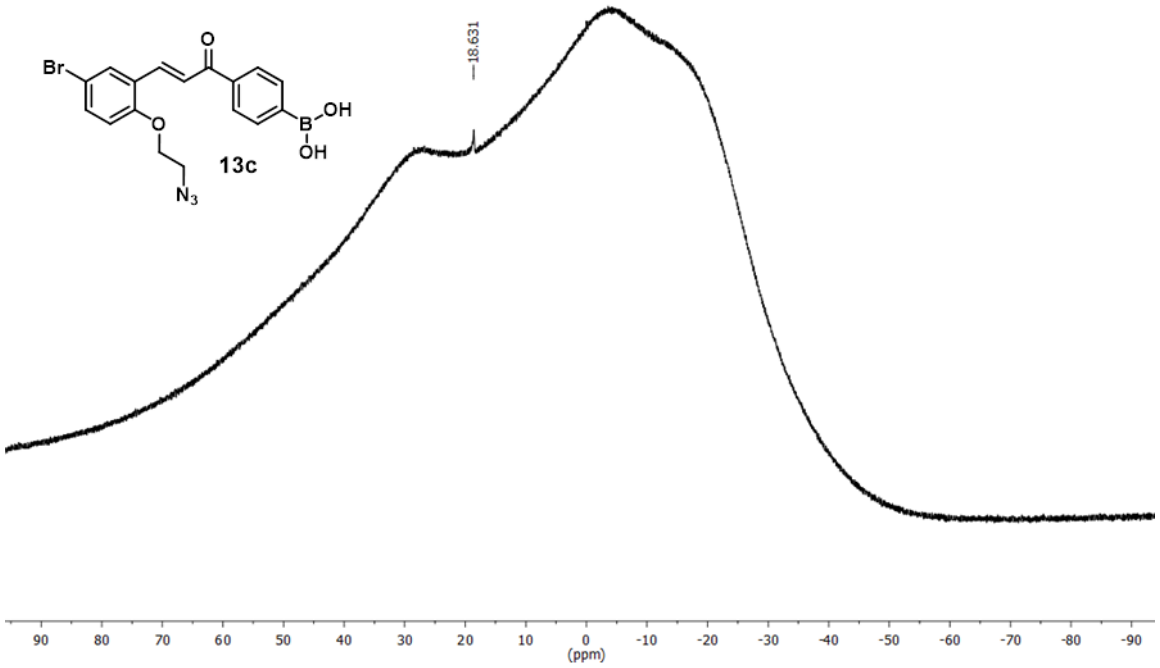

Fig. S36: 11B NMR spectra of compound 13c.

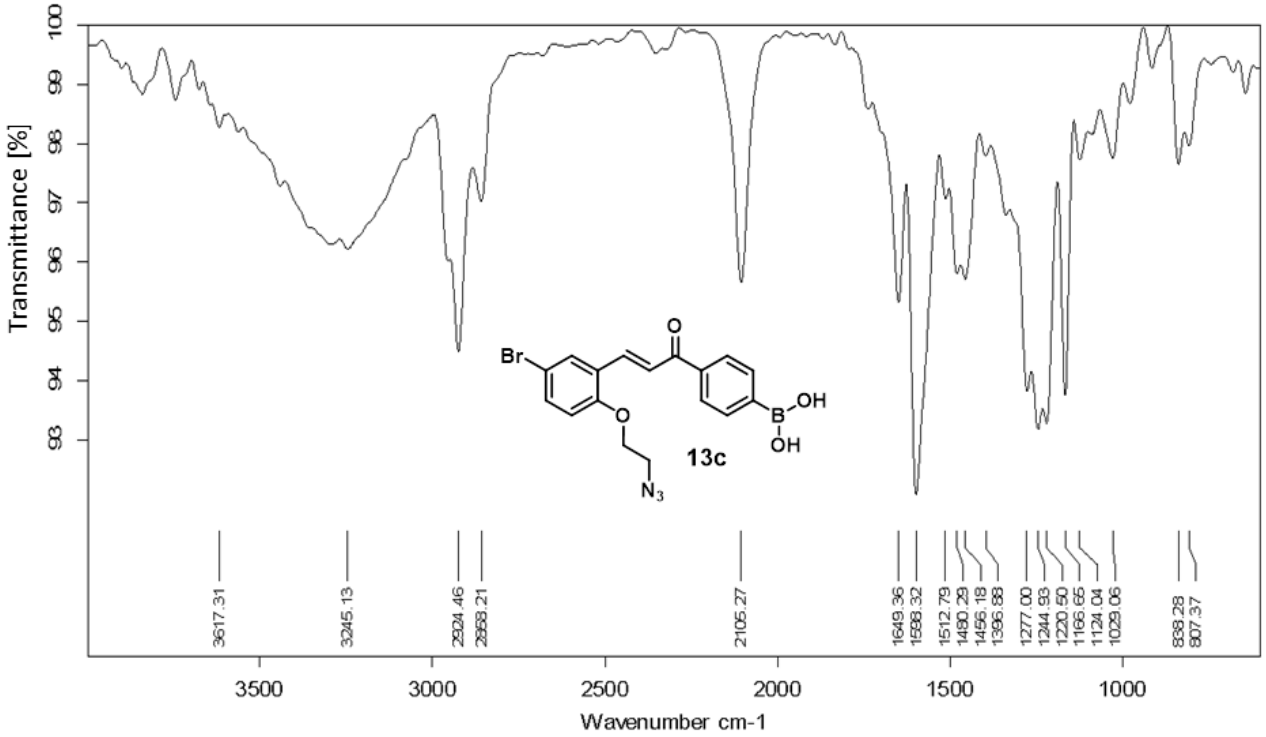

Fig. S37: FT-IR spectra of compound 13c.

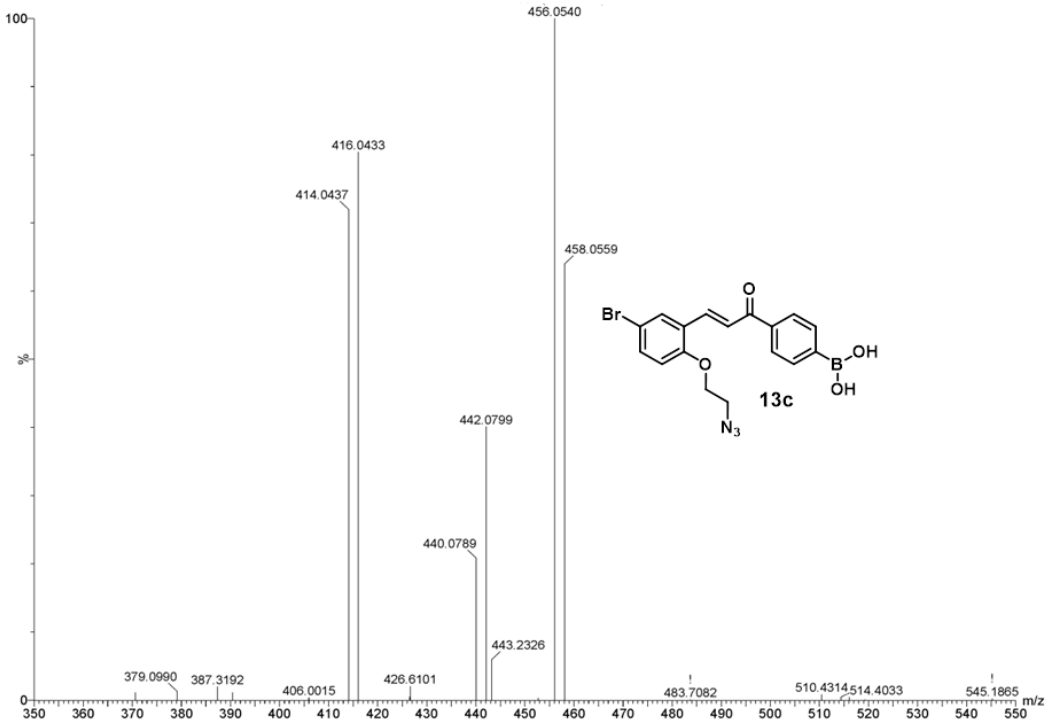

Fig. S38: HR-MS spectra of compound 13c.

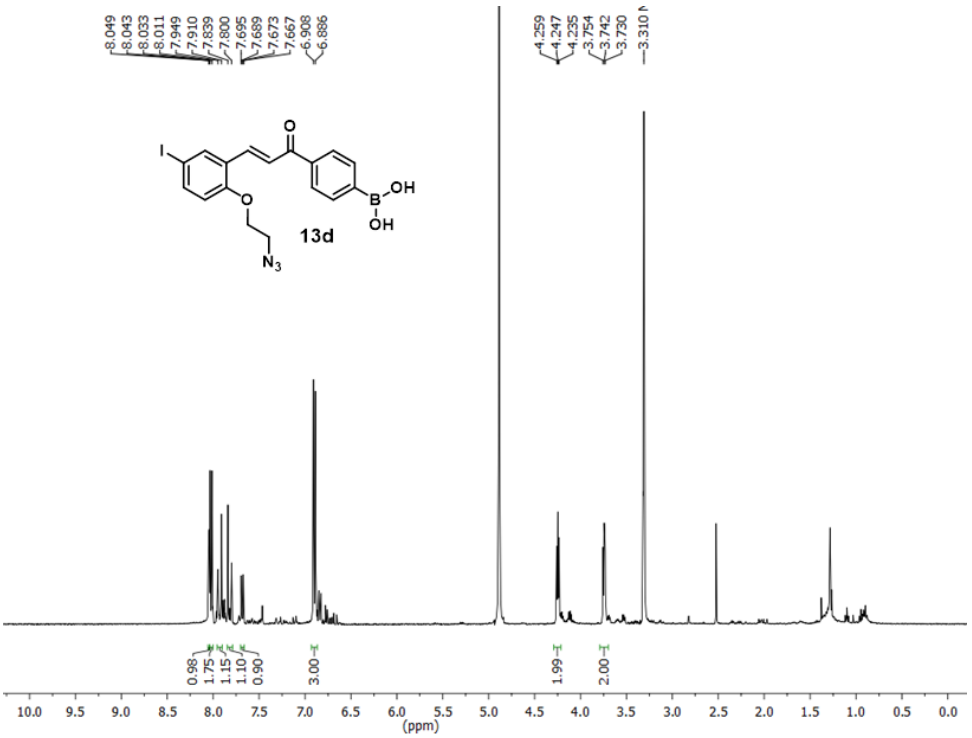

Fig. S39: 1H NMR spectra of compound 13d.

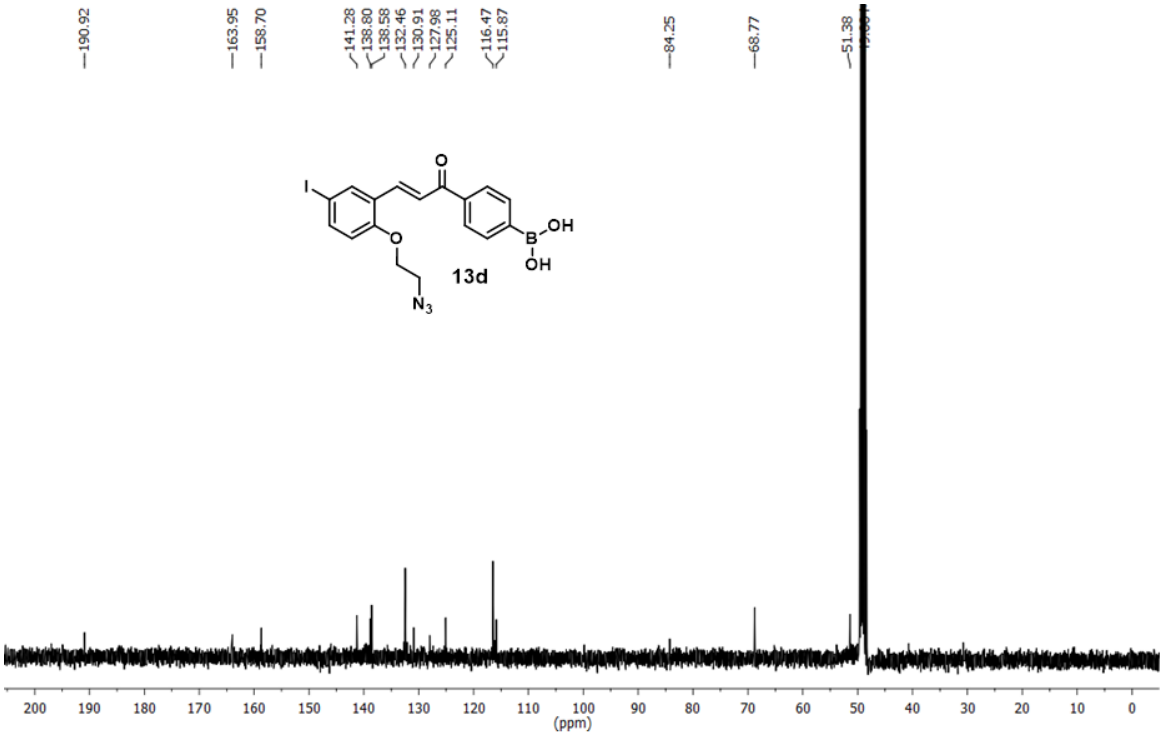

Fig. S40: 13C NMR spectra of compound 13d.

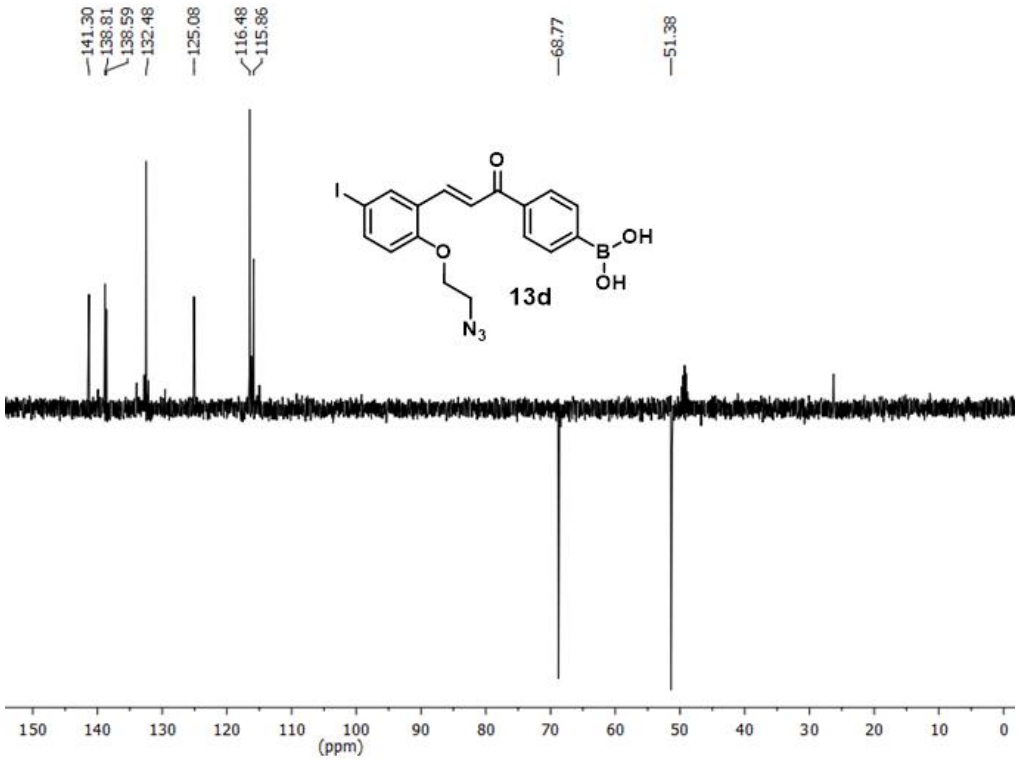

Fig. S41: 13C DEPT spectra of compound 13d.

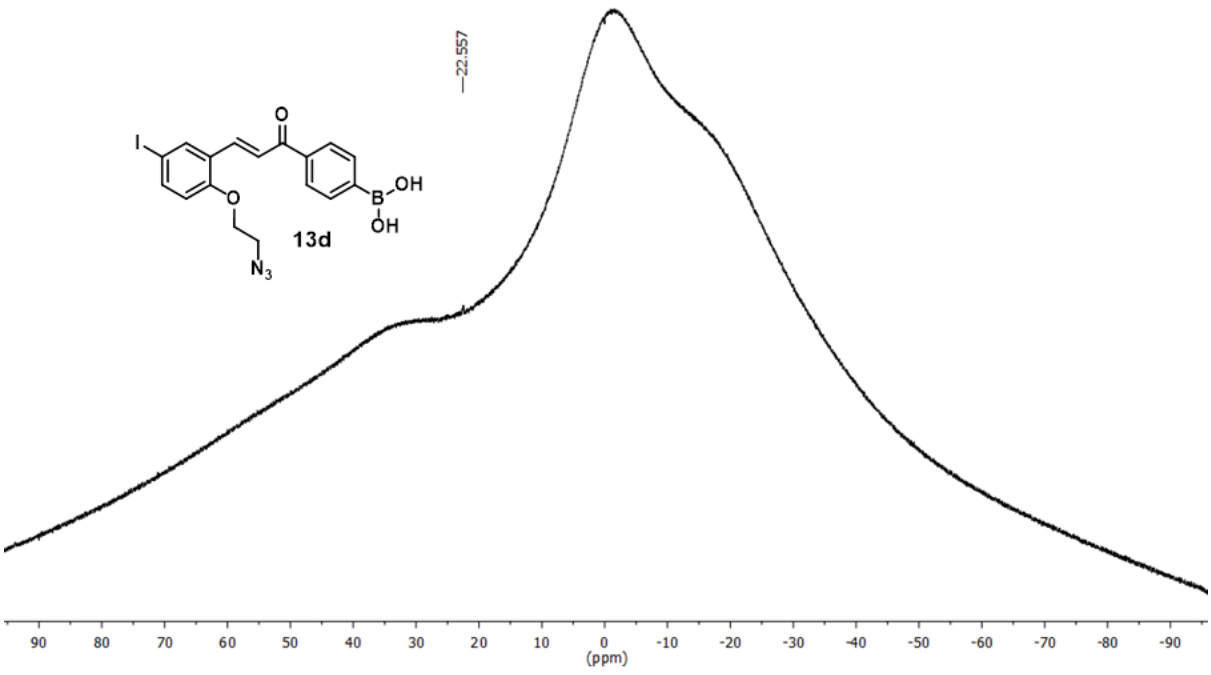

Fig. S42: 11B NMR spectra of compound 13d.

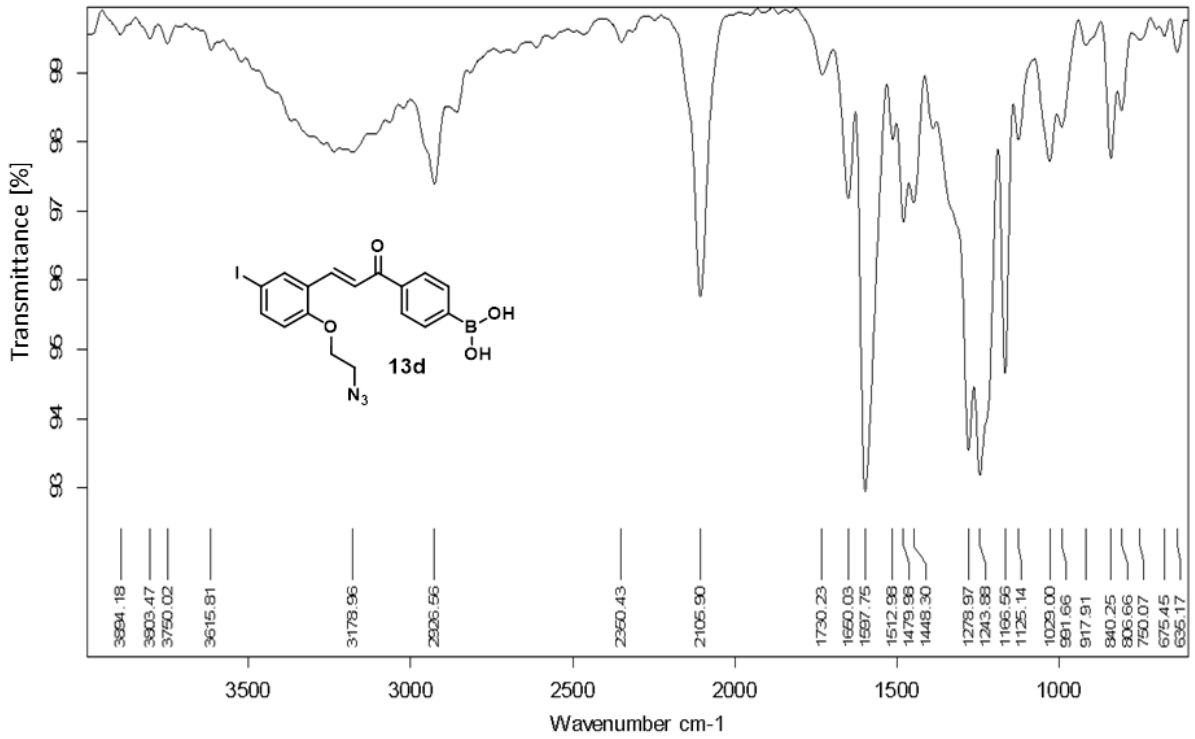

Fig. S43: FT-IR spectra of compound 13d.

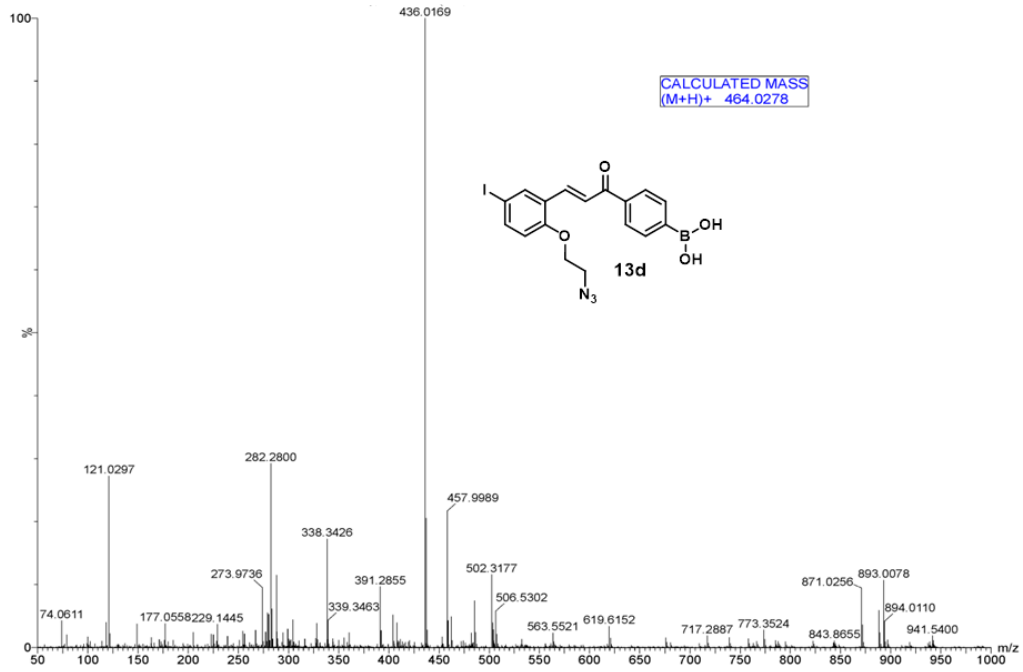

Fig. S44: HR-MS spectra of compound 13d.

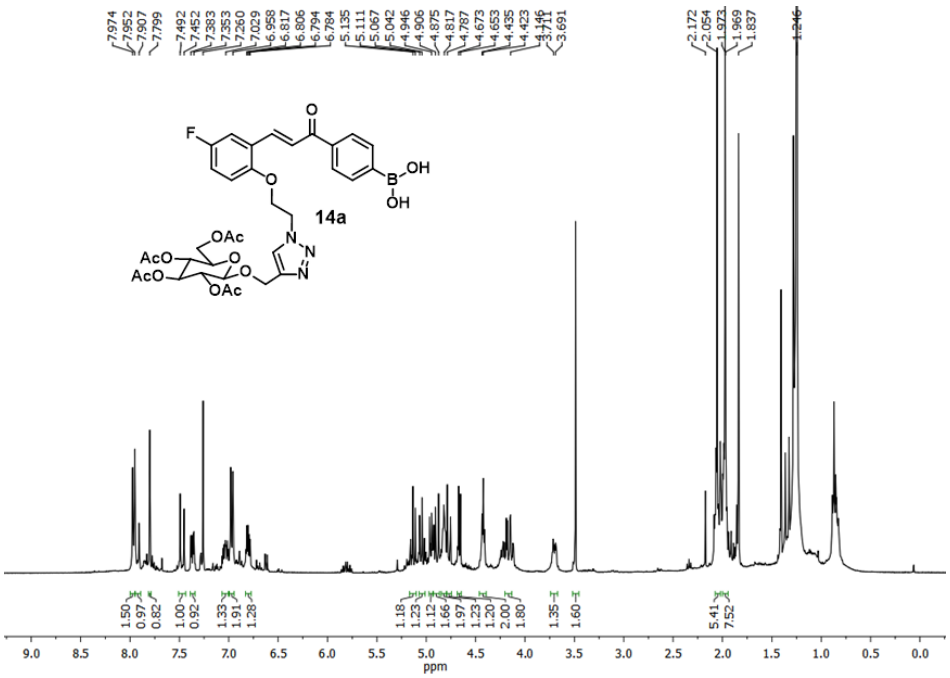

Fig. S45: 1H NMR spectra of compound 14a.

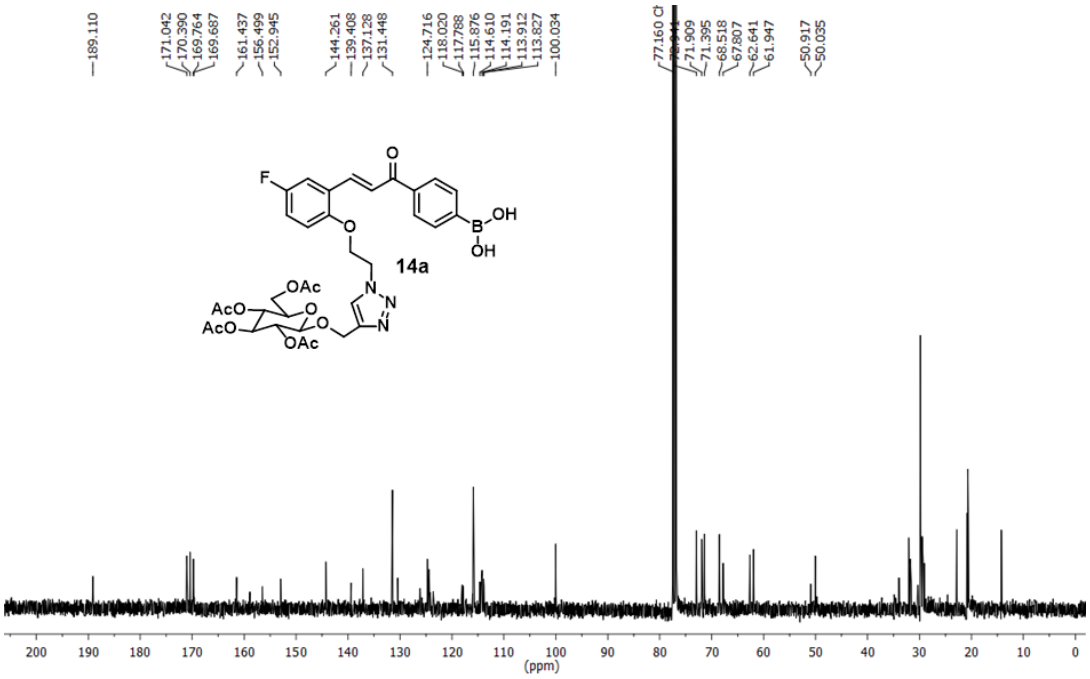

Fig. S46: 13C NMR spectra of compound 14a.

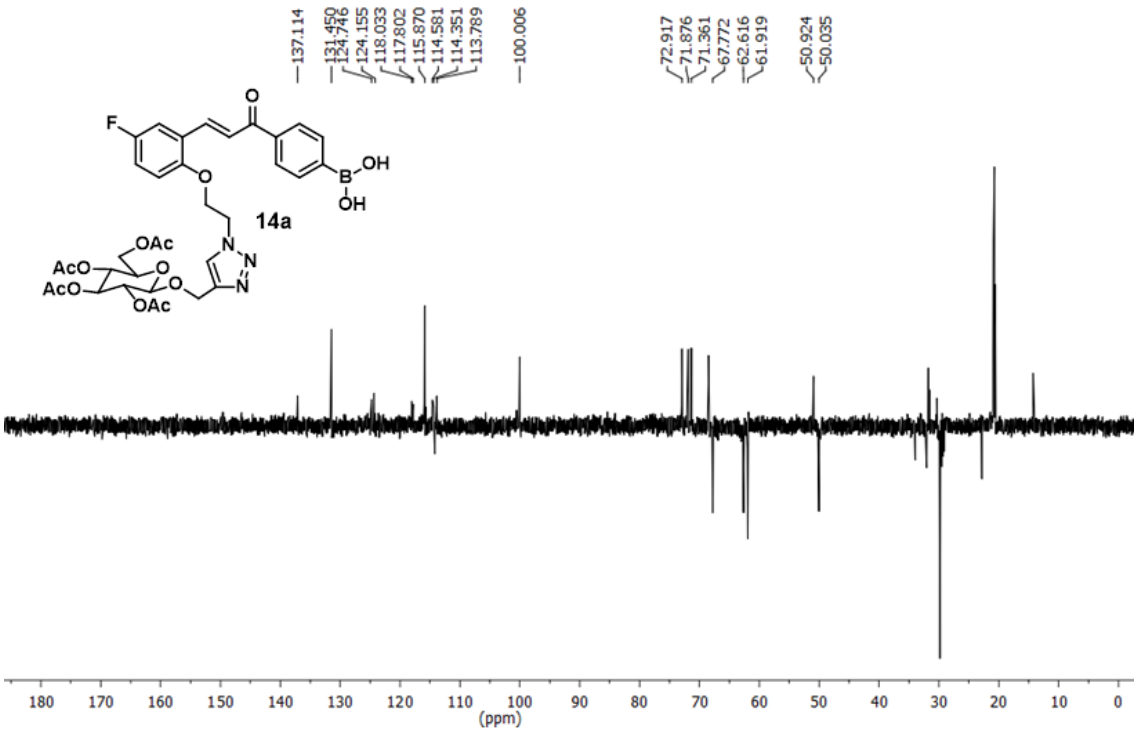

Fig. S47: 13C DEPT spectra of compound 14a.

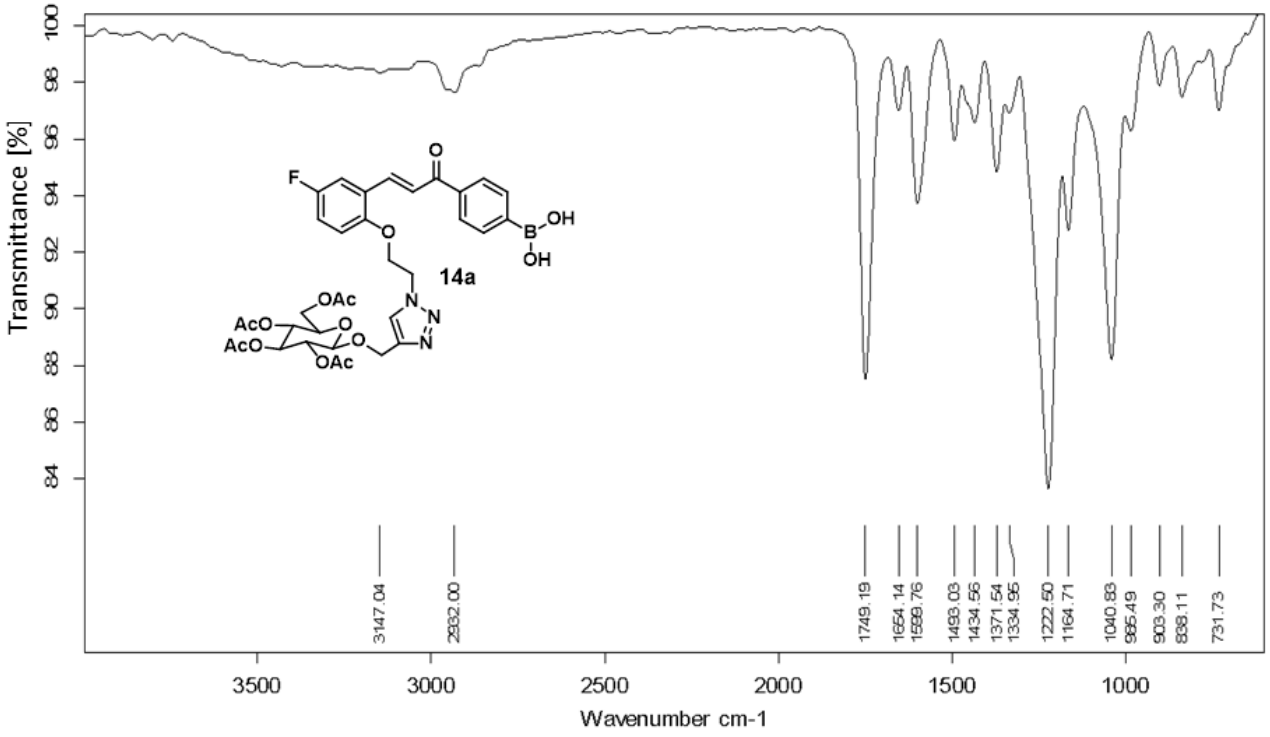

Fig. S48: FT-IR spectra of compound 14a.

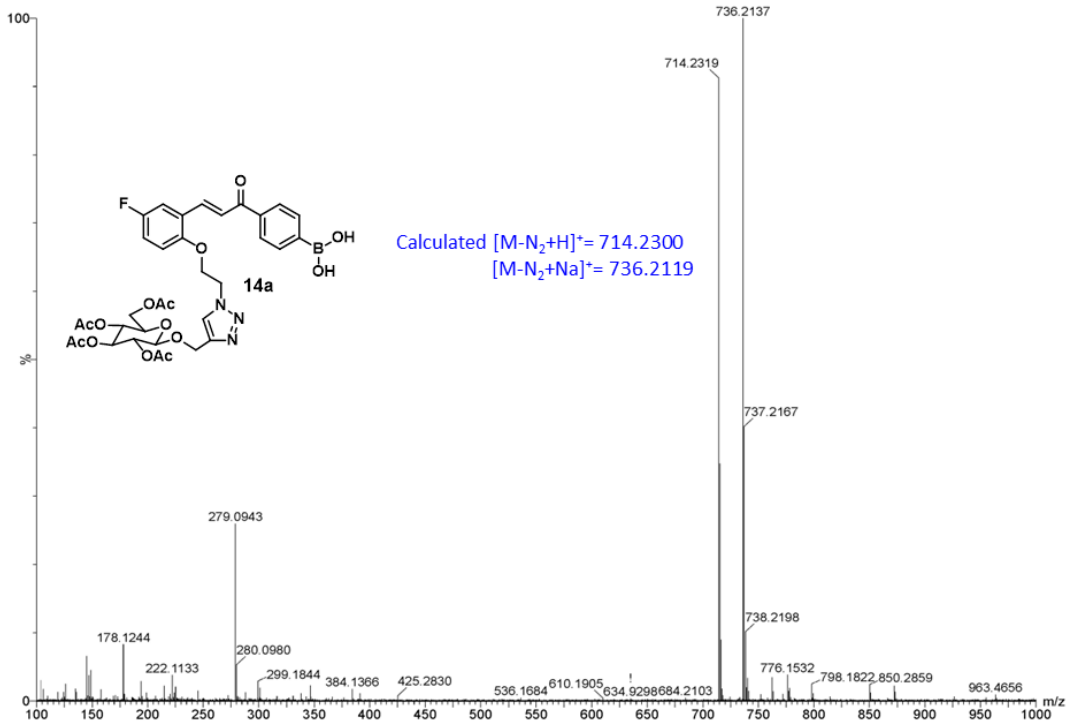

Fig. S49: HR-MS spectra of compound 14a.

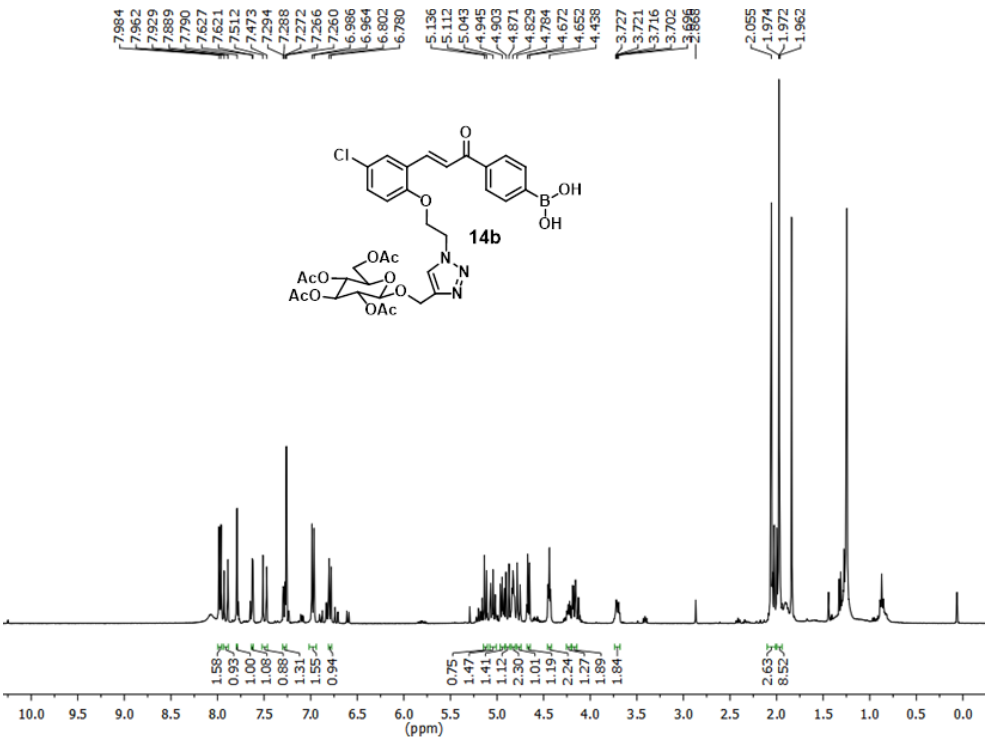

Fig. S50: 1H NMR spectra of compound 14b.

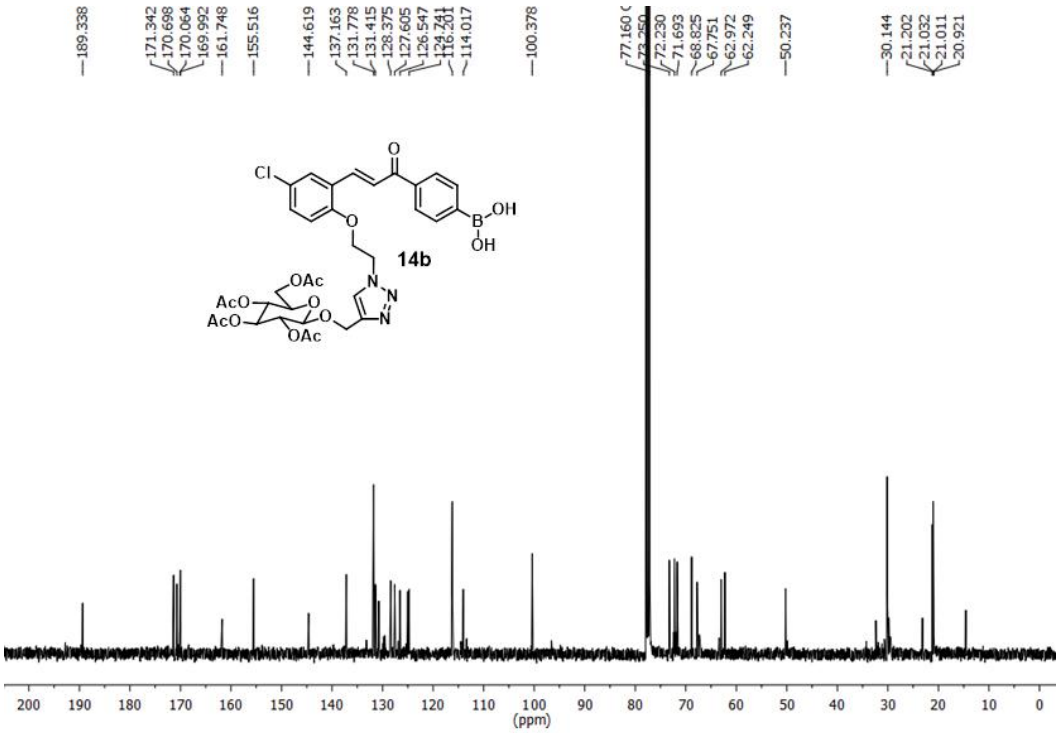

Fig. S51: 13C NMR spectra of compound 14b.

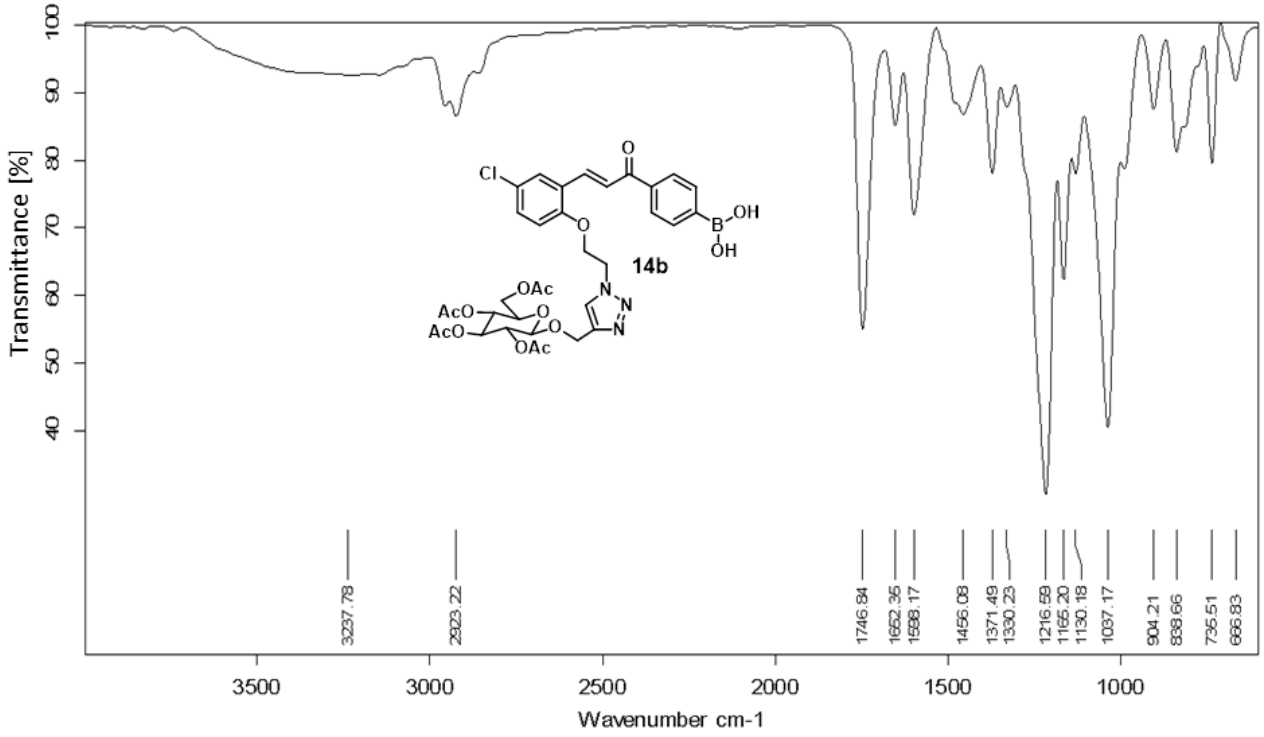

Fig. S52: FT-IR spectra of compound 14b.

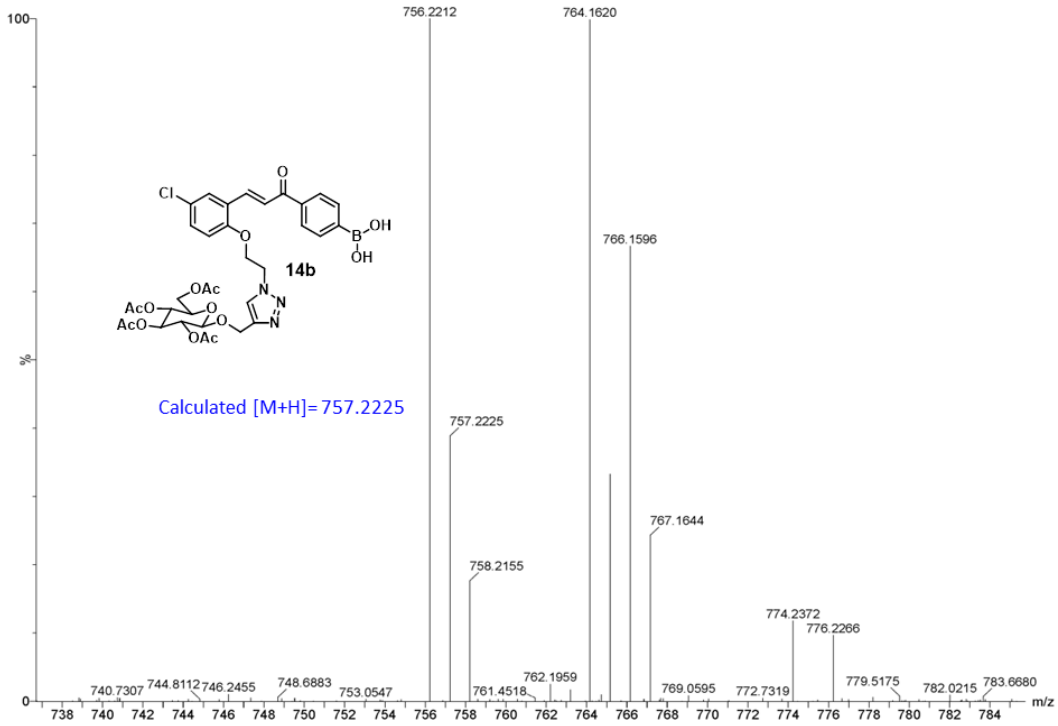

Fig. S53: HR-MS spectra of compound 14b.

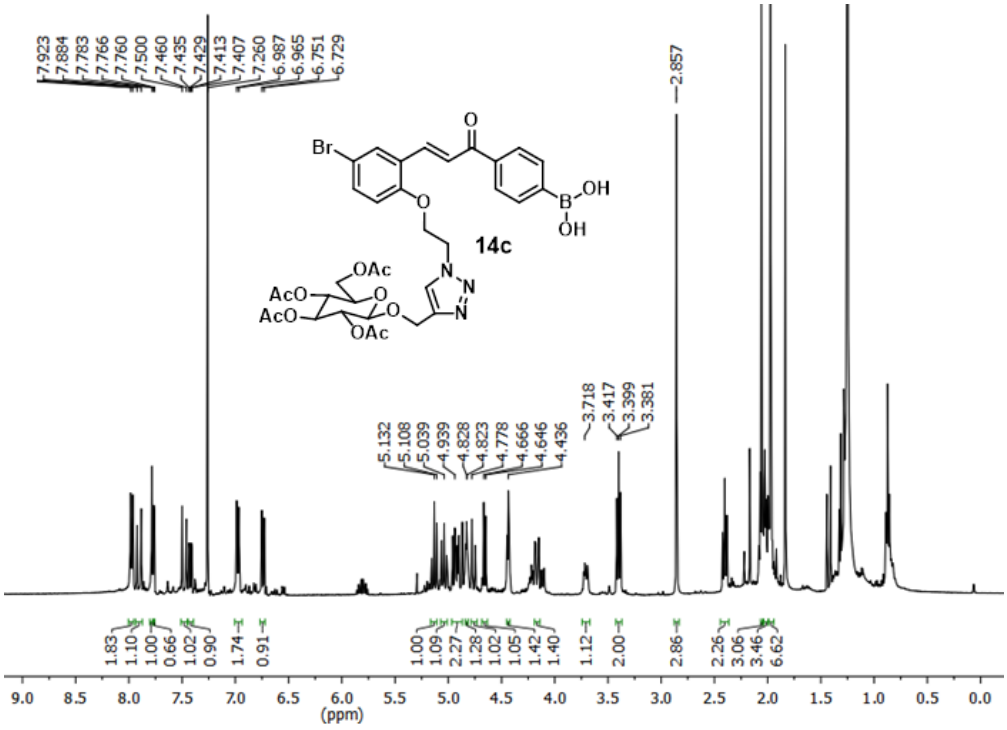

Fig. S54: 1H NMR spectra of compound 14c.

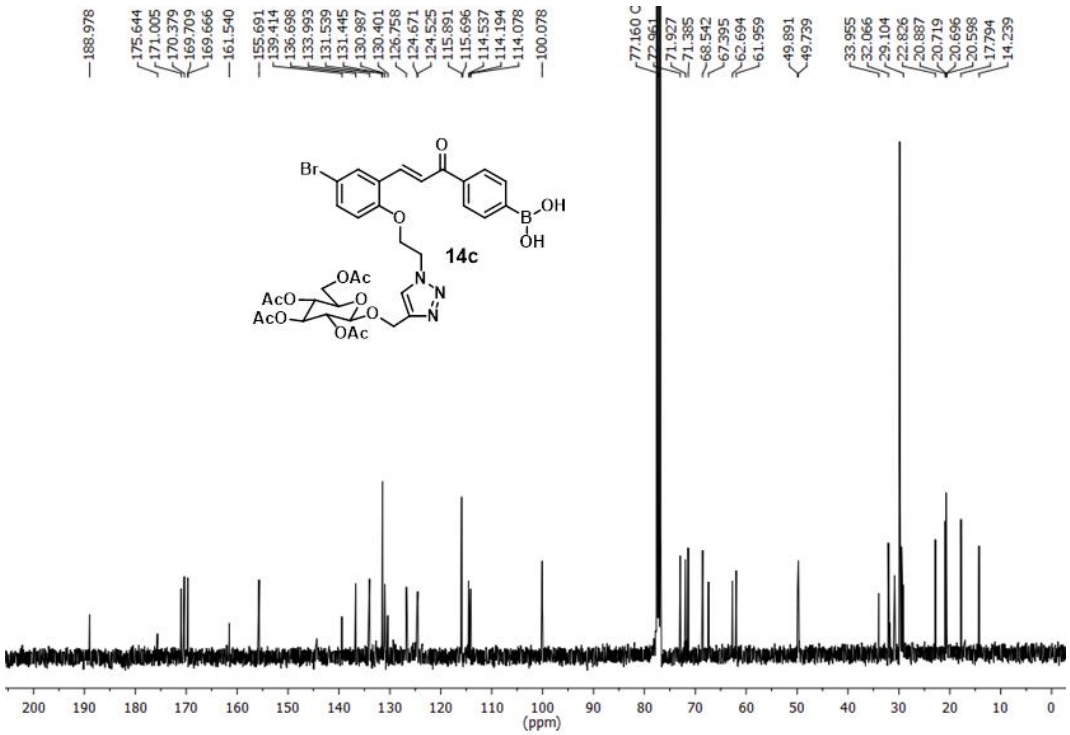

Fig. S55: 13C NMR spectra of compound 14c.

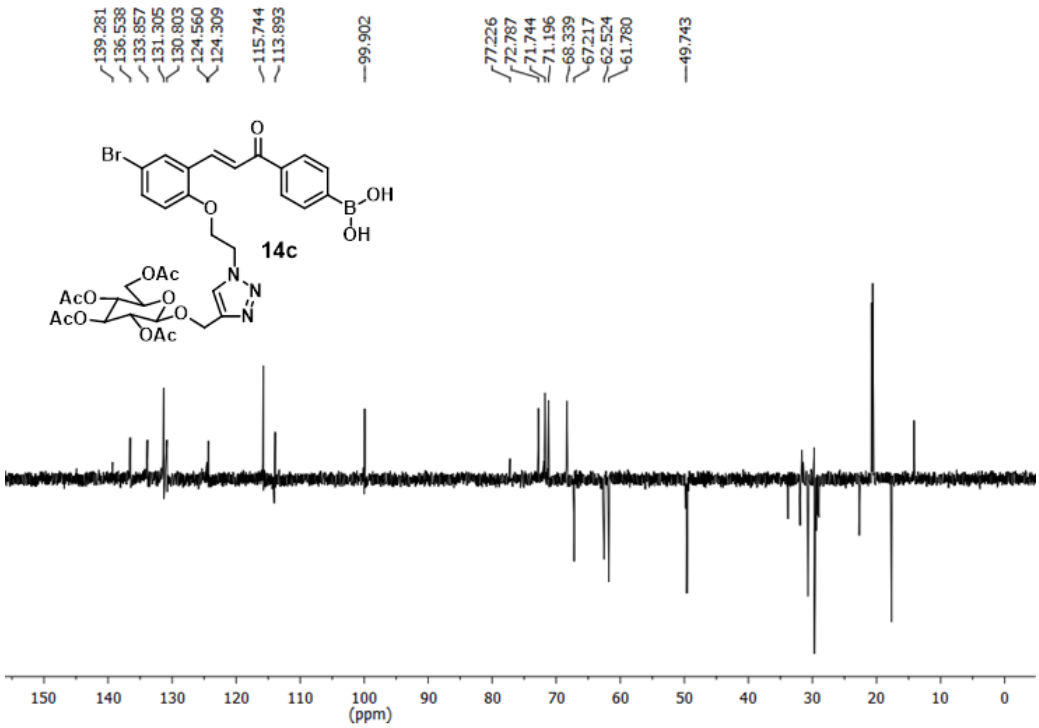

Fig. S56: 13C DEPT spectra of compound 14c.

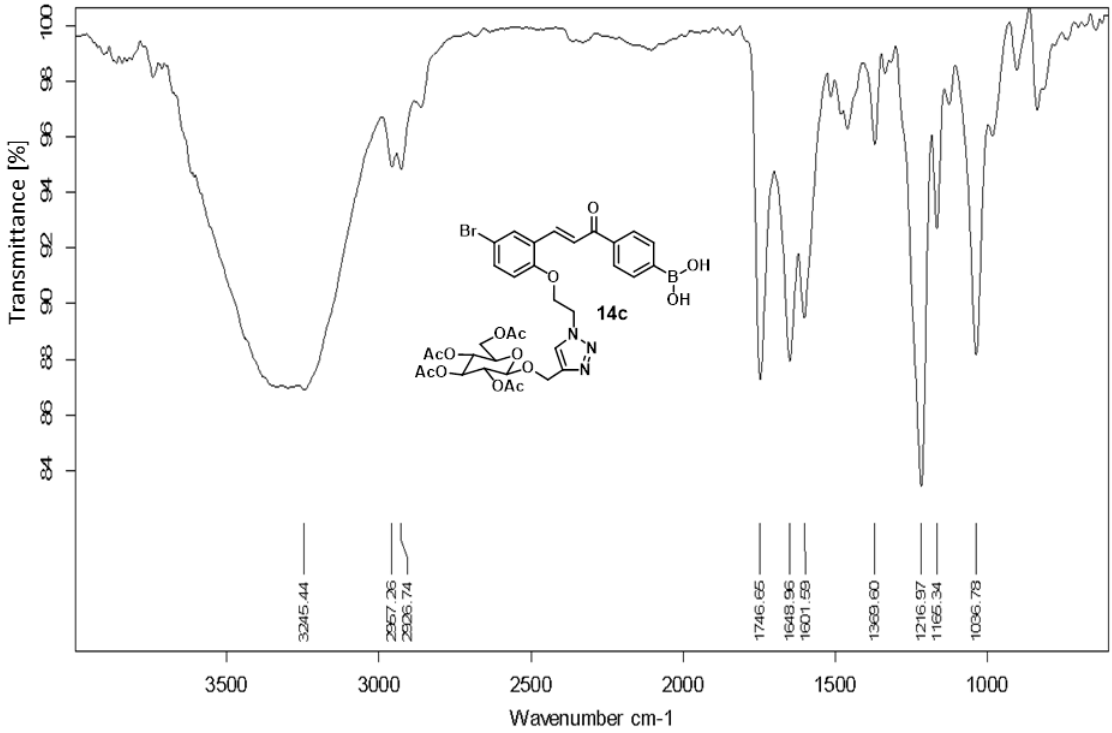

Fig. S57: FT-IR spectra of compound 14c.

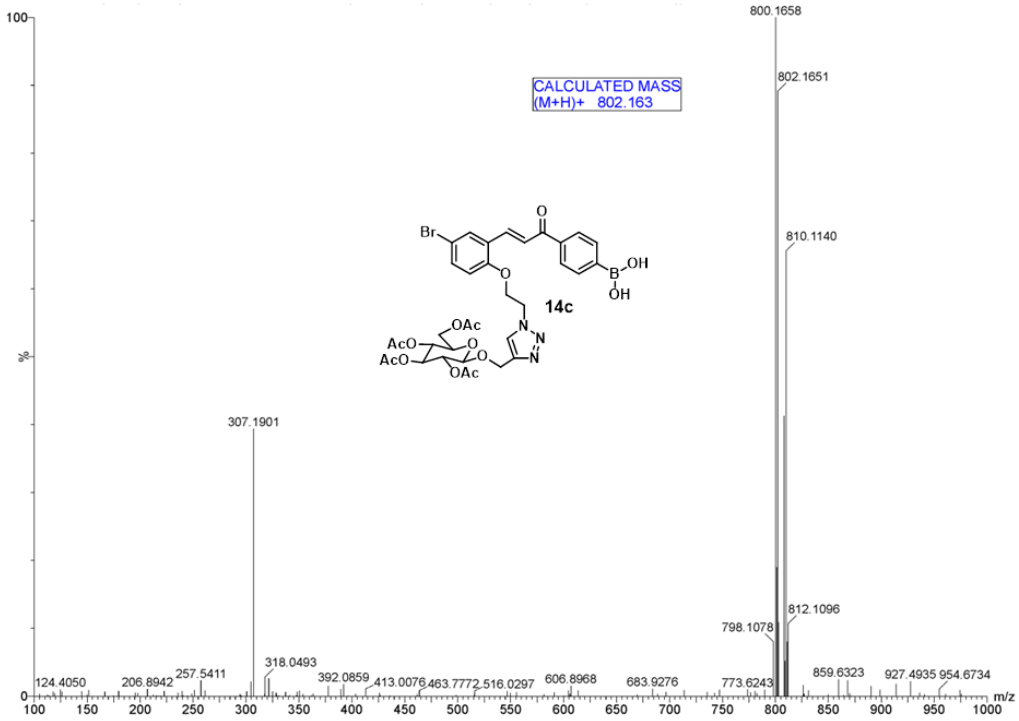

Fig. S58: HR-MS spectra of compound 14c.

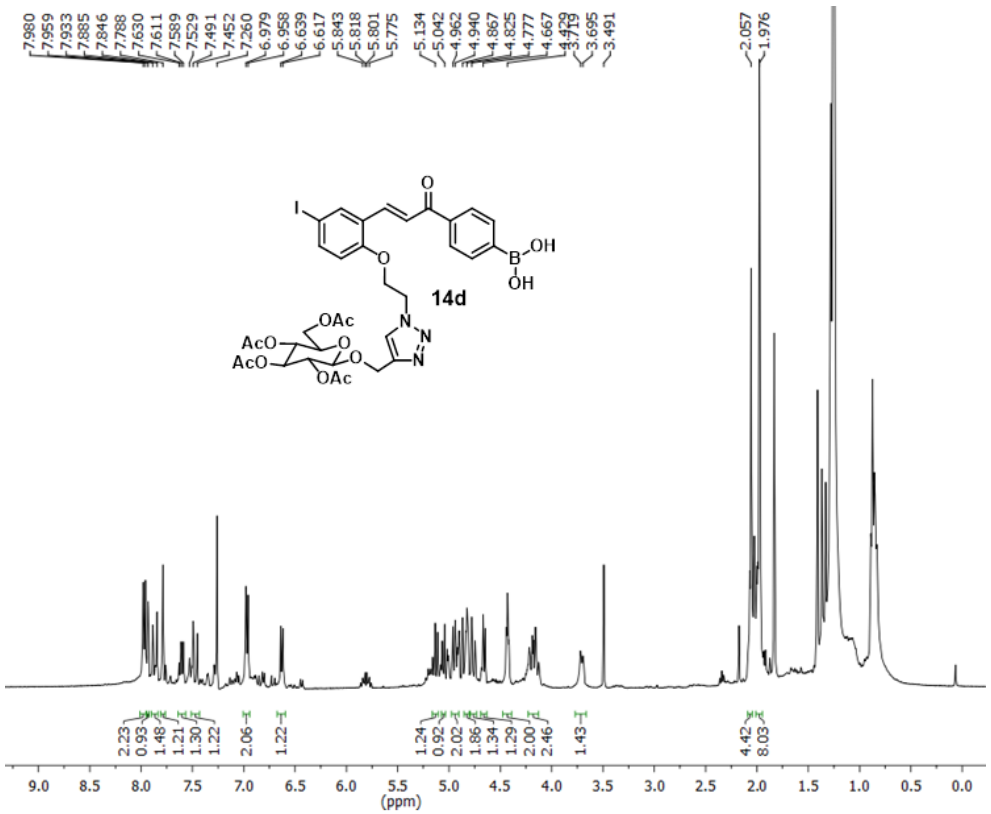

Fig. S59: 1H NMR spectra of compound 14d.

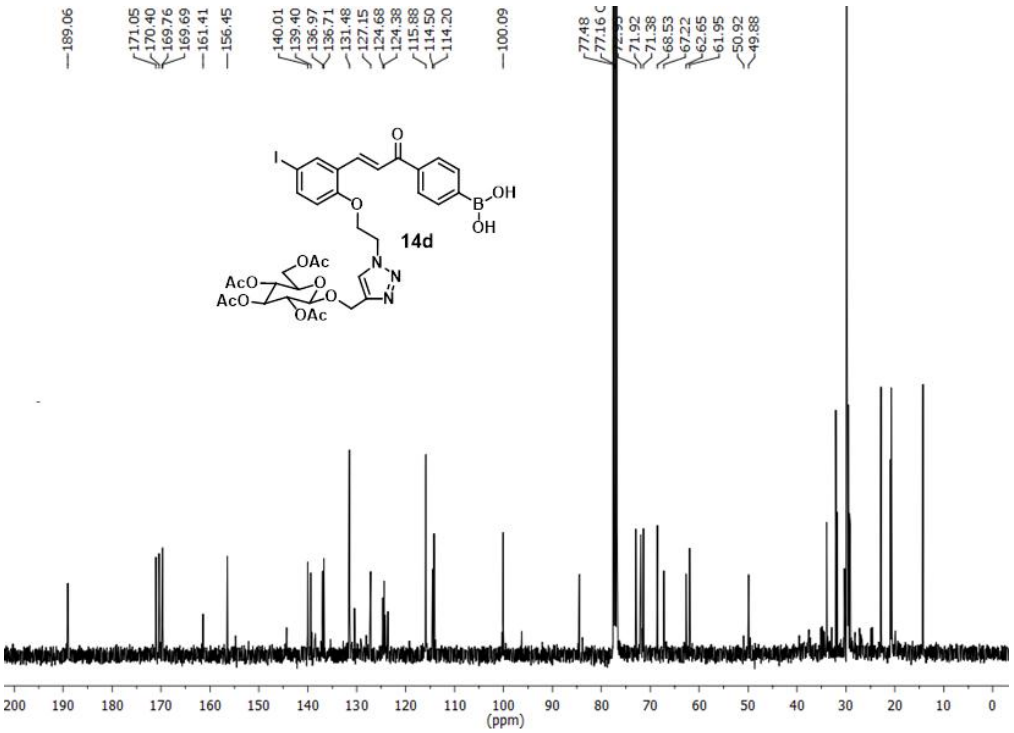

Fig. S60: 13C NMR spectra of compound 14d.

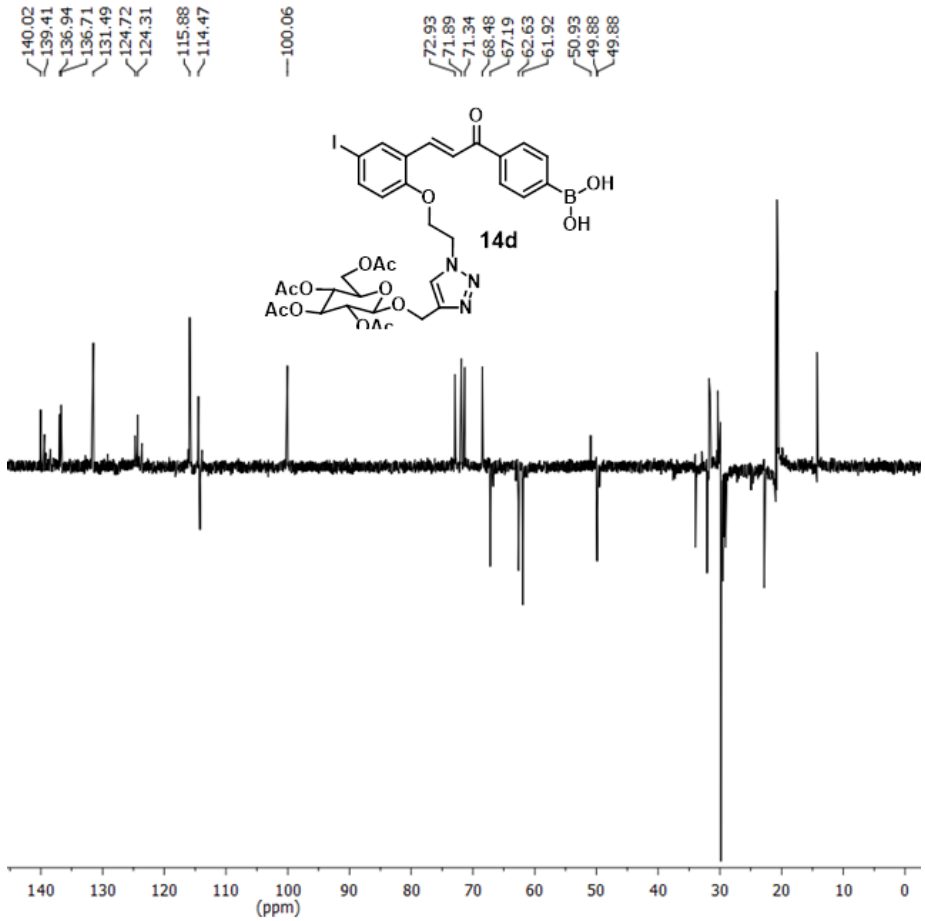

Fig. S61: 13C DEPT spectra of compound 14d.

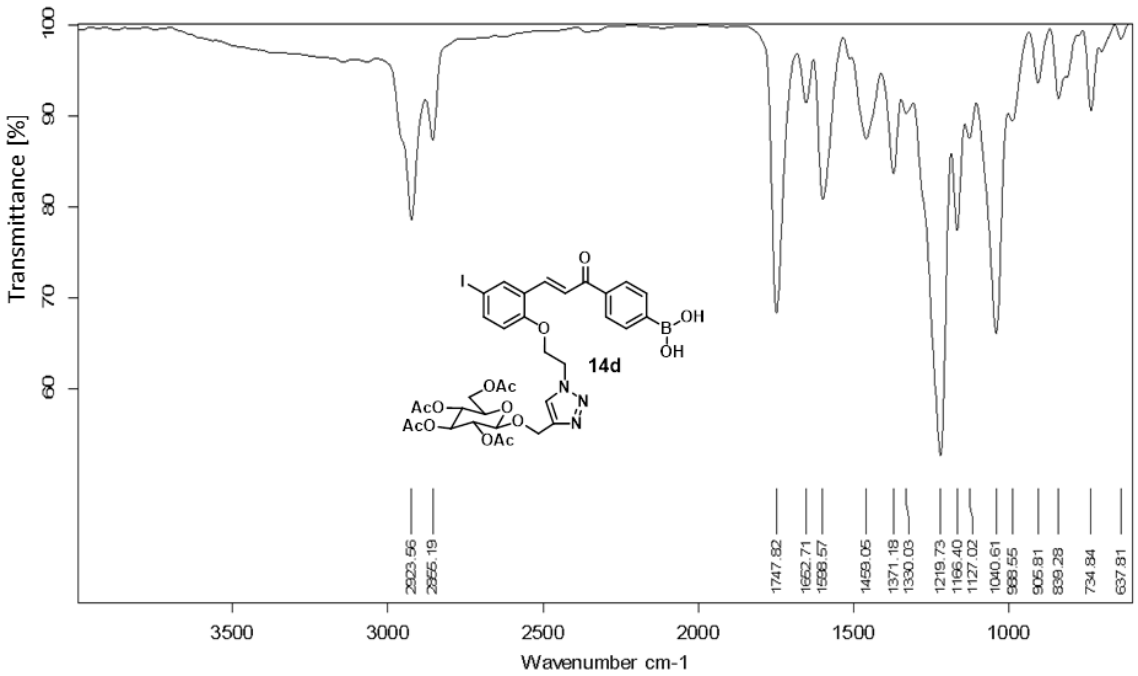

Fig. S62: FT-IR spectra of compound 14d.

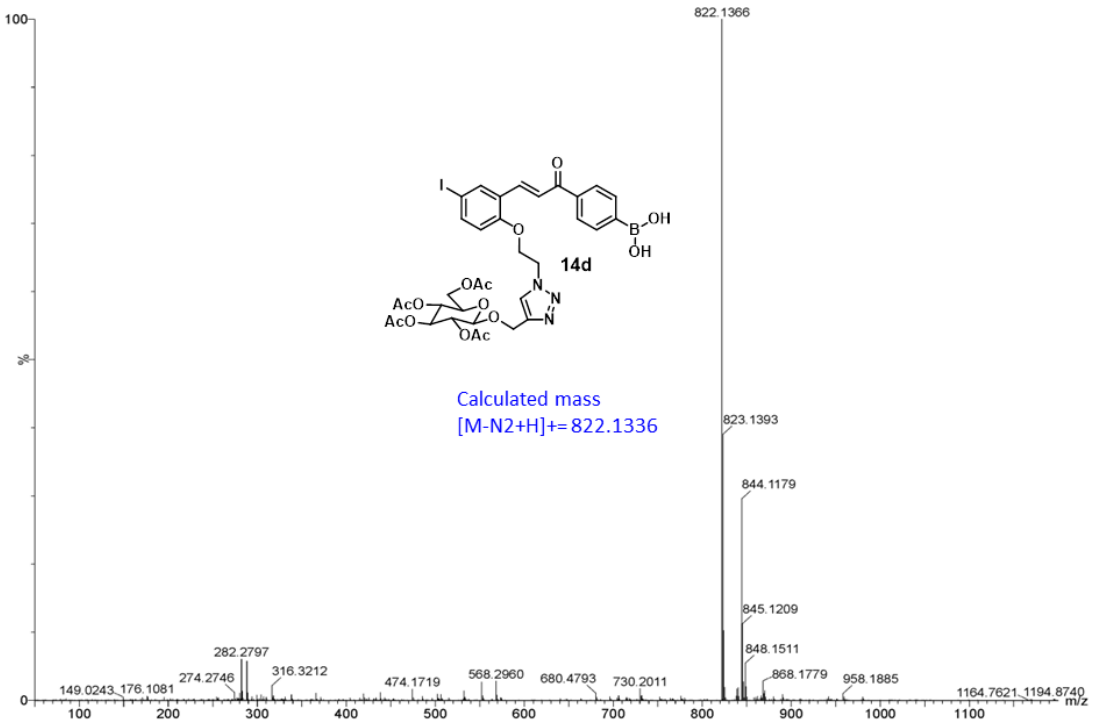

Fig. S63: HR-MS spectra of compound 14d.

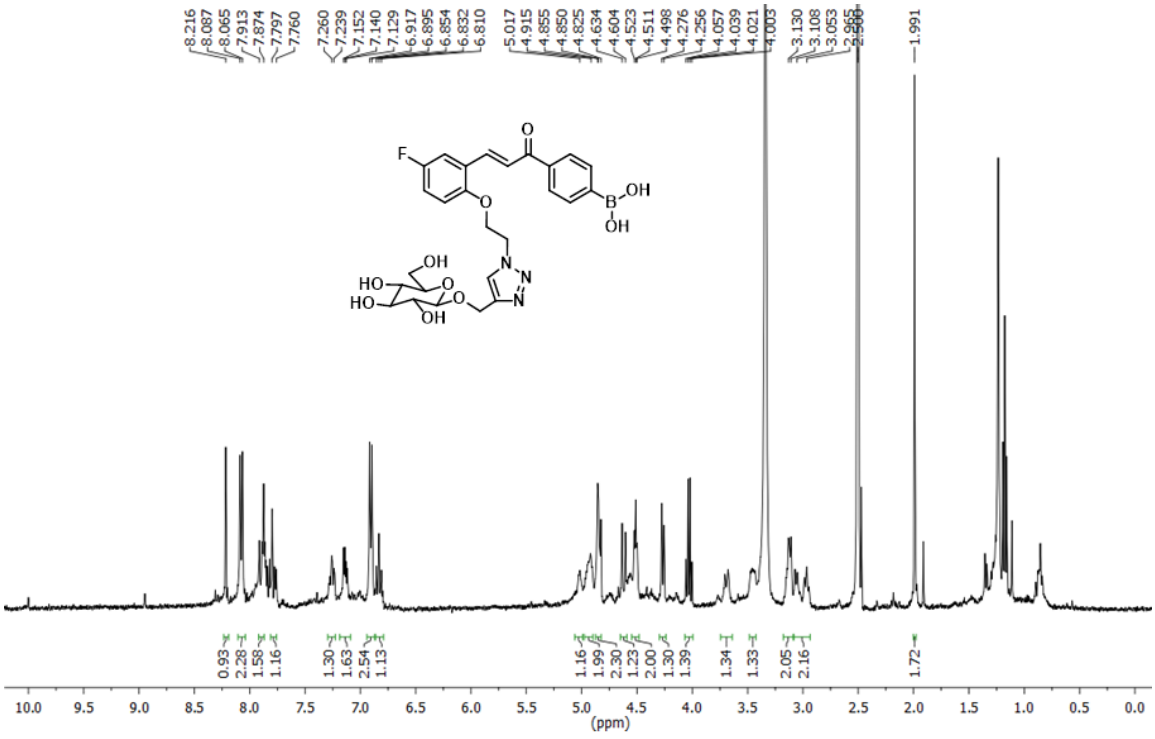

Fig. S64: 1H NMR spectra of compound 14e.

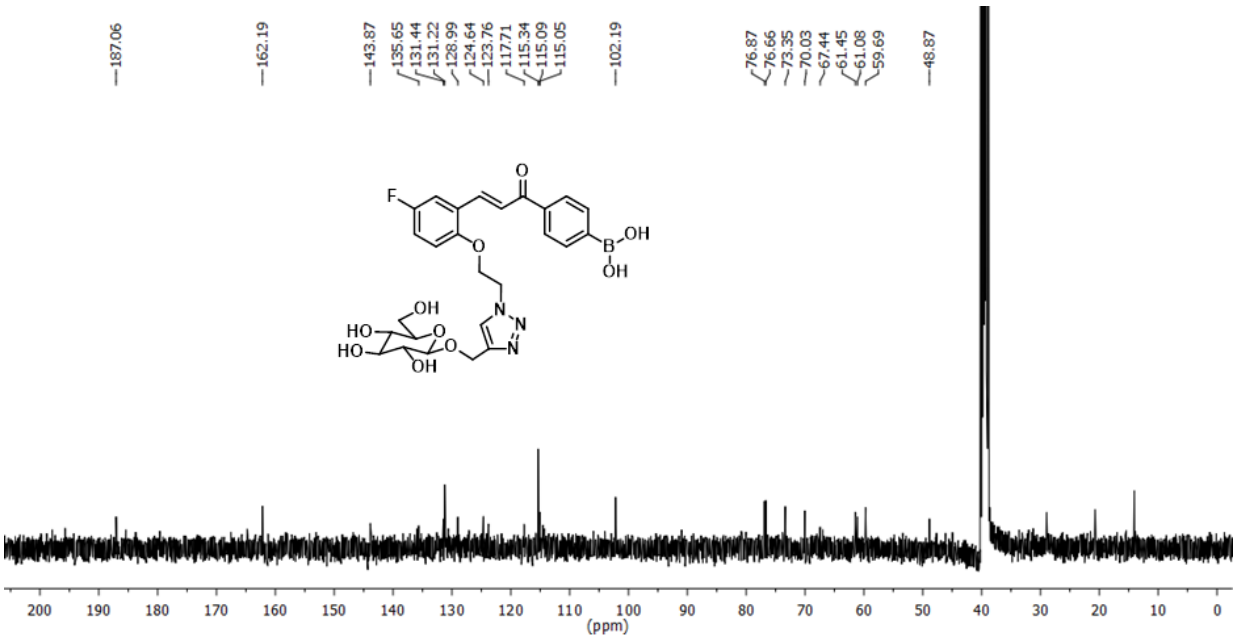

Fig. S65: 13C NMR spectra of compound 14e.

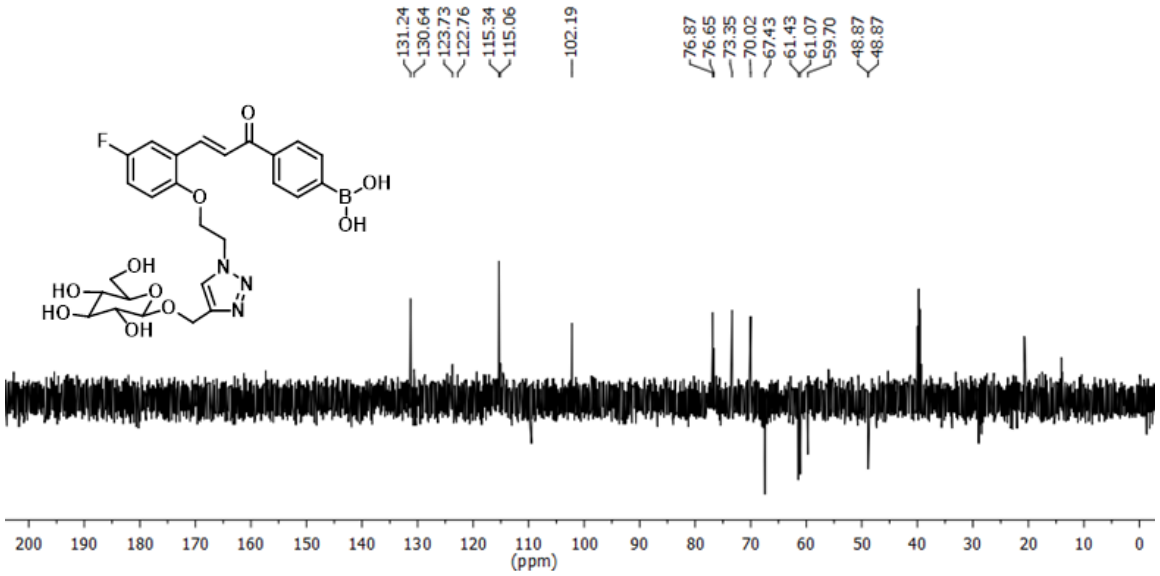

Fig. S66: 13C DEPT spectra of compound 14e.

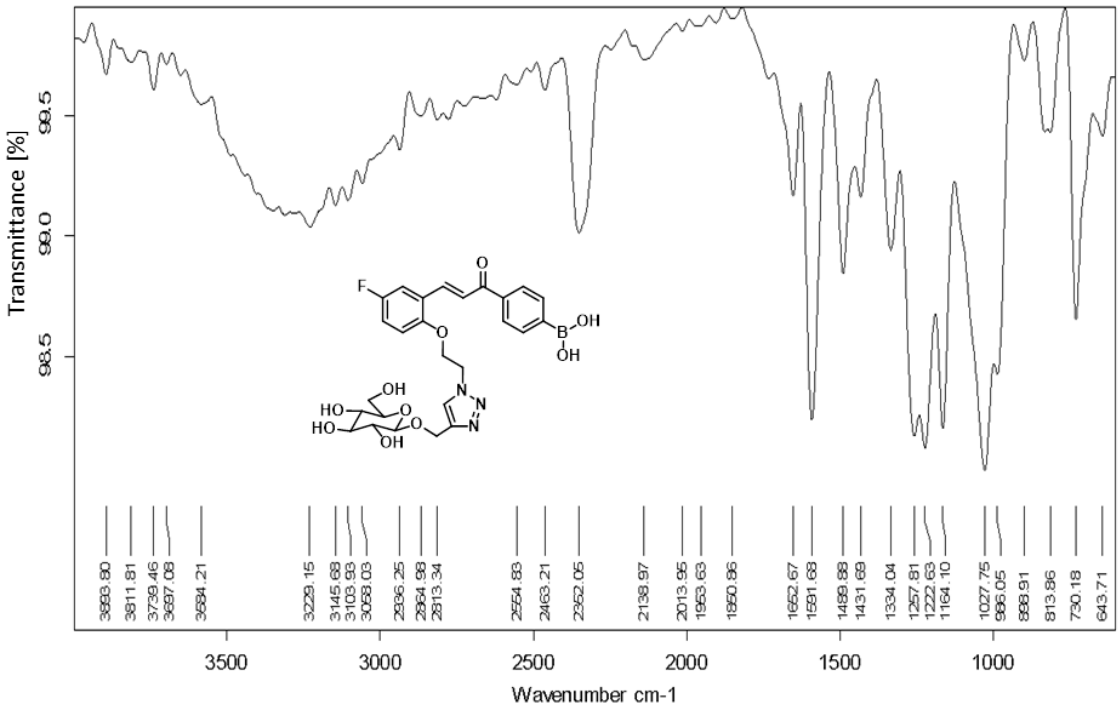

Fig. S67: FT-IR spectra of compound 14e.

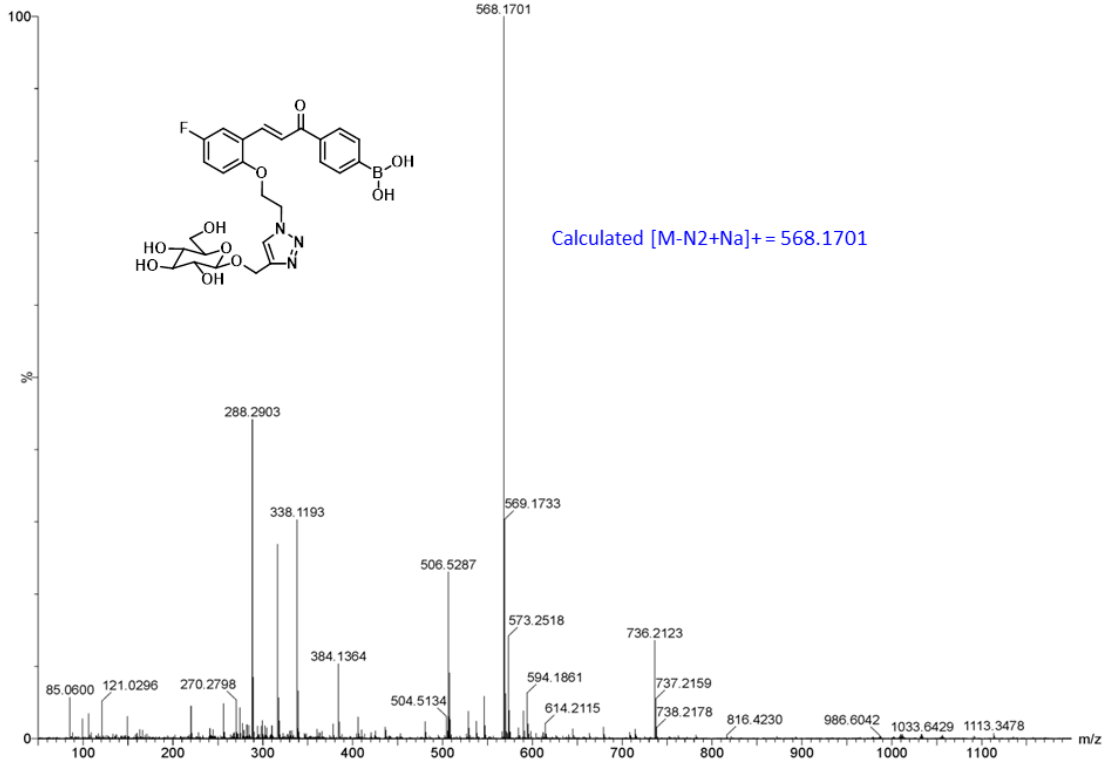

Fig. S68: HR-MS spectra of compound 14e.

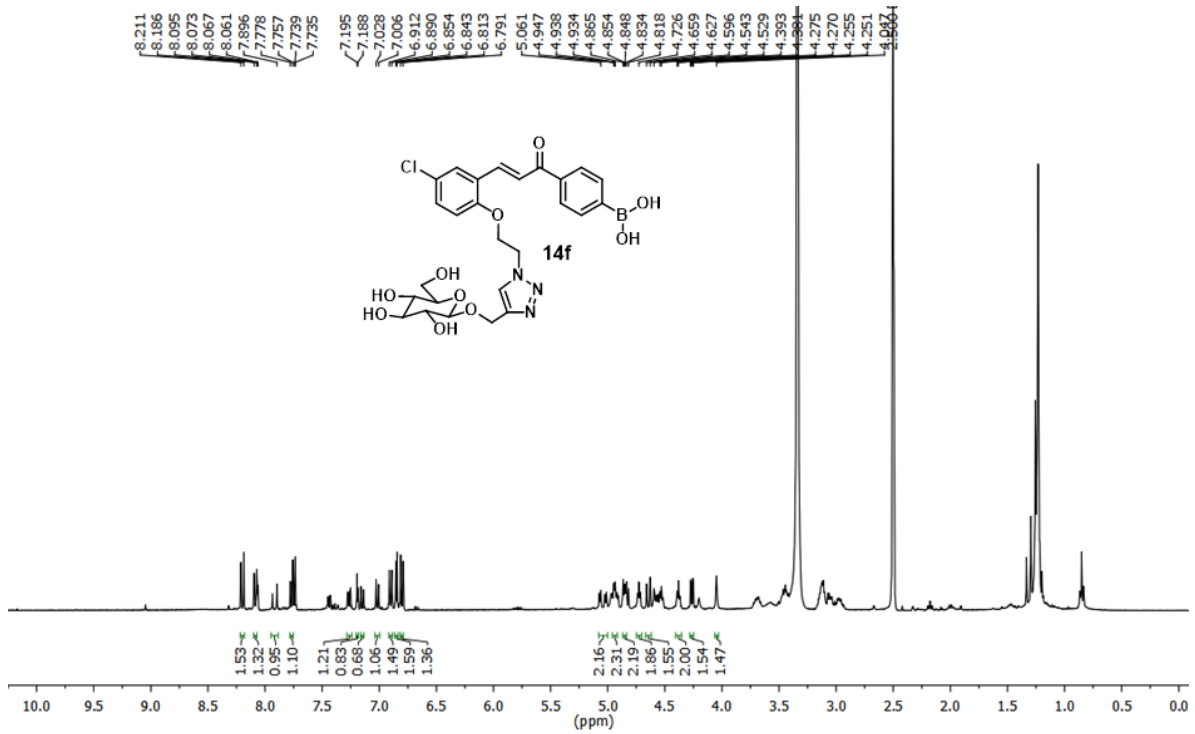

Fig. S69: 1H NMR spectra of compound 14f.

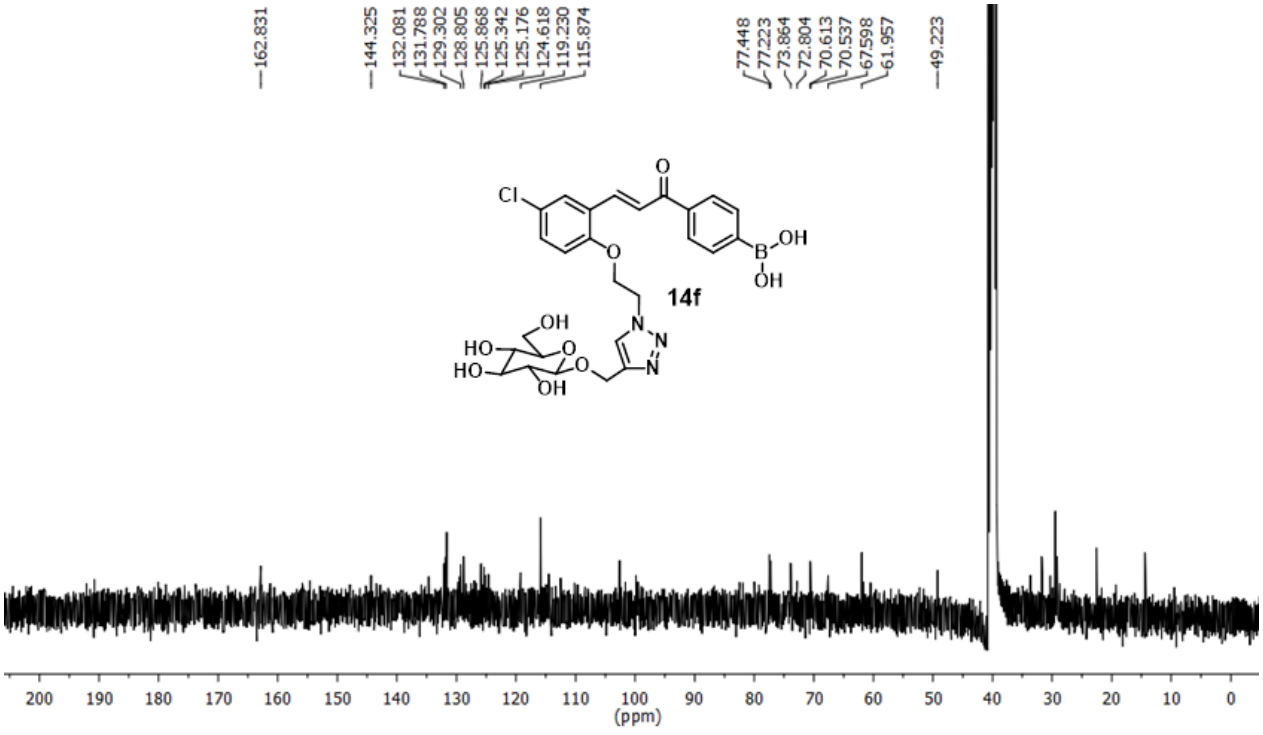

Fig. S70: 13C NMR spectra of compound 14f.

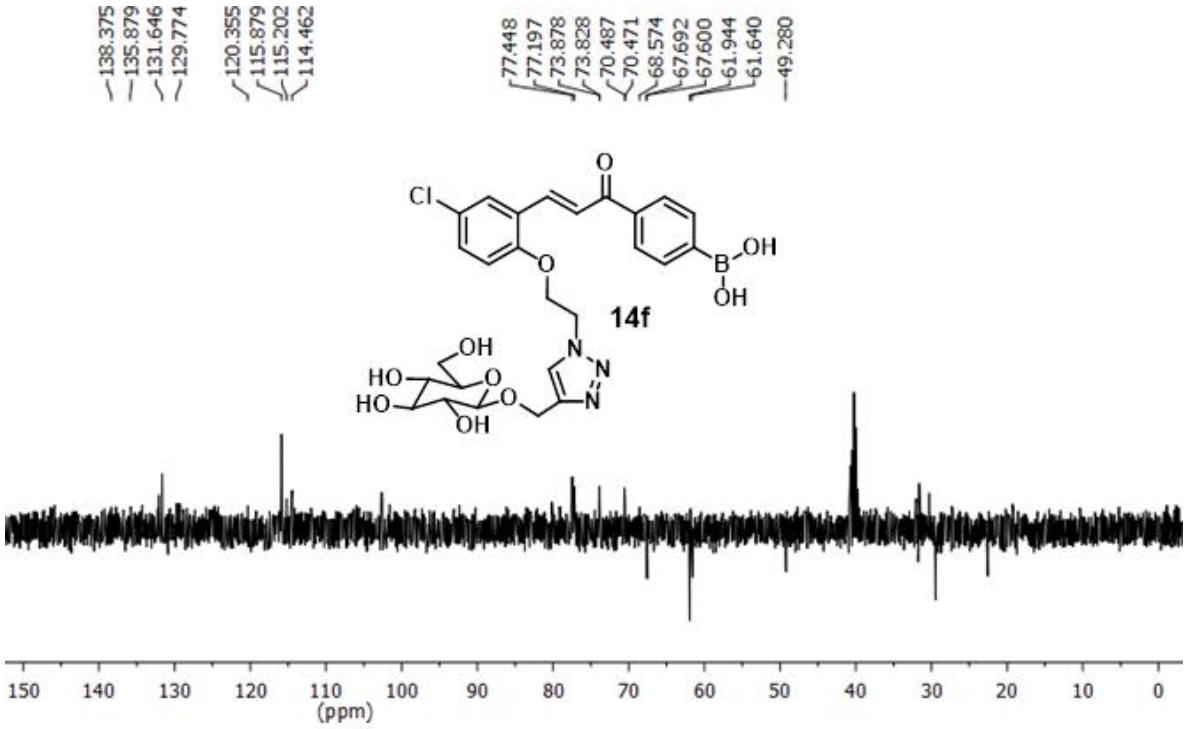

Fig. S71: 13C DEPT spectra of compound 14f.

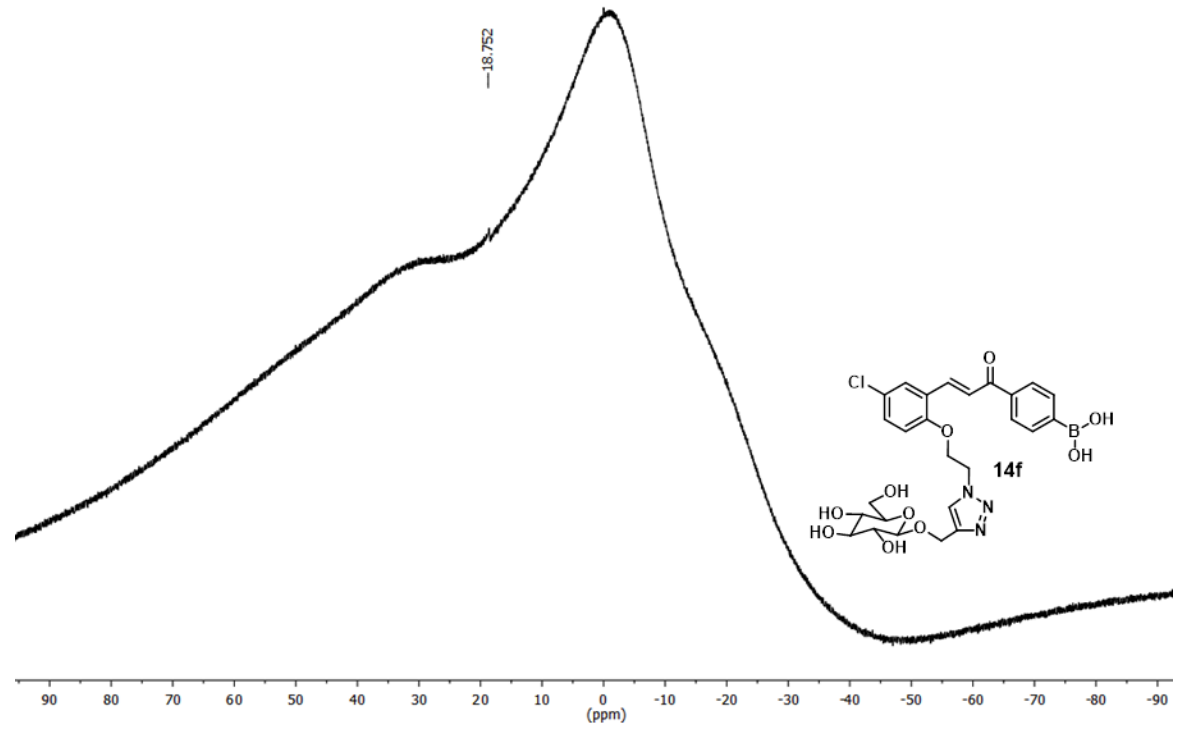

Fig. S72: 11B NMR spectra of compound 14f.

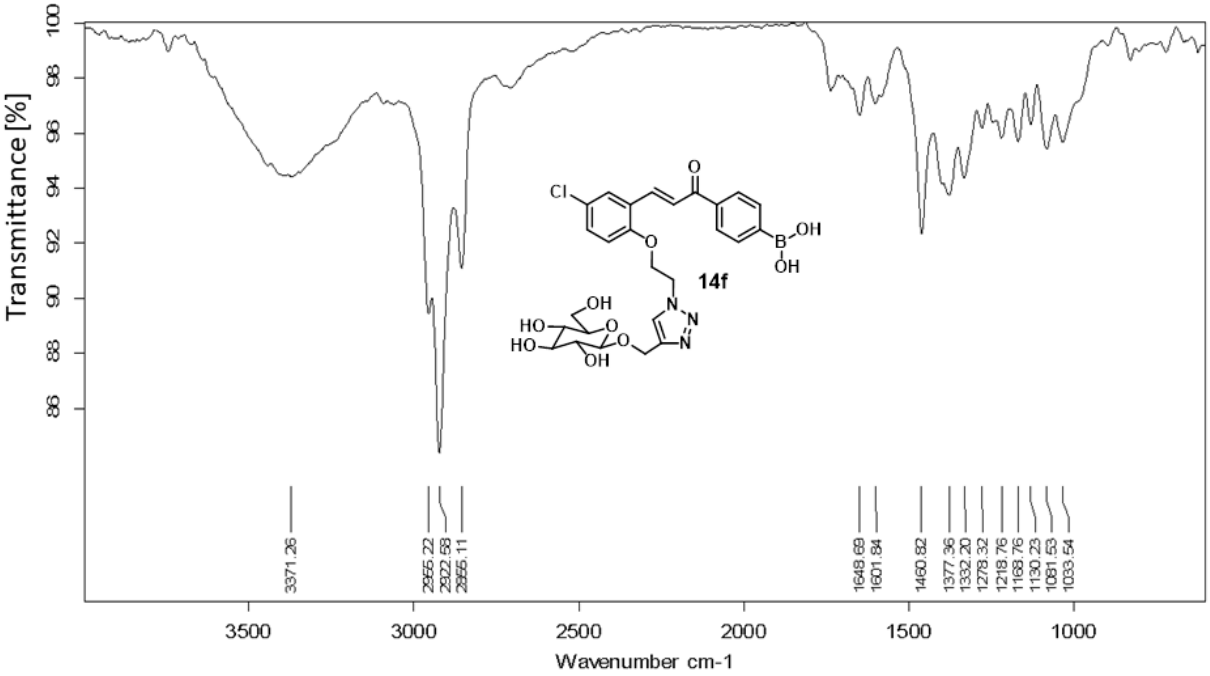

Fig. S73: FT-IR spectra of compound 14f.

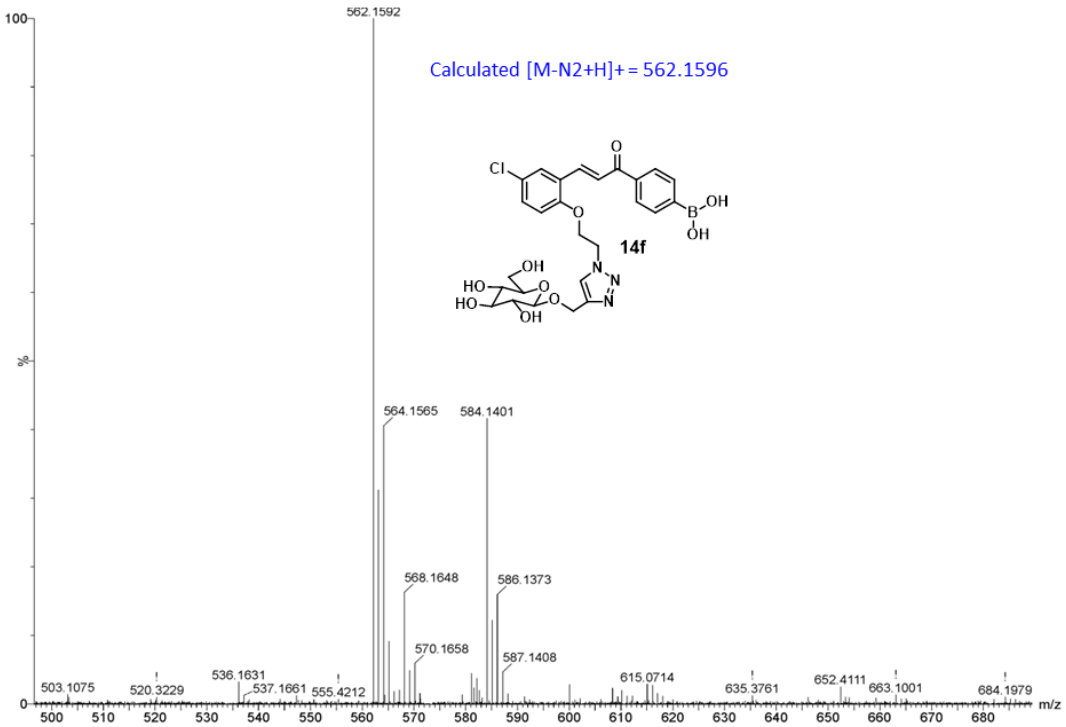

Fig. S74: HR-MS spectra of compound 14f.

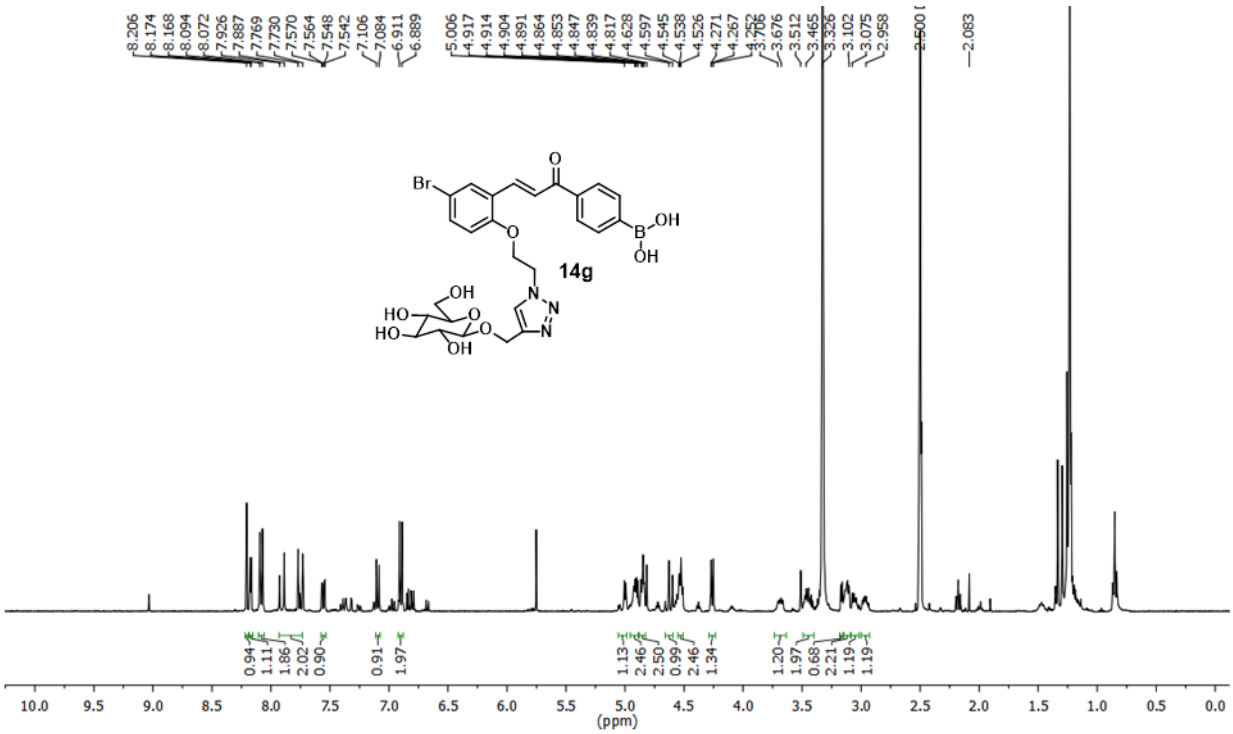

Fig. S75: 1H NMR spectra of compound 14g.

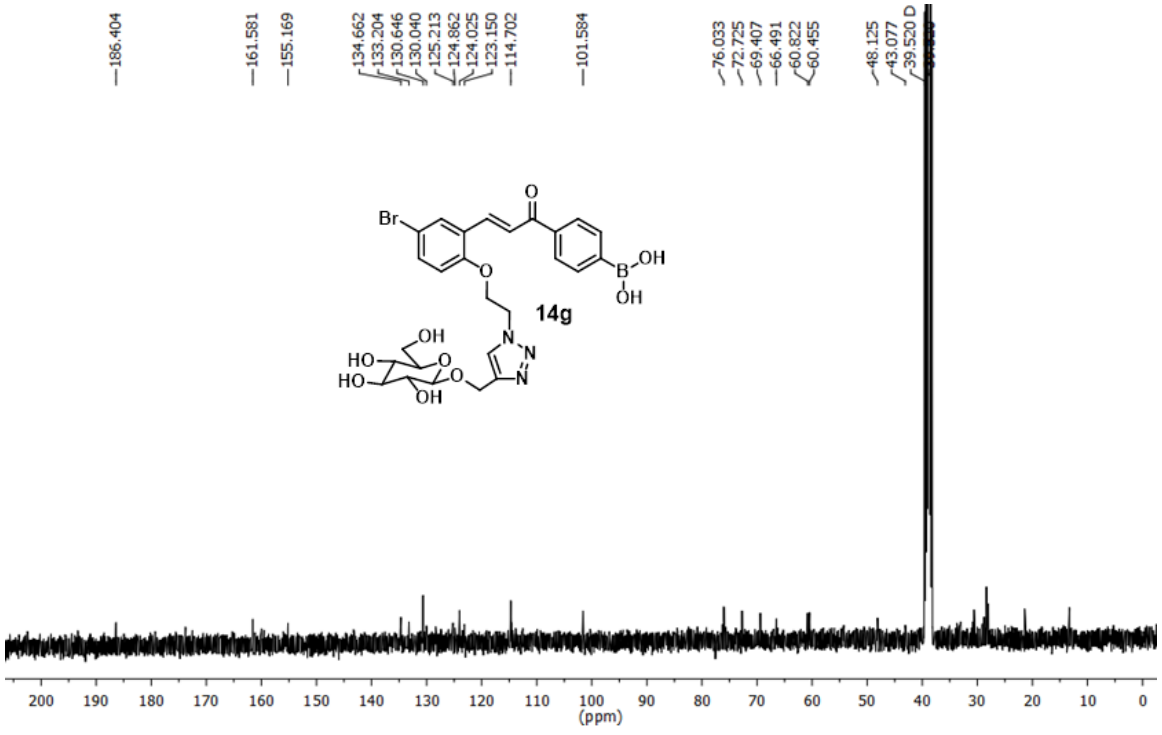

Fig. S76: 13C NMR spectra of compound 14g.

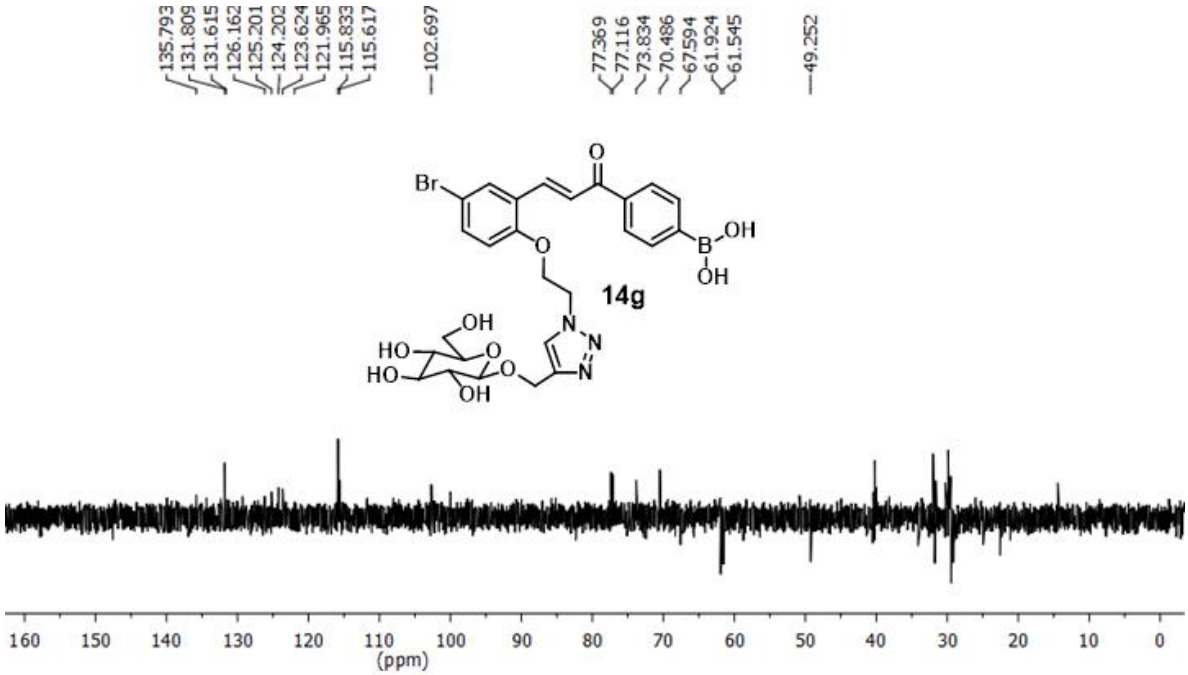

Fig. S77: 13C DEPT spectra of compound 14g.

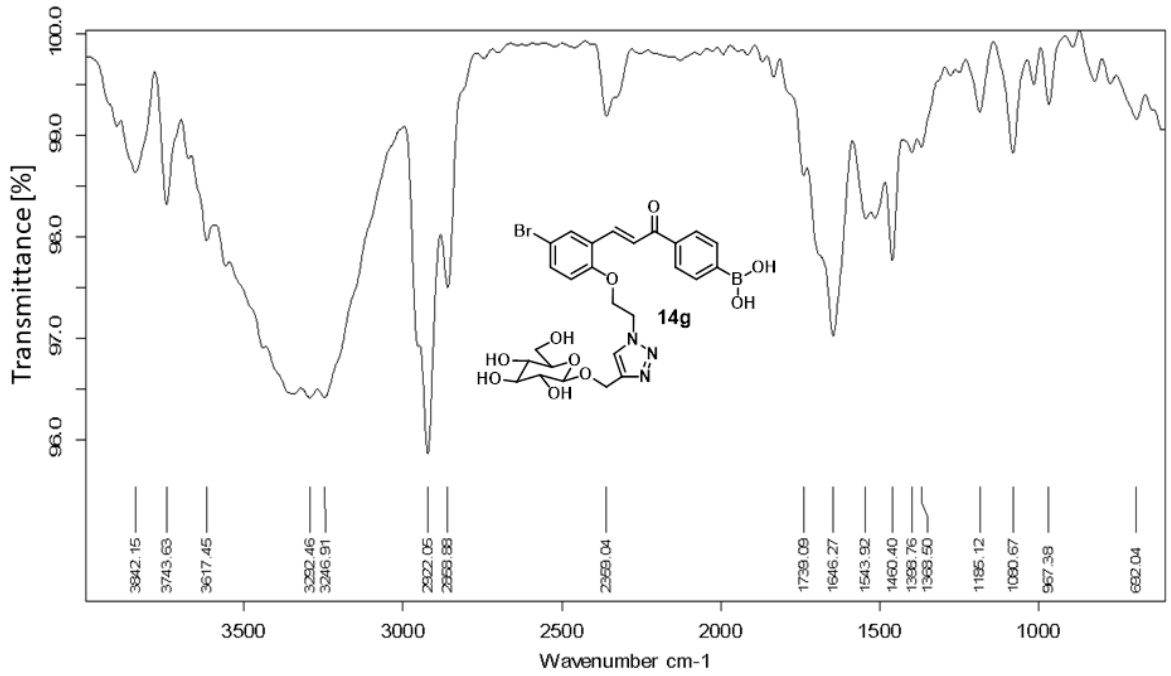

Fig. S78: FT-IR spectra of compound 14g.

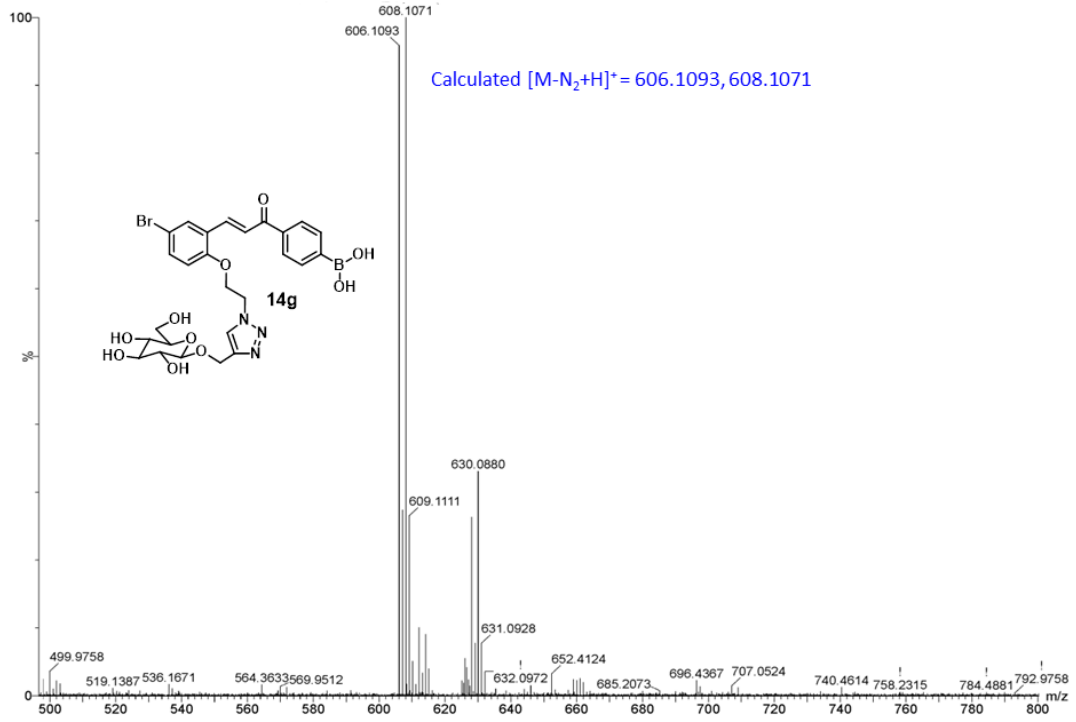

Fig. S79: HR-MS spectra of compound 14g.

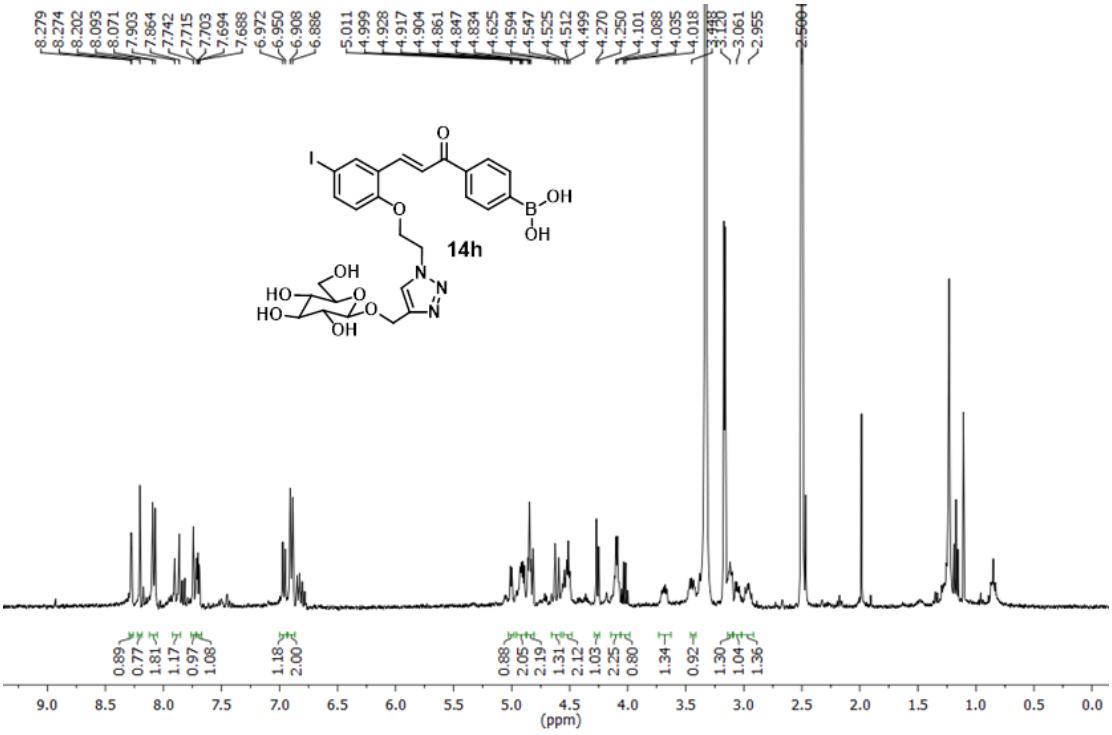

Fig. S80: 1H NMR spectra of compound 14h.

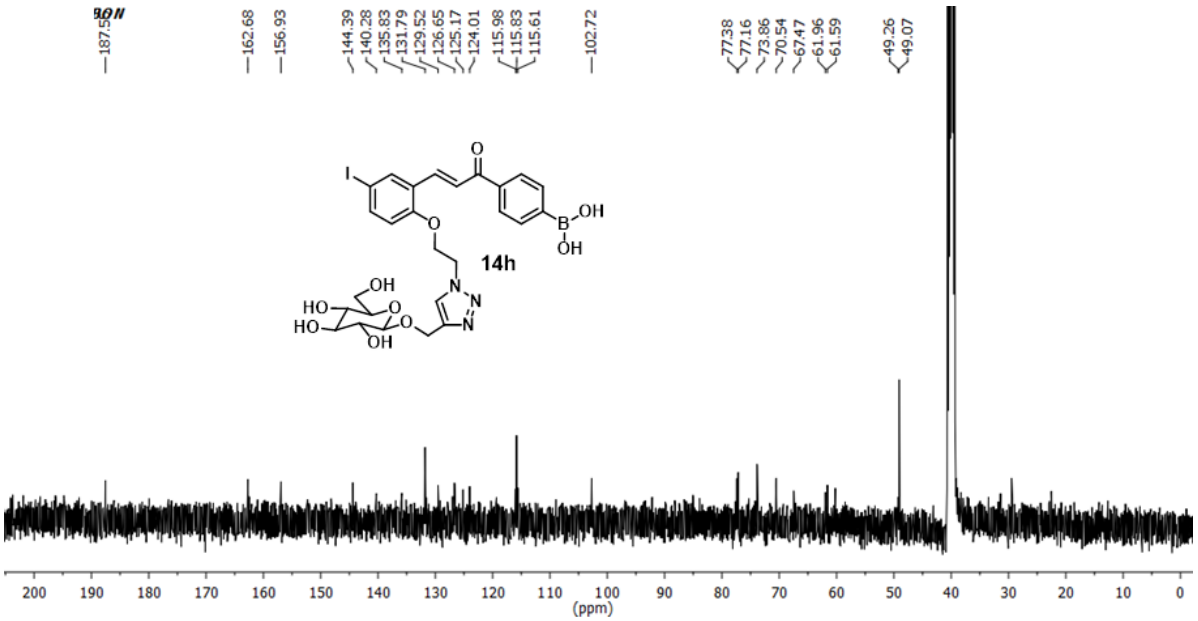

Fig. S81: 13C NMR spectra of compound 14h.

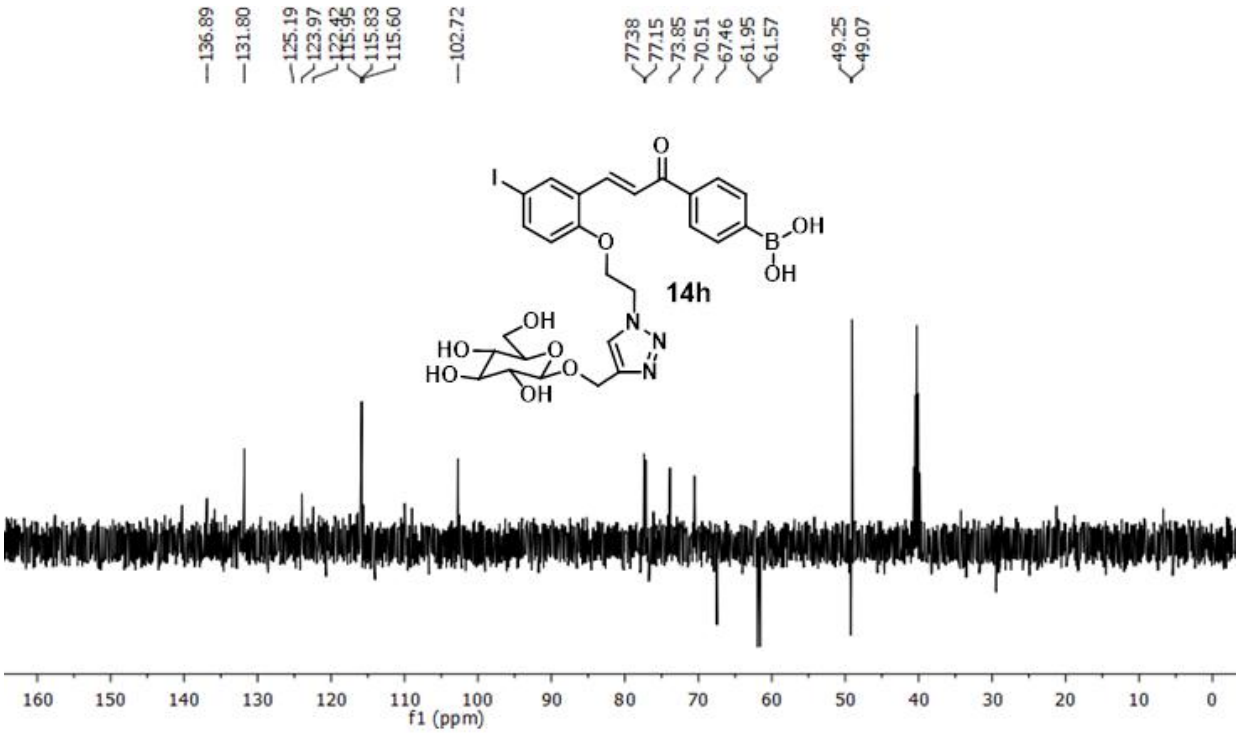

Fig. S82: 13C DEPT spectra of compound 14h.

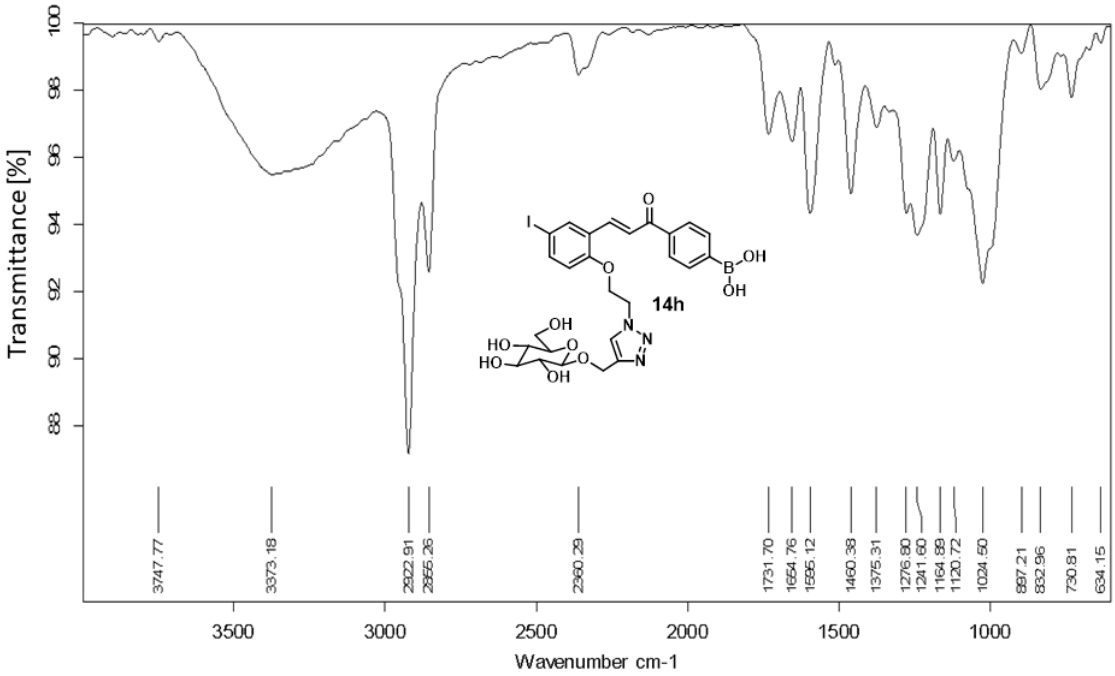

Fig. S83: FT-IR spectra of compound 14h.

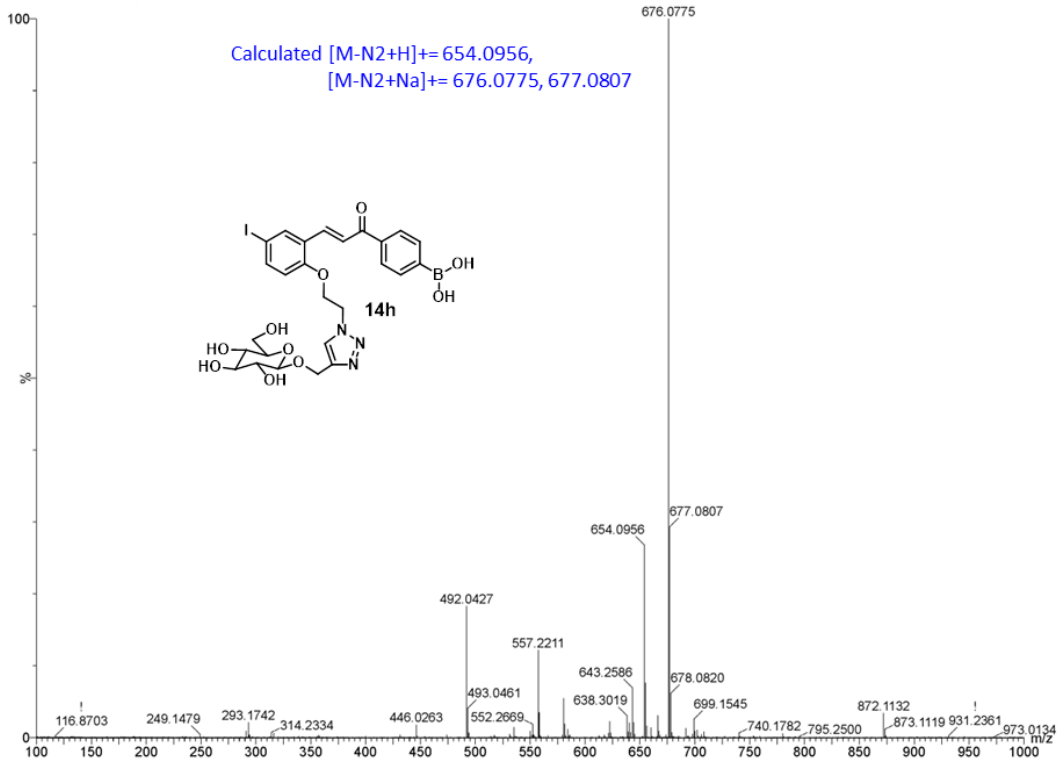

Fig. S84: HR-MS spectra of compound 14h.

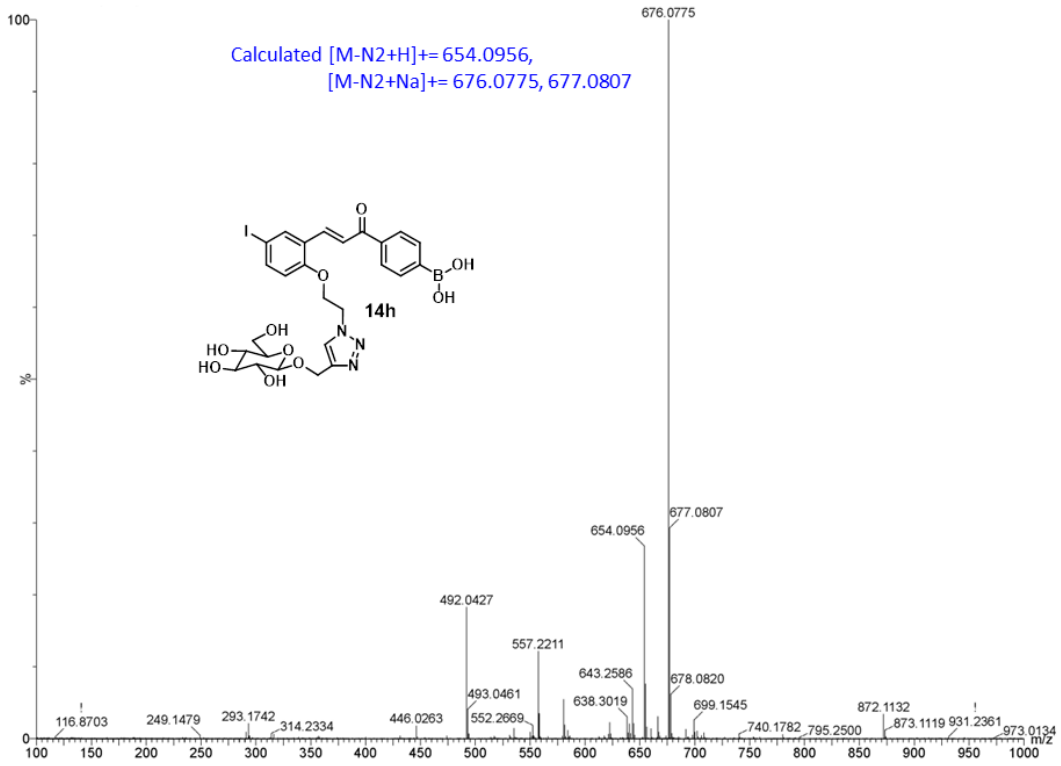

Fig. S85: HR-MS spectra of compound 14h.

2.6. Reference:

(1) Siegel, R. L.; Miller, K. D.; Jemal, A. Cancer Statistics, 2015. *Ca-Cancer J. Clin*. **2015**, *65*, 5−29.

(2) Miller, A. B.; Hoogstraten, B. F. A. U.; Staquet, M. F. A. U.; Winkler, A. Reporting Results of Cancer Treatment. *Cancer* **1981**, *47*, 207−214.

(3) Holmes, F. A.; Walters, R. S.; Theriault, R. L.; Buzdar, A. U.; Frye, D. K.; Hortobagyi, G. N.; Forman, A. D.; Newton, L. K.; Raber, M. N. Phase II Trial of Taxol, an Active Drug in the Treatment of Metastatic Breast Cancer. *J. Natl. Cancer Inst.* **1991**, *83*, 1797−1805.

(4) Silver, D. P.; Richardson, A. L.; Eklund, A. C.; Wang, Z. C.; Szallasi, Z.; Li, Q.; Juul, N.; Leong, C. O.; Calogrias, D.; Buraimoh, A.; Fatima, A. Efficacy of Neoadjuvant Cisplatin in Triple-Negative Breast Cancer. *J. Clin. Oncol.* **2010**, *28*, 1145-1153.

(5) Allegra, C. J.; Jessup, J. M.; Somerfield, M. R.; Hamilton, S. R.; Hammond, E. H.; Hayes, D. F.; McAllister, P. K.; Morton, R. F.; Schilsky, R. L. American Society of Clinical Oncology Provisional Clinical Opinion: Testing for KRAS Gene Mutations in Patients with Metastatic Colorectal Carcinoma to Predict Response to Anti− Epidermal Growth Factor Receptor Monoclonal antibody therapy. *J. Clin. Oncol.* **2009**, *27*, 2091−2096.

(6) Paridaens, R.; Biganzoli, L.; Bruning, P.; Klijn, J. G. M.; Gamucci, T.; Houston, S.; Coleman, R.; Schachter, J.; Van Vreckem, A.; Sylvester, R.; et al. Paclitaxel versus Doxorubicin as First-Line Single-Agent Chemotherapy for Metastatic Breast Cancer: a European Organization for Research and Treatment of Cancer Randomized Study with cross-over. *J. Clin. Oncol.* **2000**, *18*, 724−724.

(7) Aas, T.; Børresen, A. L.; Geisler, S.; Smith-Sørensen, B.; Johnsen, H.; Varhaug, J. E.; Akslen, L. A.; Lønning, P. E. Specific P53 Mutations are Associated with De Novo Resistance to Doxorubicin in Breast Cancer Patients. *Nat. Med*. **1996**, *2*, 811−814.

(8) Di Leo, A.; Gancberg, D.; Larsimont, D.; Tanner, M.; Jarvinen, T.; Rouas, G.; Dolci, S.; Leroy, J. Y.; Paesmans, M.; Isola, J.; et al. HER-2 Amplification and Topoisomerase IIα Gene Aberrations as Predictive Markers in Node-Positive Breast Cancer Patients Randomly Treated either with an Anthracycline-Based Therapy or with Cyclophosphamide, Methotrexate, and 5-Fluorouracil. *Clin. Cancer Res*. **2002**, *8*, 1107−1116.

(9) Meacham, C. E.; Morrison, S. J. Tumour Heterogeneity and Cancer cell Plasticity. *Nature* **2013**, *501*, 328−337.

(10) Burrell, R. A.; McGranahan, N.; Bartek, J.; Swanton, C. The Causes and Consequences of Genetic Heterogeneity in Cancer Evolution. *Nature* **2013**, *501*, 338−345.

(11) Holohan, C.; Van Schaeybroeck, S.; Longley, D. B.; Johnston, P. G. Cancer Drug Resistance: an Evolving Paradigm. *Nat. Rev. Cancer* **2013**, *13*, 714−726.

(12) Alizadeh, A. A.; Aranda, V.; Bardelli, A.; Blanpain, C.; Bock, C.; Borowski, C.; Caldas, C.; Califano, A.; Doherty, M.; Elsner, M.; Esteller, M. Toward Understanding and Exploiting Tumor Heterogeneity. *Nat. Med.* **2015**, *21*, 846−853.

(13) Ziegler, S.; Pries, V.; Hedberg, C.; Waldmann, H. Target Identification for Small Bioactive Molecules: Finding the Needle in the Haystack. *Angew. Chem. Int. Ed.* **2013**, *52*, 2744−2792.

(14) Hübel, K.; Leßmann, T.; Waldmann, H. Chemical Biology Identification of Small Molecule Modulators of Cellular Activity by Natural Product Inspired Synthesis. *Chem. Soc. Rev.* **2008**, *37*, 1361-1374.

(15) Wetzel, S.; Bon, R. S.; Kumar, K.; Waldmann, H. Biology-Oriented Synthesis. *Angew. Chem., Int. Ed.* **2011**, *50*, 10800−10826.

(16) Schreiber, S. L. Target-Oriented and Diversity-Oriented Organic Synthesis in Drug Discovery. *Science* **2000**, *287*, 1964−1969.

(17) Burke, M. D.; Schreiber, S. L. A Planning Strategy for Diversity- Oriented Synthesis. *Angew. Chem., Int. Ed*. **2004**, *43*, 46−58.

(18) Zhuang, C.; Zhang, W.; Sheng, C.; Zhang, W.; Xing, C.; Miao, Z. Chalcone: a Privileged Structure in Medicinal Chemistry. *Chem. Rev*. **2017**, *117*, 7762−7810.

(19) Yan, J.; Chen, J.; Zhang, S.; Hu, J.; Huang, L.; Li, X. Synthesis, Evaluation, and Mechanism Study of Novel Indole-Chalcone Derivatives Exerting Effective Antitumor Activity Through Micro tubule Destabilization in Vitro and in Vivo. *J. Med. Chem.* **2016**, *59*, 5264−5283.

(20) Singh, P.; Anand, A.; Kumar, V. Recent Developments in Biological Activities of Chalcones: A Mini Review. *Eur. J. Med. Chem*. **2014**, *85*, 758−777.

(21) D'arcy, P.; Brnjic, S.; Olofsson, M. H.; Fryknäs, M.; Lindsten, K.; De Cesare, M.; Perego, P.; Sadeghi, B.; Hassan, M.; Larsson, R.; Linder, S. Inhibition of Proteasome Deubiquitinating Activity as a New Cancer Therapy. *Nat. Med*. **2011**, *17*, 1636−1640.

(22) Anchoori, R. K.; Karanam, B.; Peng, S.; Wang, J. W.; Jiang, R.; Tanno, T.; Orlowski, R. Z.; Matsui, W.; Zhao, M.; Rudek, M. A.; et al. A Bis-Benzylidine Piperidone Targeting Proteasome Ubiquitin Receptor RPN13/ADRM1 as a Therapy for *Cancer. Cancer Cell* **2013**, *24*, 791−805.

(23) Diaz, D. B.; Yudin, A. K. The Versatility of Boron in Biological Target Engagement. *Nat. Chem.* **2017**, *9*, 731−742.

(24) Trippier, P. C.; McGuigan, C. Boronic Acids in Medicinal Chemistry: Anticancer, Antibacterial and Antiviral Applications. *MedChemComm* **2010**, *1*, 183−198.

(25) Watanabe, T.; Momose, I.; Abe, M.; Abe, H.; Sawa, R.; Umezawa, Y.; Ikeda, D.; Takahashi, Y.; Akamatsu, Y. Synthesis of Boronic acid Derivatives of Tyropeptin: Proteasome Inhibitors. *Bioorg. Med. Chem. Lett*. **2009**, *19*, 2343−2345.

(26) Dickinson, B. C.; Huynh, C.; Chang, C. J. A Palette of Fluorescent Probes with Varying Emission Colors for Imaging Hydrogen Peroxide Signaling in Living Cells. *J. Am. Chem. Soc.* **2010**, *132*, 5906−5915.

(27) Groll, M.; Berkers, C. R.; Ploegh, H. L.; Ovaa, H. Crystal Structure of the Boronic Acid Based Proteasome Inhibitor Bortezomib in Complex with The Yeast 20S Proteasome. *Structure* **2006**, *14*, 451−456.

(28) Chen, D.; Frezza, M.; Schmitt, S.; Kanwar, J.; Dou, Q. P. Bortezomib as the First Proteasome Inhibitor Anticancer Drug: Current Status and Future Perspectives. *Curr. Cancer Drug Targets* **2011**, *11*, 239−253.

(29) Adams, J.; Palombella, V. J.; Sausville, E. A.; Johnson, J.; Destree, A.; Lazarus, D. D.; Maas, J.; Pien, C. S.; Prakash, S.; Elliott, P. J. Proteasome Inhibitors: A Novel Class of Potent and Effective Antitumor Agents. *Cancer Res.* **1999**, *59*, 2615−2622.

(30) Curran, M. P.; McKeage, K. Bortezomib. *Drugs* **2009**, *69*, 859-888.

(31) Kumar, S. K.; Hager, E.; Pettit, C.; Gurulingappa, H.; Davidson, N. E.; Khan, S. R. Design, Synthesis, and Evaluation of Novel Boronic-Chalcone Derivatives as Antitumor Agents. *J. Med. Chem.* **2003**, *46*, 2813−2815.

(32) Achanta, G.; Modzelewska, A.; Feng, L.; Khan, S. R.; Huang, P. A Boronic-Chalcone Derivative Exhibits Potent Anticancer Activity Through Inhibition of the Proteasome. *Mol. Pharmcpl.* **2006**, *70*, 426−433.

(33) Bazzaro, M.; Anchoori, R. K.; Mudiam, M. K. R.; Issaenko, O.; Kumar, S.; Karanam, B.; Lin, Z.; Isaksson Vogel, R.; Gavioli, R.; Destro, F.; et al. α,β-Unsaturated Carbonyl System of Chalcone-Based Derivatives is Responsible for Broad Inhibition of Proteasomal Activity and Preferential Killing of Human Papilloma Virus (HPV) Positive Cervical Cancer Cells. J. *Med. Chem.* **2011**, *54*, 449−456.

(34) Arastu-Kapur, S.; Anderl, J. L.; Kraus, M.; Parlati, F.; Shenk, K. D.; Lee, S. J.; Muchamuel, T.; Bennett, M. K.; Driessen, C.; Ball, A. J.; Kirk, C. J. Nonproteasomal Targets of the Proteasome Inhibitors Bortezomib and Carfilzomib: a Link to Clinical Adverse Events. *Clin. Cancer Res.* **2011**, *17*, 2734−2743.

(35) Ruschak, A. M.; Slassi, M.; Kay, L. E.; Schimmer, A. D. Novel Proteasome Inhibitors to Overcome Bortezomib Resistance. *J. Natl. Cancer. Inst.* **2011**, *103*, 1007−1017.

(36) Chauhan, D.; Catley, L.; Li, G.; Podar, K.; Hideshima, T.; Velankar, M.; Mitsiades, C.; Mitsiades, N.; Yasui, H.; Letai, A.; et al. A Novel Orally Active Proteasome Inhibitor Induces Apoptosis in Multiple Myeloma Cells with Mechanisms Distinct from Bortezomib. *Cancer Cell* **2005**, *8*, 407−419.

(37) Su, J.; Chen, F.; Cryns, V. L.; Messersmith, P. B. Catechol Polymers for pH-Responsive, Targeted Drug Delivery to Cancer Cells. *J. Am. Chem. Soc*. **2011**, *133*, 11850−11853.

(38) Xu, W.; Ding, J.; Li, L.; Xiao, C.; Zhuang, X.; Chen, X. Acidlabile Boronate-Bridged Dextran−Bortezomib Conjugate with Up- Regulated Hypoxic Tumor Suppression. *Chem. Commun.* **2015**, *51*, 6812−6815.

(39) Frasco, M. F.; Almeida, G. M.; Santos-Silva, F.; Pereira, M. D. C.; Coelho, M. A. Transferrin Surface-Modified PLGA Nanoparticles- Mediated Delivery of a Proteasome Inhibitor to Human Pancreatic Cancer Cells. *J. Biomed. Mater. Res., Part A* **2015**, *103*, 1476−1484.

(40) Shen, S.; Du, X. J.; Liu, J.; Sun, R.; Zhu, Y. H.; Wang, J. Delivery of Bortezomib with Nanoparticles for Basal-Like Triple- Negative Breast Cancer Therapy. *J. Controlled Release* **2015**, *208*, 14−24.

(41) Kohane, D. S.; Langer, R. Biocompatibility and Drug Delivery Systems. *Chem. Sci*. **2010**, *1*, 441−446.

(42) Li, X.; Li, J.; Gao, Y.; Kuang, Y.; Shi, J.; Xu, B. Molecular Nanofibers of Olsalazine Confer Supramolecular Hydrogels for Reductive Release of An Anti-inflammatory Agent. *J. Am. Chem. Soc*. **2010**, *132*, 17707−17709.

(43) Cheetham, A. G.; Zhang, P.; Lin, Y. A.; Lock, L. L.; Cui, H. Supramolecular Nanostructures Formed by Anticancer Drug Assembly. *J. Am. Chem. Soc*. **2013**, *135*, 2907−2910.

(44) Shen, Y.; Jin, E.; Zhang, B.; Murphy, C. J.; Sui, M.; Zhao, J.; Wang, J.; Tang, J.; Fan, M.; Van Kirk, E.; Murdoch, W. J. Prodrugs Forming High Drug Loading Multifunctional Nanocapsules for Intracellular Cancer Drug Delivery. *J. Am. Chem. Soc*. **2010**, *132*, 4259−4265.

(45) Gao, Y.; Kuang, Y.; Guo, Z. F.; Guo, Z.; Krauss, I. J.; Xu, B. Enzyme-Instructed Molecular Self-Assembly Confers Nanofibers and a Supramolecular Hydrogel of Taxol Derivative. *J. Am. Chem. Soc*. **2009**, *131*, 13576−13577.

(46) Li, X. Q.; Wen, H. Y.; Dong, H. Q.; Xue, W. M.; Pauletti, G. M.; Cai, X. J.; Xia, W. J.; Shi, D.; Li, Y. Y. Self-Assembling Nanomicelles of a Novel Camptothecin Prodrug Engineered with a Redox-Responsive Release Mechanism. *Chem. Commun*. **2011**, *47*, 8647−8649.

(47) Huang, P.; Wang, D.; Su, Y.; Huang, W.; Zhou, Y.; Cui, D.; Zhu, X.; Yan, D. Combination of Small Molecule Prodrug and Nanodrug Delivery: Amphiphilic Drug Drug Conjugate for Cancer Therapy. *J. Am. Chem. Soc*. **2014**, *136*, 11748−11756.

(48) Wang, S.; Deng, H.; Huang, P.; Sun, P.; Huang, X.; Su, Y.; Zhu, X.; Shen, J.; Yan, D. Real Time Self-Tracking of an Anticancer Small Molecule Nanodrug Based on Colorful Fluorescence Variations. *RSC Adv*. **2016**, *6*, 12472−12478.

(49) Kasai, H.; Murakami, T.; Ikuta, Y.; Koseki, Y.; Baba, K.; Oikawa, H.; Nakanishi, H.; Okada, M.; Shoji, M.; Ueda, M.; et al. Creation of Pure Nanodrugs and Their Anticancer Properties. *Angew. Chem., Int. Ed*. **2012**, *51*, 10315−10318.

(50) Barua, S.; Mitragotri, S. Synergistic Targeting of Cell Membrane, Cytoplasm, and Nucleus of Cancer Cells Using Rod- Shaped Nanoparticles. *ACS Nano* **2013**, *7*, 9558−9570.

(51) Rao, H.; Sawant, A. A.; Tanpure, A. A.; Srivatsan, S. G. Posttranscriptional Chemical Functionalization of Azide-Modified Oligoribonucleotides by Bioorthogonal Click and Staudinger Reactions. *Chem. Commun.* **2012**, *48*, 498−500.

(52) da Silva, G. D.; da Silva, M. G.; Souza, E. M. P. V. E.; Barison, A.; Simões, S. C.; Varotti, F. P.; Barbosa, L. A.; Viana, G. H. R.; Villar, J. A. F. P. Design and Synthesis of New Chacones Substituted with Azide/Triazole Groups and Analysis of Their Cytotoxicity Towards HeLa Cells. *Molecules* **2012**, *17*, 10331−10343.

(53) Shao, C.; Wang, X.; Zhang, Q.; Luo, S.; Zhao, J.; Hu, Y. Acid- Base Jointly Promoted Copper(I)-Catalyzed Azide-Alkyne Cycloaddition. *J. Org. Chem.* **2011**, *76*, 6832−6836.

(54) Daly, R.; Vaz, G.; Davies, A. M.; Senge, M. O.; Scanlan, E. M. Synthesis and Biological Evaluation of a Library of Glycoporphyrin Compounds. *Chem. Eur. J.* **2012**, *18*, 14671−14679.

(55) Thomas, T. S.; Hwang, W.; Sita, L. R. End-Group-Functionalized Poly (α-olefinates) as Non-Polar Building Blocks: Self- Assembly of Sugar−Polyolefin Hybrid Conjugates. *Angew. Chem. Int. Ed.* **2016**, *55*, 4683−4687.

(56) Tait, S. W.; Green, D. R. Mitochondria and Cell Death: Outer Membrane Permeabilization and Beyond. *Nat. Rev. Mol. Cell Biol.* **2010**, *11*, 621−632.

(57) Chipuk, J. E.; Bouchier-Hayes, L.; Green, D. R. Mitochondrial Outer Membrane Permeabilization During Apoptosis: the Innocent Bystander Scenario. *Cell Death Differ*. **2006**, *13*, 1396−1402.

(58) Cossarizza, A.; Baccaranicontri, M.; Kalashnikova, G.; Franceschi, C. A New Method for the Cytofluorometric Analysis of Mitochondrial Membrane Potential using the J-aggregate Forming Lipophilic Cation 5, 5′, 6, 6′-tetrachloro-1, 1′, 3, 3′-tetraethylbenzimidazolcarbocyanine

iodide (JC-1). *Biochem. Biophys. Res. Commun*. **1993**, *197*, 40−45.

(59) Chipuk, J. E.; Green, D. R. How Do Bcl-2 Proteins Induce Mitochondrial Outer Membrane Permeabilization? *Trends Cell Biol*. **2008**, *18*, 157−164.

(60) Dewson, G.; Kluck, R. M. Mechanisms by Which Bak and Bax Permeabilise Mitochondria During Apoptosis. *J. Cell Sci.* **2009**, *122*, 2801−2808.

(61) Czabotar, P. E.; Lessene, G.; Strasser, A.; Adams, J. M. Control of Apoptosis by the BCL-2 Protein Family: Implications for Physiology and Therapy. *Nat. Rev. Mol. Cell Biol.* **2014**, *15*, 49−63.

(62) Wu, D.; Yotnda, P. Production and Detection of Reactive Oxygen Species (ROS) in Cancers. *J. Visualized Exp*. **2011**, *57*, 3357.

(63) Sengupta, S.; Sasisekharan, R. Exploiting Nanotechnology to Target Cancer. *Br. J. Cancer* **2007**, *96*, 1315−1319.

(64) Kwon, G.; Naito, M.; Yokoyama, M.; Okano, T.; Sakurai, Y.; Kataoka, K. Micelles Based on AB Block Copolymers of poly (ethylene oxide) and poly (beta-benzyl L-aspartate). *Langmuir* **1993**, *9*, 945−949.

(65) Urano, Y.; Asanuma, D.; Hama, Y.; Koyama, Y.; Barrett, T.; Kamiya, M.; Nagano, T.; Watanabe, T.; Hasegawa, A.; Choyke, P. L.; Kobayashi, H. Selective Molecular Imaging of Viable Cancer Cells with pH-Activatable Fluorescence Probes. *Nat. Med.* **2009**, *15*, 104−109.

(66) Sengupta, P.; Basu, S.; Soni, S.; Pandey, A.; Roy, B.; Oh, M. S.; Chin, K. T.; Paraskar, A. S.; Sarangi, S.; Connor, Y.; Sabbisetti, V. S. Cholesterol-Tethered Platinum II-Based Supramolecular Nanoparticle Increases Antitumor Efficacy and Reduces Nephrotoxicity. *Proc. Natl. Acad. Sci. U. S. A.* **2012**, *109*, 11294−1129965.

(67) Mallick, A.; More, P.; Ghosh, S.; Chippalkatti, R.; Chopade, B. A.; Lahiri, M.; Basu, S. Dual Drug Conjugated Nanoparticle for Simultaneous Targeting of Mitochondria and Nucleus in Cancer Cells. *ACS Appl. Mater. Interfaces* **2015**, 7, 7584−7598.

(68) Mallick, A.; More, P.; Syed, M. M. K.; Basu, S. Nanoparticle- Mediated Mitochondrial Damage Induces Apoptosis in Cancer. *ACS Appl. Mater. Interfaces* **2016**, *8*, 13218−13231.

Chapter 3

Supramolecular self-assembly of triazine-based small molecule: targeting endoplasmic reticulum in cancer cells

This chapter has been published as,

Ghosh, C.; Nandi, N.; Basu, S. *Nanoscale*, **2019**, *11*, 3326-3335.

DOI: 10.1039/c8nr08682f

3.1. Introduction:

The endoplasmic reticulum (ER), the largest endo-membrane organelle, controls myriads of sub-cellular functions, including protein and lipid biosynthesis, sensing, ion homeostasis and signaling pathways.[1-4] ER is also responsible for folding, unfolding, misfolding and post-translational modifications of nearly 30 % of total cellular protein content.[5,6] Consequently, dysregulation in ER function leads to the undesirable accumulation of unfolded/misfolded proteins (called ER stress) followed by stimulation of unfolded protein response (UPR) which ultimately elicits the apoptotic cell death machinery.[7-10] As a result, impairing ER functions in cancer cells has materialized as novel next-generation anti-cancer strategy.[11-13] However, exceedingly selective targeting of ER inside cancer cell milieu remains a foremost challenge and hence less explored. To address this, we have decided to develop supramolecular self-assembled nanoscale material which has prospective to selectively home into cancer cells.

In last couple of decades, supramolecular self-assembly has gained lots of attention as powerful tool to engineer functional nano-scale structures by bottom-up approach.[14-19] Hence, supramolecular self-assembled nanoscale materials have been explored for numerous biomedical applications including regenerative medicine, tissue engineering, ion/molecule sensing and drug delivery.[20-28] However, utilizing designed supramolecular self- assembled nano-structure for specific targeting of sub-cellular organelles, especially ER in cancer cells still remained in its infancy. Only, few groups developedlipid-based micelle,[29] liposomes[30] and polymeric nanoparticle[31] for targeting ER. Very recently, Feng et. al. engineered peptide-based enzyme-instructed crescent shaped supramolecular self-assembly for selective targeting of ER in cancer cells.[32] Moreover, ER membrane wraps around another important organelle, nucleus and forms double membrane nuclear envelop leading to ER-nuclear cross-talk.[33] Hence, we hypothesize that simultaneous targeting of ER and nuclear DNA in cancer cells would lead to improved anti-cancer efficacy.

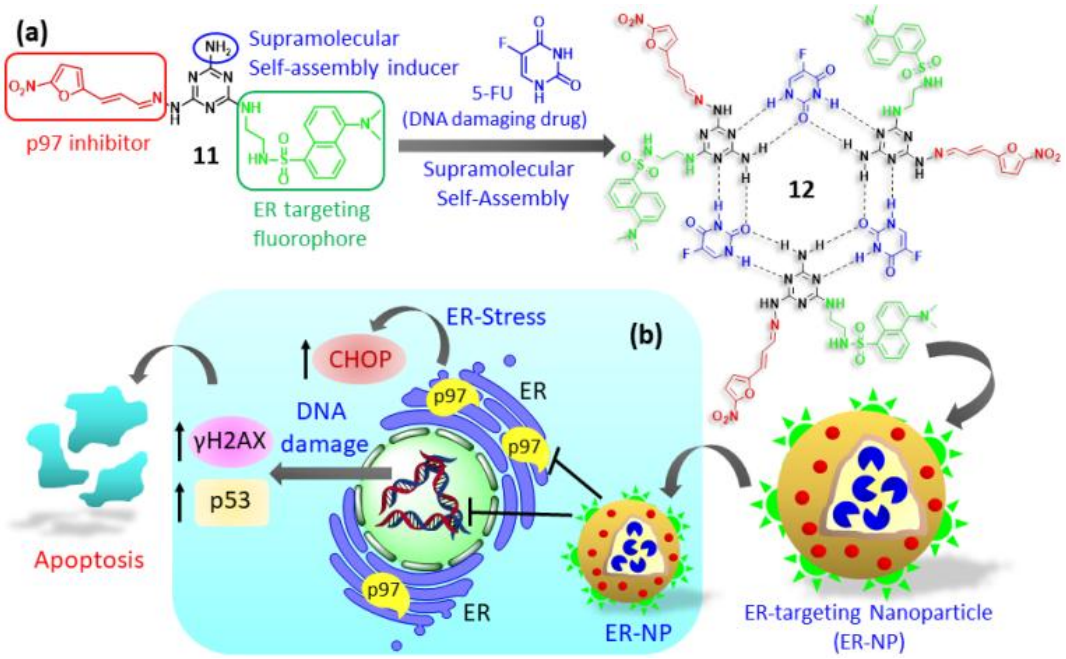

Scheme 1. (a) Structure of ER-targeted tridentate-triazine (11) and supramolecular self-assembly in presence of 5-FU to form hexameric rosette structure (12). (b) Formation of ER-NP and its mechanism of action in cancer cells.

To accomplish this, in this manuscript, we have explored supramolecular self-assembly strategy with triazine-based small molecule in presence of 5-fluoro-uracil (5FU) (DNA damaging drug). The tridentate triazine molecule formed self-assembled hexameric rosette structure through Watson-Crick based H-bonding with 5FU in equimolar mixture in water, characterized by diffusion-ordered NMR spectroscopy (DOSY). The hexameric rosette structure further lead to the formation of hitherto unobserved spherical nanoparticle by hierarchical self-assembly. These supramolecular self-assembled nanoparticles (ER-NPs) consists of fluorescent dansyl group as ER targeting moiety, 5-nitrofuran-2-acrylaldehyde as p97 inhibitor (ER stress inducer) and 5FU as nuclear DNA damaging drug. A combination of fluorescent confocal microscopy and Western blot analysis confirmed that these self-assembled nanoparticles localized into ER of HeLa cervical cancer cells through macropinocytosis followed by simultaneous induction of ER stress and nuclear DNA damage. These ER-NP-mediated ER stress triggered apoptosis and generated reactive-oxygen species (ROS) to prompt cell death much effectively compared to their building blocks. Moreover, ER-NPs initiated autophagy mechanism to overcome the ER-stress and DNA damage. Hence, combination treatment of ER-NP with chloroquine (autophagy inhibitor) improved the cell death remarkably in HeLa cells. This ER targeting supramolecular self-

assembled nanoplatform has potential to simultaneously impair multiple organelles for improved cancer therapy in future.

3.2. Result and discussion

3.2.1. Design and synthesis of tridentate triazine

To induce stress selectively in ER of the cancer cells, tridentate triazine molecule (11 in Scheme 1) was designed to contain (a) dansyl group as ER homing as well as fluorescent tag which will enable us to sub-cellular visualization,[34] (b) 5-nitrofuran-2-acrylaldehyde as p97 inhibitor on ER to induce ER stress[35-36] and (c) an amine group to enable supramolecular self-assembly by H-bonding with DNA damaging drug 5-FU to form hexameric rosette structure (12).[37-40] Synthetic scheme of compound 11 is shown in Fig. 1. First the amine group was introduced by reacting cyanuric chloride (1) with 1 equivalent of ammonia at 0°C for 24 h to obtain 4,6-dichloro-1,5-triazine-2-amine (2) in 90 % yield (Figure 1).[41] Subsequently, dansyl group was tagged with triazine core with ethylenediamine linker through the reaction of compound 2 with dansyl-ethylenediamine conjugate (5) in presence of diisopropylethyl amine as base to obtain amino-triazine-dansyl conjugate (6) in 63% yield. Dansyl-ethyelediamine conjugate (5) was synthesized in 93% yield from dansyl chloride (3) reacting with ethyleldiamine (4) at 0°C for 1 h.[42] The final chloride group in cyanuric chloride was replaced by hydrazine moiety by reacting amino-triazine- dansyl conjugate (6) with hydrazine mono-hydrate in refluxing condition for 24 h to afford hydrazine-amine-dansyl substituted triazine (7) in 84 % yield.[43] The p97 inhibitor 5-nitrofuran-2-acrylaldehyde (10) was synthesized from 5-nitrofurfuraldehyde (8) and triphenylphosphoranylidene acetaldehyde (9) by Wittig reaction for 6 h in 61% yield.[35] Finally, 5-nitrofuran-2-acrylaldehyde (10) was conjugated with compound 7 in presence of methanol to obtain the designed tridentate triazine derivative (11) in 71 % yield. We characterized all the compounds and intermediates by ^{1}H and ^{13}C-NMR spectroscopy and mass-spectroscopy (HR-MS) (Fig. S1-S23, Appendix).

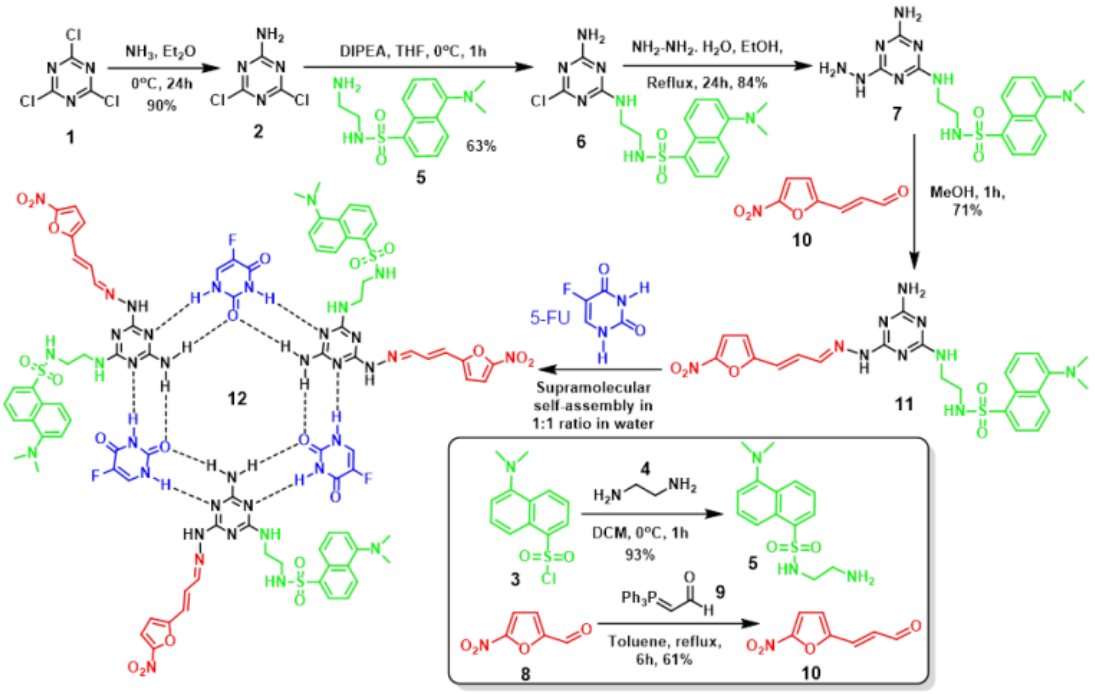

Figure 1: Synthesis of tridentate-triazine (11) and supramolecular self-assembly with 5FU.

3.2.2. Supramolecular self-assembly

To engineer supramolecular self-assembled structure, we blended compound 11 and 5-FU in a ratio-metric manner in water. We visualized the self-assembly through field-emission scanning electron microscopy (FE-SEM). Very interestingly, Figure 3 and Figure 2a demonstrated a hitherto unobserved well dispersed spherical nanoparticle formation in 1:1 mixture of compound 11 and 5-FU (ER-NP). The spherical morphology was also further confirmed by transmission electron microscopy (TEM) and atomic force microscopy (AFM) (Figure 2b, Figure 4a,b). The dynamic light scattering (DLS) experiment revealed that the ER-NP contained 250 nm mean hydrodynamic diameter with -2.4 mV zeta potential (Figure 4c,d). To confirm the supramolecular self-assembly between compound 11 and 5-FU leading to the formation of predicted rosette structure followed by hierarchical self-assembly, we performed diffusion-ordered NMR spectroscopy (DOSY). The DOSY spectra (Figure 2c) of 1:1 mixture of compound 11 and 5-FU demonstrated the formation of single remarkably slower diffusion species compared to its each component (Figure 5-7). From the DOSY spectra, we also calculated the diffusion coefficient of the predicted rosette structure to be 2.05 X 10^{-10} m^2/s. In contrast, the diffusion coefficients of for

tridentate triazine (11) and 5-FU were found to be 3.21 X 10^{-10} m^2/s and 2.57 X 10^{-10} m^2/s respectively (Figure 5-7). Interestingly, 5-FU showed much lower diffusion coefficient compared to compound 11, which might be attributed to the intermolecular H-bonded supramolecular self-assembled column like structure formed by 5-FU observed by FESEM (Figure 8). Further calculation of the molecular weight range of the 1:1 mixture of compound 11 and 5-FU was estimated from the diffusion coefficients and found consistent with the molecular weight of hexameric rosette structure.[38-44] From these electron microscopy, light scattering and DOSY spectra, it was confirmed that tridentate triazine small molecule formed supramolecular hexameric rosette structure in presence of 5-FU leading to the development of unique spherical nanoparticle (ER-NP) through hierarchical self-assembly.

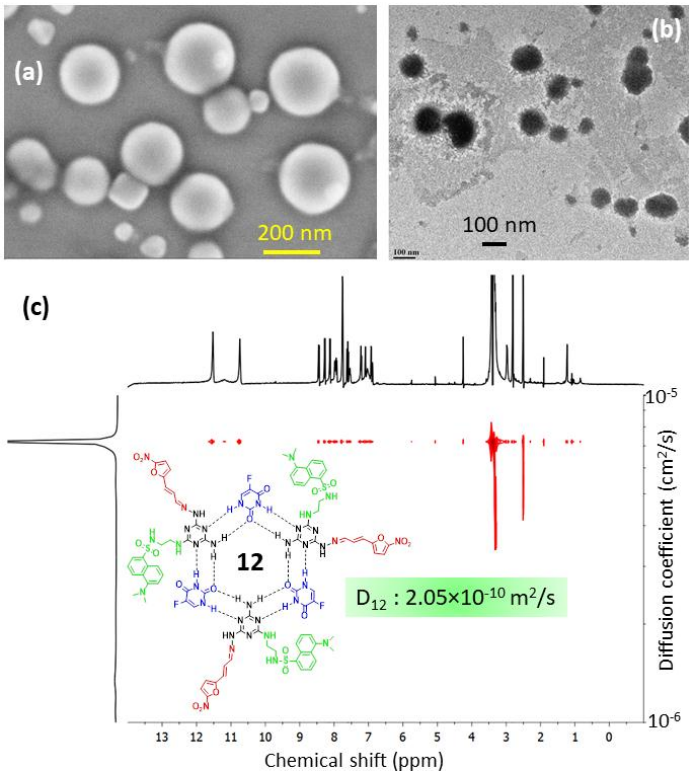

Figure 2: (a,b) FESEM and TEM images of ER-NPs. (c) DOSY spectra of supramolecular self-assembled hexameric rosette structure of compound 11 and 5FU in 1:1 mixture.

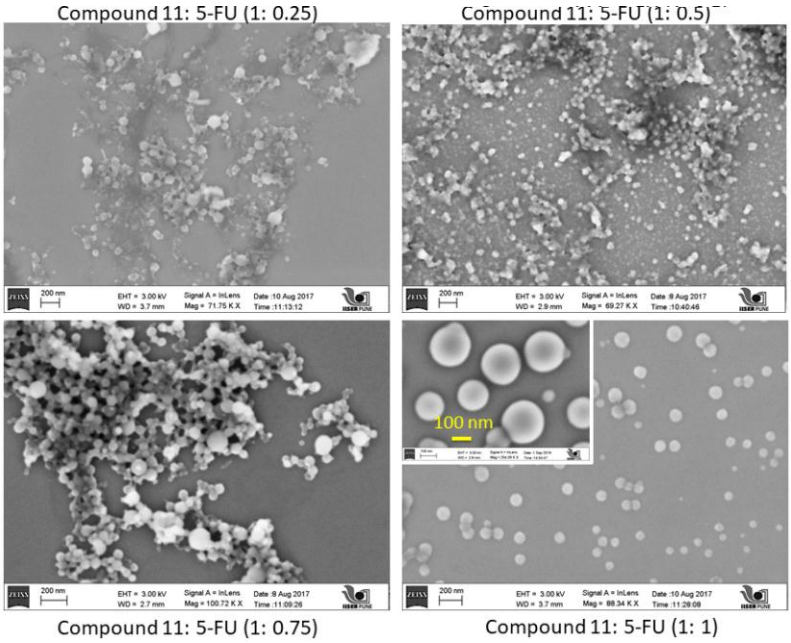

Figure 3: FESEM spectra of mixture of compound **11** and 5FU in different ratios to visualize the self-assembly.

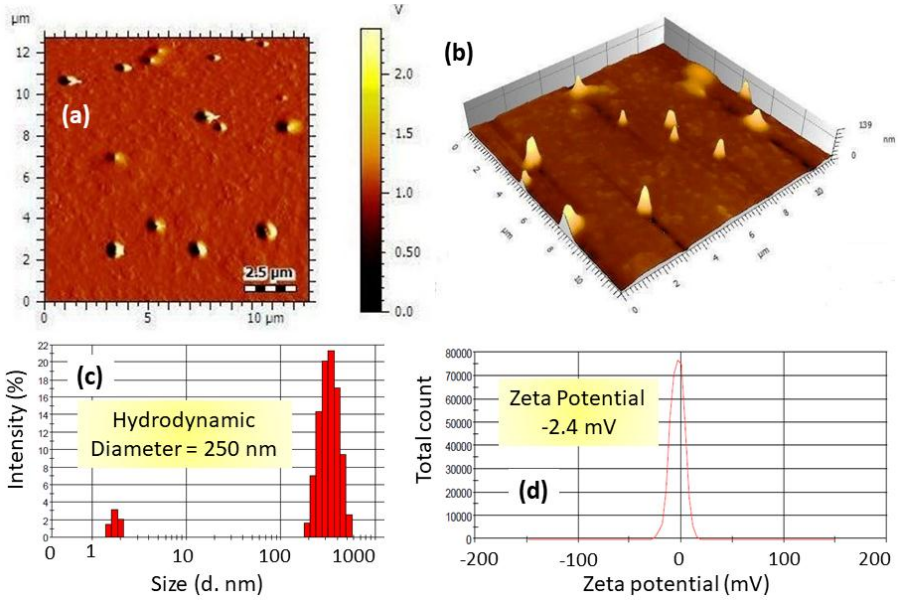

Figure 4: (a,b) 2D and 3D AFM images of ER-NPs respectively. (c, d) hydrodynamic diameter and zeta potential of ER-NPs determined by DLS.

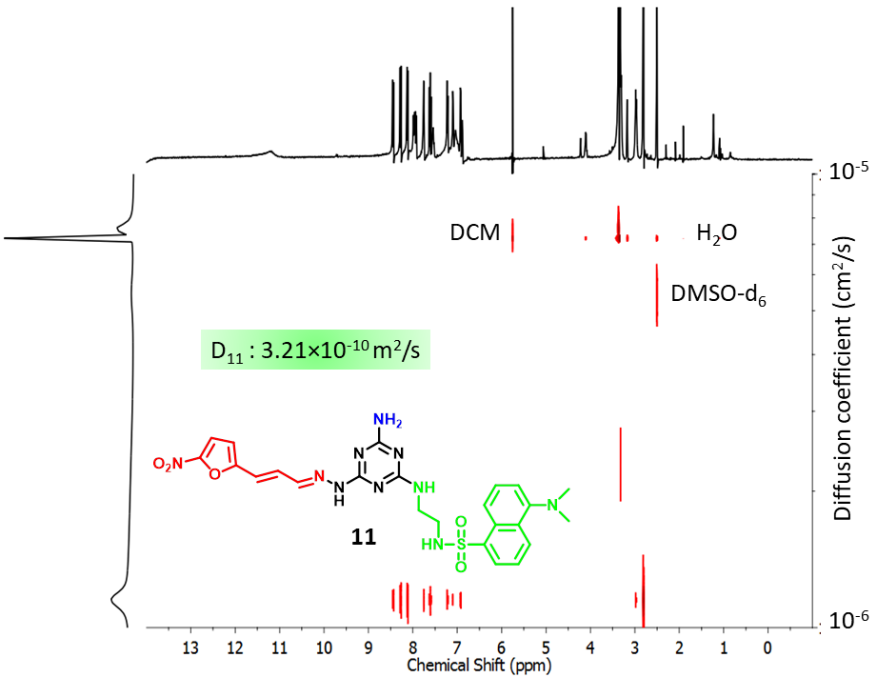

Figure 5: DOSY spectra of compound **11**.

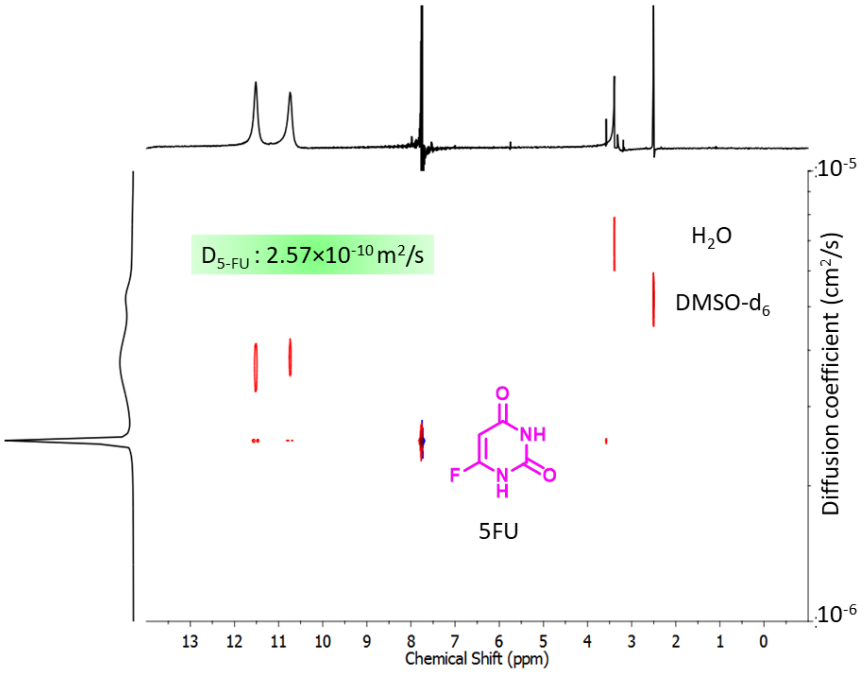

Figure 6: DOSY spectra of 5-FU.

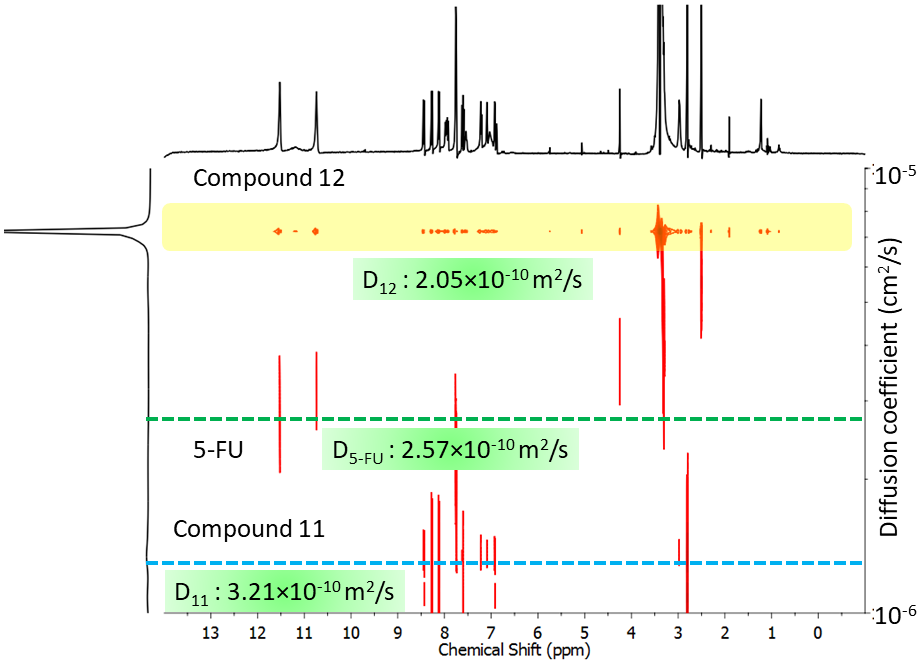

Figure 7: Comparison of diffusion coefficients of compound **11**, compound **12** and 5-FU by DOSY spectra.

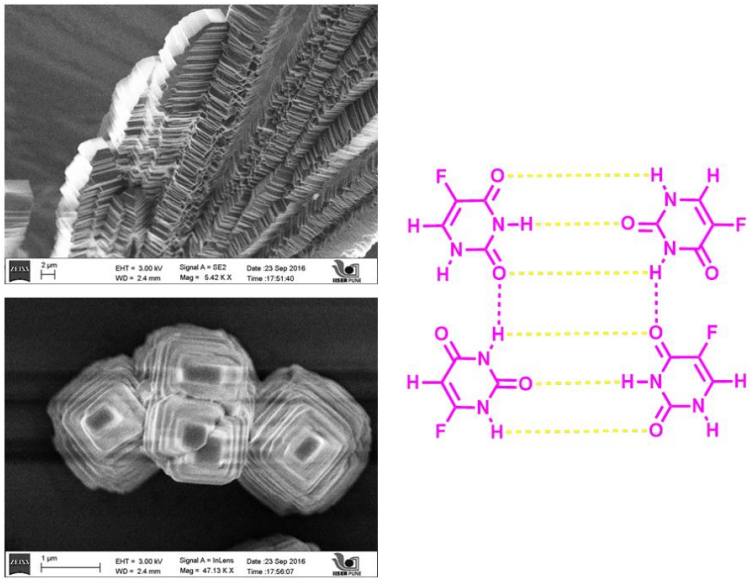

Figure 8: FESEM images and proposed H-bonding in 5-FU.

3.2.3. ER Homing:

The ER localization of tridentate triazine (11) was first evaluated by confocal laser scanning microscopy (CLSM). HeLa cells were treated with green fluorescent compound 11 in a time dependent manner (1h, 6h and 24h) and co-stained ER by ER-Tracker Red followed by visualization by CLSM. The live cell images revealed that green fluorescent compound 11

localized into red fluorescently labeled ER of HeLa cells within 1h to yield merged yellow regions and retained there for 24h (Figure 9). The confocal image based quantification by Pearson's and Mander's coefficients showed that compound 11 produced 55.2 %, 56.1% and 44.2% volume co-localization in ER at 1h, 6h and 24 h respectively (Table 1). Subsequently, we evaluated the ER localization of supramolecular self-assembled ER-NP in HeLa cells. We incubated the cells with green fluorescent ER-NPs for 30 min, 1h and 6h followed by co-staining ER with ER-Tracker Red. The visualization of the live cells under confocal microscopy revealed that ER-NPs localized into ER within 30 min and retained there for 6h (yellow regions in merged images in Figure 10a). The 3D, z-stacked images (Figure 10b) also clearly confirmed the sub-cellular homing of ER-NPs into ER. Quantification from CLSM also supported the microscopy data by showing that 68.9%, 60.1% and 52.2% volume co-localization of green fluorescent ER-NP with red fluorescently labeled ER at 30 min, 1h and 6h respectively in HeLa cells (Table 2).

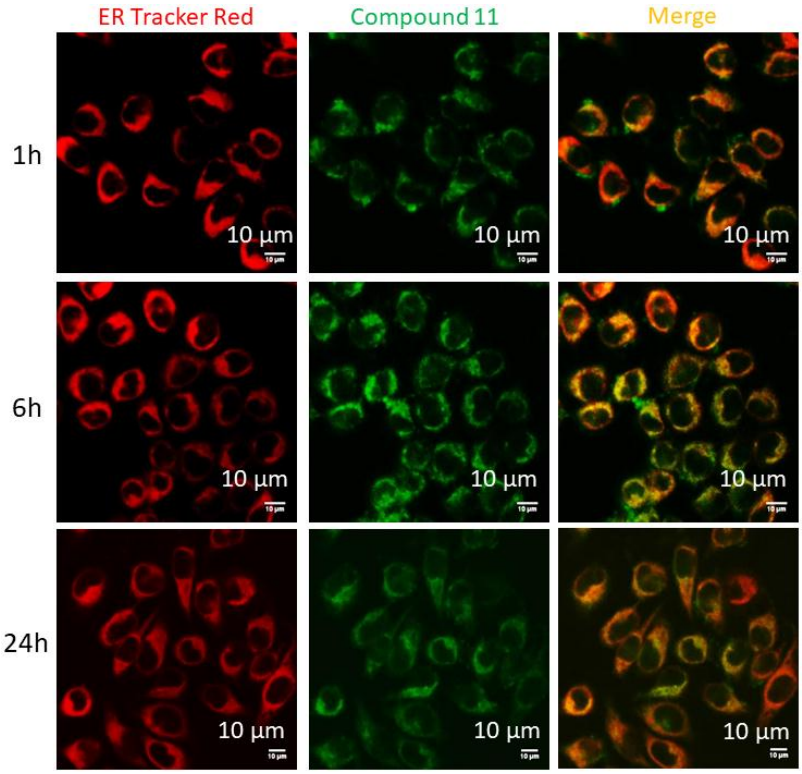

Figure 9: Confocal laser scanning microscopy (CLSM) images of compound **11** in HeLa cells in different time points (1 h, 6 h and 24 h). ER is stained by ER-Tracker Red. Scale bar = 10 µm.

		1h	6h	24h
Image Channels		C2 (green) C3 (red)	C2 (green) C3 (red)	C2 (green) C3 (red)
Pearsons' Correlation Coefficient	R	0.8821	0.8795	0.8324
Manders Coefficients	M1 (fraction of C2 overlapping C3)	0.8971	0.8913	0.8309
	M2 (fraction of C3 overlapping C2)	0.8892	0.9031	0.8458
Percent volume Co-localized		*55.23%*	*56.11%*	*44.24%*

Table 1: Quantification of co-localization of compound **11** in ER of HeLa cells at 1 h, 6 h and 24 h from CLSM.

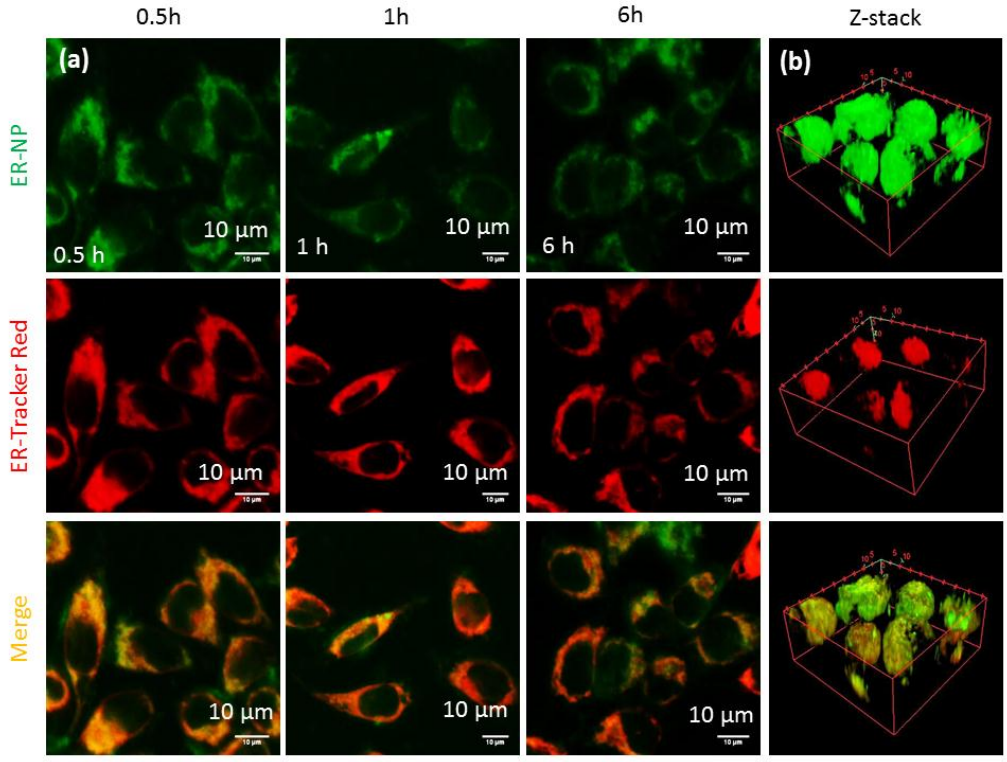

Figure 10: (a) Confocal laser scanning microscopy (CLSM) images of time dependent homing of ER-NPs (green) into ER of HeLa cells stained with ER-Tracker Red dye. (b) 3D-z-stacked confocal microscopy images of HeLa cells treated with ER-NP (green) and stained with ER-Tracker Red at 1 h. Scale bar = 10 µm.

		30mins	1h	6h
Image Channels		C2 (green) C3 (red)	C2 (green) C3 (red)	C2 (green) C3 (red)
Pearsons' Correlation Coefficient	R	0.9421	0.7995	0.9724
Manders Coefficients	M1 (fraction of C2 overlapping C3)	0.9462	0.9387	0.9204
	M2 (fraction of C3 overlapping C2)	0.9489	0.9515	0.9302
Percent volume Co-localized		*68.98%*	*60.13%*	*52.24%*

Table 2: Quantification of co-localization of ER-NPs in ER of HeLa cells at 30 min, 1 h and 6 h from CLSM.

We further evaluated the mechanism of cellular internalization of ER-NPs through endocytosis. ER-NPs localization in ER was visualized in amiloride pre-treated cells (lowest panel in Figure 11). Fluorescence microscopy-based quantification also supported the image data by showing 54.2% and 44.6% volume co-localization in genistein and chlorpromazine treated cells respectively compared to 49.8% co-localization for control cells (Table 3). However, amiloride treated cells showed only 22% volume co-localization of ER-NPs in ER. These confocal microscopy images and quantification clearly confirmed that genestein and chlorpromazine-mediated inhibition of caveolin- and clathrin-based endocytosis respectively were not instrumental in ER-NP uptake in HeLa cells. On the other hand, amiloride mediated inhibition of macropinocytosis was the operative pathway for the cellular internalization of ER-NPs followed by ER homing.

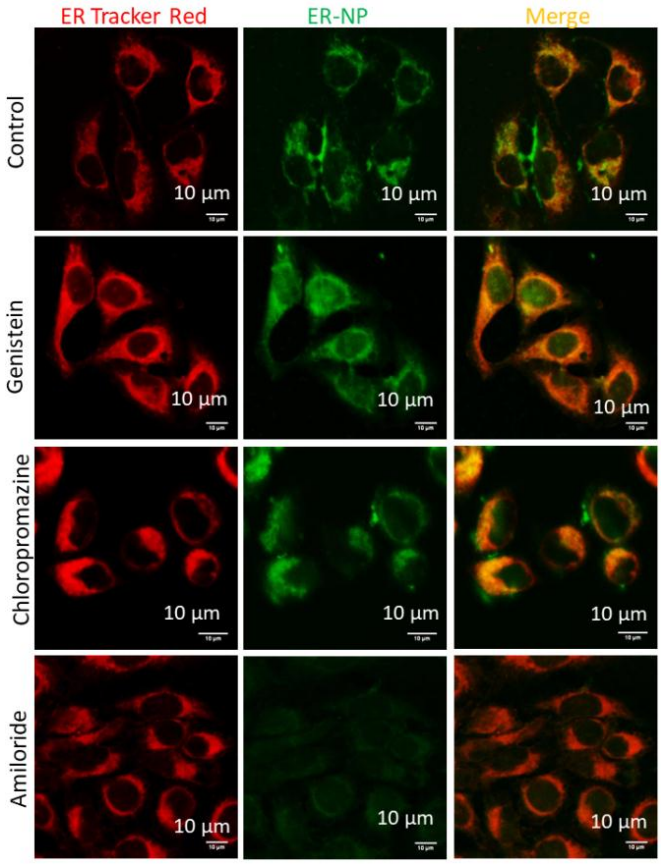

Figure 11: CLSM images of HeLa cells pre-treated with endocytosis inhibitors followed by ER-NPs (green). ER of HeLa cells were stained with ER-Tracker Red dye. Scale bar = 10 µm.

		Control	Genistein	Chlorpromazine	Amiloride
Image Channels		C2 (green) C3 (red)	C2 (green) C3 (red)	C2 (green) C3 (red)	C2 (green) C3 (red)
Pearsons' Correlation Coefficient	R	0.8121	0.8723	0.8032	0.4356
Manders Coefficients	M1 (fraction of C2 overlapping C3)	0.9588	0.9452	0.9750	0.7645
	M2 (fraction of C3 overlapping C2)	0.9880	0.9650	0.9130	0.7820
Percent volume colocalized		*49.87%*	*54.21%*	*44.61%*	*22.07%*

Table 3: Quantification of co-localization of ER-NPs into ER in HeLa cells pre-treated with different endocytosis inhibitors from CLSM.

The sub-cellular localization of ER-NPs was also assessed in other organelles like mitochondria and lysosomes. Mitochondria of the HeLa cells were stained with MitoTracker Red dye and co-localization of ER-NPs into mitochondria was visualized at 24 h post-incubation. The confocal microscopy images (Fig. 12) showed marginal overlap of green and red fluorescence signals to yield yellow regions, which was also validated by volume co-localization by only 35.5% after 24 h (Table 4). However, mitochondria and ER share large amount of common membrane called mitochondria-associated membranes (MAMs).[46] As a result, we visualized some amount of ER-NP co-localization leading to yellow merged regions in microscopy images. Similarly, lysosomal compartments in HeLa cells were stained with LysoTracker Red dye and the cells were incubated with ER-NP for 24 h. The confocal images (Figure 13) hardly showed any significant merged yellow regions, indicating that ER-NPs did not home into lysosomes. Further quantification also revealed that only 21% volume co-localization of ER-NPs into lysosomes after 24 h (Table 5). These confocal microscopy images and quantification evidently exhibited that ER-NPs were homed into ER of HeLa cells within 1h through macropinocytosis mechanism.

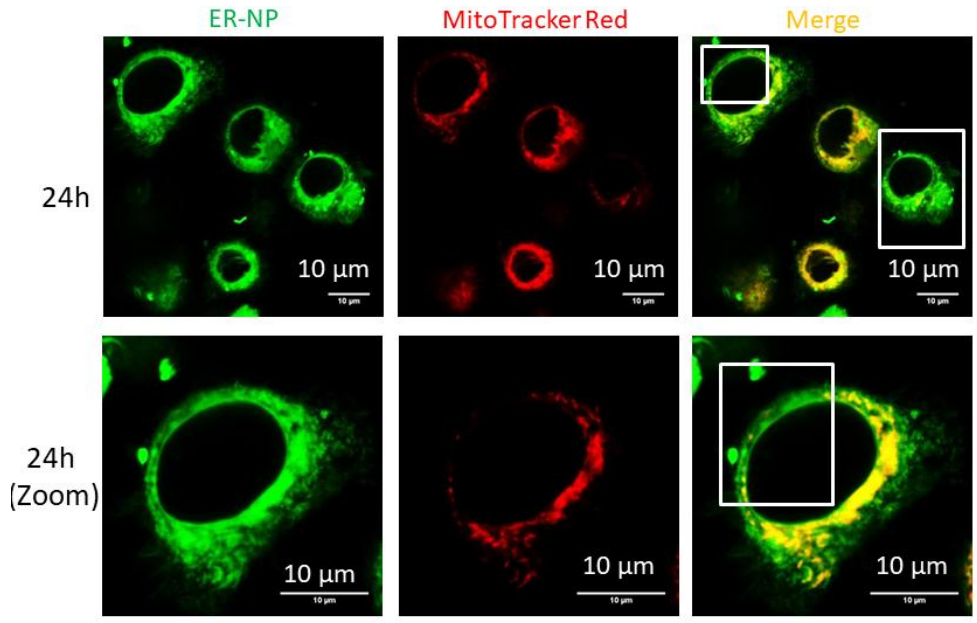

Figure 12: CLSM images of ER-NPs in HeLa cells at 24 h. Mitochondria were stained with MitoTracker Deep Red dye. Scale bar = 10 µm.

		24h	24h (Zoom)
Image Channels		C2 (green) C3 (red)	C2 (green) C3 (red)
Pearsons' Correlation Coefficient	R	0.7720	0.7890
Manders Coefficients	M1 (fraction of C2 overlapping C3)	0.8123	0.9041
	M2 (fraction of C3 overlapping C2)	0.8341	0.9205
Percent volume colocalized		*35.55%*	*39.21%*

Table 4: Quantification of co-localization of ER-NPs into mitochondria in HeLa cells at 24 h from CLSM.

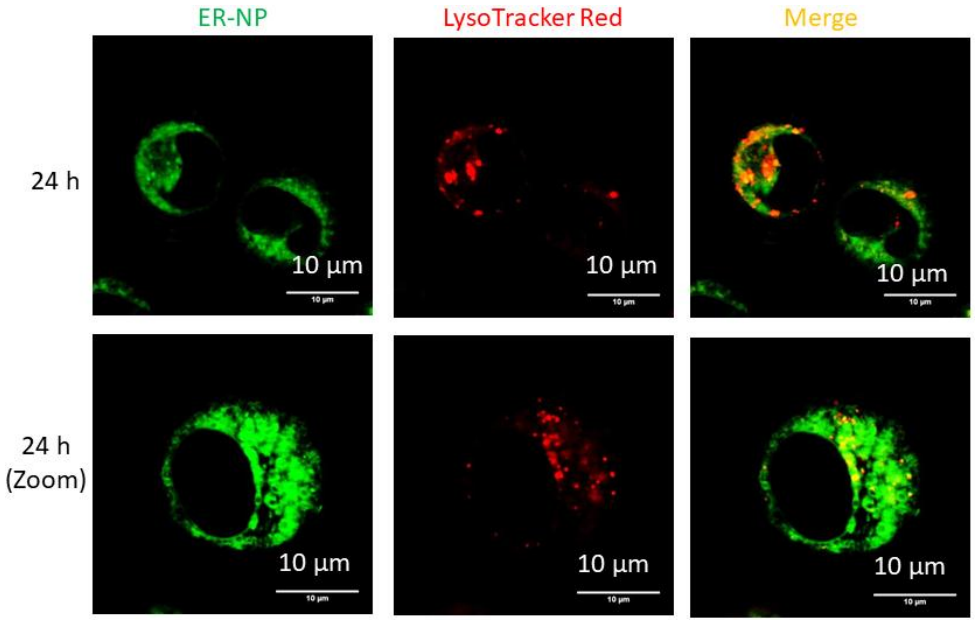

Figure 13: CLSM images of ER-NPs in HeLa cells at 24 h. Lysosomal compartments were stained with LysoTracker Red dye. Scale bar = 10 µm.

		24h	24h (zoom)
Image Channels		C2 (green) C3 (red)	C2 (green) C3 (red)
Pearsons' Correlation Coefficient	R	0.2574	0.3028
Manders Coefficients	M1 (fraction of C2 overlapping C3)	0.8200	0.8541
	M2 (fraction of C3 overlapping C2)	0.8104	0.8622
Percent volume colocalized		*21.08%*	*16.56%*

Table 5: Quantification of co-localization of ER-NPs into lysosomes in HeLa cells at 24 h from CLSM.

3.2.4. ER stress induction

After successful accumulation into ER, the supramolecular self-assembled ER-NP would induce stress in ER. One of the important markers for ER stress is c/EBP homologous protein (CHOP).[47,48] Hence, we evaluated the expression of CHOP by confocal fluorescence microscopy. The HeLa cells were treated with ER-NPs for 24 h and stained the nucleus of the cells with blue fluorescent dye DAPI. The cells were further incubated with CHOP specific primary antibody followed by treatment with red fluorescent Alexa Fluor 594-labelled secondary antibody. The cells were then visualized under fluorescence microscopy. Figure 14a evidently showed that ER-NPs induced ER stress leading to the remarkable increase in red fluorescence intensity compared to control cells which hardly showed any CHOP expression. Also quantification of red fluorescence intensity from confocal images revealed that ER-NPs increased the CHOP expression by 15.1 folds compared to control cells (Figure 15a). The expression of CHOP was further assessed by Western blot analysis after incubating HeLa cells with ER-NPs for 24 h. The gel electrophoresis in Fig. 14b unequivocally showed that ER-NP induced stress leading to the 3.3 folds increase in CHOP expression compared to non-treated control cells (Figure 15b). From these fluorescence imaging and protein expression assays, it was confirmed that ER-NPs triggered ER stress in HeLa cells.

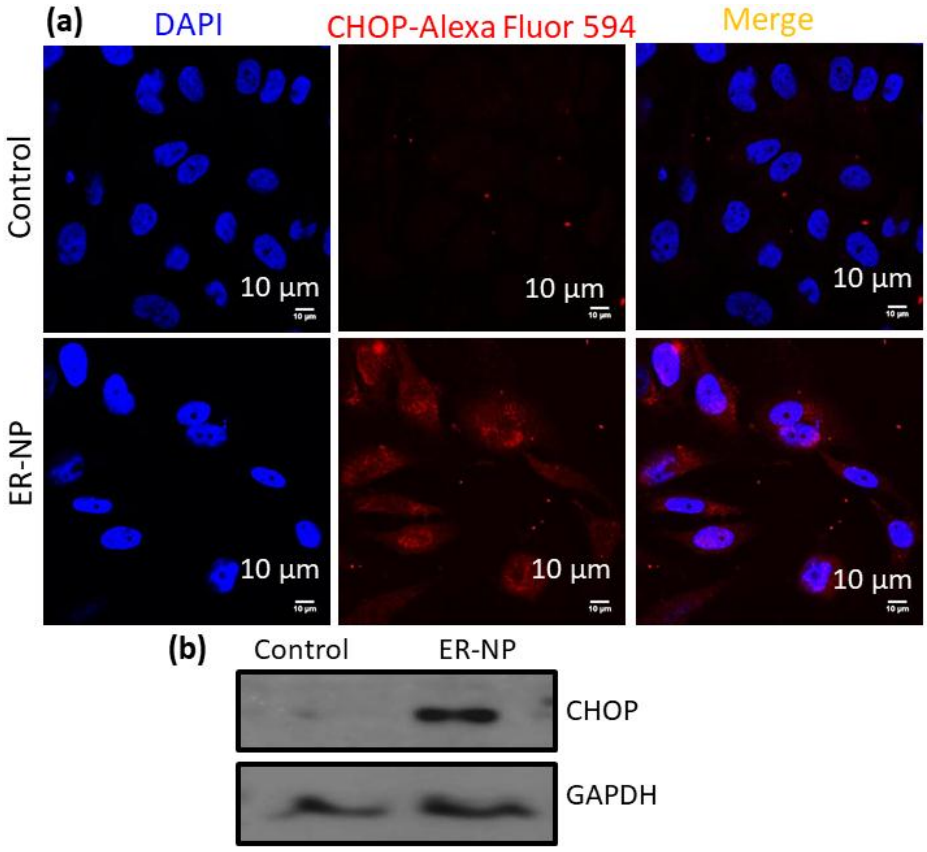

Figure 14: (a) CLSM images of HeLa cells to visualize CHOP as ER stress marker. CHOP was stained with Alexa Fluor 594-labeled antibody (red). Nuclei of HeLa cells were stained with DAPI (blue). (b) Western blot image of expression of CHOP in HeLa cells. Scale bar = 10 µm.

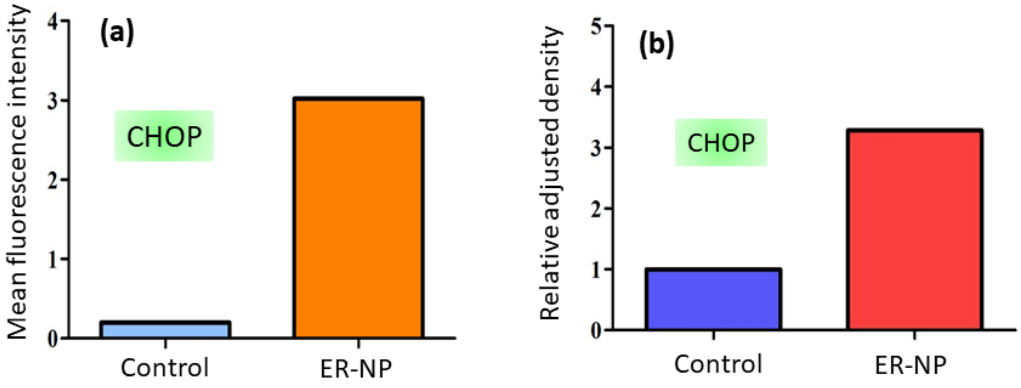

Figure 15: (a, b) Quantification of expression of CHOP in HeLa cells after treatment with ER-NPs by CLSM images and Western blot analysis respectively.

3.2.5. DNA damage

We hypothesized that ER-NP would simultaneously induce ER stress and DNA damage. To validate this hypothesis, we estimated the expression of γH2AX as one of the markers of DNA damage by fluorescence microscopy.[49] HeLa cells were treated with ER-NPs for 24 h followed by staining of nucleus with blue fluorescent dye DAPI. The cells were further incubated with γH2AX primary antibody followed by red fluorescent Alexa Fluor 594-labelled secondary antibody. The expression of γH2AX was visualized by CLSM. Figure 16a demonstrated that, untreated control cells hardly

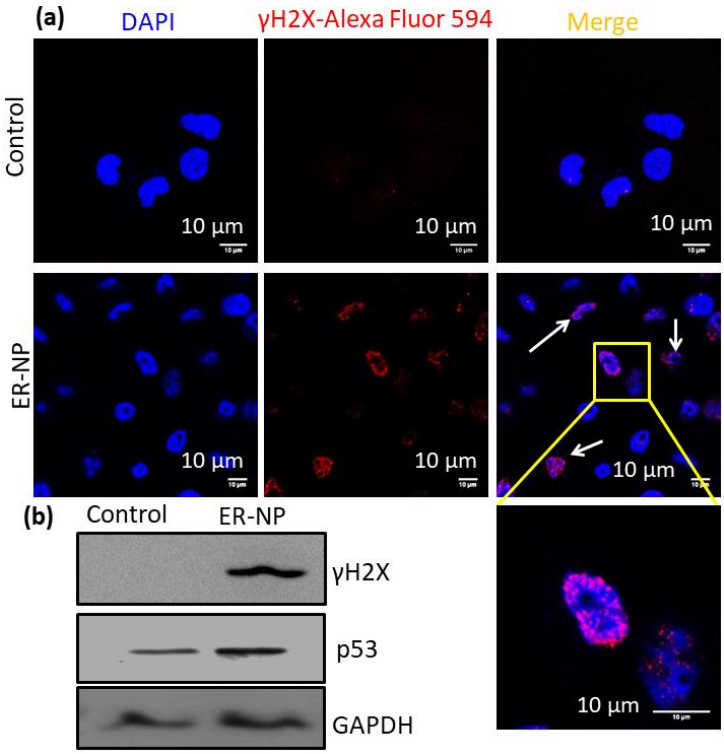

Figure 16: (a) CLSM images of HeLa cells to visualize γH2AX as DNA damage marker. γH2AX was stained with Alexa Fluor 594-labeled antibody (red). Nuclei of HeLa cells were stained with DAPI (blue). (b) Western blot image of expression of γH2AX and p53 in HeLa cells. Scale bar = 10 µm.

showed any DNA damage. On the other hand, ER-NP treated cells showed remarkable increase in γH2AX expression leading to increase in red fluorescence intensity. Moreover, the red fluorescence signals significantly overlapped with the blue fluorescently labeled nucleus showing the localization of γH2AX (Figure 16a). Also fluorescence microscopy based quantification revealed that ER-NP induced 4.8 folds increase in γH2AX expression compared to control cells (Figure 17a). Further

assessment of γH2AX and p53 (DNA damage effector) [50] by Western blot was also performed after treatment of HeLa cells with ER-NPs for 24 h. The gel electrophoresis images clearly showed that ER-NPs amplified the expression of γH2AX and p53 by 9.1 folds and 3.8 folds respectively (Figure 16b, 17b,c). From these microscopy and protein expression it was confirmed that ER-NPs triggered DNA damage in HeLa cells.

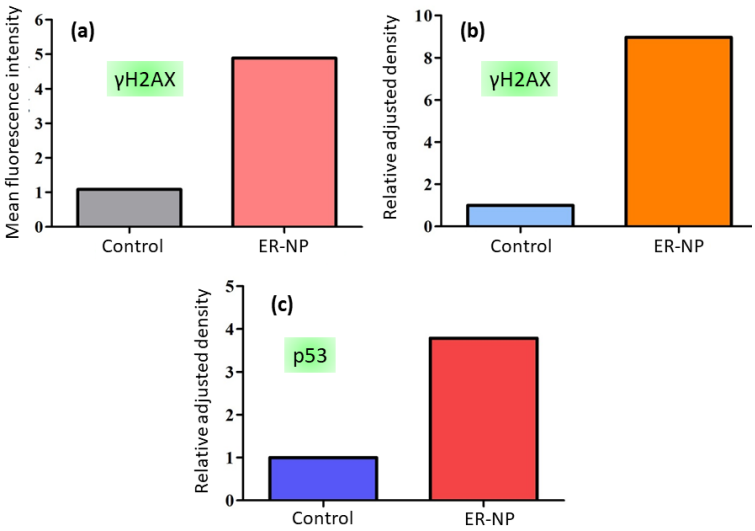

Figure 17: (a,b) Quantification of γH2AX expression in HeLa cells after treatment with ER-NPs for 24 h determined from CLSM images and Western blot analysis respectively. (c) Quantification of p53 expression in HeLa cells after treatment with ER-NPs for 24 h, determined by Western blot analysis.

3.2.6. Apoptosis and cell death

ER-NP mediated simultaneous induction of ER stress and nuclear DNA damage would generate reactive oxygen species (ROS) leading to cell death through apoptosis.[51-52] To evaluate the generation of ROS, HeLa cells were treated with ER-NPs for 24 h followed by incubation with H_2DCFDA.[53] In sub-cellular environment H_2DCFDA gets hydrolyzed by esterase and react with ROS to produce green fluorescent DCF, which can be visualized by fluorescence microscopy. Figure 18a exhibited that non-treated control cells produced negligible ROS, whereas, ER-NP induced remarkably increased amount of ROS leading to 19.1 folds increase in green fluorescence intensity compared to control cells (Figure 20a). We further evaluated the stimulation of programmed cell death (apoptosis) by ER-NPs through flow cytometry. HeLa cells were treated with ER-NPs for 24 h followed by incubation with FITC-

labeled Annexin V (green fluorescence) and propidium iodide (PI, red fluorescence dye) to stain cell surface phosphatidyl serine and nuclear DNA in apoptotic and necrotic cells respectively. From the flow cytometry data, it was found that ER-NP triggered 37.4 % and 51.8 % cells into early and late stages of apoptosis compared to control cells (Figure 18b).

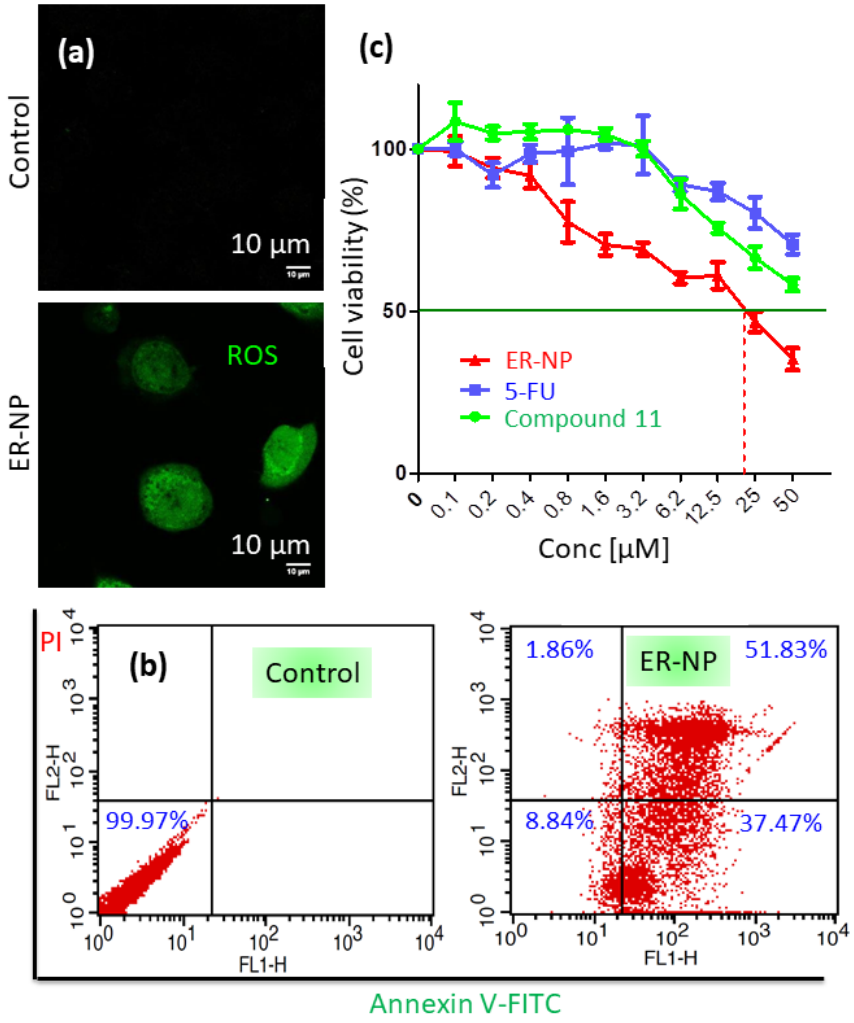

Figure 18: (a) CLSM images of ROS generation in HeLa cells. Scale bar = 10 µm. (b) Flow cytometry analysis in HeLa cells after treatment with ER-NP. Apoptotic and necrotic cells were stained with FITC-Annexin V and PI respectively. (c) Cell viability assay of ER-NP, 5FU and compound 11 in HeLa cells at 48 h post-incubation.

Induction of early and late apoptosis would push the cells into death. The cell viability assay was performed to evaluate the effect of ER-NPs. HeLa cells were treated with ER-NPs in multiple dosages for 48 h and the % of viable cells was measured by MTT assay. The cell viability assay showed that ER-NPs prompted 50% cell death (IC_{50}) at

23.2 μM concentration with 35.2% cell viability at 50 μM concentration (Figure 18c). On the other hand, 5-FU and compound 11 could induce only 70.6% and 58.2% cell viability even in highest concentration (50 μM). From the microscopy, flow cytometry and cell viability assay it was evident that ER-NPs generated ROS to trigger early/late apoptosis to induce cell death.

3.2.7. Autophagy induction and inhibition

Cancer cells can overcome ER stress and DNA damage effect by initiating cell survival mechanism called autophagy.[54-55] Hence, we evaluated the induction of autophagy by ER-NPs. HeLa cells were treated with ER-NPs for 24 h followed by incubation with Beclin-1 primary antibody as one of the markers for autophagy.[56] We visualized the cells after further incubation with red fluorescent Alexa Flour 594 labeled secondary antibody under fluorescence microscopy. From the CLSM images (Figure 19a), it was clear that control cells hardly showed any Beclin-1 expression. On contrary, ER-NP treated cells demonstrated significant increase in red fluorescence intensity (5 folds, Figure 20b) compared to control cells indicating triggering of autophagy. Furthermore, we also assessed the protein level of another autophagy marker LC3 (microtubule-associated protein 1 light chain 3)[57] by Western blot analysis. The gel electrophoresis image (Figure 19b) after treating HeLa cells with ER-NPs for 24 h, showed undoubtedly that, ER-NPs increased the expression of LC3 by 2.3 folds compared to control cells (Figure 20c). Hence it was evident that ER-NPs activated autophagy as one of the cell survival mechanisms under stress.

To inhibit autophagy and trigger augmented cell death, we intended to use ER-NPs in combination of chloroquine (CQ) as autophagy inhibitor.[58] Moreover, it was shown recently that CQ can augment the anti-cancer activity of 5FU in cancer cells.[59] Hence, we treated HeLa cells with a cocktail of varying dosages of ER-NP and CQ in 50 μM concentration and assessed the generation of ROS by H2DCFDA assay. The fluorescence microscopy images (Figure 19c) evidently showed that combination of ER-NP and CQ significantly increased the generation of ROS by 36 folds compared to control cells (Figure 20a). We finally, assessed the cell killing ability of ER-NPs in presence of CQ by MTT assay. We again incubated HeLa cells in different concentrations of ER-NP and CQ (50 μM) cocktail and cell viability was measure after 48 h. From the MTT data, it was observed that, the combination of ER-NP with CQ

showed much reduced IC_{50} = 11.9 µM (20.3 % cell viability in highest concentration) compared to IC_{50} = 23.3 µM for ER-NP only (Figure 19d). Interestingly, only CQ showed negligible cell killing even at 50 µM concentration after 48 h (Figure 20d). From these ROS and MTT assay, it was confirmed that simultaneous induction of ER stress, DNA damage and autophagy inhibition can augment anti-cancer efficacy in HeLa cervical cancer cells.

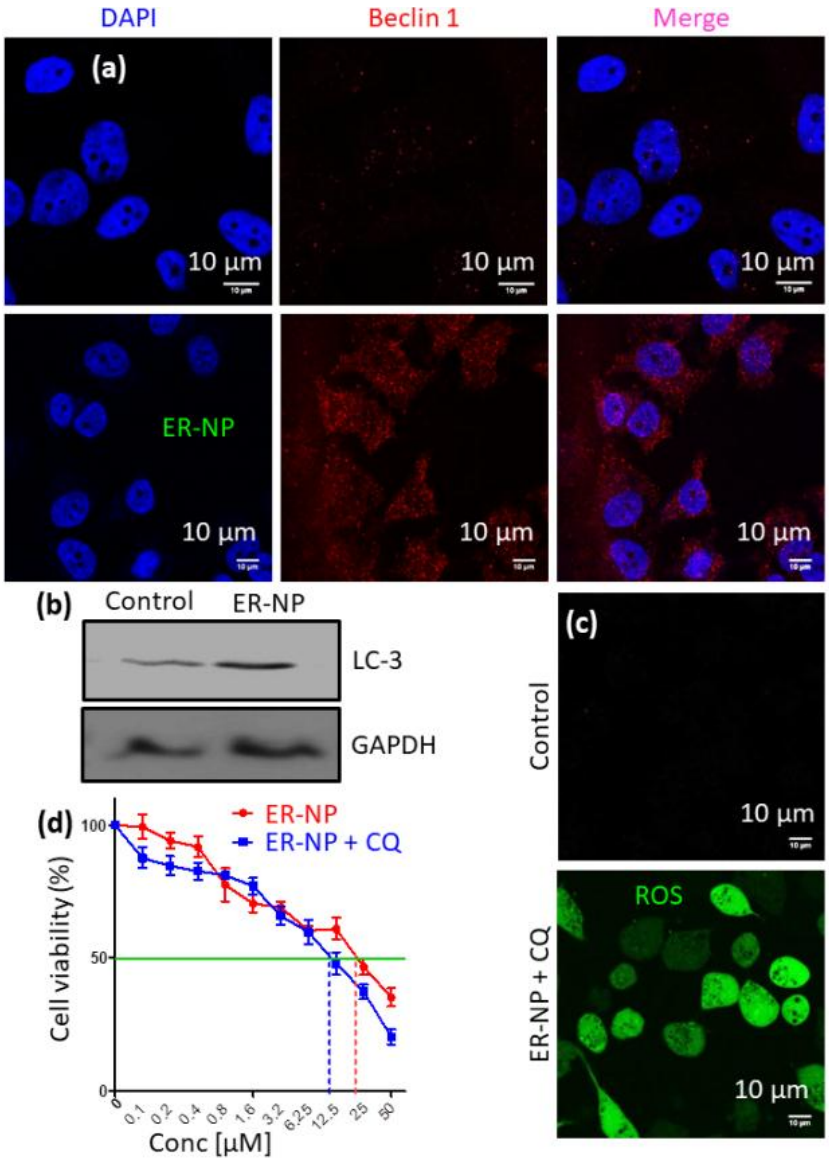

Figure 19: (a) CLSM images of HeLa cells to visualize Beclin-1 as autophagy marker. (b) Wester blot analysis for the expression of LC-3. (c) CLSM images of HeLa cells to visualize ROS. (d) Cell viability assay of ER-NP and ER-NP + CQ combination in HeLa cells at 48 h post-incubation. Scale bar = 10 µm.

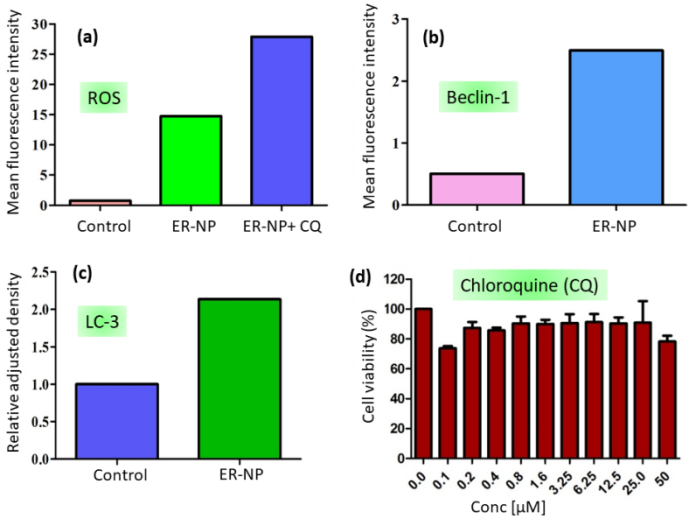

Figure 20: (a, b) Quantification of ROS generated and Beclin-1 expression from CLSM images in HeLa cells after treatment with ER-NPs for 24 h. (c) Quantification of expression of LC-3 from Western blot in HeLa cells after treatment with ER-NPs for 24 h. (d) Cell viability of HeLa cells after treatment with chloroquine (CQ) at 48 h post-incubation.

3.3. Conclusion

In conclusion, we have engineered for the first time, a supramolecular self-assembled hexameric rosette structure from triazine-based small molecule in presence of an anti-cancer drug 5-fluorouracil in water which further lead to the formation of spherical nanoscale particle (ER-NP) by hierarchical self-assembly. These ER-NPs simultaneously contained ER-localization fluorescence moiety, ER stress inducer and nuclear DNA damaging drug. Confocal microscopy, gel electrophoresis and flow cytometry revealed that ER-NPs accumulated selectively into endoplasmic reticulum of HeLa cells in a time dependent manner through macropinocytosis followed by induction of ER stress and nuclear DNA damage leading to improved cell death by apoptosis. Interestingly, ER-NPs initiated autophagy in HeLa cells which could be overcome by the combination of ER-NPs and autophagy inhibitor chloroquine, leading to much augmented cell killing efficacy. We anticipate that, this work will extend the concept of supramolecular self-assembly of small molecules to target multiple sub-cellular organelles simultaneously for improved therapeutic effect in anti-cancer therapy.

3.4. Materials & Methods.

3.4.1. Materials

Cyanuric chloride, dansyl chloride, ethylenediamine, hydrazine monohydrate, 5-Nitrofuryladehyde, triphenyl-phosphoranylidene acetaldehyde, 5-fluorouracil, JC1, H2DCFDA, MTT, solvents were procured from Sigma-Aldrich. Cell culture media was purchased from HiMedia. All the primary and secondary antibodies were obtained from Cell Signaling, Biolegend and Abcam. Confocal microscopy was performed by a Zeiss LSM 710 machine. Flow cytometry was performed using a BD FACS Calibur flow cytometer.

3.4.2. Experimental Procedure

3.4.2.a. Synthesis of 4,6-dichloro-1,3,5-triazin-2-amine (2).

Ammonia (1 equiv) was diluted in 10% ether and added drop wise vigorously stirred solution of cyanuric chloride (1 equiv) in 5 ml ether at -15 °C to -10 °C for 1 h. The resulting mixture was stirred at 0°C for 24 h. Diethyl ether was evaporated to dryness and the residue was treated with 50 mL water. Insoluble solid was filtered off and dried over anhydrous P_2O_5 to obtain compound **2**.

Yield = 90 %.

^{1}H NMR (DMSO-d6, 400 MHz): δ = 11.18 (s, 2H).

^{13}C NMR (DMSO-d6, 100 MHz): δ = 149.88, 149.78, 148.33.

ESI-MS: Observed m/z for $[M+H]^+$ = 164.9735.

3.4.2.b. Synthesis of N-(2-aminoethyl)-5-(dimethylamino) naphthalene-1-sulfonamide (5).

Dansyl chloride (**3**, 1 equiv.) was dissolved in dry dichloromethane and added drop wise in excess ethylenediamine (**4**, 10 equiv.) in dry dichloromethane at 0 °C. The reaction mixture was stirred at 0 °C for 1 h. Reaction progress was monitored by thin layer chromatography (TLC). After completion of reaction the solution was acidified with HCl (1N) and 20 mL water was added. The reaction mixture was poured into 10 mL DCM and the organic layer was extracted. The DCM layer was concentrated and dried over Na_2SO_4, filtered and evaporated. The crude product was purified by silica gel colume chromatography using 5% methanol in DCM as mobile phase.

Yield = 93%.

^{1}H NMR ($CDCl_3$, 400 MHz): δ = 8.54 (s, 1H), 8.30 (*d*, *J* = 8.7 Hz, 1H), 7.495(*dd*, *J* = 8.7Hz, 1.2 Hz, 1H), 8.25 (*d*, *J* = 7.3 Hz, 1H), 7.54 (*ddd*, *J* = 18.9 Hz, 8.5 Hz, 7.5 Hz, 2H), 7.18 (*d*, *J* = 7.1 Hz, 2H), 2.91 (*d*, *J* = 5.3 Hz, 2H), 2.89 (s, 6H), 2.70 (m, 2H).

^{13}C NMR ($CDCl_3$, 100 MHz): δ = 152.15, 134.77, 130.61, 129.80, 128.55, 123.34, 118.85, 115.35, 45.55, 40.92.

ESI-MS: Observed m/z for $[M+H]^+$ = 294.1276.

3.4.2.c. Synthesis of N-(2-(4-amino-6-chloro-1,3,5-triazin-2-yl)amino)ethyl)-5-(dimethylamino)naphthalene-1-sulfonamide (6).

4,6-dichloro-1,3,5-triazin-2-amine (2, 1 equiv.) was dissolved in THF. N-(2-aminoethyl)-5-(dimethylamino) naphthalene-1-sulfonamide and DIPEA were dissolved in 20 mL THF and was added drop wise using dropping funnel into the 4,6-dichloro-1,3,5-triazin-2-amine (**2**) solution. Temperature of the reaction was maintained at -15 °C for 50 min. The reaction mixture was allowed to run further 30 min at 0 °C. After completion of the reaction, THF was evaporated and washed with water three times. The reaction mixture was filtered and washed with ice water. The solid compound was dried over anhydrous P_2O_5.

Yield = 63 %.

^{1}H NMR (DMSO-d6, 400 MHz): δ = 8.92 (s, 1H), 8.47 (*d*, *J* = 8.5 Hz, 1H), 8.25 (*d*, *J* = 8.6 Hz, 1H), 8.09 (*dd*, *J* = 11.6 Hz, 6.6 Hz, 2H), 7.60 (*dt*, *J* = 18.5 Hz, 8.0 Hz, 2H), 7.28 (*d*, *J* = 7.4 Hz, 1H); 3.67 (s, 2H), 3.27 (*d*, *J* = 6.2 Hz, 2H), 2.99 (*d*, *J* = 6.2 Hz, 2H)

^{13}C NMR (DMSO-d6, 100 MHz): δ = 170.55, 169.20, 168.27, 165.25, 135.76, 133.37, 129.40, 129.14, 128.88, 128.77, 128.36, 128.18, 127.181, 127.68, 123.66, 122.87, 119.25, 117.53, 115.32, 64.94, 45.12, 40.68.

ESI-MS: Observed m/z $[M+Na]^+$ = 422.1180.

3.4.2.d. Synthesis of N-(2-(4-amino-6-hydrazinyl-1,3,5-triazin-2-yl)amino)ethyl)-5-(dimethylamino)naphthalene-1-sulfonamide (7).

Hydrazine monohydrate (5 equiv) was added drop wise to a solution of compound **6** (in 2 mL ethanol). The reaction mixture was stirred at refluxing condition for 24 h. After completion of the reaction solvent was evaporated and reaction mixture was

washed with water. The reaction mixture was filtered and washed with ice water. After filtration the solid compound was collected and dried over anhydrous P_2O_5.

Yield = 84%.

^{1}H NMR (DMSO-d6, 400 MHz): δ = 8.45 (*d*, *J* = 8.5 Hz, 1H), 8.25 (*d*, *J* = 8.6 Hz, 1H), 8.10 (*d*, *J* = 7.2 Hz, 7.78 Hz, 1H), 7.78 (s, 1H), 7.59 (m, 2H), 7.24 (*d*, *J* = 7.4 Hz, 1H), 6.64 (s, 1H), 3.23 (s, 2H), 2.91 (s, 2H), 2.82 (s, 6H).

^{13}C NMR (DMSO-d6, 100 MHz): δ = 167.26, 151.38, 129.44, 129.04, 128.19, 127.88, 123.62, 120.20, 119.00, 115.4, 45.10, 42.37.

ESI-MS: Observed m/z for $[M+H]^+$= 418.1773.

3.4.2.e. Synthesis of (E)-3-(5-nitrofuran-2-yl) acrylaldehyde (10).

5-Nitrofuryladehyde (**8**, 1 equiv) and triphenylphosphoranylidene acetaldehyde (**9**, 1 equiv) were dissolved in dry toluene. The reaction mixture was refluxed for 6 h. The reaction mixture was cooled to room temperature and toluene was evaporated. 20 mL dichloromethane and 20 mL water were added into the reaction mixture. The organic layer was extracted and dried over anhydrous Na_2SO_4. The crude product was purified by silica gel column chromatography using 25% ethyl acetate/hexane as mobile phase.

Yield = 61%.

^{1}H NMR ($CDCl_3$, 400 MHz): δ = 9.76 (*d*, *J* = 7.4 Hz, 1H), 7.41 (*d*, *J* = 3.8 Hz, 1H), 7.30 (s, 1H), 6.95 (*d*, *J* = 3.8 Hz, 1H), 6.88 (*dd*, *J* = 16 Hz, 7.4 Hz, 1H),

^{13}C NMR ($CDCl_3$, 100 MHz): δ = 191.84, 151.99, 134.61, 131.02, 116.70, 113.40

ESI-MS: Observed m/z $[M+H]^+$ = 168.0276.

3.4.2.f. Synthesis of N-(2-((4-amino-6-(2-((1E,2E)-3-(5-nitrofuran-2-yl)allylidene)hydrazinyl)-1,3,5-triazin-2-yl)amino)ethyl)-5-(dimethylamino)naphthalene-1-sulfonamide (11).

Compound **7** and compound **10** were dissolved in dry methanol and the reaction mixture was stirred at room temperature for 1 h. Methanol was evaporated and compound 11 was purified by silica gel column chromatography using 10 % MeOH in DCM as mobile phase.

Yield = 71%.

^{1}H NMR (MeOH-d4, 400 MHz): δ = 11.19 (s, 1H), 8.44 (*d*, *J* = 8.5 Hz, 1H), 8.27 (*d*, *J* = 8.6 Hz, 1H), 8.12 (*d*, *J* = 7.3 Hz, 1H), 7.94 (m, 1H), 7.76 (*t*, *J* = 4.5 Hz, 1H), 7.60 (*t*, *J* = 8.1 Hz, 1H), 7.54 (*t*, *J* = 7.8 Hz, 1H), 7.21 (*d*, *J* = 7.6 Hz, 1H), 7.09 (*t*, *J* = 3.5 Hz, 2H), 6.90 (*dd*, *J* = 15.9 Hz, 4.7 Hz, 2H), 3.31 (*d*, *J* = 5.9 Hz, 2H), 3.17 (*d*, *J* = 5.1 Hz, 1H), 2.97 (*d*, *J* = 5.4 Hz, 2H), 2.80 (s, 6H).

^{13}C NMR (MeOH-d4, 100 MHz): δ = 172.03, 168.23, 155.46, 151.38, 151.19, 142.14, 138.42, 135.70, 131.12, 129.49, 129.06, 128.37, 127.80, 125.90, 123.59, 121.13, 121.13, 118.96, 115.67, 115.12, 112.81, 48.63, 46.00, 45.07, 44.47.

ESI-MS: Observed m/z for $[M-N_2+H]^+$= 567.1888.

3.4.3. Experimental procedure of Dynamic light scattering (DLS):

Procedure is discussed in chapter 1.[60]

3.4.4. Experimental procedure of Field-emission scanning electron microscopy (FESEM):

Procedure is discussed in chapter 1.[60]

3.4.5. Experimental procedure of Atomic force microscopy (AFM):

Procedure is discussed in chapter 1.[60]

3.4.6. Experimental procedure of Transmission Electron Microscopy (TEM):

Procedure is discussed in chapter 1. [60]

3.4.7. Experimental procedure of Diffusion-Ordered NMR spectroscopy (DOSY):

25 mM samples of the 1:1 mixture of compound 11 and 5FU, Compound 11 and 5FU were used to obtain DOSY spectra. A 400 MHz NMR spectrometer with a dual broadband probe was used to acquire the spectra at 25 °C. The spectra were acquired with DgcsteSL sequence using a diffusion delay of 50 ms for 10 values for the diffusion gradient strength from 1 000 to 30000. A recycle delay of 2 ms was used for the accumulation of 64 scans for each value of the diffusion gradient strength.

3.4.8. Experimental procedure of Live Cells Imaging of ER, mitochondria and lysosome:

10^5 HeLa cells per well were seeded in a Lab Tek chamber and incubated 12 h for attachment. The cells were treated with ER-NPs with (5µg/ml of fluorophore) in different time points. After treatment the media was removed and cells were washed with chilled PBS.

Followed by the cells were stained with respective organelle staining dye ER-Tracker Red, Mito-Tracker Deep Red and Lyso-Tracker Deep Red to stain Endoplasmic Reticulum, mitochondria and lysosome respectively. After incubation with organelle staining dye for 1h, cells were washed with cold PBS thrice. Finally the cells were imaged with Zeiss LSM 710 confocal microscope.

3.4.9. Experimental procedure of Western blotting:

Procedure is discussed in chapter 1. [61] (Primary antibodies are required GADD153/CHOP, γH2AX, p53, LC-3 and GAPDH).

3.4.10. Experimental procedure of Immunofluorescence assay:

2×10^4 HeLa cells were placed on coverslip and kept overnight for attachment. Cells were then treated with ER-NPs at 25 µM concentration for 24 h. After the drug treatment the cells were washed with chilled PBS, fixed with 4% paraformaldehyde (15mins) and permeabilized with permeabilization buffer for 15mins. The permeabilization buffer (PBS containing 0.1–0.25% Triton X-100) was removed and washed with cold PBS, subsequently the cells was incubated with blocking agent (PBS containing 0.3% tween and 1% BSA) for 1h. Further the blocking agent was washed off and the cells was incubated with primary antibody (dilution followed according product protocol) for 3h and finally it was incubated with Alexa Fluor-594 conjugated secondary antibody solution (dilution followed according product protocol) for 45mins. Cells were washed with chilled PBS and mounted on a glass slide using DAPI-Diamond antifade reagent. Cellular imaging was performed by using confocal microscopy.[61]

3.4.11. Experimental procedure of Apoptosis by flow cytometry:

2 lakh HeLa cells were seeded and allowed overnight for growing. Cells were treated with ER-NPs at 25 µM concentration for 24 h. After treatment the cells were washed with PBS and trypsinized to collect the cells. After collecting cells 5 µL of Annexin V and 10 µL propidium iodide and 400 µL binding buffer was added (followed according to product manual). Finally cells were analyzed using flow cytometer.[61]

3.4.12. Experimental procedure of ROS generation assay:

Procedure is discussed in chapter 1.[61]

3.4.13. Experimental procedure of Cell Viability (MTT assay):

Procedure is discussed in chapter 1. [61]

3.5. Appendices:

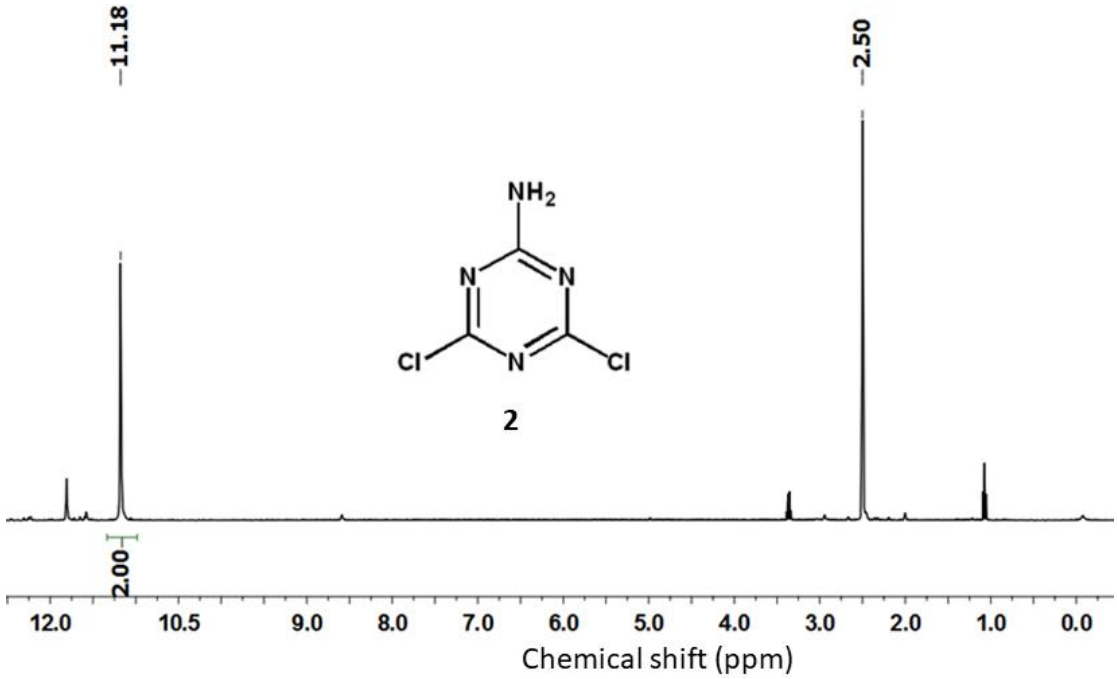

Fig. S1: ^{1}H NMR spectra of compound **2**.

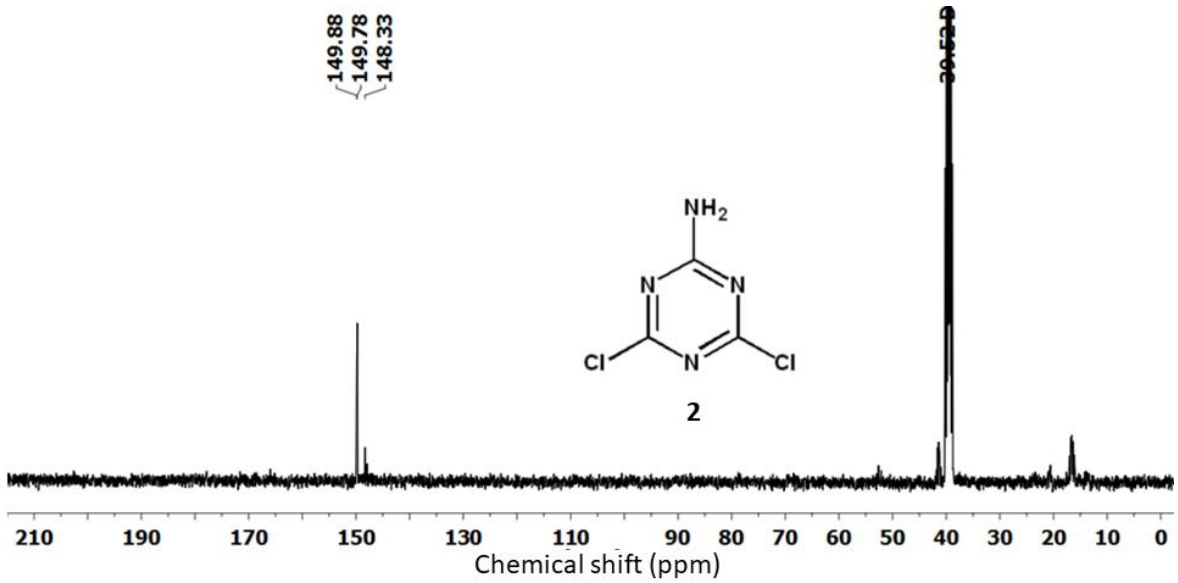

Fig. S2: ^{13}C NMR spectra of compound **2**.

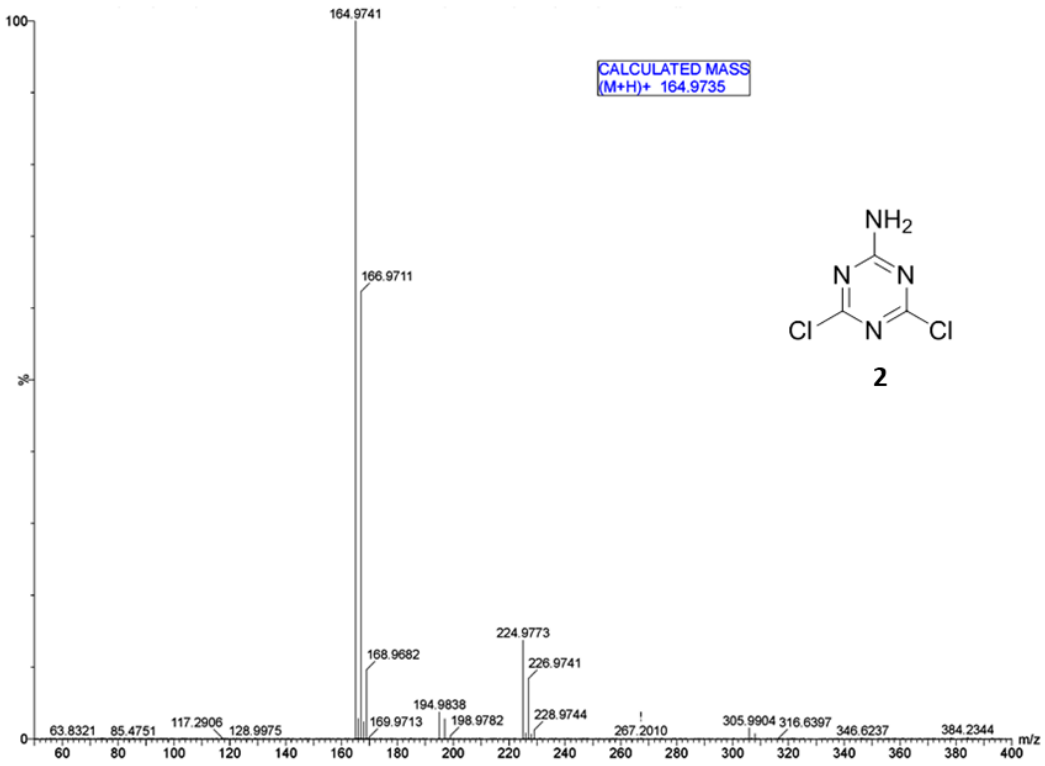

Fig. S3: HR-MS spectra of compound **2**.

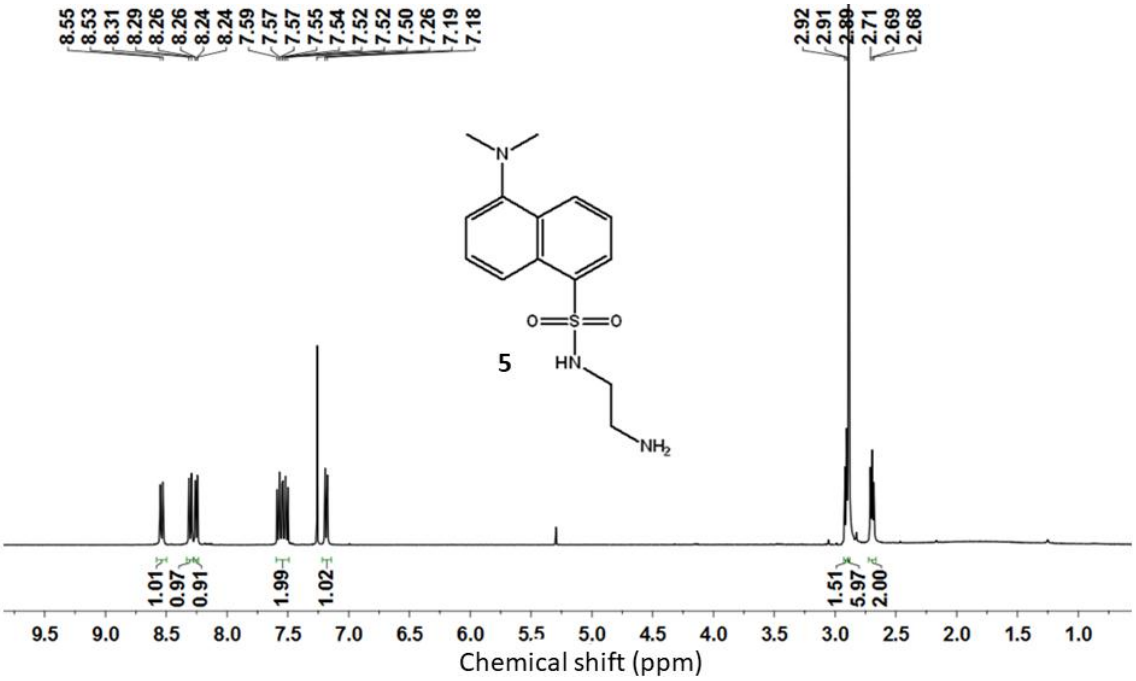

Fig. S4: ^{1}H NMR spectra of compound **5**.

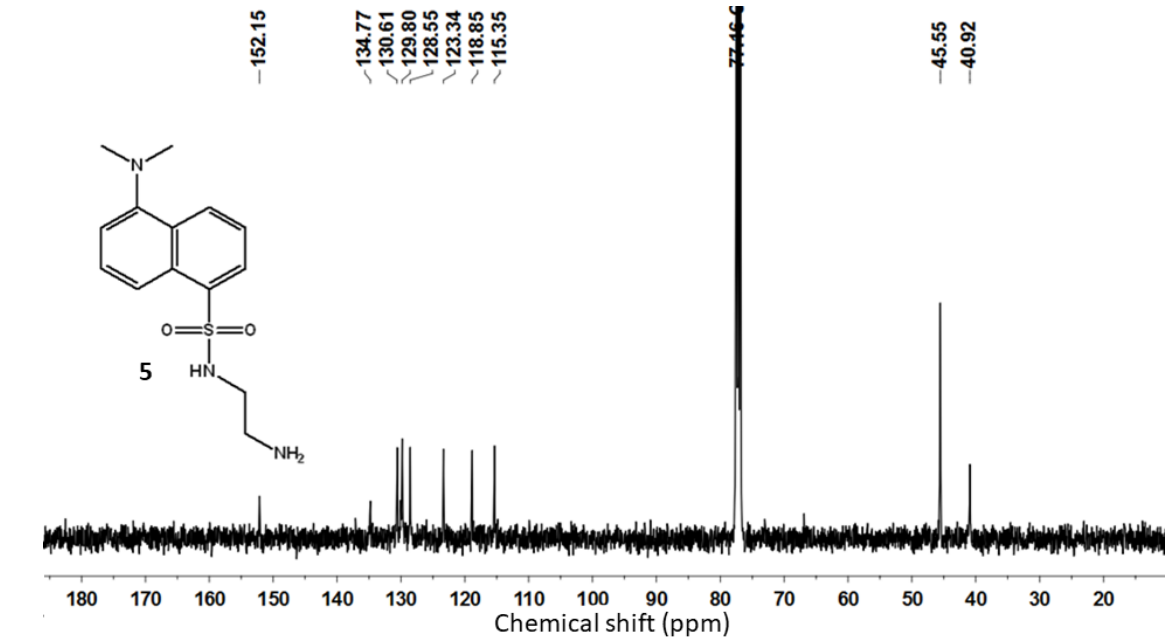

Fig. S5: ^{13}C NMR spectra of compound **5**.

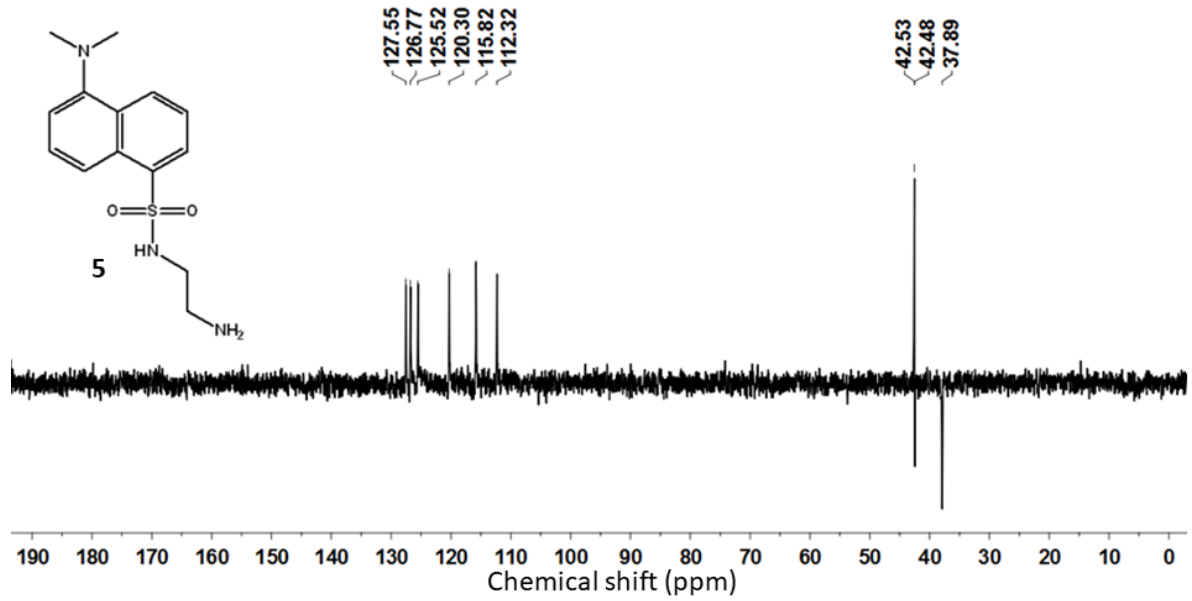

Fig. S6: ^{13}C DEPT spectra of compound **5**.

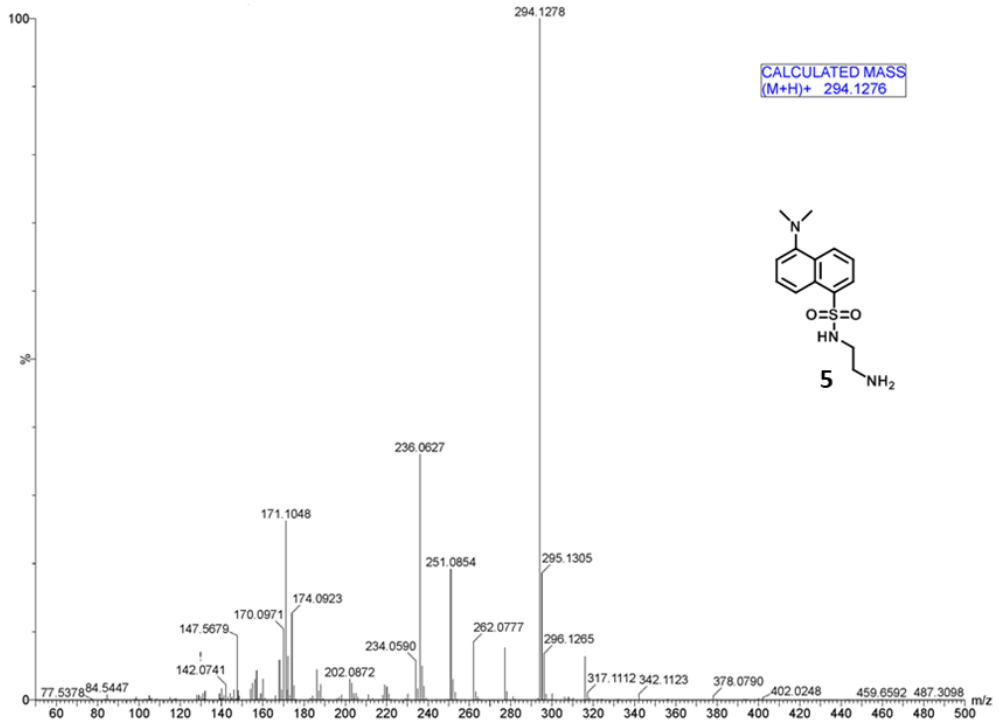

Fig. S7: HR-MS spectra of compound **5**.

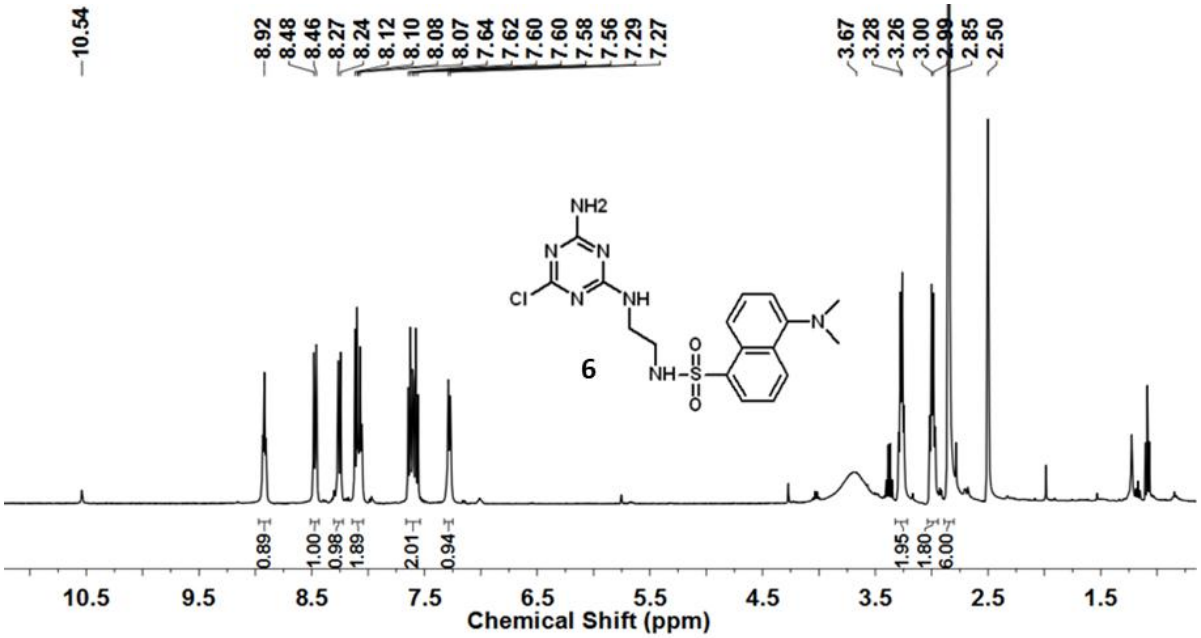

Fig. S8: ^{1}H NMR spectra of compound **6**.

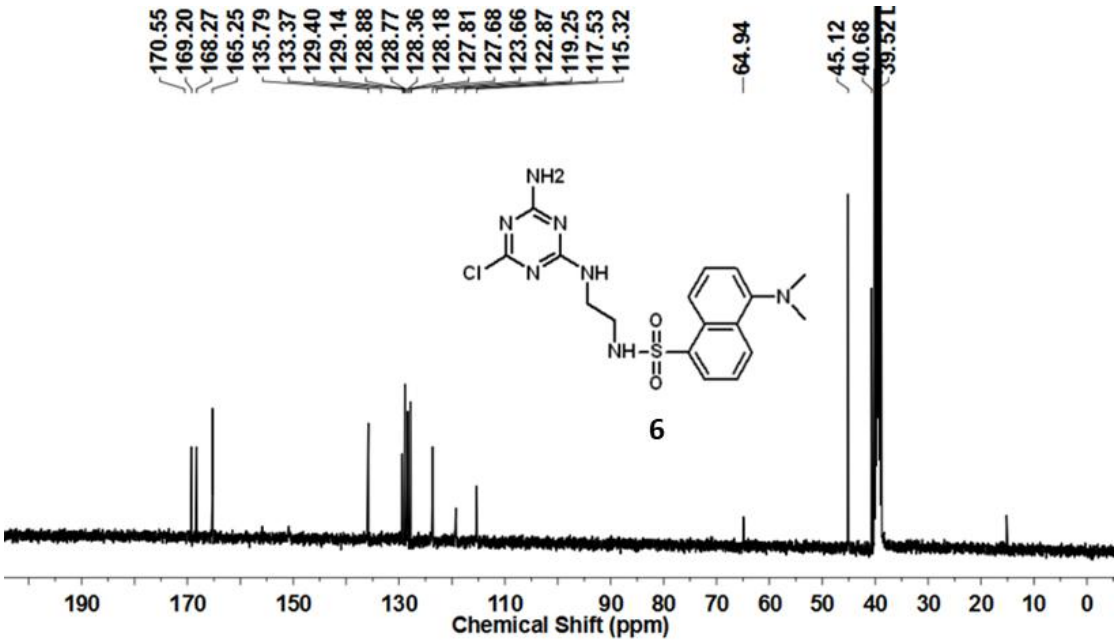

Fig. S9: ^{13}C NMR spectra of compound **6**.

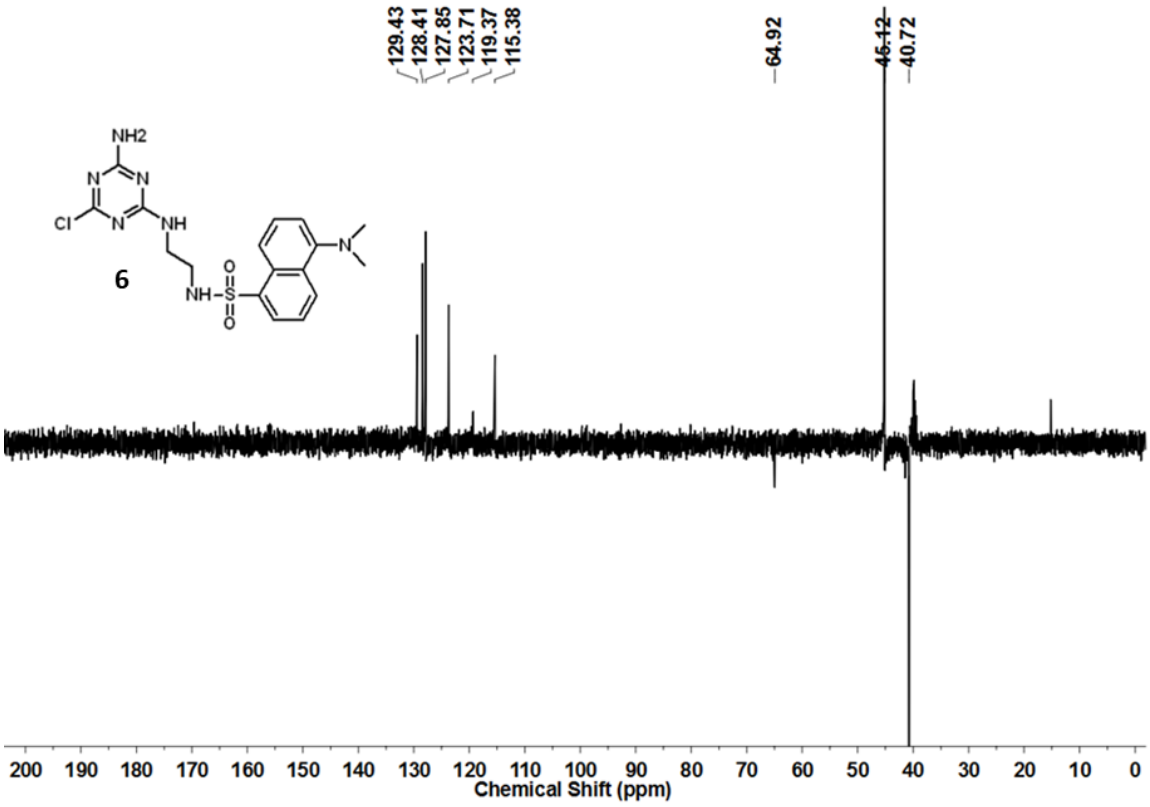

Fig. S10: ^{13}C DEPT spectra of compound **6**.

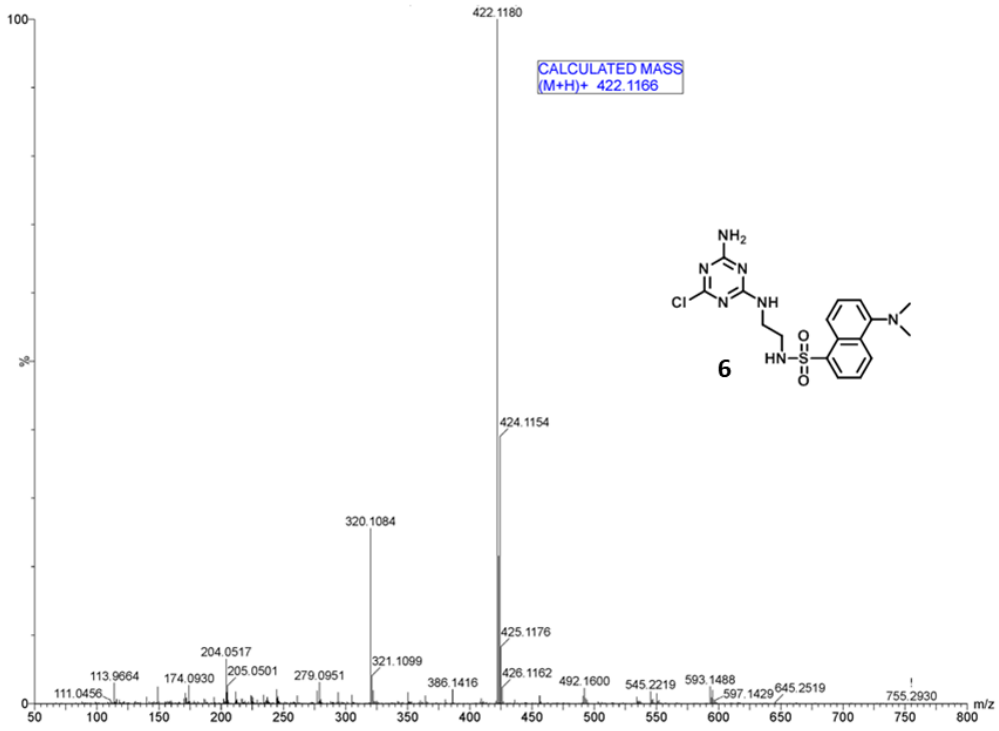

Fig. S11: HR-MS spectra of compound **6**.

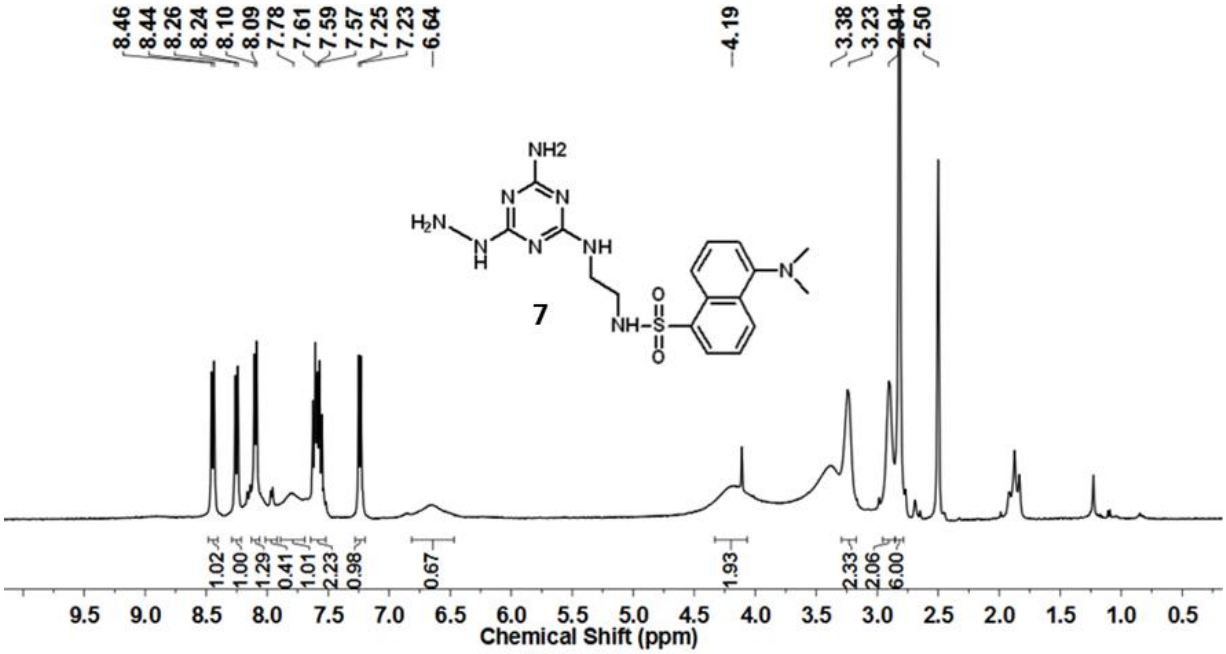

Fig. S12: ^{1}H NMR spectra of compound **7**.

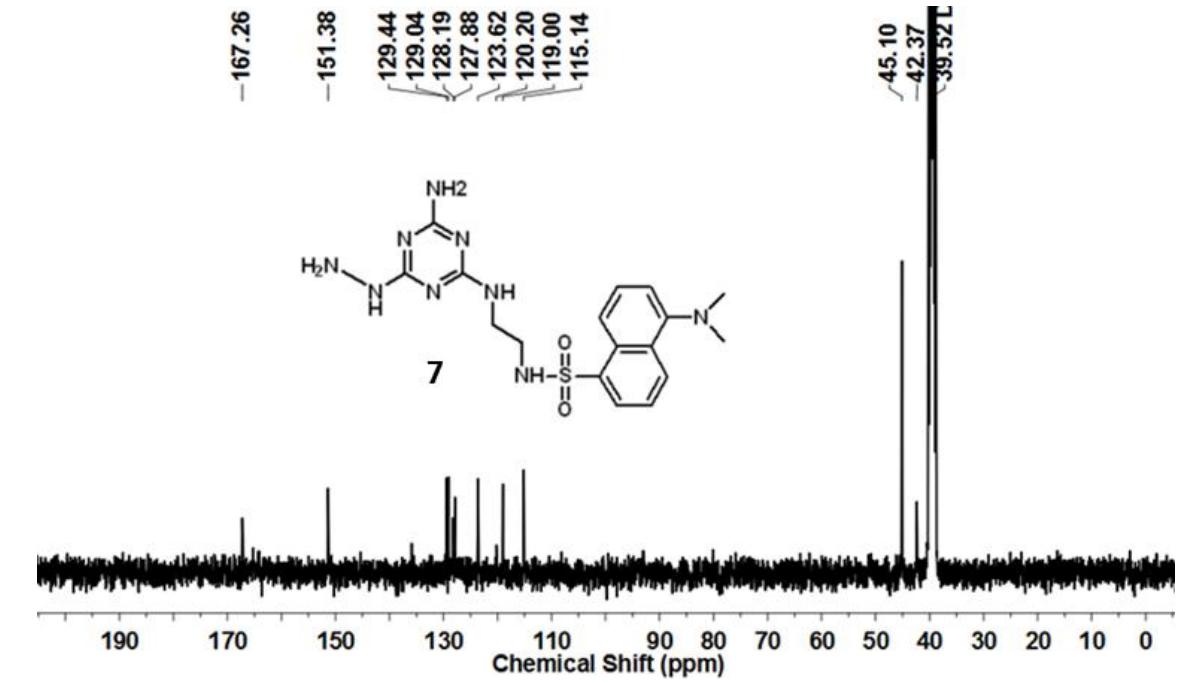

Fig. S13: ^{13}C NMR spectra of compound **7**.

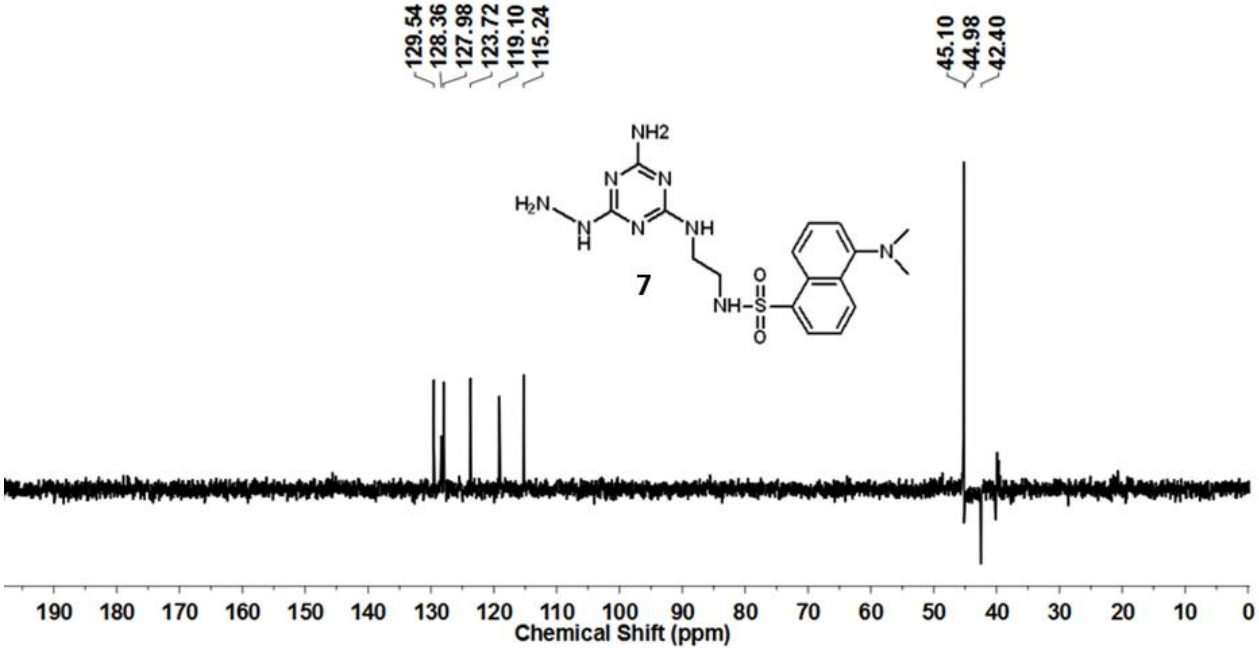

Fig. S14: ^{13}C DEPT spectra of compound **7**.

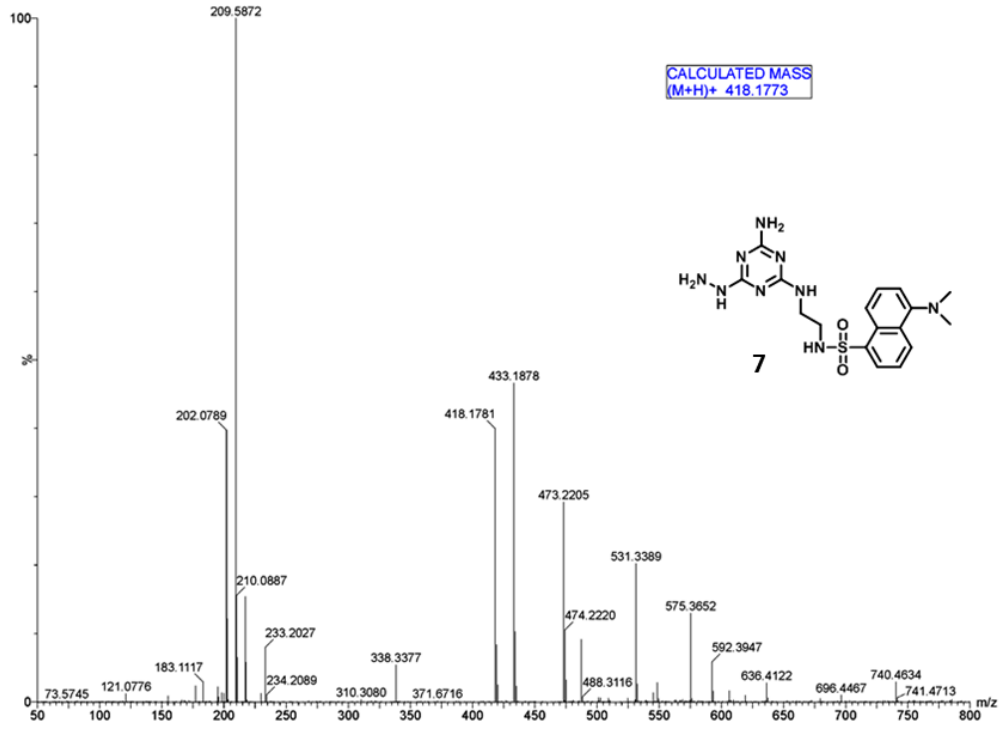

Fig. S15: HR-MS spectra of compound **7**.

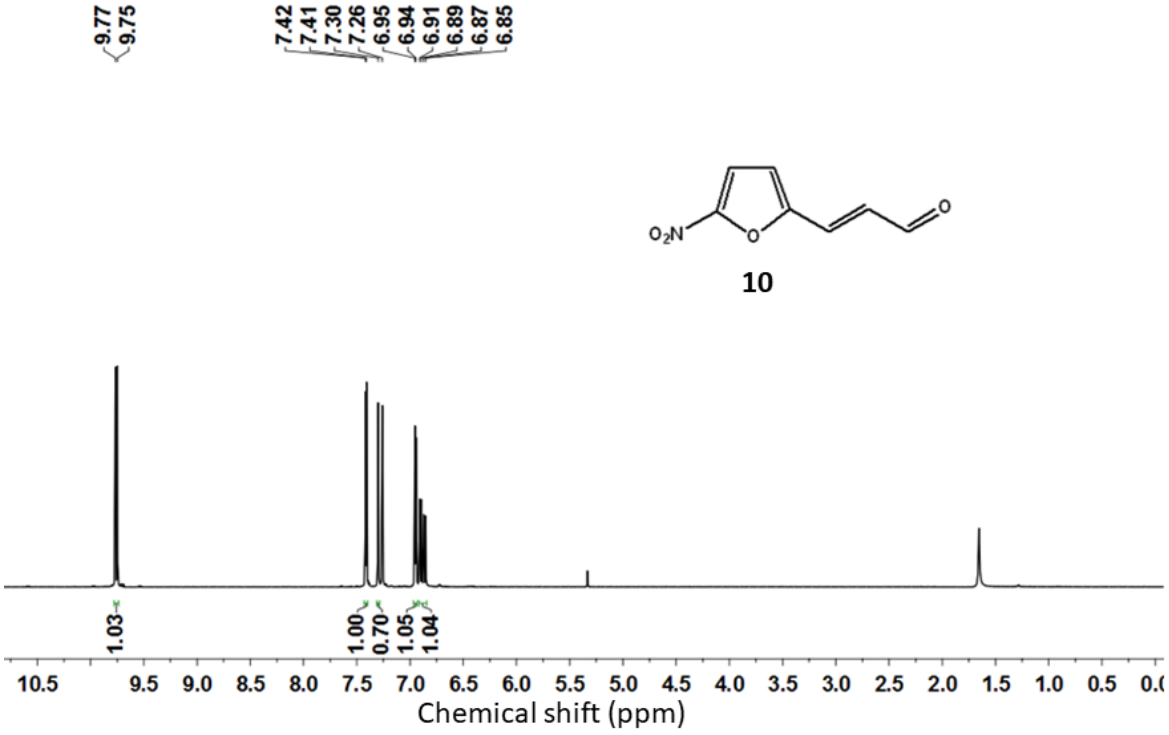

Fig. S16: ^{1}H NMR spectra of compound **10**.

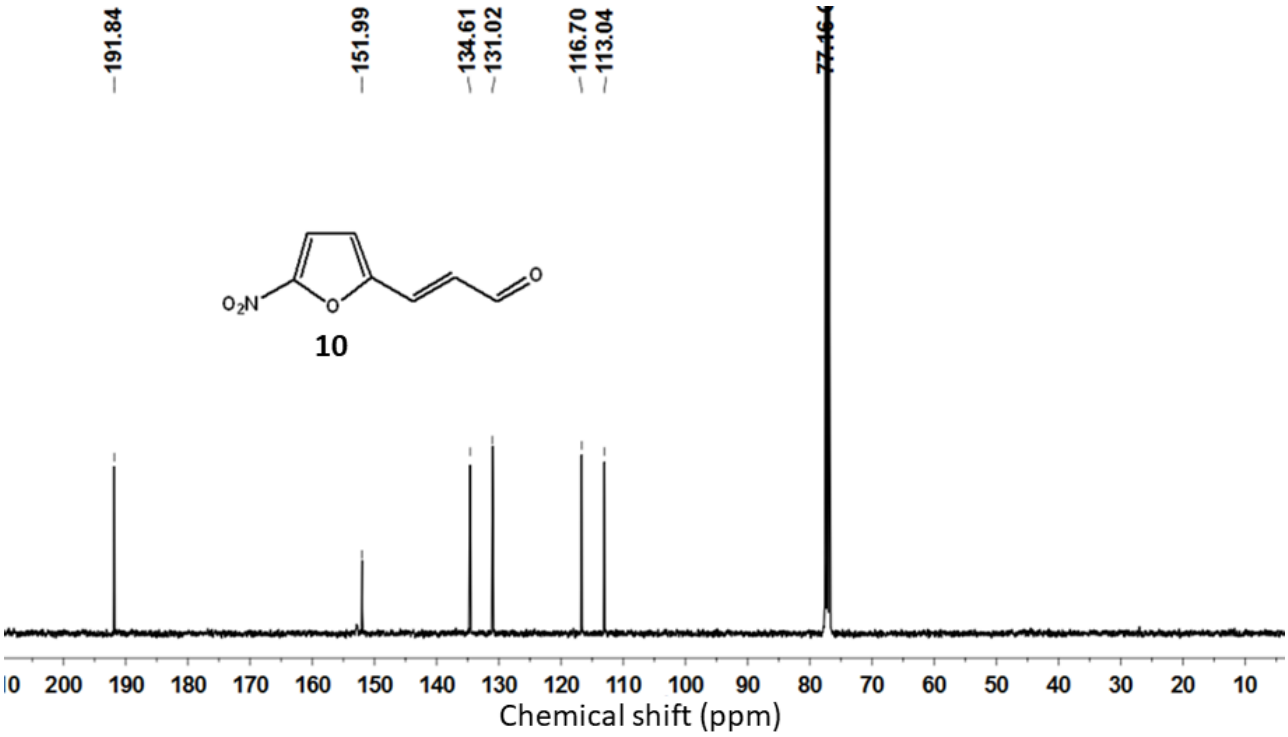

Fig. S17: ^{13}C NMR spectra of compound **10**.

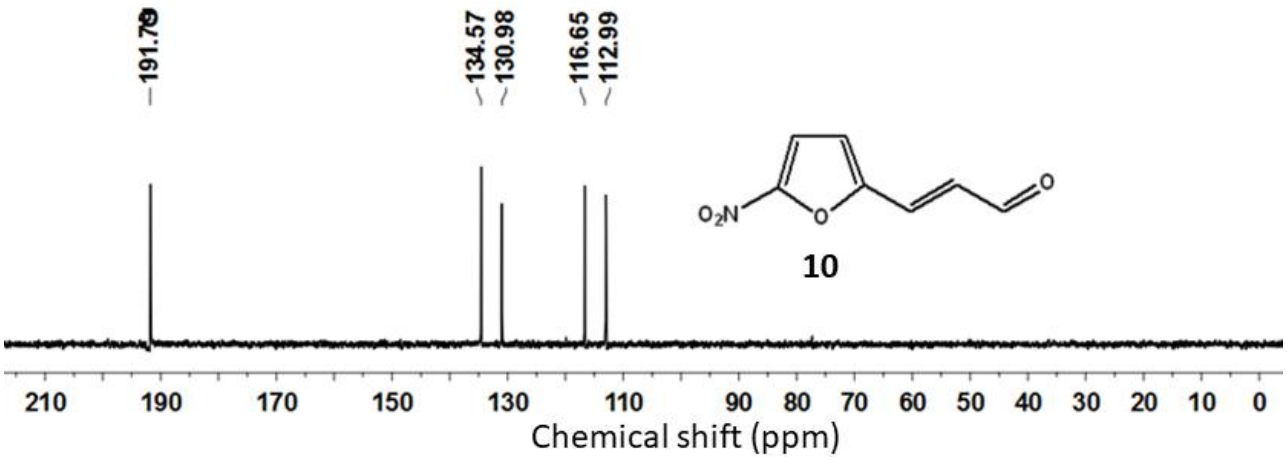

Fig. S18: ^{13}C DEPT spectra of compound **10**.

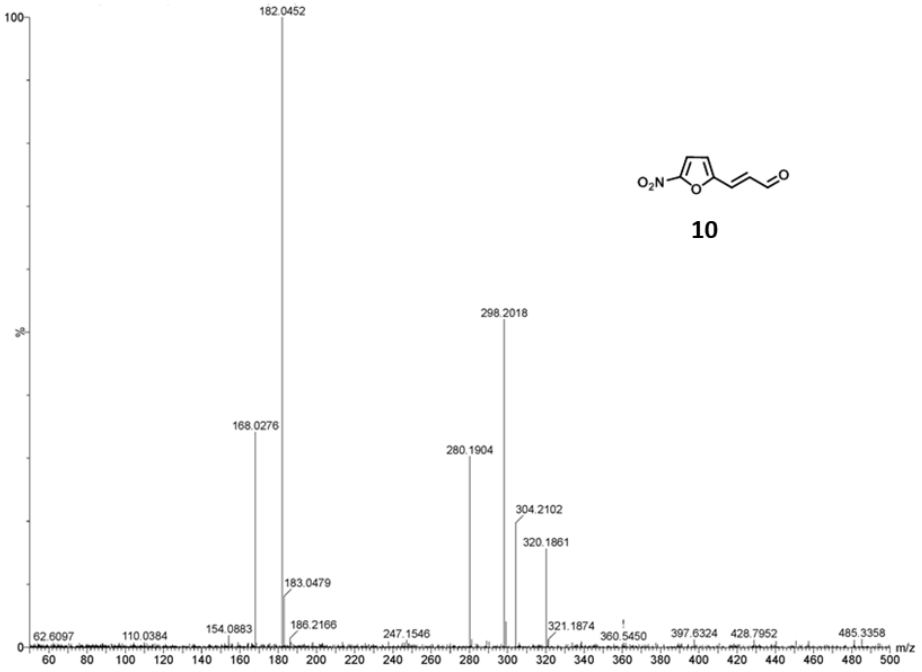

Fig. S19: HR-MS spectra of compound **10**.

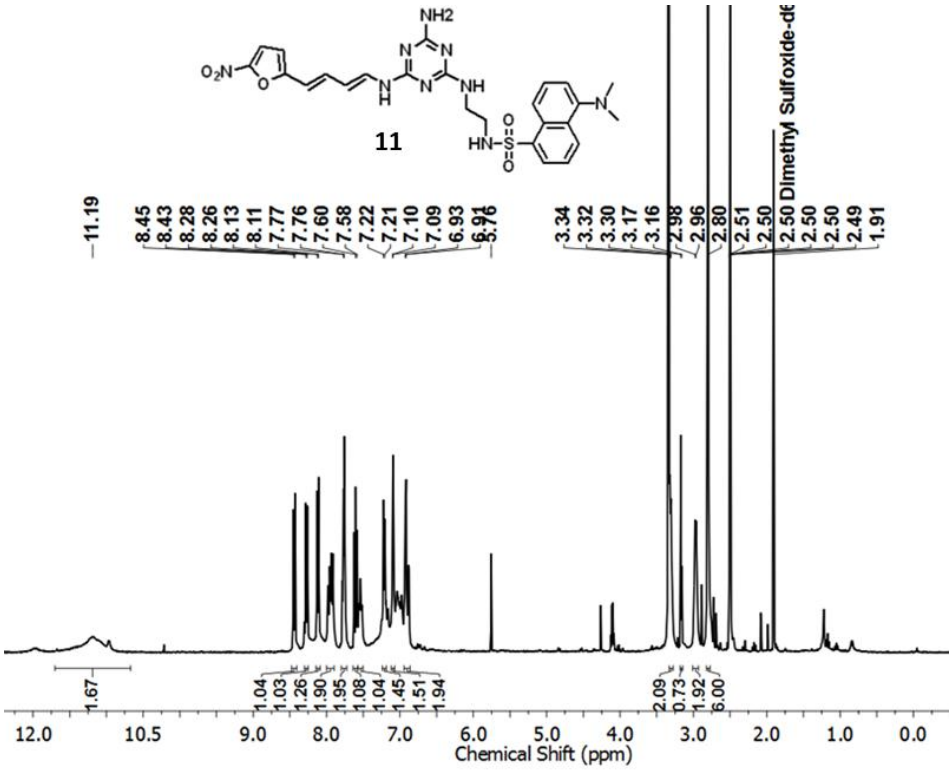

Fig. S20: ^{1}H NMR spectra of compound **11**.

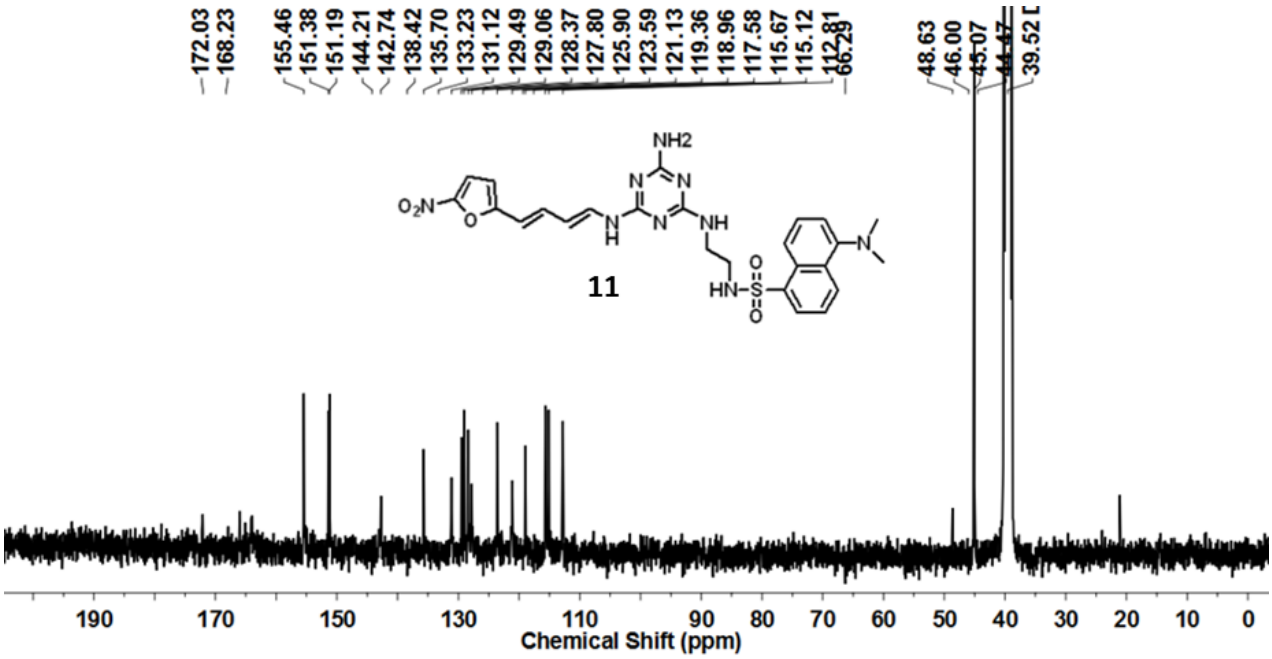

Fig. S21: ^{13}C NMR spectra of compound **11**.

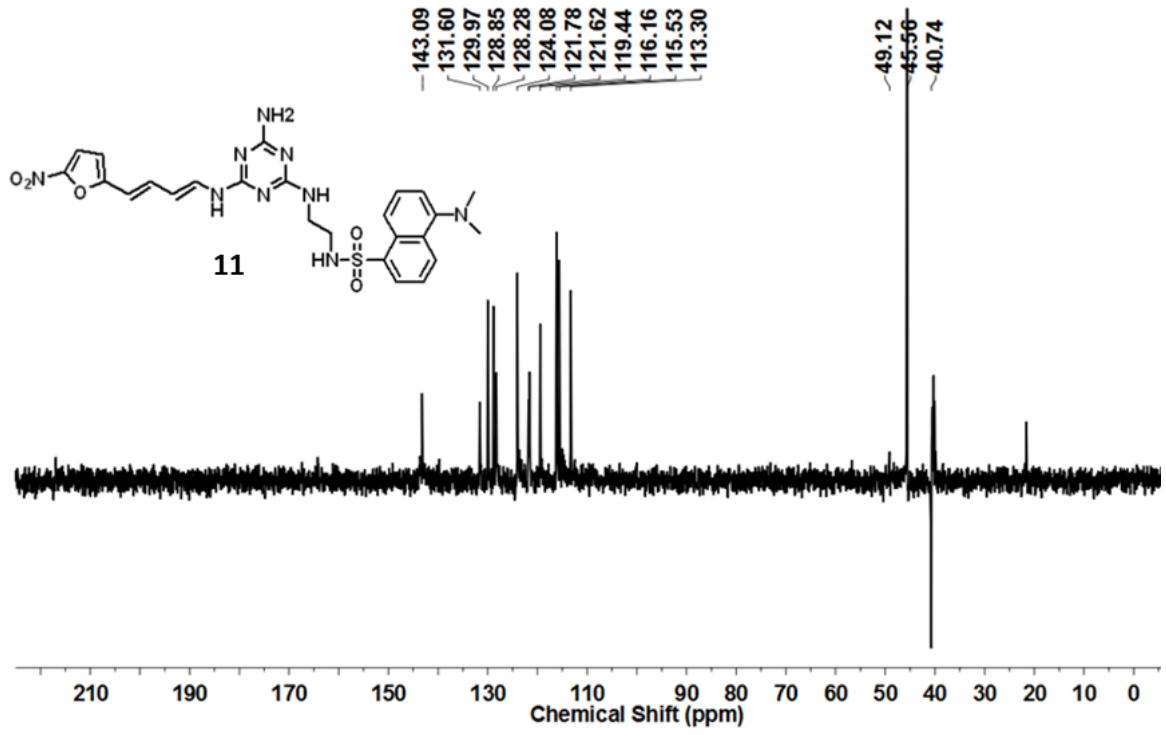

Fig. S22: ^{13}C DEPT spectra of compound **11**.

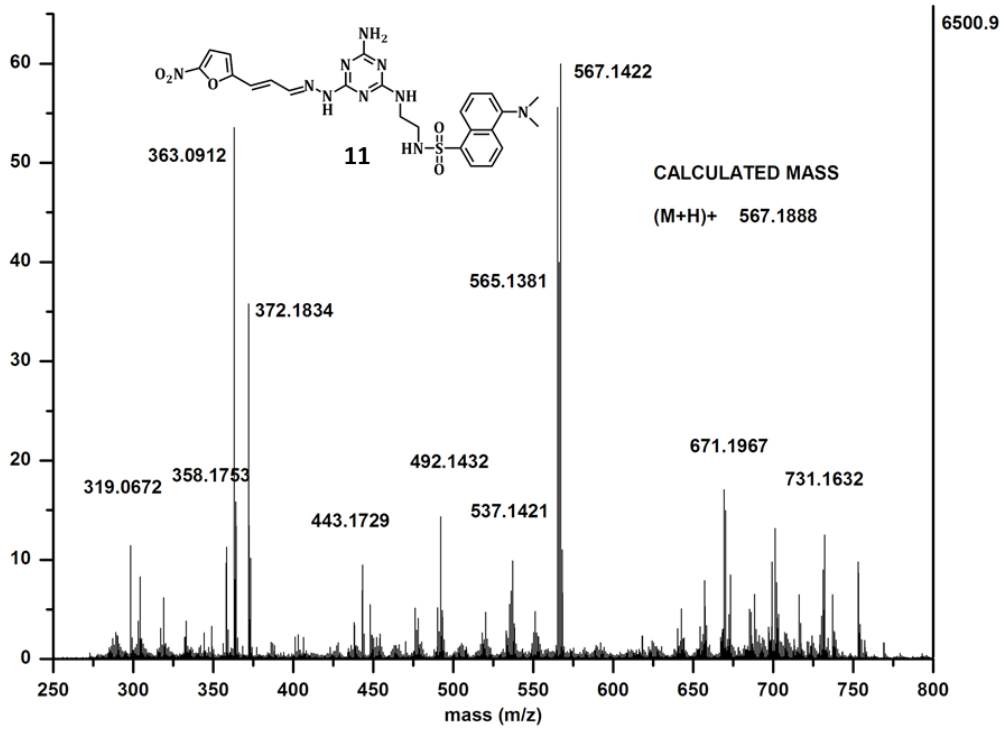

Fig. S23: HR-MS spectra of compound **11**.

3.5. Reference:

1. Anelli, T.; Sitia, R. Protein quality control in the early secretory pathway. *EMBO. J.* **2008**, *27*, 315-327.

2. Pizzo, P.; Pozzan, T. Mitochondria–endoplasmic reticulum choreography: structure and signaling dynamics. *Trends Cell Biol*. **2007**, *17*, 511-517.

3. Ma, Y.; Hendershot, L. M. ER chaperone functions during normal and stress conditions. *J. Chem. Neuroanat*. **2004**, *28*, 51-65.

4. Kim, I.; Xu, W.; Reed, J. C. Cell death and endoplasmic reticulum stress: disease relevance and therapeutic opportunities. *Nat. Rev. Drug Discov*. **2008**, *7*, 1013-1030.

5. Shoulders, M. D.; Ryno, L. M.; Genereux, J. C.; Moresco, J. J.; Tu, P. G.; Wu, C.; Yates, J. R.; Su, AI.; Kelly, J. W.; Wiseman, R. L. Stress-independent activation of XBP1s and/or ATF6 reveals three functionally diverse ER proteostasis environments. *Cell Rep.* **2013**, *3*, 1279-1292.

6. Hetz, C. The unfolded protein response: controlling cell fate decisions under ER stress and beyond. *Nat. Rev. Mol. Cell Biol.* **2012**, *13*, 89-102.

7. Raina, K.; Noblin, D. J.; Serebrenik, Y. V.; Adams, A.; Zhao, C.; Crews, C. M. Targeted protein destabilization reveals an estrogen-mediated ER stress response. *Nat. Chem. Biol*. **2014**, *10*, 957-962.

8. Maly, D. J.; Papa, F. R. Druggable sensors of the unfolded protein response. *Nat. Chem. Biol*. **2014**, *10*, 892-901.

9. Wang, M.; Kaufman, R. J. Protein misfolding in the endoplasmic reticulum as a conduit to human disease. *Nature* **2016**, *529*, 326-335.

10. Smith, M. H.; Ploegh, H. L.; Weissman, J. S. Road to ruin: targeting proteins for degradation in the endoplasmic reticulum. *Science*, **2011**, *334*, 1086-1090.

11. Wang. M.; Kaufman, R. *J.* The impact of the endoplasmic reticulum protein-folding environment on cancer development. *Nat. Rev. Cancer*. **2014**, *14*, 581-597.

12. Kim, I.; Xu, W.; Reed, J. C. Cell death and endoplasmic reticulum stress: disease relevance and therapeutic opportunities. *Nat. Rev. Drug Discov*. **2008**, *7*, 1013-1030.

13. Healy, S. J.; Gorman, A. M.; Mousavi-Shafaei, P.; Gupta, S.; Samali, A. Targeting the endoplasmic reticulum-stress response as an anticancer strategy. *Eur. J. Pharmacol*. **2009**, *625*, 234-246.

14. Hartgerink, J. D.; Beniash, E.; Stupp, S. I. Self-assembly and mineralization of peptide-amphiphile nanofibers. *Science* **2001**, *294*, 1684-1688.

15. Stupp, S. I.; LeBonheur, V. V.; Walker, K.; Li, L. S.; Huggins, K. E.; Keser, M.; Amstutz, A. Supramolecular materials: self-organized nanostructures. *Science* **1997**, *276*, 384-389.

16. Whitesides, G. M.; Mathias, J. P.; Seto, C. T. Molecular self-assembly and nanochemistry: a chemical strategy for the synthesis of nanostructures. *Science* **1991**, *254*, 1312-1319.

17. Lehn, J. M.; Lehn, J. M. Towards complex matter: supramolecular chemistry and self-organization. *Proc. Natl. Acad. Sci*. **2002**, *99*, 4763-4768.

18. Lehn, J. M. Supramolecular Chemistry—Scope and Perspectives Molecules, Supermolecules, and Molecular Devices (Nobel Lecture) *Angew. Chem. Int. Ed.* **1988**, *27*, 89-112.

19. Davey, R. J., Schroeder, S. L.; ter Horst, J. H. Nucleation of organic crystals—a molecular perspective. *Angew. Chem. Int. Ed.* **2013**, *52*, 2166-2179.

20. Boekhoven, J.; Stupp, S. I. 25th anniversary article: supramolecular materials for regenerative medicine. *Adv. Mater*. **2014**, *26*, 1642-1659.

21. Stupp, S. I. Self-assembly and biomaterials. *Nano Lett*. **2010**, *10*, 4783-4786.

22. Zhang, S. Fabrication of novel biomaterials through molecular self-assembly. *Nat. Biotechnol*. **2003**, *21*, 1171-1178.

23. Kim, D. S.; Chang, J.; Leem, S.; Park, J. S.; Thordarson P.; Sessler, J. L. Redox-and pH-Responsive Orthogonal Supramolecular Self-Assembly: An Ensemble Displaying Molecular Switching Characteristics. *J. Am. Chem. Soc.* **2015**, *137*, 16038-16042.

24. Ren, C.; Zhang, J.; Chen, M.; Yang, Z. Self-assembling small molecules for the detection of important analytes. *Chem. Soc. Rev*. **2014**, *43*, 7257-7266.

25. Schnaider, L.; Brahmachari, S.; Schmidt, N. W.; Mensa, B.; Shaham-Niv, S.; Bychenko, D.; Adler-Abramovich, L.; Shimon, L. J. W.; Kolusheva, S.; DeGrado W. F.; Gazit, E. Self-assembling dipeptide antibacterial nanostructures with membrane disrupting activity. *Nat. Commun*. **2017**, *8*, 1365.

26. Sengupta, P.; Basu, S.; Soni, S.; Pandey, A.; Roy, B.; Oh, M. S.; Chin, K. T.; Paraskar, A. S.; Sarangi, S.; Connor, Y.; Sabbisetti, V. S.; Kopparam, J.; Kulkarni, A.; Muto, K.; Amarasiriwardena, C.; Jayawardene, I.; Lupoli, N.; Dinulescu, D. M.; Bonventre, J. V.; Mashelkar, R. A.; Sengupta, S. Cholesterol-tethered platinum II-based supramolecular nanoparticle increases antitumor efficacy and reduces nephrotoxicity. *Proc. Natl. Acad. Sci. U S A.* **2012**, *109*, 11294-11299.

27. Zhao, H.; Feng, H.; Liu, D.; Liu, J.; Ji, N.; Chen, F.; Luo, X.; Zhou, Y.; Dan, H.; Zeng, X.; Li, J.; Sun, C.; Meng, J.; Ju, X.; Zhou, M.; Yang, H.; Li, L.; Liang, X.; Chu, L.; Jiang, L.;

He, Y.; Chen, Q. Self-assembling monomeric nucleoside molecular nanoparticles loaded with 5-FU enhancing therapeutic efficacy against oral cancer. *ACS Nano.* **2015**, *9*, 9638-9651.

28. Datta, S.; Misra, S. K.; Saha, M. L.; Lahiri, N.; Louie, J.; Pan, D.; *Stang, P. J.* Orthogonal self-assembly of an organoplatinum(II) metallacycle and cucurbit[8]uril that delivers curcumin to cancer cells. *Proc. Natl. Acad. Sci*. **2018**, *115*, 8087-8092.

29. Wang, J.; Fang, X.; Liang, W. Pegylated phospholipid micelles induce endoplasmic reticulum-dependent apoptosis of cancer cells but not normal cells. *ACS Nano.* **2012**, *6*, 5018-5030.

30. Pollock, S.; Antrobus, R.; Newton, L.; Kampa, B.; Rossa, J.; Latham, S.; Nichita, N. B.; Dwek, R. A.; Zitzmann, N. Uptake and trafficking of liposomes to the endoplasmic reticulum. *FASEB J*. **2010**, *24*, 1866-1878.

31. Sneh-Edri, H.; Likhtenshtein, D.; Stepensky, D. Intracellular targeting of PLGA nanoparticles encapsulating antigenic peptide to the endoplasmic reticulum of dendritic cells and its effect on antigen cross-presentation in vitro. *Mol. Pharm*. **2011**, *8*, 1266-1275.

32. Feng, Z.; Wang, H.; Wang, S.; Zhang, Q.; Zhang, X.; Rodal, A. A.; Xu, B. Enzymatic Assemblies Disrupt the Membrane and Target Endoplasmic Reticulum for Selective Cancer Cell Death. *J. Am. Chem. Soc.* **2018**, *140*, 9566-9573.

33. Phillips, M. J.; Voeltz, G. K. Structure and function of ER membrane contact sites with other organelles. *Nat. Rev. Mol. Cell. Biol*. **2016**, *17*, 69-82.

34. Liu, Y.; Lok, C. N.; Ko, B. C.; Shum, T.Y.; Wong, M. K.; Che, C. M. Subcellular localization of a fluorescent artemisinin derivative to endoplasmic reticulum. *Org Lett*. **2010**, *12*, 1420-1423.

35. Meinig, J. M.; Fu, L.; Peterson, B. R. Synthesis of fluorophores that target small molecules to the endoplasmic reticulum of living mammalian cells. *Angew. Chem. Int. Ed*. **2015**, *54*, 9696-9835.

36. Wang, Q.; Shinkre, B. A.; Lee, J. G.; Weniger, M. A.; Liu, Y.; Chen, W.; Wiestner, A.; Trenkle, W. C.; Ye, Y. The ERAD inhibitor Eeyarestatin I is a bifunctional compound with a membrane-binding domain and a p97/VCP inhibitory group. *PLoS One*. **2010**, *5*, e15479.

37. Roy, B.; Bairi, P.; Nandi, A. K. Supramolecular assembly of melamine and its derivatives: nanostructures to functional materials. *RSC Advances* **2014**, *4*, 1708-1734.

38. Avakyan, N.; Greschner, A. A.; Aldaye, F.; Serpell, C.J.; Toader, V.; Petitjean, A.; Sleiman, H. F. Reprogramming the assembly of unmodified DNA with a small molecule. *Nat. Chem*. **2016**, *8*, 368-376.

39. Ma, M.; Bong, D. Determinants of cyanuric acid and melamine assembly in water. *Langmuir*. **2011**, *27*, 8841-8853.

40. Seto, C.T.; Whitesides, G.M. Molecular self-assembly through hydrogen bonding: supramolecular aggregates based on the cyanuric acid-melamine lattice. *J. Am. Chem. Soc.* **1993**, *115*, 905-916.

41. Zeng, Y.; Pratumyot, Y.; Piao, X.; Bong, D. Discrete assembly of synthetic peptide–DNA triplex structures from polyvalent melamine–thymine bifacial recognition. *J. Am. Chem. Soc.* **2011**, *134*, 832-835.

42. Banerjee, R.; Pace, N. J.; Brown, D. R.; Weerapana, E. 1, 3, 5-Triazine as a modular scaffold for covalent inhibitors with streamlined target identification. *J. Am. Chem. Soc.* **2013**, *135*, 2497-2500.

43. Baliani, A.; Bueno, G. J.; Stewart, M. L.; Yardley, V.; Brun, R.; Barrett, M. P.; Gilbert, I. H. Design and synthesis of a series of melamine-based nitroheterocycles with activity against trypanosomatid parasites. *J. Med. Chem.* **2005**, *48*, 5570-5579.

44 Timmerman, P., Weidmann, J.L., Jolliffe, K.A., Prins, L.J., Reinhoudt, D.N., Shinkai, S., Frish, L.; Cohen, Y. NMR diffusion spectroscopy for the characterization of multicomponent hydrogen-bonded assemblies in solution. *J. Chem. Soc., Perkin Trans 2*. **2002**, *10*, 2077-2089.

45. Doherty, G. J.; McMahon. H. T. Mechanisms of endocytosis. *Annu. Rev. Biochem*. **2009**, *78*, 857-902.

46. Rowland, A. A.; Voeltz, G. K. Endoplasmic reticulum–mitochondria contacts: function of the junction. *Nat. Rev. Mol. Cell Biol*. **2012**, *13*, 607-625.

47. Nishitoh, H. CHOP is a multifunctional transcription factor in the ER stress response. *J. Biochem*. **2012**, *15*, 217-219.

48. Oyadomari, S.; Mori, M. Roles of CHOP/GADD153 in endoplasmic reticulum stress. *Cell Death Differ*. **2004**, *11*, 381-389.

49. Kuo, L. J.; Yang, L. X. γ-H2AX-a novel biomarker for DNA double-strand breaks. *In vivo* **2008**, *22*, 305-309.

50. Shieh, S.Y.; Ikeda, M., Taya, Y.; Prives, C. DNA damage-induced phosphorylation of p53 alleviates inhibition by MDM2. *Cell* **1997**, *91*, 325-334.

51. Zeeshan, H. M.; Lee, G. H.; Kim, H. R.; Chae, H. J. Endoplasmic reticulum stress and associated ROS. *Int. J. Mol. Sci*. **2016**, *17*, 327.

52. Kang, M. A.; So, E. Y.; Simons, A. L.; Spitz, D. R.; Ouchi, T. DNA damage induces reactive oxygen species generation through the H2AX-Nox1/Rac1 pathway. *Cell Death*. Dis. **2012**, *3*, e249.

53. Roy, A.; Xu. D.; Poisson. J.; Zhang, Y. A protocol for computer-based protein structure and function prediction. *J. Vis. Exp.* **2011**, *3*, e3259.

54. Ogata. M.; Saito, A.; Morikawa, K; Kondo, S.; Kanemoto, S.; Murakami, T.; Taniguchi, M.; Tanii, I.; Yoshinaga, K.; Shiosaka, S.; Hammarback, J. A.; Urano, F.; Imaizumi, K. Autophagy is activated for cell survival after endoplasmic reticulum stress. *Mol. Cell Biol.* **2006**, *26*, 9220-9231.

55. Sica, V.; Galluzzi, L.; Bravo-San Pedro, J. M.; Izzo, V.; Maiuri, M. C.; Kroemer, G. Organelle-specific initiation of autophagy. *Mol. Cell*. **2015**, *59*, 522-539.

56. Cao, Y.; Klionsky D. J. Physiological functions of Atg6/Beclin 1: a unique autophagy-related protein. *Cell Res.* **2007**, *17*, 839-849.

57. Tanida, I.; Ueno, T.; Kominami, E. LC3 and Autophagy. *Methods Mol. Biol.* **2008**, *445*, 77-88.

58. Kimura, T.; Takabatake, Y.; Takahashi, A.; Isaka, Y. Chloroquine in cancer therapy: a double-edged sword of autophagy. *Cancer Res.* **2012**, *73*, 3-7.

59. Sasaki, K.; Tsuno, N.H.; Sunami, E.; Tsurita, G.; Kawai, K.; Okaji, Y.; Nishikawa, T.; Shuno, Y.; Hongo, K.; Hiyoshi, M.; Kaneko, M.; Sasaki, K.; Tsuno, N.H.; Sunami, E.; Tsurita, G.; Kawai, K.; Okaji, Y.; Nishikawa, T.; Shuno, Y.; Hongo, K.; Hiyoshi, M; Kaneko,

M. Chloroquine potentiates the anti-cancer effect of 5-fluorouracil on colon cancer cells. *BMC cancer* **2010**, *10*, 370.

60. Mallick, A.; More, P.; Ghosh, S.; Chippalkatti, P.; Chopade, B. A.; Lahiri, M.; Basu, S. Dual drug conjugated nanoparticle for simultaneous targeting of mitochondria and nucleus in cancer cells. *ACS Appl. Mater. Interfaces* **2015**, ***7***, 7584-7598.

61. Mallick, A.; More, P.; Syed, M. M. K.; Basu, S. Nanoparticle-mediated mitochondrial damage induces apoptosis in cancer. *ACS Appl. Mater. Interfaces* **2016**, *8*, 13218-13231.

Chapter 4

Nanoparticle Mediated ER Stress in Cancer Cells through Unfolded Protein Response

Manuscript under revision

4.1. Introduction:

Endoplasmic reticulum (ER) is an important organelle and functions in folding and assembling of cellular proteins, synthesis of lipids and storage of free calcium, which are all dependent on the ER internal homeostasis.[1] ER stress also known as unfolded protein response (UPR),[2-4] a well-studied issue in cell biology, refers to an important cellular self-protection mechanism which can be activated to counteract the stressed situation when in the condition of overloading unfolded proteins or even from direct ER damage.[5] ER stress usually happens for a short-term with provoking a series of transcriptional activities for cell survival, but prolonged ER stress activates apoptotic cell death pathways.[6-7] As a result, impairing ER functions in cancer cells has materialized as novel next-generation anti-cancer strategy.[8] However, exceedingly selective targeting of ER inside cancer cell milieu remains a foremost challenge and hence less explored.[9-11] To address this, we have developed lipidic nanoscale material which has prospective to selectively home into cancer cells.

There are many nanocarrier are developed to deliver small molecule drugs, genes, siRNAs [12] and proteins successfully into tumor tissues through passive and active targeting. Although targeting organelles by nanocarrier remains largely unexplored. Only, few groups developed lipid-based micelle, liposomes and polymeric nanoparticle for targeting ER.[13-16] Very recently, Feng et. al. engineered peptide-based enzyme-instructed crescent shaped supramolecular self-assembly for selective targeting of ER in cancer cells.[17] The unfolded protein response (UPR) acts as adaptive responses, induces the expression of ER-resident chaperones, such as glucoseregulated protein (GRP)-78 and (GRP)-94.[18] Thus targeting ER-resident chaperon GRP-94 is an important strategy to induce ER stress.[19-21] However, strategies for selective targeting of ER are critical task due to ER membrane overlap between other important organelles such as mitochondria, nucleus and endosome.[10] Recently we have developed supramolecular self-assembly of triazine based small molecule which can concurently target ER and nucleus in cancer cells.

To address the leading important issues, herein we have engineered two types of lipidic nanoparticles (NPs) in which one lipidic nanoparticle comprised of Tosylated napthalimide dodecyl conjugate (Tos-Nap-Docecyl conjugate) and 17AAG (HSP 90 inhibitor), similarly other lipidic nanoparticle comprised of Cholesterol napthalimide conjugated (Chol-Nap conjugate) and 17AAG(HSP-90 inhibitor). Interestingly the Chol-Nap-17AAGnps were

localized into lysosome, whereas the Tos-Nap-17AAGnps were localized in endoplasmic reticulum (ER) by caveloae mediated endocytosis within 1 h and homed within 24h in ER. These Tos-Nap-17AAGnps induced up-regulation of ER chaperon GRP94 and C/EBP homologous protein CHOP/GADD153. This nanoparticle-mediated ER stress triggered the nucleus damage leading to increased expression of γH2AX and p53. Interestingly, these Tos-Nap-17AAGnps exhibited improved effects in cervical cancer cells (HeLa) with respect to free 17AAG. These nanoparticles could be used as a platform to deliver HSP90 inhibitor into ER of cancer cells to impart ER stress which leads to programmed cell death.

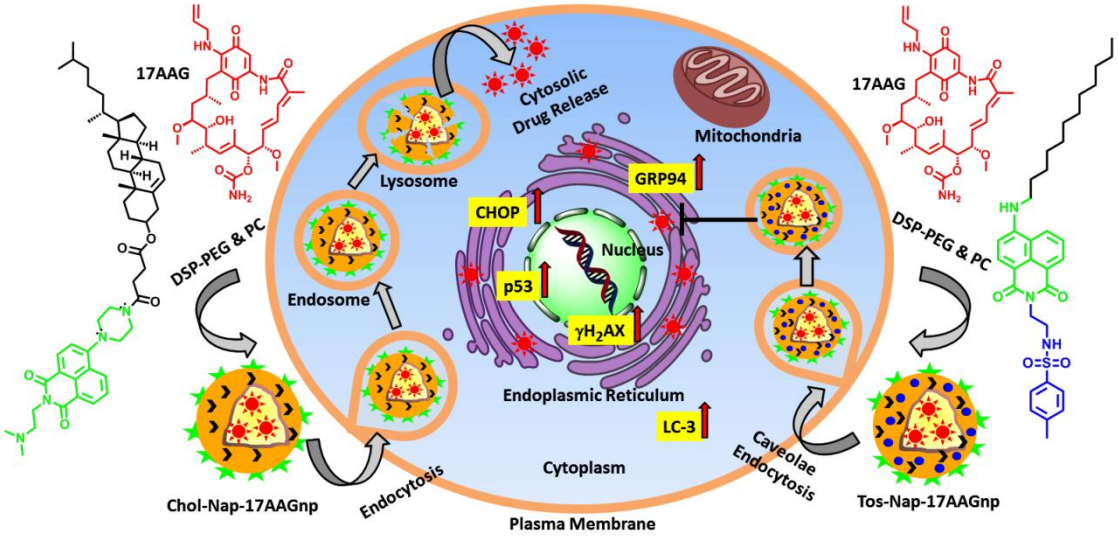

Scheme 1: Schematic representation of ER targeting lipidic nanoparticle

4.2. Result and Discussion:

4.2.1. Engineering of ER targeting Nanoparticles: To target ER resident chaperon [22] GRP-94 specifically we have designed two types of nanoparticles Chol-Nap-17AAGnp and Tos-Nap-17AAGnp (Scheme 1). These two types of nanoparticle have common fluorophores 1,8-naphthalimide scaffolds due to their outstanding photophysical characteristics and easy preparation. The hydrophobic parts of these nanoparticles are different in one nanoparticle contains cholesterol and other contains dodecyl moiety. The ER targeting moiety sulfonamide group was attached in Tos-Nap-17AAGnp, whereas other nanoparticle Chol-Nap-17AAGnp has no ER targeting moiety. Synthetic scheme of compound Tosylated Napthalimide dodecyl conjugate and Cholesterol Napthalimide conjugate is shown in Figure 1. First the sulfonamide group was appended with 4-Bromo-1,8-napthalimide through condensation

reaction in ethanol at refluxing condition for 6 h to obtained compound 3. Finally the dodecyl moiety was tagged with napthalimide core through the reaction of compound 3 and dodecyl amine in presence of 2-methoxyethanol as a solvent at 90 ^{o}C for 12 h to obtain Tosylated Napthalimide deodecyl conjugate (compound 5).

Similarly, N,N`ethylenediamine was tagged with napthalimide through condensation reaction in ethanol at 80 ^{o}C for 6 h to obtained compound 11. The piperazine group was attached with napthalimide core of compound 11 through the reaction between compound 11 and piperazine in presence of 2-Methoxyethanol at 90 ^{o}C for 6 h to obtain compound 13. Finally the compound 13 was tagged with cholesterol through the reaction of cholesterol succinic acid and compound 13 to get Cholesterol Napthalimide conjugate (compound 14). We characterized all the compounds and intermediates by ^{1}H, ^{13}C NMR, DEPT spectroscopy and Mass-spectroscopy (HR-MS). These conjugates were used to make two types of nanoparticles using lipid-hydration technique with DSPE-PEG and PC (1:2). We have chosen 17AAG drug for targeting ER resident chaperon GRP-94 for ER stress, encapsulated in these two types of nanoparticles to make Tos-Nap-17AAGnp and Chol-Nap-17AAGnp respectively. To ensure prolonged blood circulation of this nanoparticle we have taken DSPE-PEG and were made lipidic nanoparticle with 200nm size. The size and shape of the nanoparticles is one of the key factors to be successfully accumulated into the tumor tissues by leaky vasculature which is known as enhanced permeability and retention (EPR) effect. The mean hydrodynamic diameter of the Tos-Nap-17AAGnp & Chol-Nap-17AAGnp were determined to be 157.87 ± 0.5 nm and 183.74 ± 0.5 nm (Figure 2 a,b) by dynamic light scattering (DLS). Further, we visualized the nanoparticles in order to understand the shape of the nanoparticle by electron microscopy. The FESEM image (Figure 2) clearly showed that Tos-Nap-17AAGnp & Chol-Nap-17AAGnp were spherical in shape and size having <200 nm in diameter. The shape and hight of these nanoparticles were also confirmed by AFM images (Figure 2 a,b). We evaluated dual drug loading in the nanoparticle via UV-vis at λ_{max} = 412 nm of Chol-Nap conjugate , λ_{max} = 455 nm of Tos-Nap-Dodecyl conjugate (Figure 3 a,c) and λ_{max}= 331 nm of 17AAG. The loading of Chol-Nap conjugate and 17AAG in Chol-Nap-17AAGnp were 1214.41 µg/mL and 1765.16 µg/mL respectively (Figure 3 d). Similarly, the loading of Tos-Nap-Dodecyl conjugate and 17AAG in Tos-Nap-17AAGnp were 2066.5 µM and 2357.12 µM respectively (Figure 3b). Finally, we evaluated the fluorescence emission spectra of Chol-Nap conjugate and Tos-Nap conjugate, and found that 568nm and 533nm peaks respectively (Figure 3a, c).

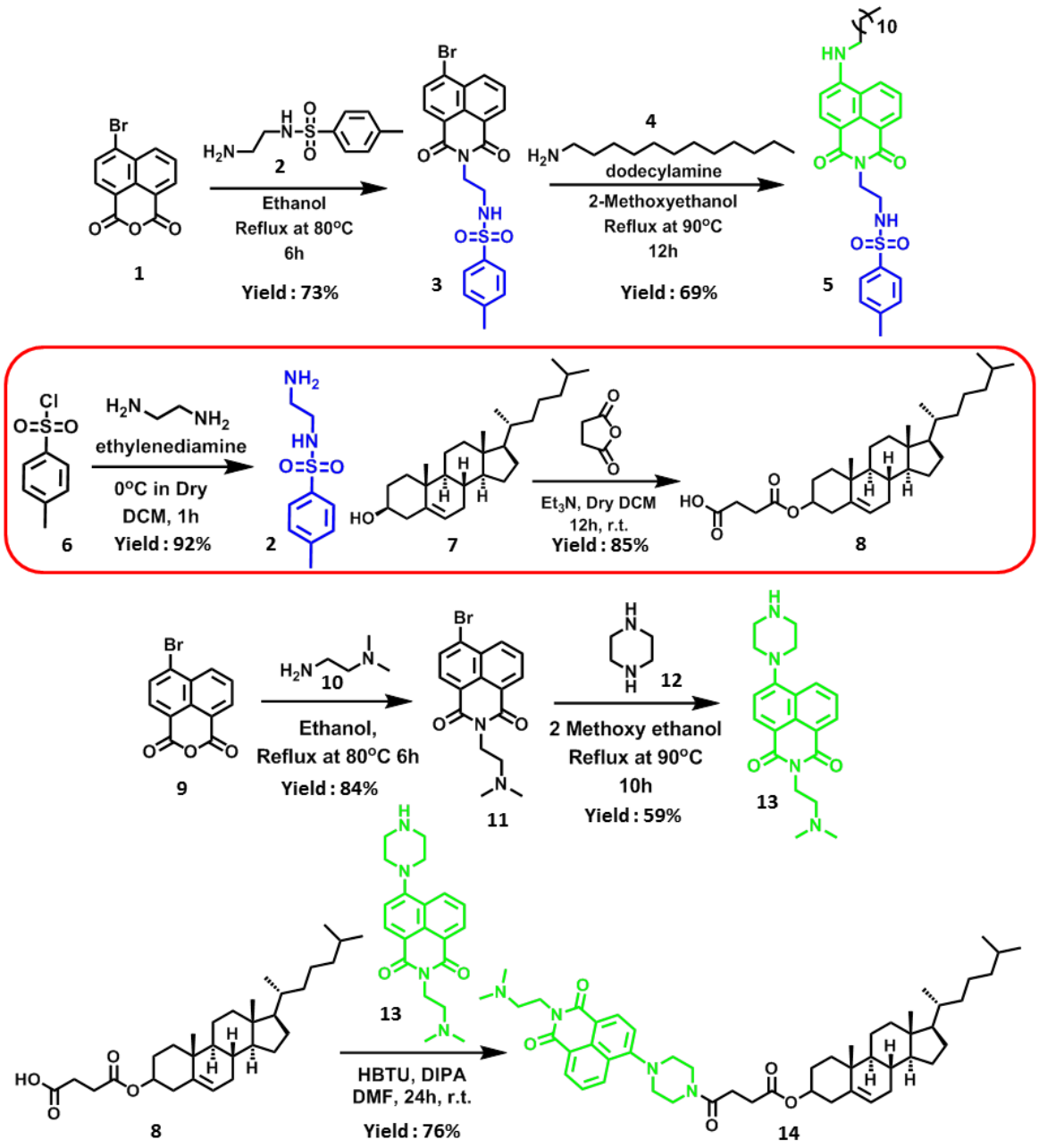

Figure 1: Synthesis of (a). Tosylated-napthalimide dodecyl conjugate, (b). Cholesterol-napthalimide conjugate.

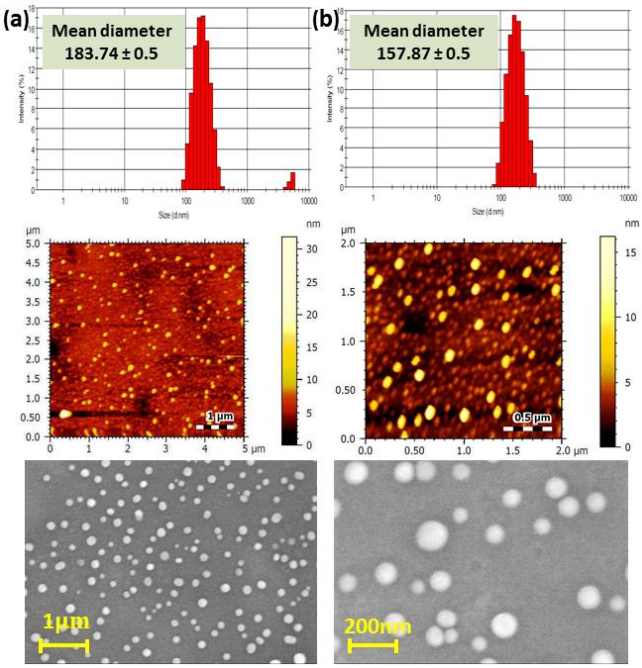

Figure 2: Characterization of lipidic nanoparticle DLS, AFM & FESEM (a) Tos-Nap-17AAGnp, (b). Chol-Nap-17AAGnp.

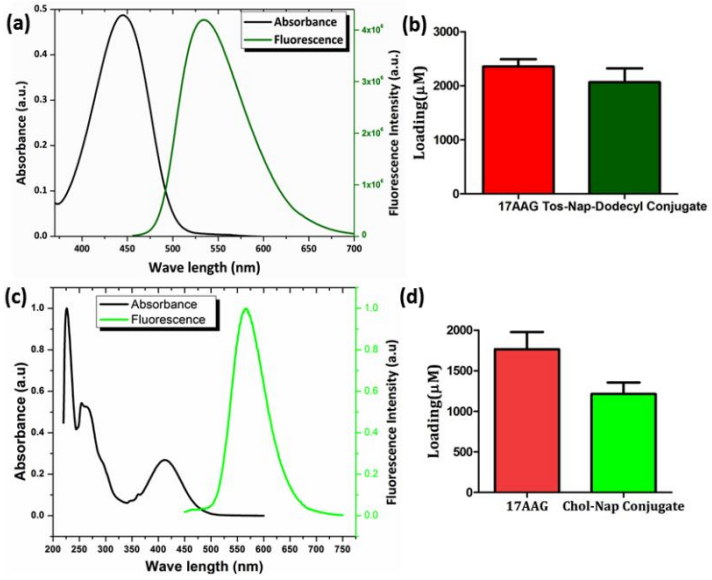

Figure 3: (a) Excitation & Emission spectra of Tos-Nap-17AAGnp, (b) Loading of 17AAG & Tos-Nap-Dodecyl conjugate in lipidic nanoparticle, (c). Excitation & Emission spectra of Chol-Nap-17AAGnp, (d). Loading of 17AAG & Chol-Nap conjugate in lipidic nanoparticle.

4.2.2. Cellular Internalization and ER Homing. In spite of the advancement of nanovectors to deliver the chemotherapeutic drugs to different organelle, the actual mechanism of endoplasmic reticulum homing of nanovectors is not clearly understood.[23-29] To address this, we have assessed the cellular uptake mechanism of two types of lipidic nanoparticles Chol-Nap-17AAGnp and Tos-Nap-17AAGnp in HeLa cervical cancer cells using confocal microscopy. First HeLa cells were treated with two different types of nanoparticle in a time dependent manner (1 h, 3 h, 6 h and 24 h) and co-stained the endoplasmic reticulum with ER-tracker red followed by visualization by CLSM. The live cells images revealed that the Chol-Nap-17AAGnp showed minimal co-localization in ER, also validated by volume co-localization by only 9.78%, 18.06%, 31.78% and 29.32% after 1 h, 3 h, 6 h and 24 h respectively (Figure 5 & Table 2). Whereas the Tos-Nap-17AAGnp co-localized in ER within 1 h shows percent volume co-localization 48.55% and homing into ER with time progress 3 h, 6 h and 24 h volume co-localization 42.24%, 65.13% and 59.24% respectively (Figure 4 & Table 1).

We further evaluated the localization of these two types of nanoparticle in lysosome of HeLa cells were stained with lysotracker read followed by the two types of nanoparticles Chol-Nap-17AAGnp and Tos-Nap-17AAGnp were treated individually in a time dependent manner and visualized by CLSM. The confocal images revealed that green fluorescent compound Chol-Nap-17AAGnp localized into red fluorescently labeled lysosome of HeLa cells in 24h. The confocal image based quantification by Pearson's and Mender's coefficients shows that Chol-Nap-17AAGnp produced 24.54% and 56.05% volume co-localization in lysosome at 1h, and 24h respectively (Figure 7a, Table 5). Similarly, the HeLa cells were treated with Tos-Nap-17AAGnp in time dependent manner (1h and 24h) and co-stained lysosome by lysotracker red and visualized in confocal microscopy. The confocal images showed that marginal overlap of green and red fluorescence signals to yield yellow regions, which also validated by volume co-localization by only 11.08% and 21.56% in 1h and 24h respectively (Figure 6a, Table 3). We also assessed the localization of these nanoparticles Chol-Nap-17AAGnp and Tos-Nap-17AAGnp in mitochondria. Mitochondria of Hela cells were stained with Mito-Tracker Red dye and co-localization of individual nanoparticles were visualized at 1h and 24h post incubation. The confocal images showed marginal overlap of green and red fluorescence signals to yield yellow regions in both the nanoparticles treatment. which validated by volume co-localization 14.03% and 25.67% after 1h and 24h respectively for Chol-Nap-17AAGnp (Figure 7b, Table 6) similarly volume co-localization 24.55% and

35.32% in 1h and 24h respectively for Tos-Nap-17AAGnp (Figure 6b, Table 4). These confocal microscopy images and quantification evidently exhibited that Tos-Nap-17AAGnp were homed into ER of HeLa cells within 1h.

We further evaluated the mechanism of cellular internalization of Tos-Nap-17AAGnp through endocytosis. Cells can engulf molecules/nanoparticles in different endocytosis mechanism[30] including clathrin, caveolin mediated endocytosis and macropinocytsis. To understand the cellular uptake mechanism, we pre-treated the HeLa cells with individual endocytosis inhibitors like genistein, chloropromazine and amiloride followed by the incubation with Tos-Nap-17AAGnp for 1h and co-stained ER with ER-Tracker Red dye. We visualized the live cells under confocal microscopy. Interestingly, amiloride and chlorpromazine pre-treated cells showed no significant change in ER homing of Tos-Nap-17AAGnp compared to control no-inhibitor treated cells evident from the merged yellow regions generated from the co-localization of green fluorescent Tos-Nap-17AAGnp and red fluorescent signal from ER-Tracker Red (Figure 8). However, a remarkably significant reduction of Tos-Nap-17AAGnp localization in ER was visualized in genistein pre-treated cells. (Fluorescence microscopy-based quantification also supported the image data by showing 60.24% and 44.98% volume co-localization in amiloride and chlorpromazine treated cells respectively compared to 55.56% co-localization for control cells. However, genistein treated cells showed only 24.61% volume co-localization of Tos-Nap-17AAGnp in ER (Table 7). These confocal microscopy images and quantification clearly confirmed that amiloride and chlorpromazine-mediated inhibition of macropinocytosis and clathrin-based endocytosis respectively were not instrumental in ER-NP uptake in HeLa cells. On the other hand, genestein mediated inhibition of caveolin-based endocytosis was the operative pathway for the cellular internalization of Tos-Nap-17AAGnp followed by ER homing.

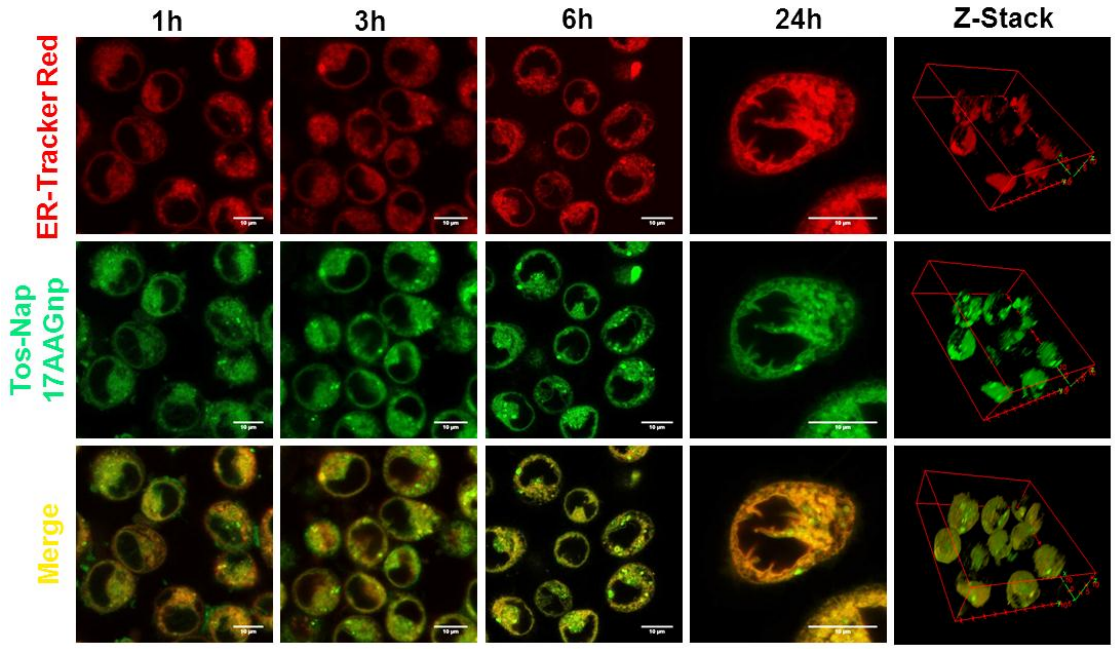

Figure 4: Confocal laser scanning microscopy (CLSM) images of lipdic nanoparticle Tos-Nap-17AAGnp in HeLa cells in different time points (1 h, 3h, 6 h and 24 h). ER is stained by ER-Tracker Red. Scale bar = 10 μm.

ER Imaging Tos-Nap-17AAGnp		1h	3h	6h	24h
Image Channels		C2 (green) C3 (red)	C2 (green) C3 (red)	C2 (green) C3 (red)	C2 (green) C3 (red)
Pearsons' Correlation Coefficient	R	0.6347	0.9724	0.8995	0.9081
Manders Coefficients	M1 (fraction of C2 overlapping C3)	0.9078	0.9304	0.9683	0.9706
	M2 (fraction of C3 overlapping C2)	0.9390	0.9602	0.9615	0.9927
Percent volume colocalized		*48.55%*	*42.24%*	*65.13%*	*59.24%*

Table 1: Quantification of co-localization of Tos-Nap-17AAGnp in ER of HeLa cells at 1 h, 3h, 6h & 24h from CLSM.

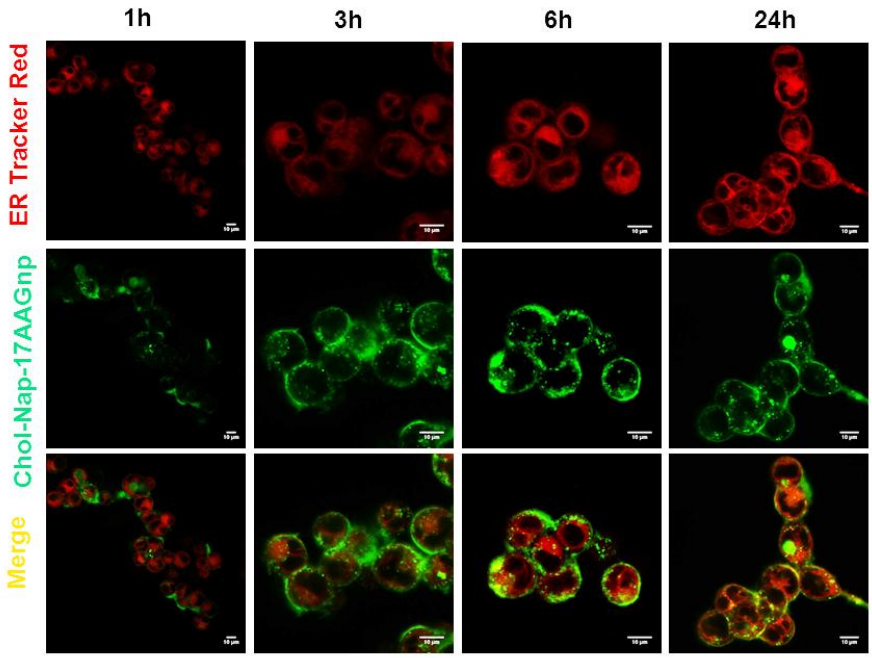

Figure 5: Confocal laser scanning microscopy (CLSM) images of lipdic nanoparticle Chol-Nap-17AAGnp in HeLa cells in different time points (1 h, 3h, 6 h and 24 h). ER is stained by ER-Tracker Red. Scale bar = 10 μm.

ER Imaging Chol-Nap-17AAGnp		1h	3h	6h	24h
Image Channels		C2 (green) C3 (red)	C2 (green) C3 (red)	C2 (green) C3 (red)	C2 (green) C3 (red)
Pearsons' Correlation Coefficient	R	0.5482	0.6103	0.6704	0.6173
Manders Coefficients	M1 (fraction of C2 overlapping C3)	0.7035	0.8001	0.8341	0.7372
	M2 (fraction of C3 overlapping C2)	0.8332	0.8645	0.8987	0.8325
Percent volume colocalized		*9.78%*	*18.06%*	*31.78%*	*29.32%*

Table 2: Quantification of co-localization of Chol-Nap-17AAGnp in ER of HeLa cells at 1 h, 3h, 6h & 24h from CLSM.

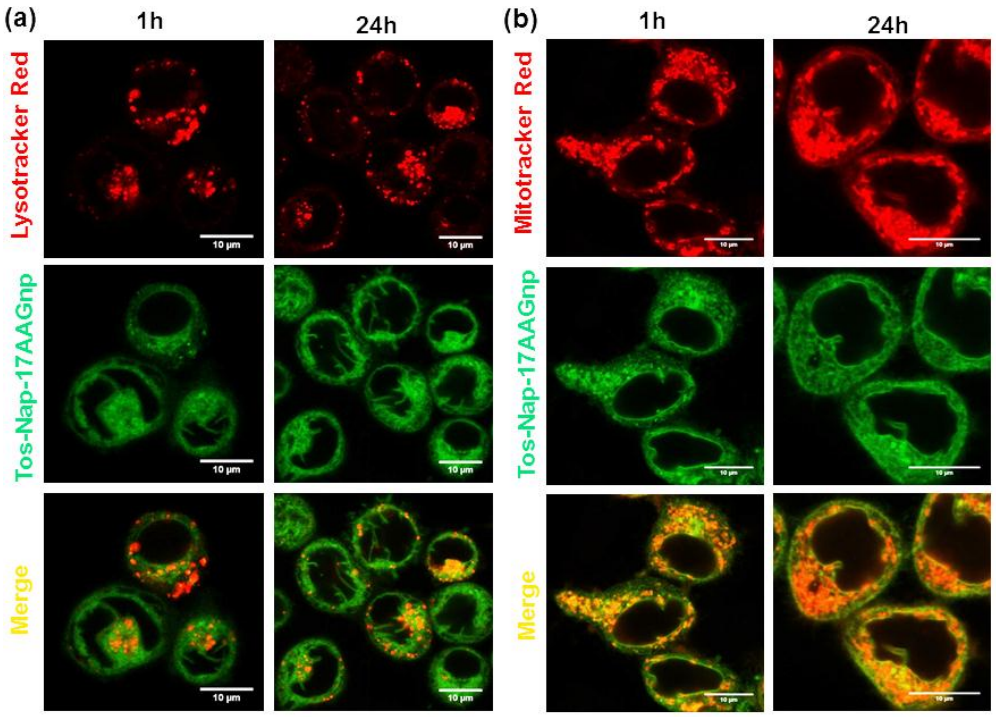

Figure 6: CLSM images of Tos-Nap-17AAGnp in HeLa cells at 1h & 24 h (a) Lysosome were stained by Lysotracker Red, (b). Mitochondria were stained with MitoTracker Deep Red dye. Scale bar = 10 μm.

Lysosome Imaging Tos-Nap-17AAGnp		1h	24h
Image Channels		C2 (green) C3 (red)	C2 (green) C3 (red)
Pearsons' Correlation Coefficient	R	0.2128	0.3865
Manders Coefficients	M1 (fraction of C2 overlapping C3)	0.8607	0.8695
	M2 (fraction of C3 overlapping C2)	0.7624	0.9087
Percent volume colocalized		*11.08%*	*21.56%*

Table 3: Quantification of co-localization of Tos-Nap-17AAGnp into lysosomes in HeLa cells at 1h & 24h from CLSM.

Mitochondria Imaging Tos-Nap-17AAGnp		1h	24h
Image Channels		C2 (green) C3 (red)	C2 (green) C3 (red)
Pearsons' Correlation Coefficient	R	0.6820	0.7700
Manders Coefficients	M1 (fraction of C2 overlapping C3)	0.8949	0.9166
	M2 (fraction of C3 overlapping C2)	0.9170	0.9672
Percent volume colocalized		24.55%	35.32%

Table 4: Quantification of co-localization of Tos-Nap-17AAGnp into Mitochondria in HeLa cells at 1h & 24 h from CLSM.

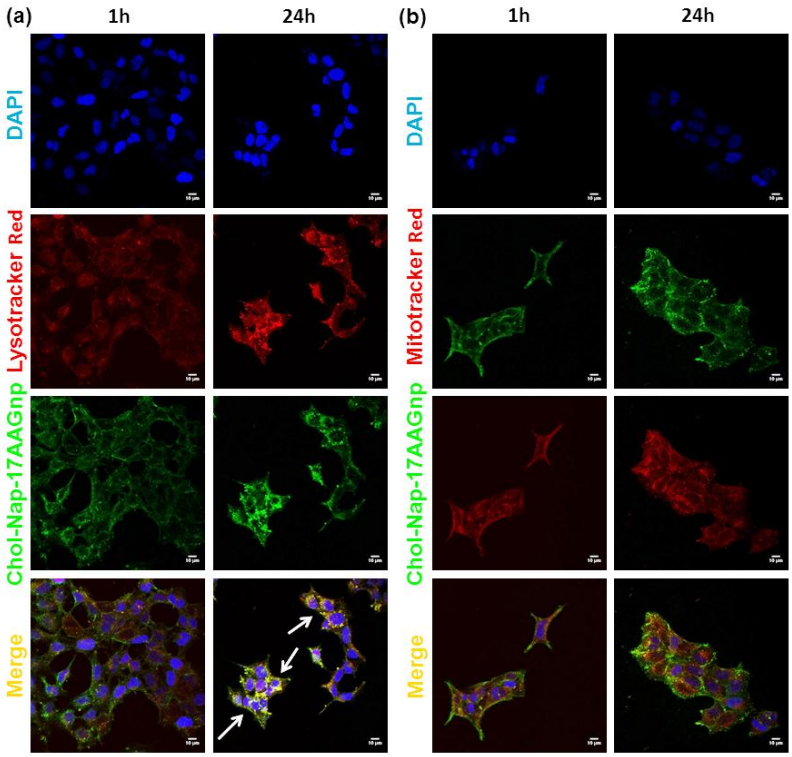

Figure 7: CLSM images of Chol-Nap-17AAGnp in HeLa cells at 1h & 24 h (a) Lysosome were stained by Lysotracker Red, (b). Mitochondria were stained with MitoTracker Deep Red dye. Scale bar = 10 μm.

Lysosome Imaging Chol-Nap-17AAGnp		1h	24h
Image Channels		C2 (green) C3 (red)	C2 (green) C3 (red)
Pearsons' Correlation Coefficient	R	0.6581	0.9321
Manders Coefficients	M1 (fraction of C2 overlapping C3)	0.9121	0.9351
	M2 (fraction of C3 overlapping C2)	0.9332	0.9981
Percent volume colocalized		*24.54%*	*56.05%*

Table 5: Quantification of co-localization of Chol-Nap-17AAGnp into lysosomes in HeLa cells at 1h & 24h from CLSM.

Mitochondria Imaging Chol-Nap-17AAGnp		1h	6h
Image Channels		C2 (green) C3 (red)	C2 (green) C3 (red)
Pearsons' Correlation Coefficient	R	0.5421	0.6901
Manders Coefficients	M1 (fraction of C2 overlapping C3)	0.8200	0.8651
	M2 (fraction of C3 overlapping C2)	0.8641	0.8945
Percent volume colocalized		*14.03%*	*25.67%*

Table 6: Quantification of co-localization of Chol-Nap-17AAGnp into Mitochondria in HeLa cells at 1h & 24 h from CLSM.

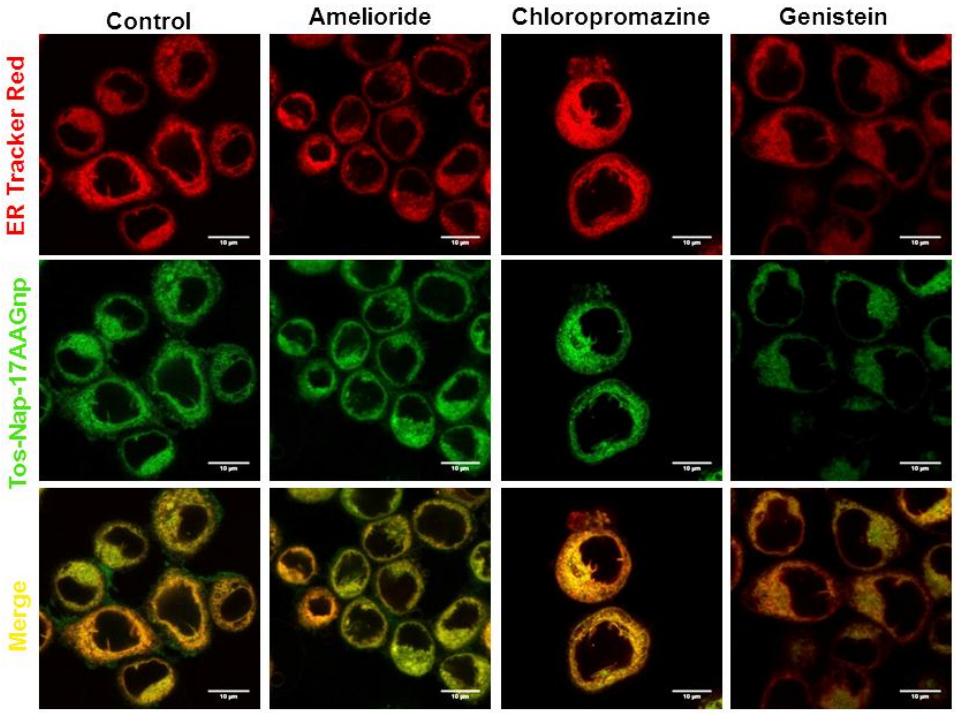

Figure 8: CLSM images of HeLa cells pre-treated with endocytosis inhibitors followed by Tos-Nap-17AAGnp (green) treated for 1h, ER of HeLa cells were stained with ER-Tracker Red dye. Scale bar = 10 µm.

Treatment Time		Control	Amiloride	Genistein	Chlorpromazine
Image Channels		C2 (green) C3 (red)	C2 (green) C3 (red)	C2 (green) C3 (red)	C2 (green) C3 (red)
Pearsons' Correlation Coefficient	R	0.8735	0.9073	0.6032	0.8795
Manders Coefficients	M1 (fraction of C2 overlapping C3)	0.9588	0.9810	0.7490	0.9623
	M2 (fraction of C3 overlapping C2)	0.9880	0.9839	0.7643	0.9793
Percent volume colocalized		*55.56%*	*60.24%*	*24.61%*	*54.98%*

Table 7: Quantification of co-localization of Tos-Nap-17AAGnp into ER in HeLa cells pre-treated with different endocytosis inhibitors from CLSM.

4.2.3. ER Stress Induction: After successful accumulation into ER, the lipidic nanoparticle Tos-Nap-17AAGnp would induce stress in ER. One of the important markers for ER stress is c/EBP homologous protein (CHOP).[31] Hence, we evaluated the expression of CHOP by confocal fluorescence microscopy. The HeLa cells were treated with Tos-Nap-17AAGnps for 24 h and stained the nucleus of the cells with blue fluorescent dye DAPI. The cells were further incubated with CHOP specific primary antibody followed by treatment with red fluorescent Alexa Fluor 594-labelled secondary antibody. The cells were then visualized under fluorescence microscopy (Figure 9a) evidently showed that Tos-Nap-17AAGnp induced ER stress leading to the remarkable increase in red fluorescence intensity compared to control cells which hardly showed any CHOP expression.

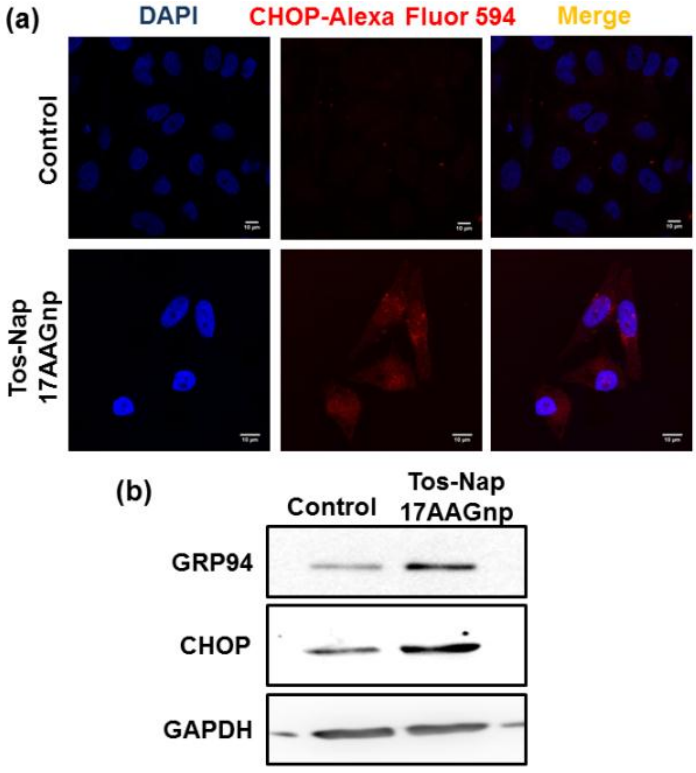

Figure 9: (a) CLSM images of HeLa cells to visualize CHOP as ER stress marker. CHOP was stained with Alexa Fluor 594-labeled antibody (red). Nuclei of HeLa cells were stained with DAPI (blue). (b) Western blot image of expression of CHOP in HeLa cells. Scale bar = 10 μm.

Also quantification of red fluorescence intensity from confocal images revealed that Tos-Nap-17AAGnp increased the CHOP expression by 18.6 folds compared to control cells (Figure 10a). The expression of CHOP was further assessed by Western blot analysis after

incubating HeLa cells with ER-NPs for increase in CHOP expression compared to non-treated control cells (Figure 9b & 10b). Further we assessed the Glucose Regulatory Protein 94 (GRP-94) after the treatment of Tos-Nap-17AAGnp and showed upregulation of GRP-94 with respect to control (Figure 9b & 10c). From these fluorescence imaging and protein expression assays, it was confirmed that Tos-Nap-17AAGnp triggered ER stress in HeLa cells.

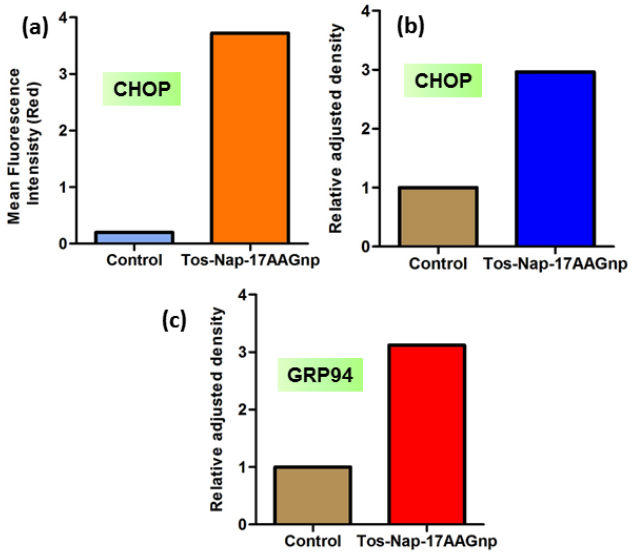

Figure 10: (a,b) Quantification of CHOP expression in HeLa cells after treatment with Tos-Nap-17AAGnp for 24 h determined from CLSM images and Western blot analysis respectively. (c) Quantification of GRP94 expression in HeLa cells after treatment with Tos-Nap-17AAGnp for 24 h, determined by Western blot analysis.

4.2.4. DNA Damage: We hypothesized that Tos-Nap-17AAGnp would simultaneously induce ER stress and DNA damage.[32] To validate this hypothesis, we estimated the expression of γH2AX as one of the markers of DNA damage by fluorescence microscopy. HeLa cells were treated with Tos-Nap-17AAGnp for 24 h followed by staining of nucleus with blue fluorescent dye DAPI. The cells were further incubated with γH2AX primary antibody followed by red fluorescent Alexa Fluor 594-labelled secondary antibody. The expression of γH2AX was visualized by CLSM. (Figure 11a) demonstrated that, untreated control cells hardly showed any DNA damage. On the other hand, Tos-Nap-17AAGnp treated cells showed remarkable increase in γH2AX expression leading to increase in red fluorescence intensity. Moreover, the red fluorescence signals significantly overlapped with the blue fluorescently labeled nucleus showing the localization of γH2AX (Figure 11a).

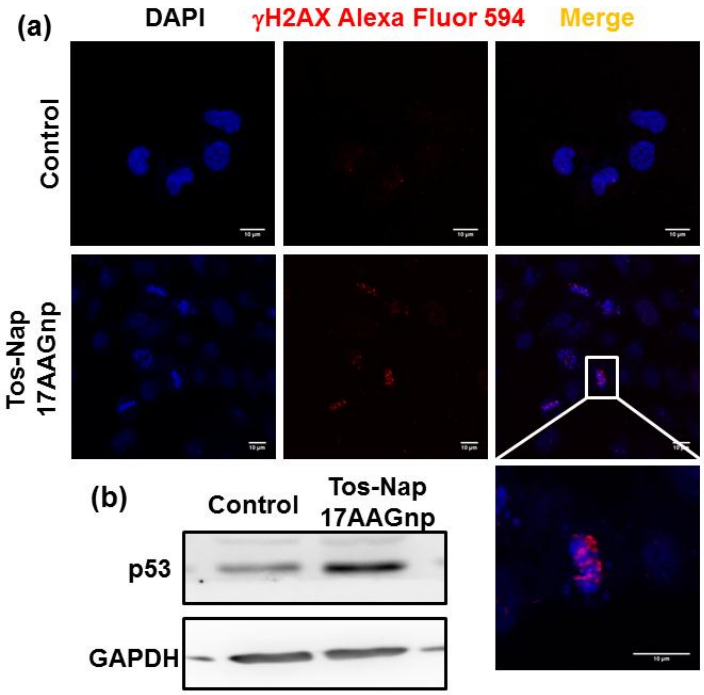

Figure 11: (a) CLSM images of HeLa cells to visualize γH2AX as DNA damage marker. γH2AX was stained with Alexa Fluor 594-labeled antibody (red). Nuclei of HeLa cells were stained with DAPI (blue). (b) Western blot image of expression of γH2AX and p53 in HeLa cells. Scale bar = 10 μm.

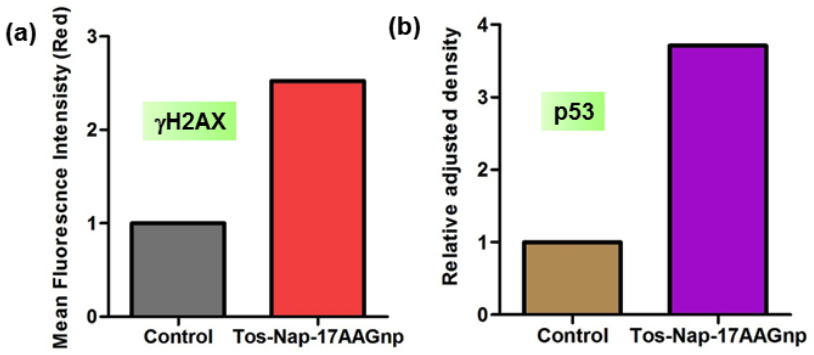

Figure 12: (a). Quantification of γH2AX expression in HeLa cells after treatment with Tos-Nap-17AAGnp for 24 h determined from CLSM images, (b) Quantification of p53 expression in HeLa cells after treatment with Tos-Nap-17AAGnp for 24 h, determined by Western blot analysis.

Also fluorescence microscopy based quantification revealed that Tos-Nap-17AAGnp induced 2.5 folds increase in γH2AX expression compared to control cells (Figure 12a). Further assessment of p53 (DNA damage effector) [33] by Western blot was also performed after treatment of HeLa cells with Tos-Nap-17AAGnp for 24 h. The gel electrophoresis images

clearly showed that lipidic nanoparticle (Tos-Nap-17AAGnp) amplified the expression of p53 by 3.7 folds (Figure 11b, 12b). From these microscopy and protein expression it was confirmed that Tos-Nap-17AAGnp triggered DNA damage in HeLa cells.

4.2.5. Apoptosis & Cell Death: Simultaneous ER stress and DNA damage leads to cell alteration of cell cycle.[34-35] To evaluate the effect of nanoparticle mediated ER stress induction on cell cycle, we incubated HeLa cells with 5µM of Tos-Nap-17AAGnp and free 17AAG respectively for 24h and quantified the number of cells present in different stages of cell cycle by flow cytometry. It was found that, 51.85%, 11.51% and 31.70% cells were in G1, S and G2/M phase respectively after treatment with Tos-Nap-17AAGnp as compare to 74.95%, 6.42% and 13.08% cells were in G1, S and G2/M phase with no treatment control (Figure 13a) On the other hand, in free 17AAG treatment, 48.82%, 8.20% and 34.17% cells were found in G1, S and G2/M phase respectively. Hence, the flow cytometric analysis exhibited that Tos-Nap-17AAGnp inhibiting cell cycle in similar fashion with free 17AAG treatment. We further evaluated the stimulation of programmed cell death (apoptosis) by Tos-Nap-17AAGnp through flow cytometry. HeLa cells were treated with Tos-Nap-17AAGnp for 24 h followed by incubation with FITC-labeled Annexin V (green fluorescence) and propidium iodide (PI, red fluorescence dye) to stain cell surface phosphatidyl serine and nuclear DNA in apoptotic and necrotic cells respectively. From the flow cytometry data, it was found that Tos-Nap-17AAGnp triggered 76.05% cells into late stages of apoptosis compared to control cells. Induction of early and late apoptosis would push the cells into death. The cell viability assay was performed to evaluate the effect of Tos-Nap-17AAGnp. HeLa cells were treated with Tos-Nap-17AAGnp in multiple dosages for 48 h and the % of viable cells was measured by MTT assay. The cell viability assay showed that Tos-Nap-17AAGnp prompted 50% cell death (IC_{50}) at 3 µM concentration. On the other hand, Chol-Nap-17AAGnp and free 17AAG showed 50% cell death (IC50) at 6.25 µM and 5 µM respectively (Figure 14a). From the flow cytometry and cell viability assay it was evident that Tos-Nap-17AAGnp generated late apoptosis to induce cell death.

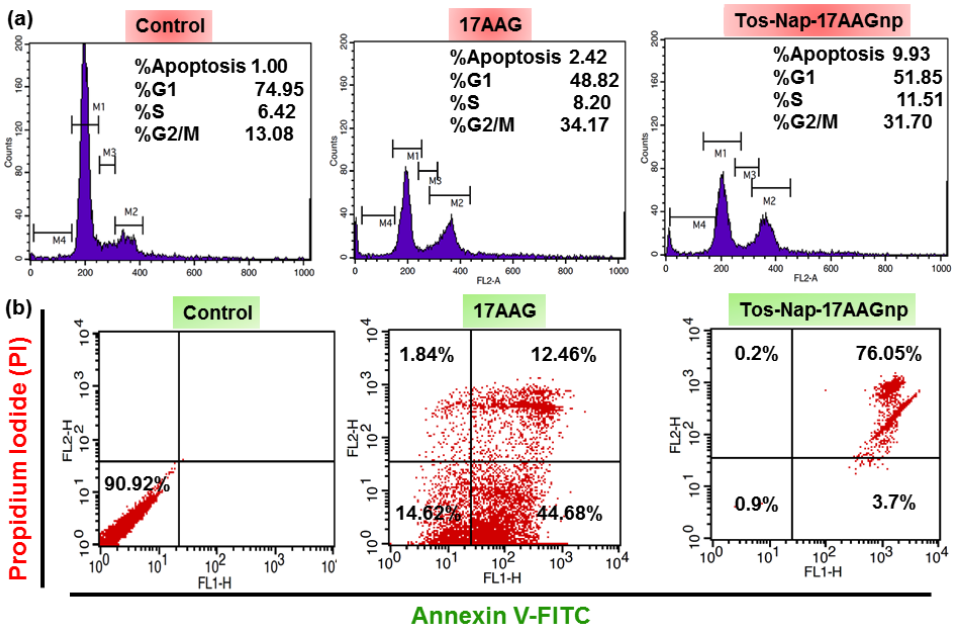

Figure 13: Treatment of Tos-Nap-17AAGnp and 17AAG in HeLa cells (a) Cell Cycle analysis at 24h post-incubation (b) Flow cytometry analysis at 24h post-incubation, Apoptotic and necrotic cells were stained with FITC-Annexin V and PI respectively.

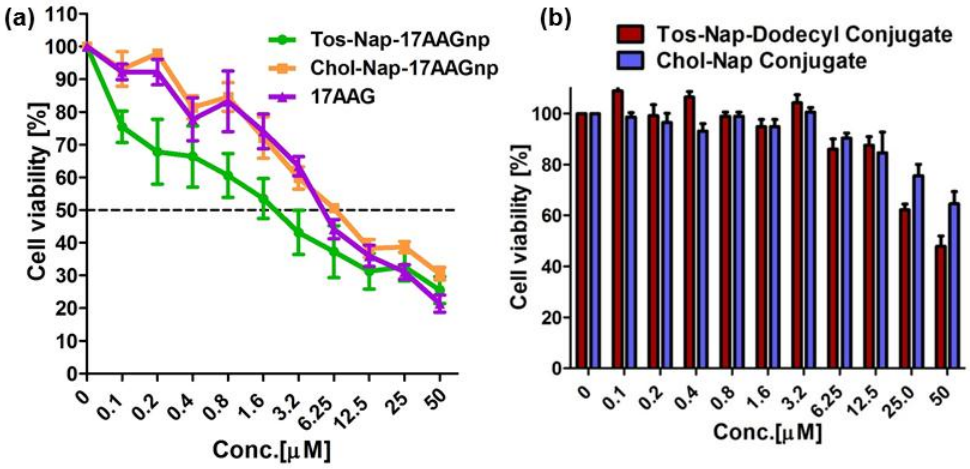

Figure 14: (a). Cell viability assay at 48h post-incubation in HeLa cells (a). Tos-Nap-17AAGnp, Chol-Nap-17AAGnp and 17AAG, (b). Tos-Nap-Dodecyl Conjugate & Chol-Nap Conjugate.

4.2.6. Autophagy Induction & Inhibition: Cancer cells can overcome ER stress and DNA damage effect by initiating cell survival mechanism called autophagy.[36-38] Hence, we evaluated the induction of autophagy by Tos-Nap-17AAGnp. HeLa cells were treated with Tos-Nap-17AAGnp for 24 h followed by incubation with Beclin-1 primary antibody as one of the markers for autophagy. We visualized the cells after

further incubation with red fluorescent Alexa Flour 594 labeled secondary antibody under fluorescence microscopy. From the CLSM images (Figure 15a), it was clear that control cells hardly showed any Beclin-1 expression. On contrary, Tos-Nap-17AAGnp treated cells demonstrated significant increase in red fluorescence intensity by 1.97 folds (Figure 16a) compared to control cells indicating triggering of autophagy. Furthermore, we also assessed the protein level of another autophagy marker LC3 (microtubule-associated protein 1 light chain 3) by Western blot analysis. The gel electrophoresis image (Figure 15b) after treating HeLa cells with Tos-Nap-17AAGnp for 24 h, showed undoubtedly that, Tos-Nap-17AAGnp increased the expression of LC3 by 1.63 folds compared to control cells (Figure 16b). Hence it was evident that Tos-Nap-17AAGnp activated autophagy as one of the cell survival mechanisms under stress.

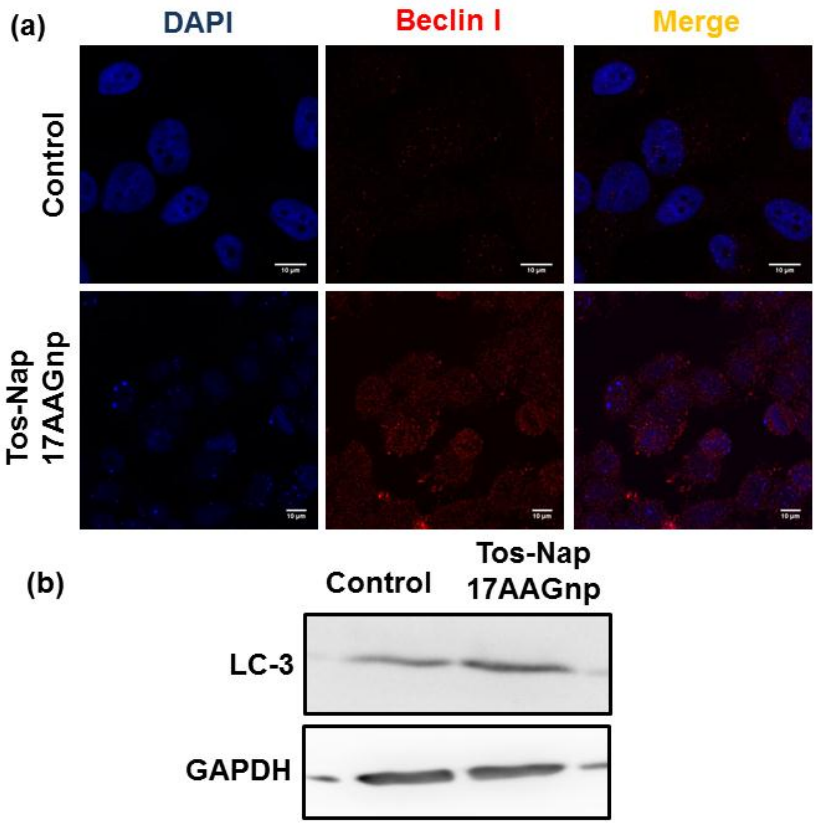

Figure 15: (a) CLSM images of HeLa cells to visualize Beclin-1 as autophagy marker. (b) Western blot analysis for the expression of LC-3.

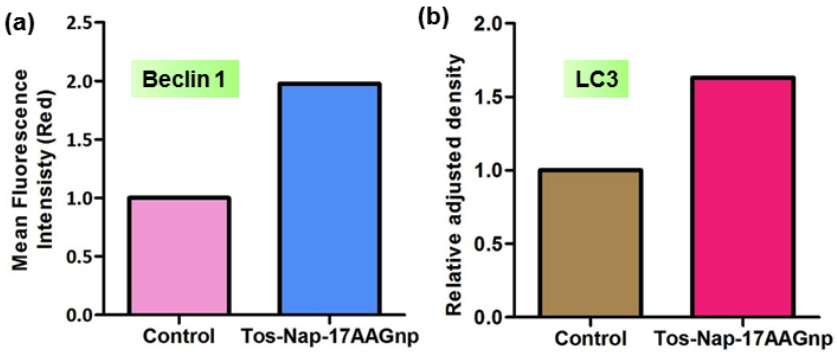

Figure 16: (a). Quantification of Beclin 1expression in HeLa cells after treatment with Tos-Nap-17AAGnp for 24 h determined from CLSM images, (b) Quantification of LC3 expression in HeLa cells after treatment with Tos-Nap-17AAGnp for 24 h, determined by Western blot analysis.

To inhibit autophagy and trigger augmented cell death, we intended to use Tos-Nap-17AAGnp in combination of chloroquine (CQ) as autophagy inhibitor.[39] Moreover, it was shown recently that CQ can augment the anti-cancer activity of 5FU in cancer cells. Hence, we assessed the cell killing ability of Tos-Nap-17AAGnp in presence of CQ by MTT assay. We incubated HeLa cells in different concentrations of Tos-Nap-17AAGnp and CQ (50 μM) cocktail and cell viability was measure after 48 h. From the MTT data, it was observed that, the combination of Tos-Nap-17AAGnp with CQ showed much reduced IC_{50} = 200 nM (21.4 % cell viability in highest concentration) compared to IC_{50} = 3 μM for Tos-Nap-17AAGnp only (Figure 17a). On the other hand, IC_{50} value of 17AAG in combination with CQ is 500 nM and less effective as compared to combination treatment of Tos-Nap-17AAG and CQ (Figure 17b). Interestingly, only CQ showed negligible cell killing even at 50 μM concentration after 48 h (Chapter 3, Figure 20d). From these MTT assay, it was confirmed that simultaneous induction of ER stress, DNA damage and autophagy inhibition can augment anti-cancer efficacy in HeLa cervical cancer cells.

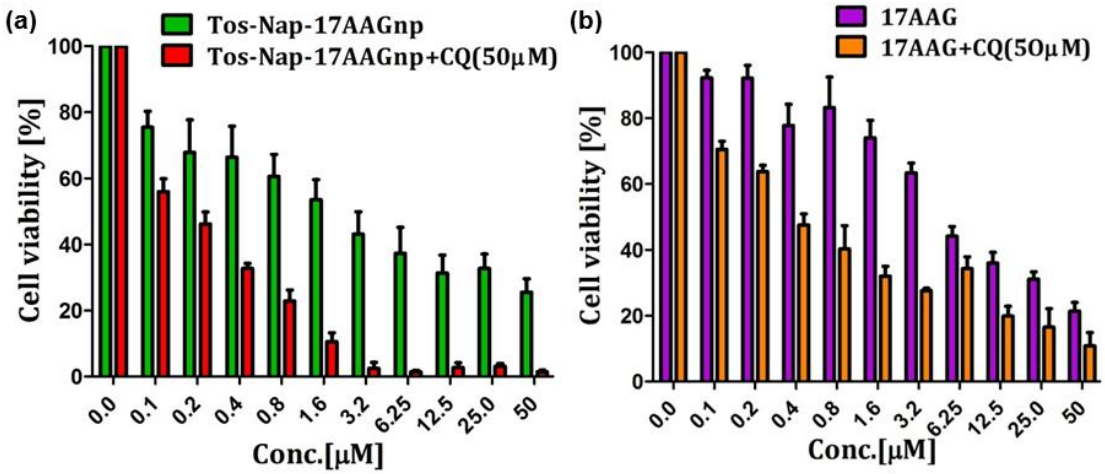

Figure 17: Cell viability assay of (a). Tos-Nap-17AAGnp and Tos-Nap-17AAGnp + CQ. (b). 17AAG & 17AAG + CQ combination in HeLa cells at 48 h post-incubation. Scale bar = 10 μm.

4.3. Conclusion:

In conclusion, we have engineered lipidic nanoparticle containing sulfonamide group in the conjugate which selectively goes to ER. These lipidic nanoparticles Tos-Nap-17AAGnp induce ER stress which subsequently induces nuclear DNA damage. Confocal microscopy, gel electrophoresis and flow cytometry revealed that Tos-Nap-17AAGnp accumulated selectively into endoplasmic reticulum of HeLa cells in a time dependent manner through caveloae mediated endocytosis followed by induction of ER stress and nuclear DNA damage leading to programmed cell death (apoptosis). Interestingly, Tos-Nap-17AAGnp initiated autophagy in HeLa cells which could be overcome by the combination of Tos-Nap-17AAGnp and autophagy inhibitor chloroquine, leading to much augmented cell killing efficacy. We anticipate that, this work will extend the concept of lipidic ER targeting nanoparticle to target specific sub-cellular organelle endoplasmic reticulum for improved therapeutic effect in anti-cancer therapy.

4.4. Experimental Methods & Materials:

4.4.1. Materials:

Commercially available chemicals and solvents were used without further purification and distillation. Chemical reactions were carried out in inert gas (nitrogen gas) condition. Pre-coated silica gel aluminum sheets 60F254 are used for analytical thin-layer chromatography (TLC), was obtained from EMD Millipore Laboratories. Cell culture media (Dulbecco's modified Eagle's medium (DMEM)) and 3-(4,5- dimethylthiazol-2-yl)-2,5-diphenyltetrazolium bromide (MTT) were purchased from HiMedia. Sodium dodecyl sulfate (SDS), Hanks' balanced salts, N-(2 hydroxyethyl)piperazine-N′-ethanesulfonic acid sodium salt, propidium iodide, Lab Tek chamber slide 8 wells, 5,5′,6,6′-tetrachloro-1,1′,3,3′ tetraethylbenzimidazolylcarbocyanine iodide (JC 1 dye)and 2′,7′-dichlorofluoresceindiacetate (DCFH-DA) were obtained from Sigma-Aldrich. All of the primary and secondary antibodies were obtained from Cell Signaling Technology, Biolegend, and Abcam. Confocal laser scanning microscopy was performed by a Zeiss LSM 710 machine. Flow cytometry analysis was performed using a BD FACS Calibur flow cytometer. Each sample was done in triplicate.

4.4.2. Experimental Procedure:

4.4.2.a. Synthesis of N-(2-aminoethyl)-4-methylbenzenesulfonamide (Compound 3):

p-Tolune sulfonyl chloride (1 eq) was dissolved in dry dichloromethane and added drop wise into stirred solution of excess ethylenediamine (10 eq) at 0^{o}C over a period of 30mins. The reaction mixture was stirred at 0^{o}C for 1h, further allowed to stir 18h at room temperature. The resulting reaction mixture was diluted with 10ml DCM and neutralized with 1(N) HCl. The organic layer was extracted and the aqueous layer basified with 10(N) NaOH (to make pH 10). The aqueous layer further extracted with 5ml DCM and concentrated all organic layers. The organic layer was dried over Na_2SO_4 filtered and evaporated. The product was pure and no need for column chromatography.

Yield: 87.45%

^{1}H NMR ($CDCl_3$, 400MHz): δ =7.75 (d, 8.29 Hz, 2H), 7.29 (d, 7.96 Hz, 2H), 3.12 (t, 5.2 Hz, 2H), 2.97 (t, 5.2 Hz, 2H), 2.81 (t, 6.4 Hz, 2H), 2.408 (s, 3H).

^{13}C NMR ($CDCl_3$, 100MHz): δ = 143.78, 143.62, 137.11, 136.91, 130.03, 127.31, 45.31, 41.07, 21.77.

ESI-HRMS: Observed m/z for $[M+H]^+$ = 215.0654

4.4.2b. Synthesis of N-(2-(6-bromo-1,3-dioxo-1H-benzo[de]isoquinolin-2(3H)-yl)ethyl)-4-methylbenzenesulfonamide (compound 3):

4-Bromo-1,8-Napthalicanhydride (1 eq) was dissolved in dry ethanol and added slowly into ethanolic solution of N-(2-aminoethyl)-4-methylbenzenesulfonamide (1.2 eq). The resulting mixture was refluxed at 80^{o}C and allowed to stir for 6h. After completion the ethanol was evaporated and the crude product was concentrated. Finally the crude product was purified by column chromatography using 3% MeOH/ DCM as mobile phase.

Yield: 73.58%

^{1}H NMR ($CDCl_3$, 400MHz): δ = 8.58 (m, 2H), 8.32 (d, 7.87 Hz, 1H), 8.05 (d, 7.87 Hz, 1H), 7.86 (dd, 7.37 Hz, 8.44 Hz, 1H), 7.52 (d, 8.27 Hz, 2H), 6.73 (d, 7.95 Hz, 2H), 5.10 (m, 1H), 4.27 (t, 4.5 Hz, 2H), 3.49 (t, 4.5 Hz, 2H), 1.95 (s, 3H).

^{13}C NMR ($CDCl_3$, 100MHz): δ =164.20, 142.82, 137.30, 133.78, 132.42, 131.56, 131.42, 131.30, 130.88, 130.72, 129.31, 129.10, 128.30, 126.80, 122.75, 121.84, 42.60, 39.36, 21.28.

ESI-HRMS: Observed m/z for $[M+H]^+$ = 473.3410

4.4.2.c. Synthesis of N-(2-(6-(dodecylamino)-1,3-dioxo-1H-benzo[de]isoquinolin-2(3H)-yl)ethyl)-4-methylbenzenesulfonamide (compound 5):

Compound 3 was dissolved into 2-methoxyethanol and the deodecylamine was added drop wise at room temperature. The resulting reaction mixture was refluxed at 90^{o}C for 24h. After completion of the reaction, the 2-methoxyethanol was evaporated and 10 ml chilled ethanol was added. The precipitated product was filtered and washed with chilled water. The crude product was purified by column chromatography using 2% MeOH/DCM as mobile phase.

Yield: 66.95%

^{1}H NMR ($CDCl_3$, 400MHz): δ = 8.43 (d, 7.31 Hz, 1H), 8.34 (d, 8.47 Hz, 1H), 8.09 (d, 8.13 Hz, 1H), 7.59 (t, 7.6 Hz, 1H), 7.53 (d, 8.4 Hz, 2H), 6.74 (d, 8.06 Hz, 2H), 6.69 (d, 8.50Hz, 1H), 5.47 (t, 4.65 Hz, 1H), 5.39 (t, 4.83 Hz, 1H), 4.24 (dd, 4.58 Hz, 6.23 Hz, 2H), 3.43 (m, 4H), 1.93 (s, 3H), 1.26 (s, 2H), 0.87 (s, 3H).

^{13}C NMR ($CDCl_3$, 100MHz): δ = 165.20, 164.62, 149.89, 142.59, 134.97, 131.38, 129.93, 129.22, 126.77, 126.24, 124.72, 122.57, 120.03, 109.44, 109.44, 104.41, 43.57, 43.14, 38.85, 31.99, 29.71, 29.42, 29.02, 27.25, 22.77, 21.19, 14.20.

ESI-HRMS: Observed m/z [M+H]+ = 578.3052

4.4.2.d. Synthesis of 6-bromo-2-(2-(dimethylamino)ethyl)-1H-benzo[de]isoquinoline-1,3(2H)-dione (compound 11):

4-Bromo-1,8-napthalic anhydride (1g, 3.60 mmol, 1 eq.) and N,N`-dimethylethylenediamine (381.78 mg, 4.33 mmol, 1.2 eq.) was mixed in ethanol and stirred for 5 mins. The reaction mixture was refluxed at 60^{o}C to 70^{o}C for 8h. After reflux the reaction mixture was filtered and washed with chilled ethanol twice. The solid compound was dried over P_2O_5 and no further purification is required.

Yield: 82.51%

^{1}H NMR ($CDCl_3$, 400MHz): δ = 8.65(dd, 7.30 Hz, 1.07 Hz, 1H), 8.56 (dd, 8.52, 1.08, 1H), 8.40 (dd, 7.87 Hz, 1H), 8.03 (d, 7.87 Hz, 1H), 7.84 (dd, 7.2 Hz, 1.2 Hz, 1H), 4.33 (t, 6.8 Hz, 2H), 2.67 (t, 7.2 Hz, 2H), 2.36 (s, 3H).

^{13}C NMR ($CDCl_3$, 100MHz): δ = 163.51, 133.13, 131.92, 131.11, 130.92, 130.47, 130.12, 128.91, 127.89, 122.92, 122.06, 56.73, 45.53, 38.05.

ESI-HRMS: Observed m/z [M+Na]+ = 347.0395

4.4.2.e. Synthesis of 2-(2-(dimethylamino)ethyl)-6-(piperazin-1-yl)-1H-benzo[de]isoquinoline-1,3(2H)-dione (compound 13):

Compound 11 was dissolved into 2-methoxyethanol and the piperazine (3 eq.) was added drop wise at room temperature. The resulting reaction mixture was refluxed at 90^{o}C for 24h. After completion of the reaction, the 2-methoxyethanol was evaporated and 10 ml chilled ethanol was added. The precipitated product was filtered and washed with chilled water and ethanol. The crude product was purified by column chromatography using 5% MeOH/DCM as mobile phase.

Yield: 64.96%

^{1}H NMR ($CDCl_3$, 400MHz): δ = 8.57 (dd, 7.27 Hz, 1.10 Hz, 1H), 8.51 (d, 8.06 Hz, 1H), 8.40 (dd, 8.42 Hz, 1.06 Hz, 1H), 7.68 (dd, 8.36 Hz, 7.37 Hz, 1H), 7.21 (d, 8.09 Hz, 1H), 4.33 (t, 6.8 Hz, 2H), 3.24 (s, 8H), 2.69 (t, 7.20 Hz, 2H), 2.384 (s, 6H).

^{13}C NMR ($CDCl_3$, 100MHz): δ = 164.66, 164.17, 156.40, 132.77, 131.31, 130.43, 130.13, 126.34, 125.81, 123.36, 116.89, 115.15, 57.00, 54.26, 46.18, 45.68, 37.91.

ESI-HRMS: Observed m/z for $[M+H]^{+}$= 353.4460

4.4.2.f. Synthesis of 4-(((8S,9S,10R,13R,14S,17R)-10,13-dimethyl-17-((R)-6-methylheptan-2-yl)-2,3,4,7,8,9,10,11,12,13,14,15,16,17-tetradecahydro-1H-cyclopenta[a]phenanthren-3-yl)oxy)-4-oxobutanoic acid (Compound 8):

Cholesterol (500 mg, 1.293 mmol, 1 equiv) and Succinic anhydride (390.66 mg, 3.879 mmol, 3 eq.) were dissolved in DCM.and slowly triethylamine (392.51 mg, 541 µL, 540.65 mmol) was added dropwise, allowed to stir for 24h. The reaction was then quenched with dilute HCl and H_2O. The compound was extracted from organic layer. Crude product was purified by silica gel (100−200 mesh size) column chromatography by using 10% ethylacetate/Hexane as mobile phase.

Yield: 72.50%

^{1}H NMR ($CDCl_3$, 400MHz): δ = δ = 5.36 (1H, d, J = 4 Hz), 4.68 – 4.58 (1H, m, J = 11.8 Hz), 2.68 (2H, t, J = 6.9 Hz), 2.60 (2H, t, J = 6.9 Hz), 2.31 (2H, d, J = 7.8 Hz), 2.04 – 1.93 (2H, m), 1.87 (1H, d, J = 2.6 Hz), 1.85 – 1.78 (2H, m), 1.66 – 1.41 (8H, m), 1.40 – 1.23 (5H, m,), 1.22 – 1.04 (8H, m), 1.01 (3H, s), 0.91 (3H, d, J = 6.5 Hz), 0.87 (3H, d, J = 1.8 Hz), 0.85 (3H, d, J = 1.7 Hz), 0.67 (3H, s).

^{13}C NMR ($CDCl_3$, 100MHz): δ = δ = 178.2, 171.7, 139.7, 122.9, 77.5, 77.2, 76.8, 74.7, 56.8, 56.3, 50.1, 42.4, 39.9, 39.7, 38.1, 37.1, 36.7, 36.3, 35.9, 32.0, 29.4, 29.1, 28.4, 28.2, 27.8, 24.4, 23.98, 22.9, 22.7, 21.2, 19.4, 18.9, 12.0.

ESI-HRMS: Observed m/z for $[M + Na]^+$ = 509.3504

4.4.2.g. Synthesis of (8S,9S,10R,13R,14S,17R)-10,13-dimethyl-17-((R)-6-methylheptan-2-yl) 2,3,4,7,8,9,10,11,12,13,14,15,16,17-tetradecahydro-1H-cyclopenta[a]phenanthren-3-yl 4-(4-(2-(2-(dimethylamino)ethyl)-1,3-dioxo-2,3-dihydro-1H-benzo[de]isoquinolin-6-yl)piperazin-1-yl)-4-oxobutanoate. (Compound 14):

Cholesterol succinate (200 mg, 0.4109 mmol, 1 equiv) was dissolved in dry DMF. and stirred continuously for 5mins at 0 °C in inert atmosphere. In the rection mixture HBTU (270.31mg, 0.821 mmol, 2 equiv) was added followed by addition of DIPEA (207.89 mg, 287.93 µL, 0.2.0545 mmol, 5 equiv). The reaction mixture was cooled down and compound 13 (147.52 mg, 0.4159 mmol, 1.2 equiv) was added to it. The reaction was stirred at room temperature for 24 h. The reaction was then quenched with 0.1 N HCl (10 mL) and H_2O (40 mL).and the compound was separated from organic layer.. Crude product was purified by silica gel (100−200 mesh size) column chromatography by using 3% MeOH/DCM as mobile phase.

Yield: 69.17%

^{1}H NMR ($CDCl_3$, 400MHz): δ = 8.60 (d, 7.26 Hz, 1H), 8.52 (d, 8.06 Hz, 1H), 8.42 (d, 7.68 Hz, 1H), 7.73 (m, 1H), 7.22 (d, 8.09, 1H), 5.37 (d, 4.66 Hz, 1H), 4.97 (m, 1H), 4.63 (s, 1H), 4.39 (t, 6.76 Hz, 2H), 3.93 (s, 2H), 3.83 (s, 2H), 3.24 (m, 5H), 2.86 (t, 6.63 Hz, 3H), 2.70 (s, 4H), 2.49 (s, 6H), 2.34 (d, 7.82 Hz, 2H), 2.02 (m, 3H), 1.85 (m, 3H), 1.39 (s, 2H), 1.32 (s, 3H), 1.24 (s, 3H), 1.02 (s, 4H), 0.97 (m, 4H), 0.87 (m, 6H), 0.85 (m, 6H), 0.67(s, 3H).

^{13}C NMR ($CDCl_3$, 100MHz): δ = 172.64, 170.28, 164.61, 164.12, 155.42, 139.80, 139.42, 132.68, 131.53, 130.09, 130.04, 126.42, 126.25, 124.12, 123.41, 122.81, 117.60, 115.55, 114.20, 56.84, 56.51, 56.28, 53.13, 50.17, 45.65, 45.02, 42.02, 42.46, 42.46, 42.06, 39.88, 39.66, 38.26, 37.13, 36.73, 36.33, 35.94, 32.07, 32.00, 31.78, 29.31, 29.10, 28.37, 28.16, 28.08, 27.93, 24.43, 23.97, 22.96, 22.84, 22.71, 21.18, 19.47, 18.86, 14.26, 12.00.

ESI-HRMS: Observed m/z for $[M-N_2+H]^+$= 821.5588

4.4.3. Dynamic light scattering (DLS):

Procedure is discussed in chapter 1.[40]

4.4.4. Field-emission scanning electron microscopy (FESEM):

Procedure is discussed in chapter 1.[40]

4.4.5.. Atomic force microscopy (AFM):

Procedure is discussed in chapter 1.[40]

4.4.6. Transmission Electron Microscopy (TEM):

Procedure is discussed in chapter 1.[40]

4.4.7. Cell viability assay (MTT Assay):

Procedure is discussed in chapter 1.[40]

4.4.8. Apoptosis by FACS:

Procedure is discussed in chapter 2. [40]

4.4.9. Live Cells Imaging of Endoplasmic Reticulum, Mitochondria and Lysosome:

Procedure is discussed in chapter 2.[40]

4.4.10. Western blotting:

Procedure is discussed in chapter 1.[40]

4.4.11. Immunofluorescence Assay:

Procedure is discussed in chapter 2.[40]

4.5. Appendices:

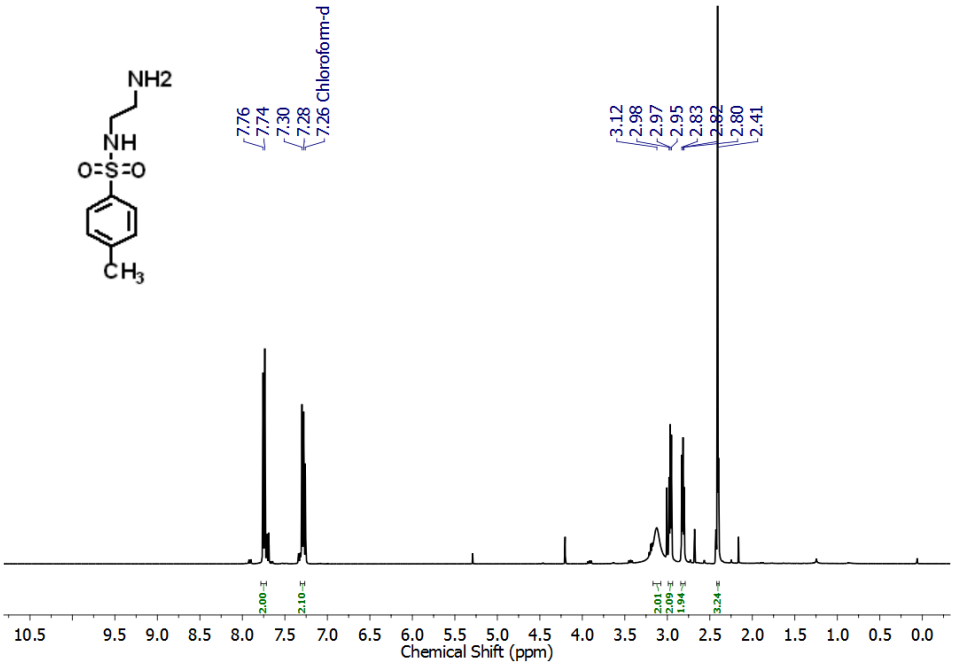

Fig. S1: ^{1}H NMR spectra of compound 2

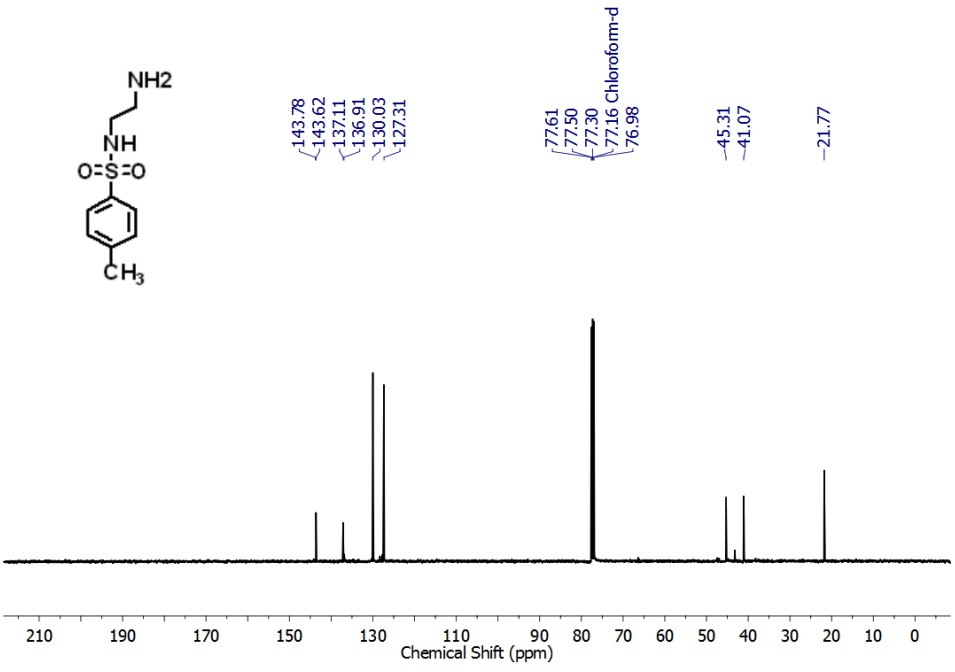

Fig. S2: ^{13}C NMR spectra of compound 2

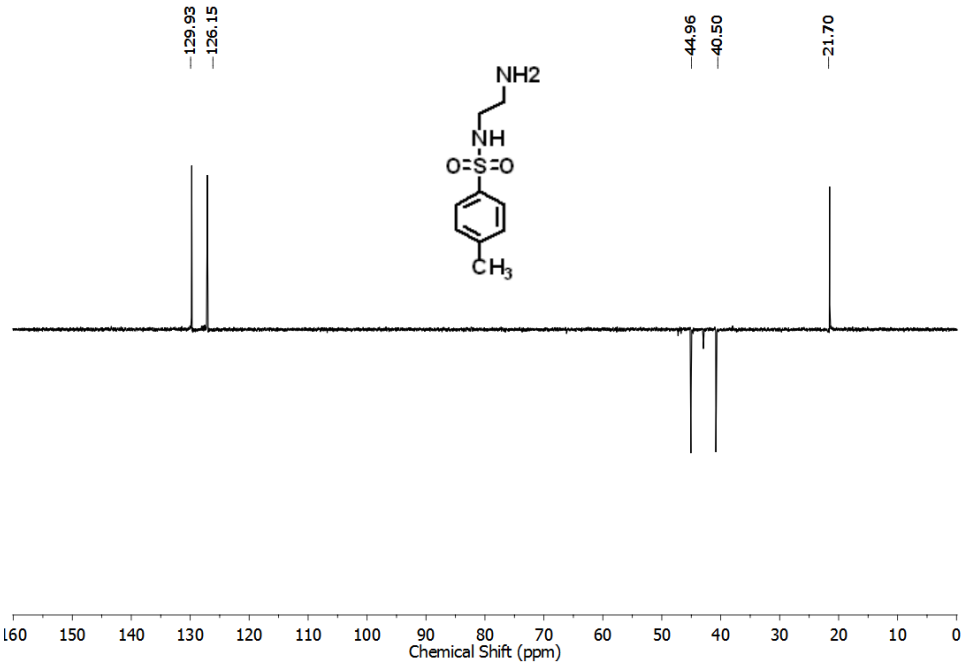

Fig. S3: DEPT spectra of compound 2

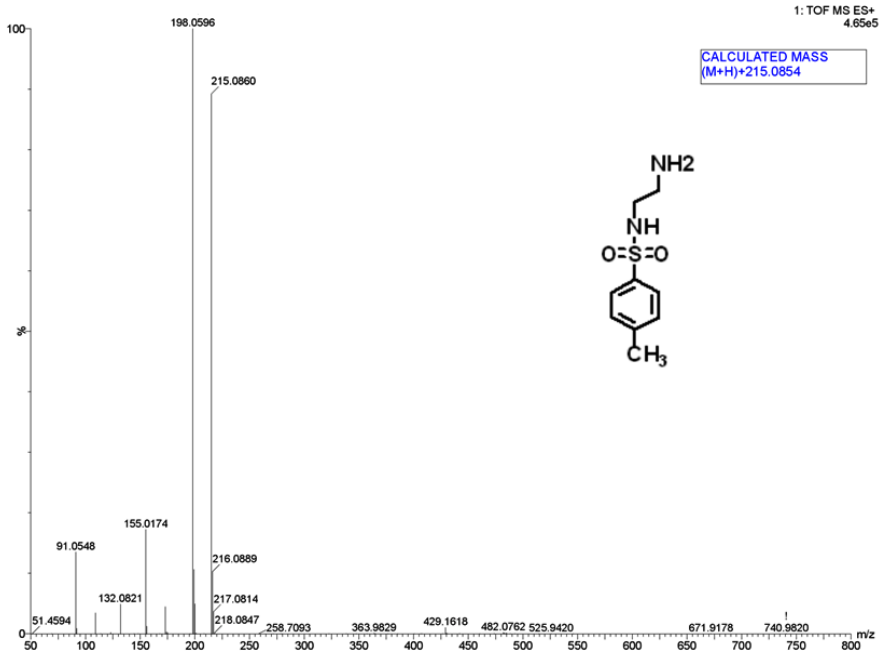

Fig. S4:HR-MS spectra of compound 2

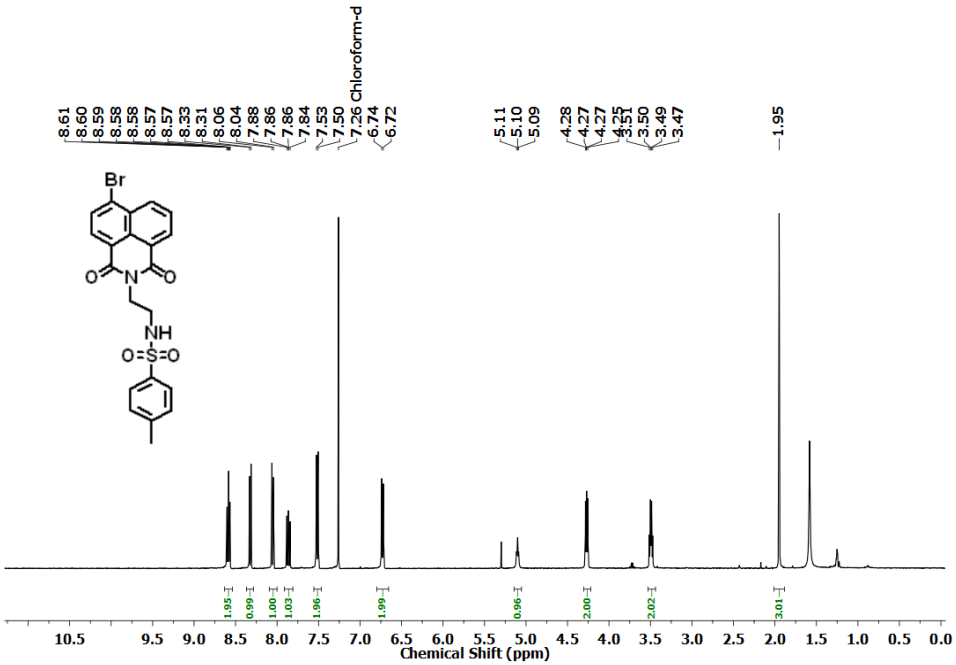

Fig. S5: ^{1}H NMR spectra of compound 3

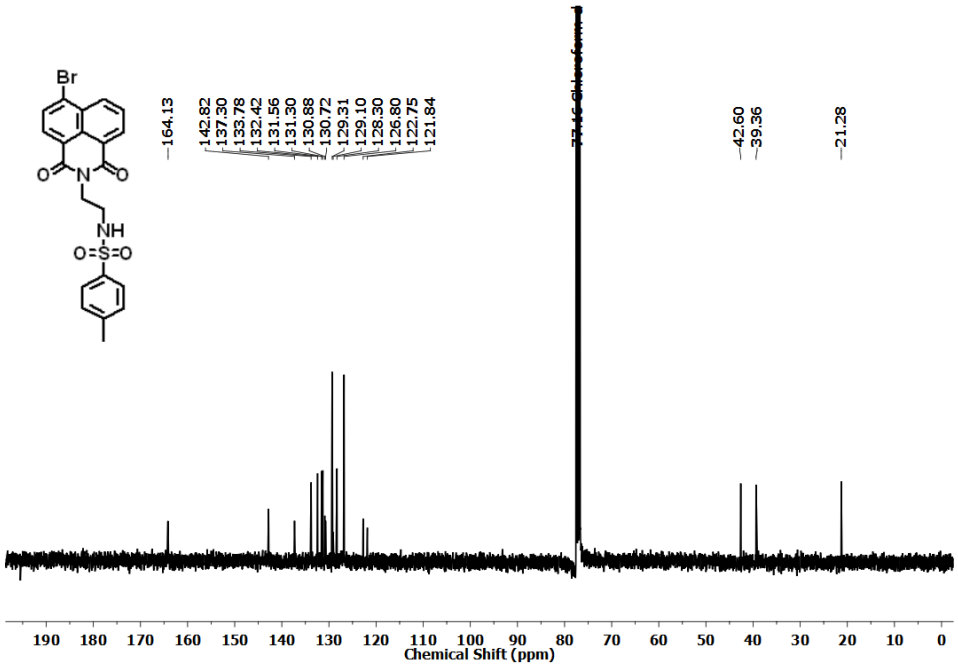

Fig. S6: ^{13}C NMR spectra of compound 3

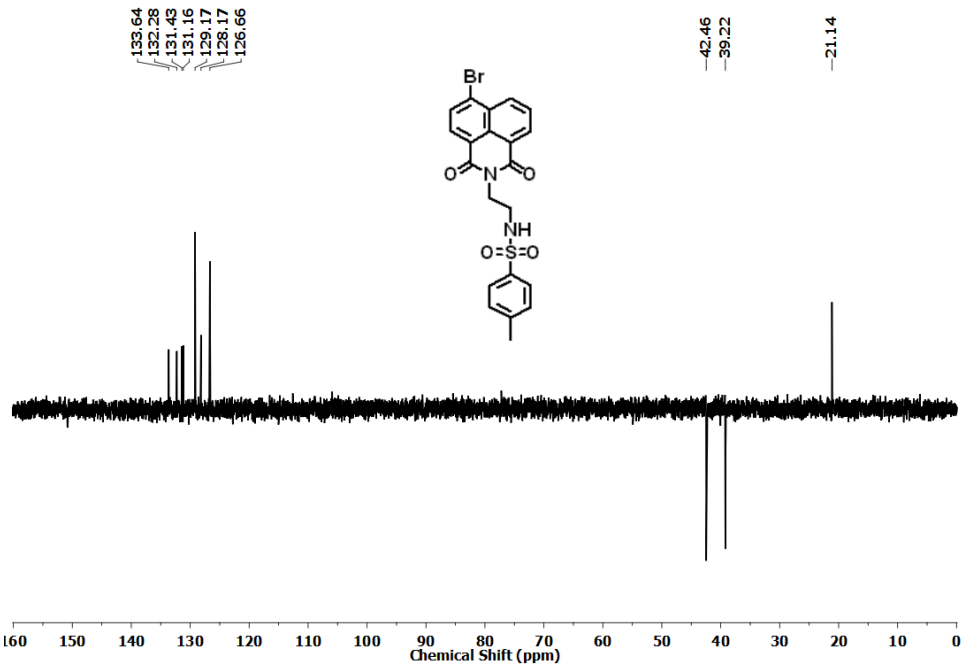

Fig. S7: DEPT spectra of compound 3

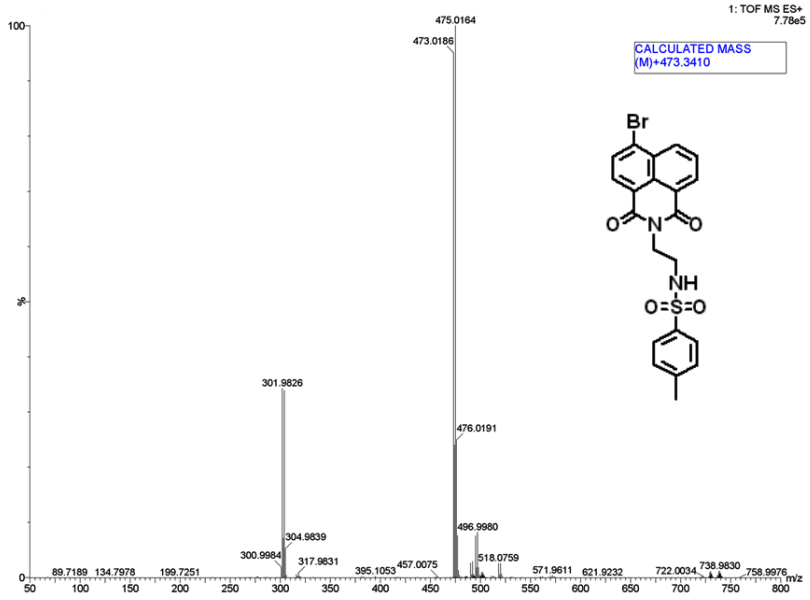

Fig. S8:HR-MS spectra of compound 3

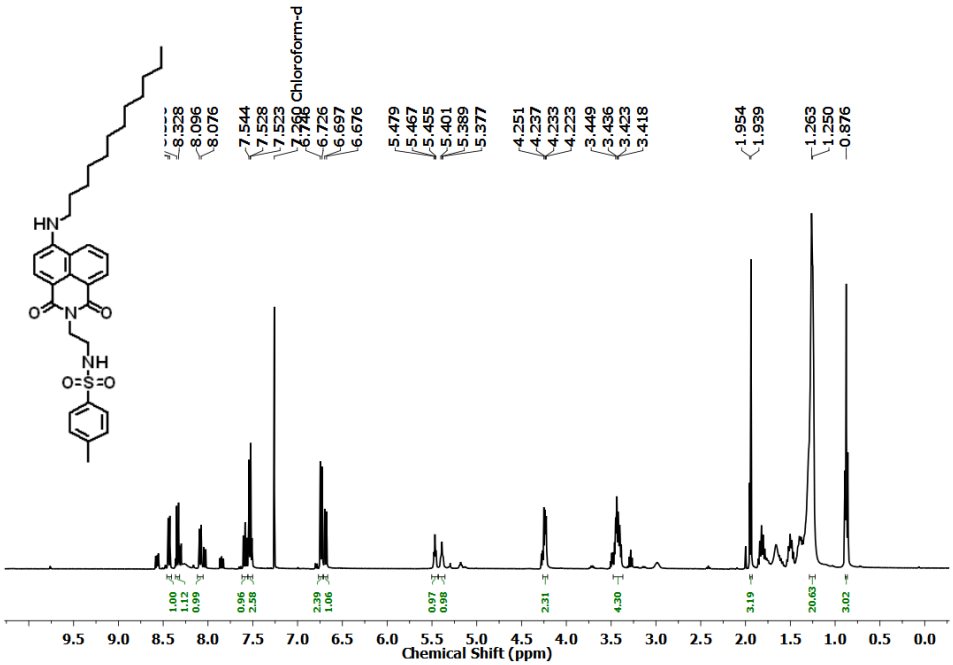

Fig. S9: ^{1}H NMR spectra of compound 5

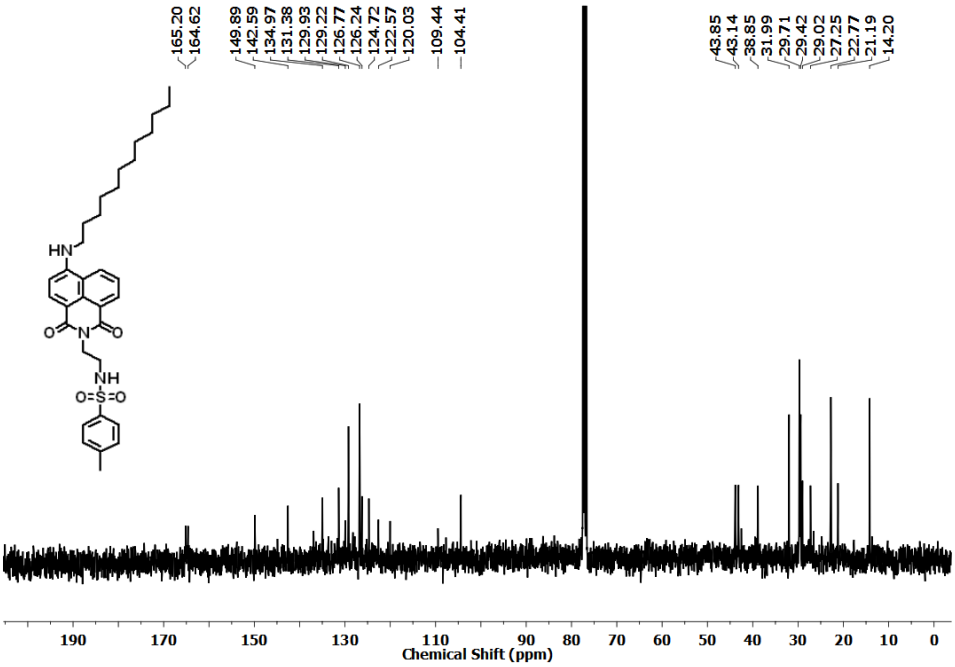

Fig. S10: ^{13}C NMR spectra of compound 5

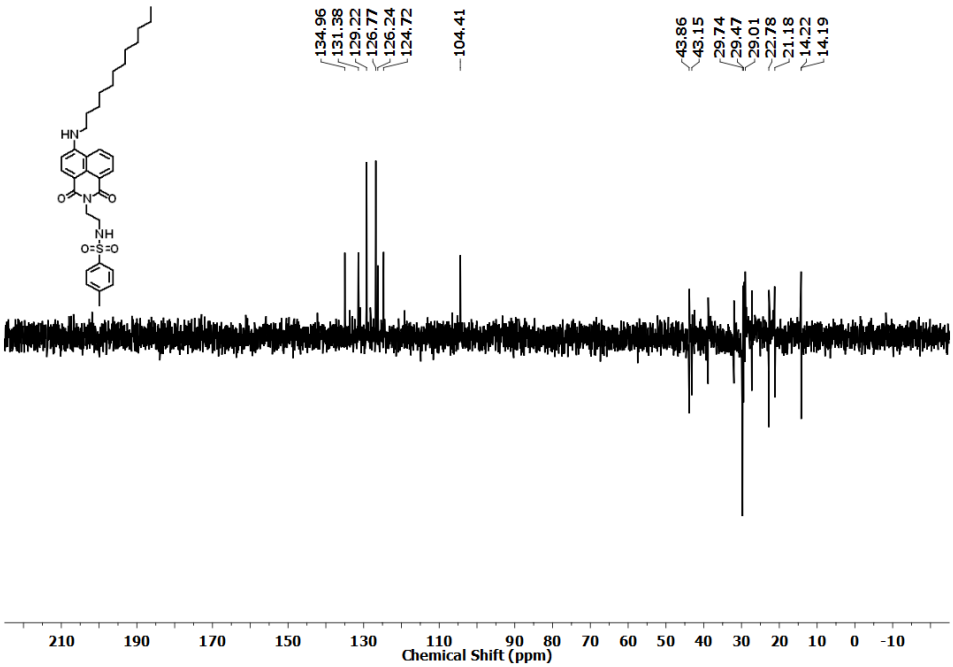

Fig. S11: DEPT spectra of compound 5

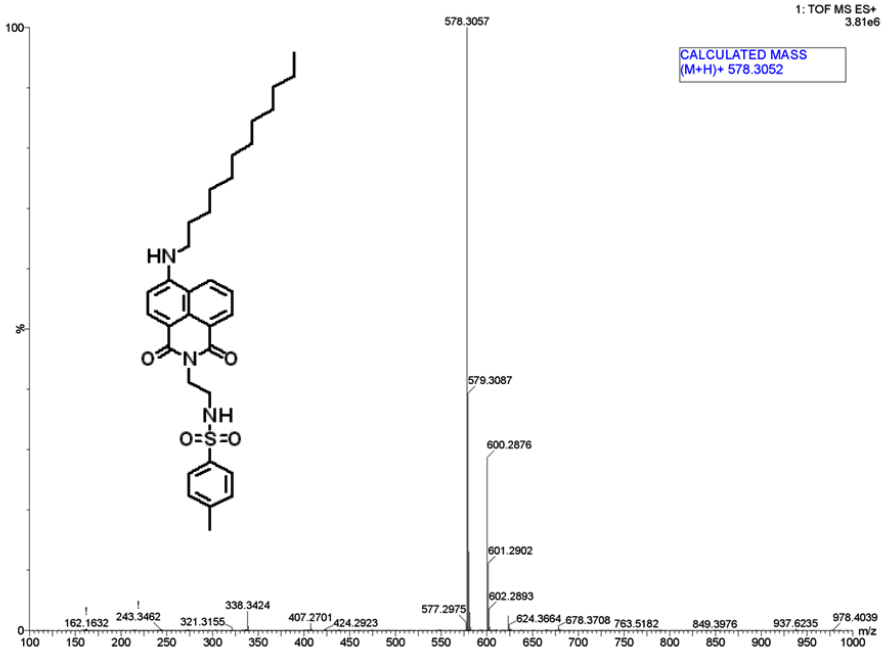

Fig. S12: HR-MS spectra of compound 5

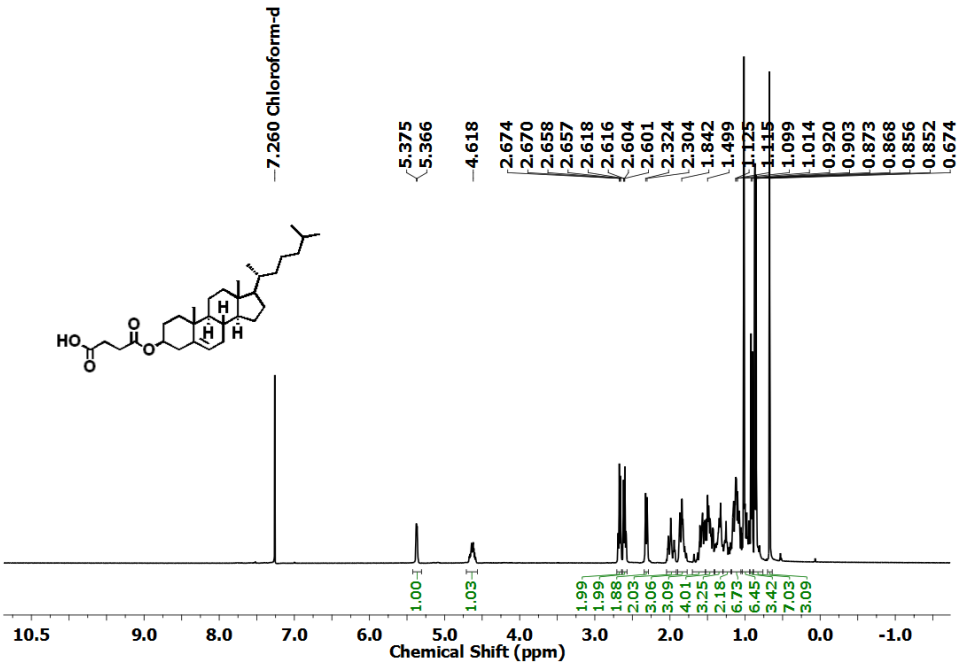

Fig S13: ^{1}H NMR spectra of compound 8

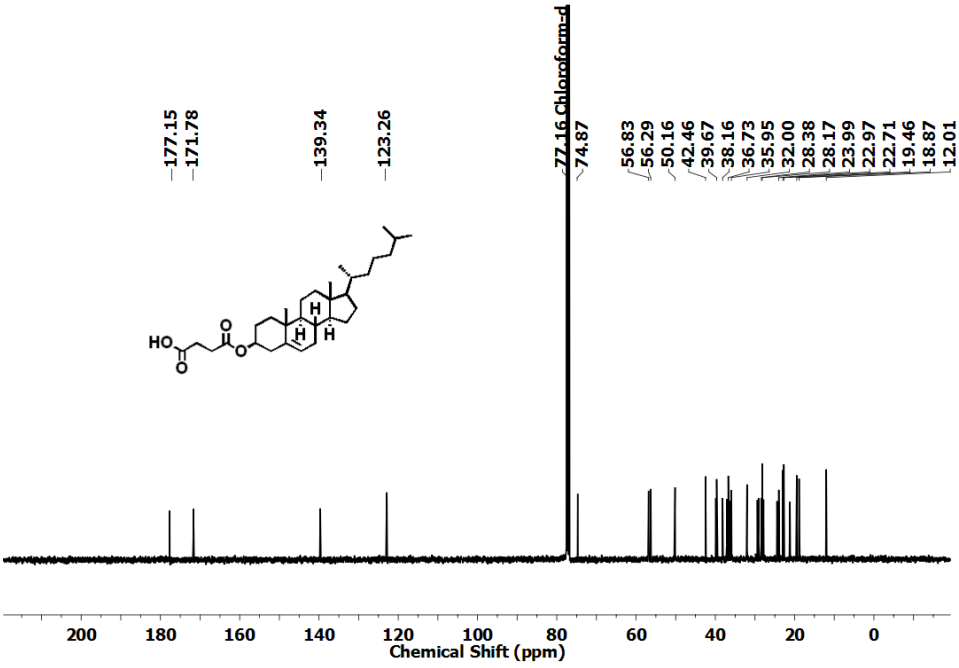

Fig S14: ^{13}C NMR spectra of compound 8

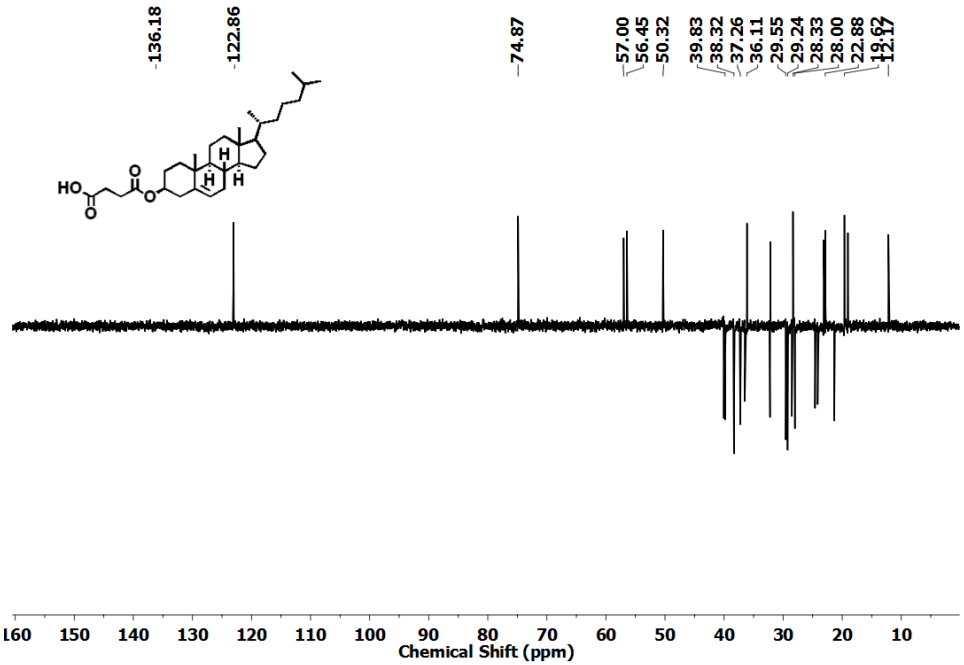

Fig S15: DEPT spectra of compound 8

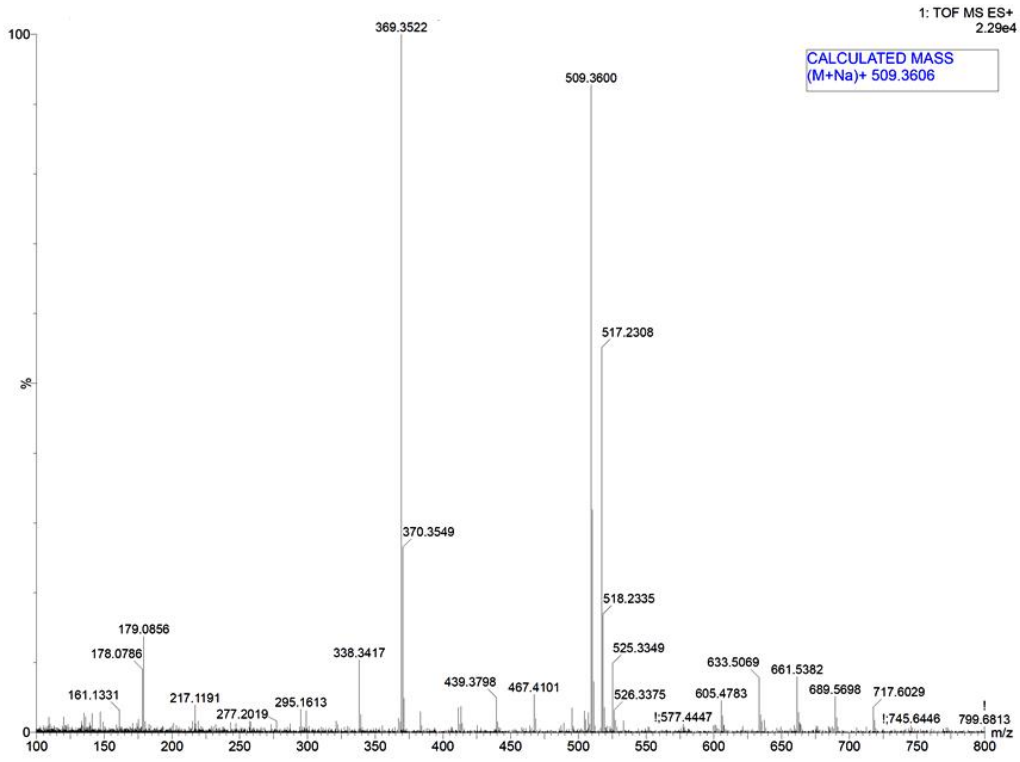

Fig S16: HR-MS spectra of compound 8

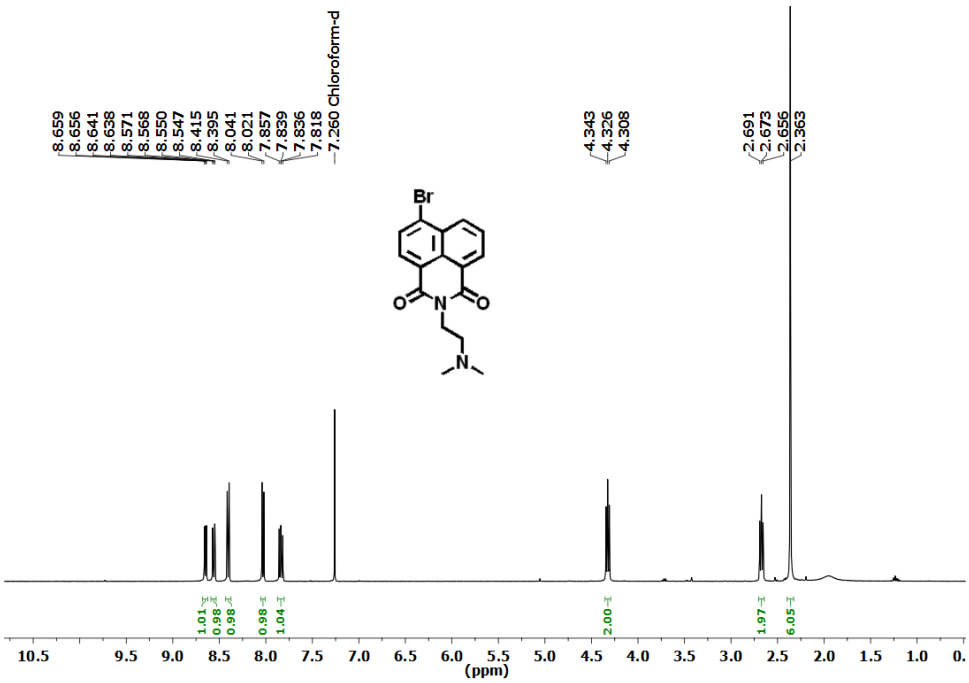

Fig. S17: ^{1}H NMR spectra of compound 11

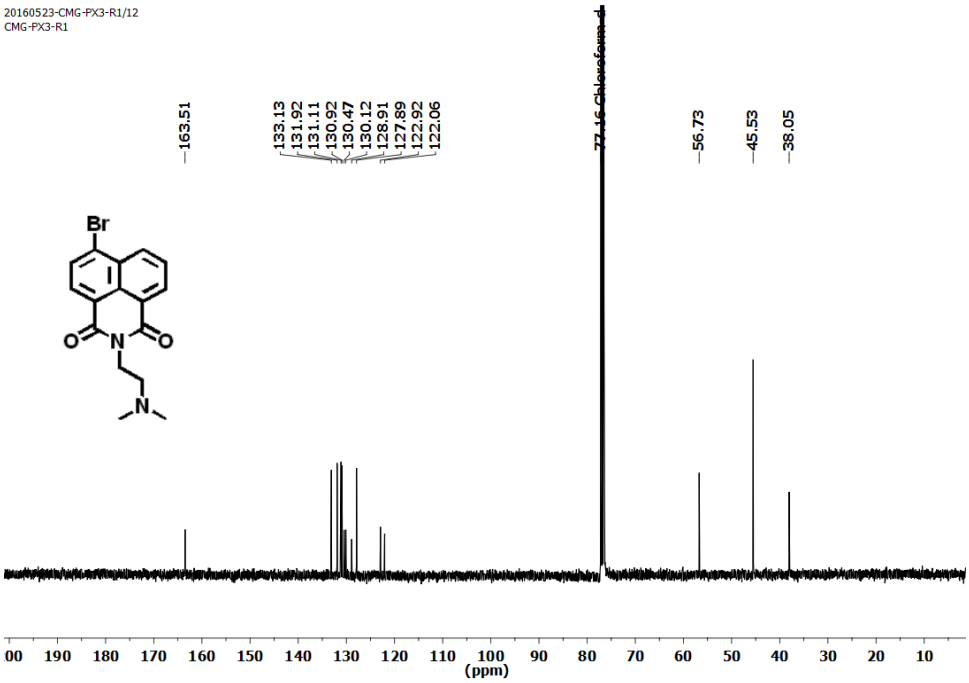

Fig. S18: ^{13}C NMR spectra of compound 11

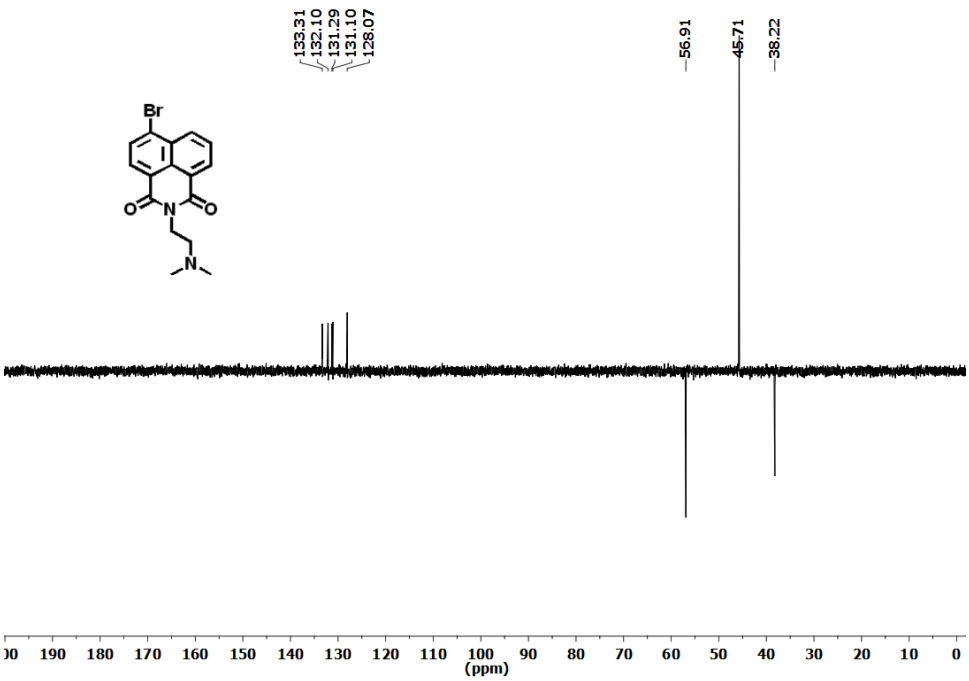

Fig. S19:DEPT spectra of compound 11

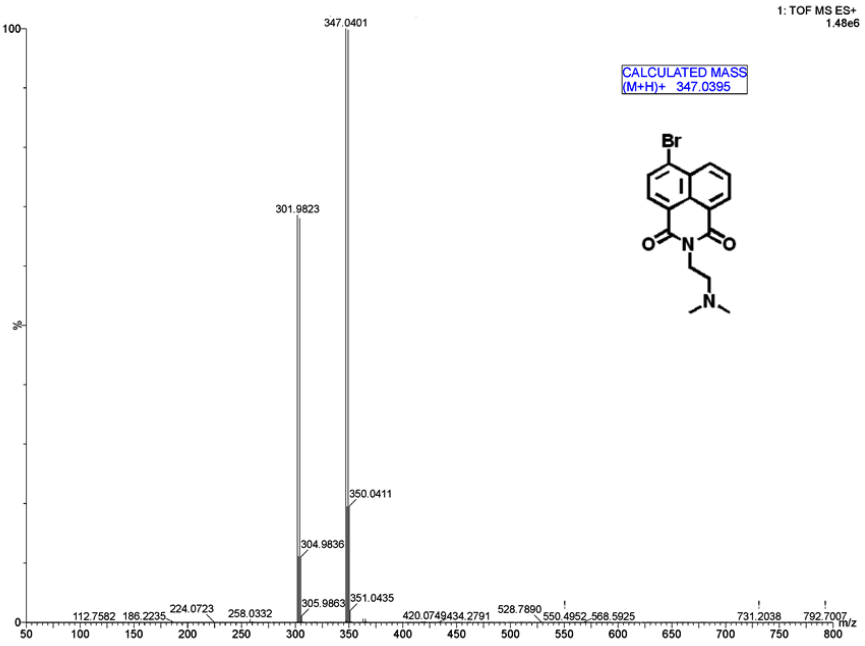

Fig. S20: HR-MS spectra of compound 11

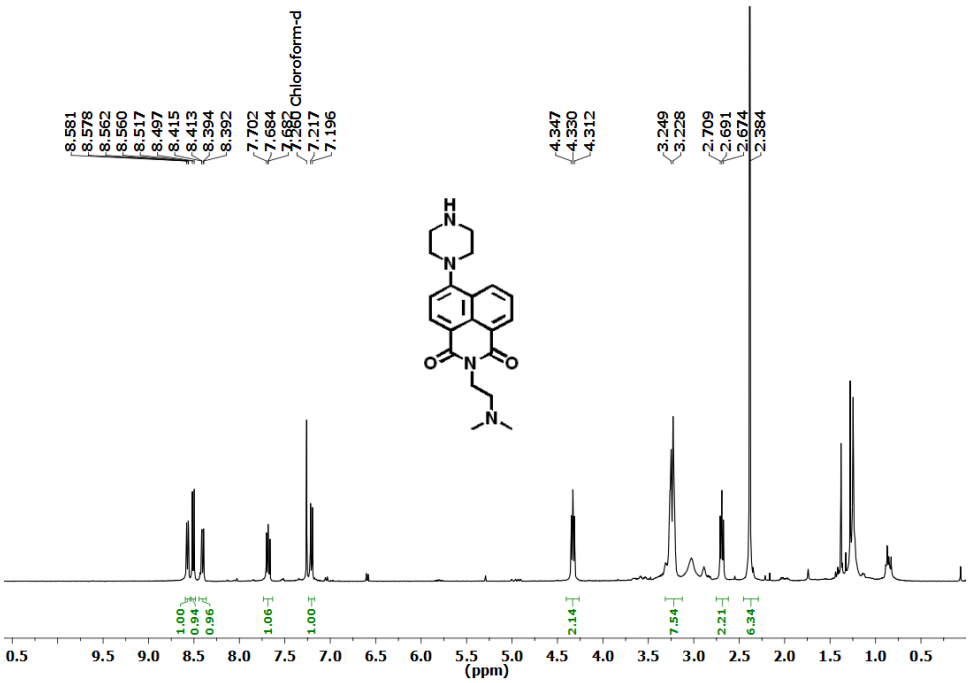

Fig. S21: ^{1}H NMR spectra of compound 13

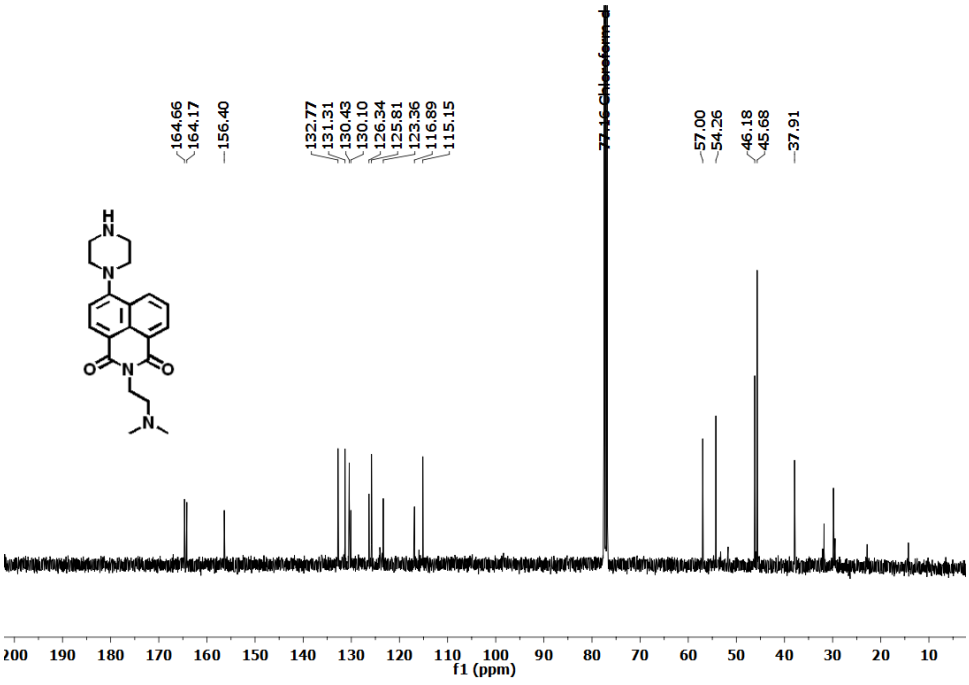

Fig. S22: ^{13}C NMR spectra of compound 13

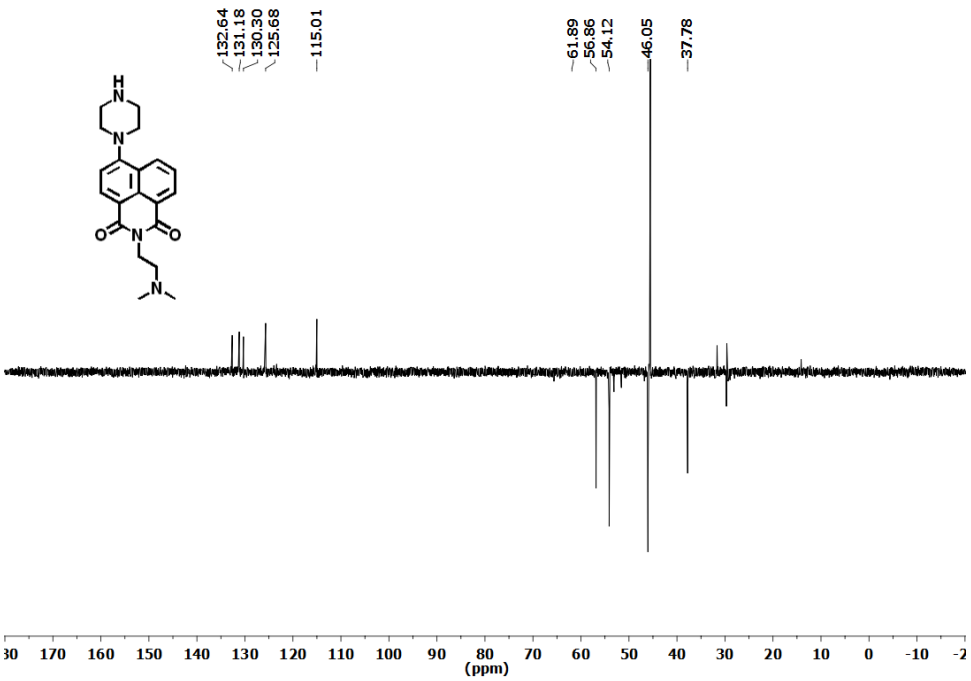

Fig. S23: DEPT spectra of compound 13

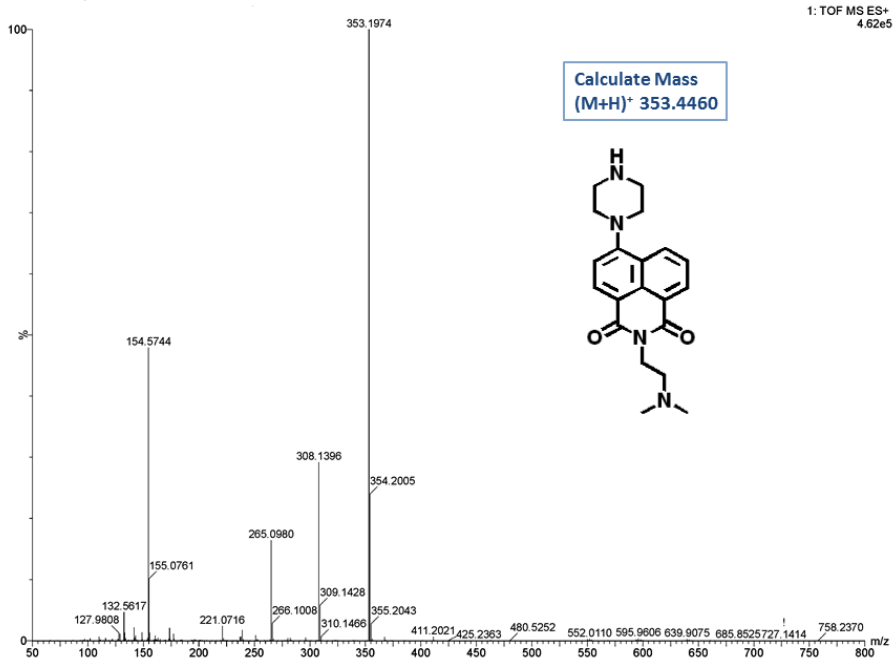

Fig. S24: HR-MS spectra of compound 13

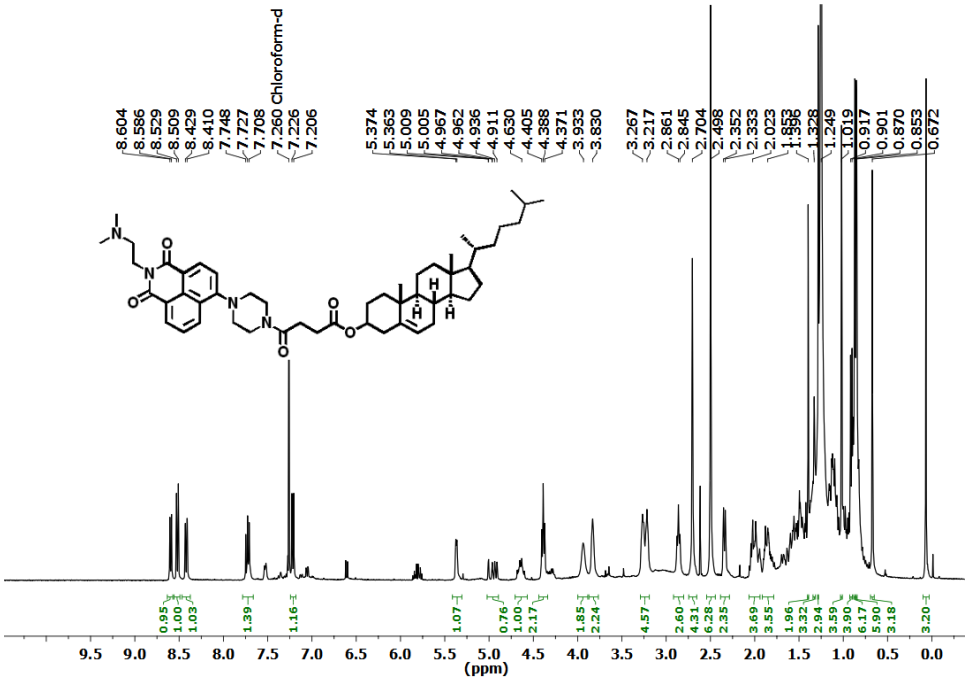

Fig. S25: ^{1}H NMR spectra of compound 14

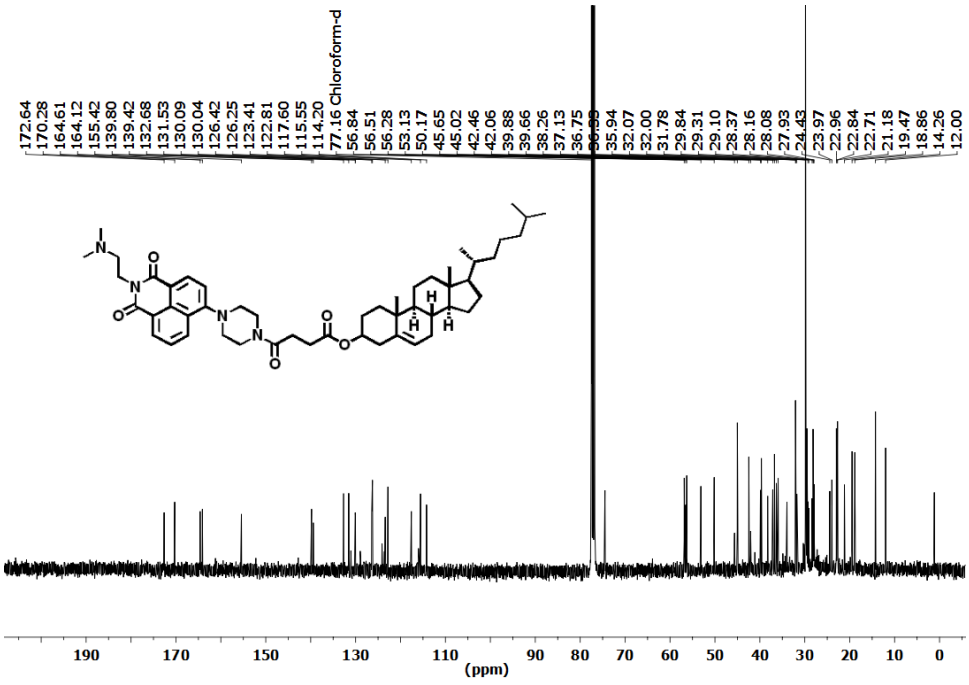

Fig. S26: ^{13}C NMR spectra of compound 14

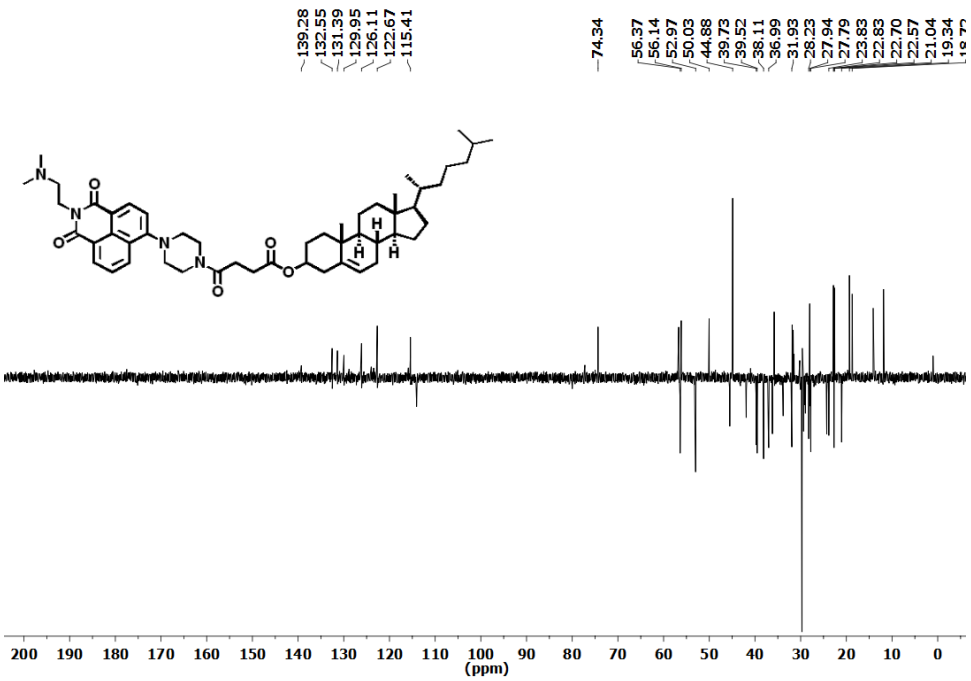

Fig. S27: DEPT spectra of compound 14

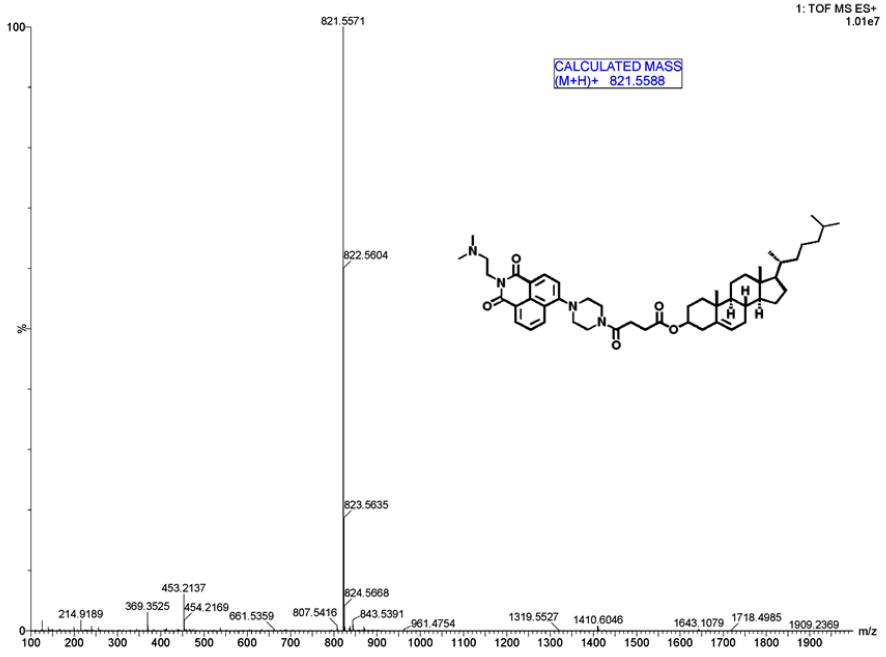

Fig. S28: HR-MS spectra of compound 14

4.6. Reference:

1. Walter, P.; Ron, D. The unfolded protein response: from stress pathway to homeostatic regulation. *Science* **2011**, *334*, 1081-1086.

2. 4. Kim, I.; Xu, W.; Reed, J. C. Cell death and endoplasmic reticulum stress: disease relevance and therapeutic opportunities. *Nat. Rev. Drug Discov*. **2008**, *7*, 1013-1030.

3. 1. Smith, M. H.; Ploegh, H. L.; Weissman, J. S. Road to ruin: targeting proteins for degradation in the endoplasmic reticulum. *Science* **2011**, *334*, 1086-1090.

4. Maly, D. J.; Papa, F. R. 2014. Druggable sensors of the unfolded protein response. *Nat. Chem. Biol.* **2014**, *10*, 892.

5. Hetz, C. The unfolded protein response: controlling cell fate decisions under ER stress and beyond. *Nat. Rev. Mol. Cell Biol*. **2012**, *13*, 89-102.

6. Wang, M.; Kaufman, R. J. Protein misfolding in the endoplasmic reticulum as a conduit to human disease. *Nature* **2016**, *529*, 326-335.

7. Smith, M. H.; Ploegh, H. L.; Weissman, J. S. Road to ruin: targeting proteins for degradation in the endoplasmic reticulum. *Science* **2011**, *334*, 1086-1090.

8. 13. Healy, S. J.; Gorman, A. M.; Mousavi-Shafaei, P.; Gupta, S.; Samali, A. Targeting the endoplasmic reticulum-stress response as an anticancer strategy. *Eur. J. Pharmacol*. **2009**, *625*, 234-246.

9. Phillips, M. J.; Voeltz, G. K. Structure and function of ER membrane contact sites with other organelles. *Nat. Rev. Mol. cell Biol.* **2016**, *17*, 69.

10. Bhat, T. A.; Chaudhary, A. K., Kumar, S., O'Malley, J.; Inigo, J. R.; Kumar, R.; Yadav, N.; Chandra, D. Endoplasmic reticulum-mediated unfolded protein response and mitochondrial apoptosis in cancer. *Biochimi. Biophys. Acta (BBA)-Reviews on Cancer* **2017**, *1867*, 58-66.

11. Wu, H.; Carvalho, P.; Voeltz, G. K. Here, there, and everywhere: The importance of ER membrane contact sites. *Science* **2018**, *361*, 5835.

12. Kanasty, R.; Dorkin, J. R.; Vegas, A.; Anderson, D. Delivery Materials for siRNA Therapeutics. *Nat. Mater*. **2013**, *12*, 967−977.

13. Pollock, S.; Antrobus, R.; Newton, L.; Kampa, B.; Rossa, J.; Latham, S.; Nichita, N. B.; Dwek, R. A.; Zitzmann, N. Uptake and trafficking of liposomes to the endoplasmic reticulum. *FASEB J.* **2010**, *24*, 1866-1878.

14. Costin, G. E.; Trif, M.; Nichita, N.; Dwek, R. A.; Petrescu, S. M. pH-sensitive liposomes are efficient carriers for endoplasmic reticulum-targeted drugs in mouse melanoma cells. *Biochem. Biophys. Res. Commun.* **2002**, *293*, 918-923.

15. Chen, R.; Huo, L.; Shi, X., Bai, R.; Zhang, Z.; Zhao, Y.; Chang, Y.; Chen, C. Endoplasmic reticulum stress induced by zinc oxide nanoparticles is an earlier biomarker for nanotoxicological evaluation. *ACS nano* **2014**, *8*, 2562-2574.

16. Sneh-Edri, H.; Likhtenshtein, D.; Stepensky, D. Intracellular targeting of PLGA nanoparticles encapsulating antigenic peptide to the endoplasmic reticulum of dendritic cells and its effect on antigen cross-presentation in vitro. *Mol .Pharma.* **2011**, *8*, 1266-1275.

17. Feng, Z.; Wang, H.; Wang, S.; Zhang, Q.; Zhang, X.; Rodal, A. A.; Xu, B. Enzymatic Assemblies Disrupt the Membrane and Target Endoplasmic Reticulum for Selective Cancer Cell Death. *J. Am. Chem. Soc.* **2018**, *140*, 9566-9573.

18. Marzec, M.; Eletto, D.; Argon, Y. GRP94: An HSP90-like protein specialized for protein folding and quality control in the endoplasmic reticulum. *Biochim .Biophys. Acta (BBA)-Mol. Cell Res.* **2012**, *1823*, 774-787.

19. Taiyab, A.; Sreedhar, A. S.; Rao, C. M. Hsp90 inhibitors, GA and 17AAG, lead to ER stress-induced apoptosis in rat histiocytoma. *Biochem. Pharma.* **2009**, *78*, 142-152.

20. Duerfeldt, A. S.; Peterson, L. B.; Maynard, J. C.; Ng, C. L.; Eletto, D.; Ostrovsky, O.; Shinogle, H. E.; Moore, D. S.; Argon, Y.; Nicchitta, C. V.; Blagg, B. S. Development of a Grp94 inhibitor. *J. Am. Chem. Soc.* **2012**, *134*, 9796-9804.

21. Won, Y. W.; Yoon, S. M.; Sonn, C. H.; Lee, K. M.; Kim, Y. H. Nano self-assembly of recombinant human gelatin conjugated with α-tocopheryl succinate for Hsp90 inhibitor, 17-AAG, delivery. *ACS nano* **2011**, *5*, 3839-3848.

22. Marcu, M. G.; Doyle, M.; Bertolotti, A.; Ron, D.; Hendershot, L.; Neckers, L. Heat shock protein 90 modulates the unfolded protein response by stabilizing IRE1α. *Mol. and Cellular Biol.* **2002**, *22*, 8506-8513.

23.McMahon, B. K.; Pal, R.; Parker, D. A bright and responsive europium probe for determination of pH change within the endoplasmic reticulum of living cells. *Chem. Commun.* **2013**, *49*, 5363-5365.

24. Hakamata, W.; Tamura, S.; Hirano, T.; Nishio, T. Multicolor imaging of endoplasmic reticulum-located esterase as a prodrug activation enzyme. *ACS Med. Chem. Lett.* **2014**, *5*, 321-325.

25. Lee, H.; Yang, Z.; Wi, Y.; Kim, T.W.; Verwilst, P.; Lee, Y. H.; Han, G. I.; Kang, C. Kim, J. S. BODIPY–Coumarin Conjugate as an Endoplasmic Reticulum Membrane Fluidity Sensor and Its Application to ER Stress Models. *Bioconjugate Chem*. **2015**, *26*, 2474-2480.

26. Abate, C., Hornick, J. R.; Spitzer, D.; Hawkins, W. G.; Niso, M.; Perrone, R.; Berardi, F. Fluorescent derivatives of σ receptor ligand 1-cyclohexyl-4-[3-(5-methoxy-1, 2, 3, 4-tetrahydronaphthalen-1-yl) propyl] piperazine (PB28) as a tool for uptake and cellular localization studies in pancreatic tumor cells. *J. Med. Chem.* **2011**, *54*, 5858-5867.

27. Liu, Y.; Lok, C. N.; Ko, B. C. B.; Shum, T. Y. T.; Wong, M. K.; Che, C. M. Subcellular localization of a fluorescent artemisinin derivative to endoplasmic reticulum. *Org. Lett.* **2010**, *12*, 1420-1423.

28. Jurášek, M.; Rimpelová, S.; Kmoníčková, E.; Drašar, P.; Ruml, T. Tailor-made fluorescent trilobolide to study its biological relevance. *J. Med. Chem*. **2014**, *57*, 7947−7954.

29. Yang, Z.; He, Y.; Lee, J. H.; Chae, W. S.; Ren, W. X.; Lee, J. H.; Kang, C.; Kim, J. S. A Nile Red/BODIPY-based bimodal probe sensitive to changes in the micropolarity and microviscosity of the endoplasmic reticulum. *Chem.Commun.* **2014**, *50*, 11672-11675.

30. Fichter, K. M.; Ingle, N. P.; McLendon, P. M.; Reineke, T. M. Polymeric nucleic acid vehicles exploit active interorganelle trafficking mechanisms. *ACS nano* **2012**, *7*, 347-364.

31. Oyadomari, S.; Mori, M. Roles of CHOP/GADD153 in endoplasmic reticulum stress. *Cell Death Differ*. **2004**, *11*, 381-389.

32. Kuo, L. J.; Yang, L. X. γ-H2AX-a novel biomarker for DNA double-strand breaks. *In vivo* **2008**, *22*, 305-309.

33. Shieh, S.Y.; Ikeda, M., Taya, Y.; Prives, C. DNA damage-induced phosphorylation of p53 alleviates inhibition by MDM2. *Cell* **1997**, *91*, 325-334.

34. Tabas, I.; Ron, D. Integrating the mechanisms of apoptosis induced by endoplasmic reticulum stress. *Nat. Cell Biol.* **2011**, *13*, 184.

35. Wang, J.; Fang, X.; Liang, W. Pegylated phospholipid micelles induce endoplasmic reticulum-dependent apoptosis of cancer cells but not normal cells. *ACS nano* **2012**, *6*, 5018-5030.

36. Yang, Z. J.; Chee, C. E.; Huang, S.; Sinicrope, F. A. The Role of Autophagy in Cancer: Therapeutic Implications. *Mol. Cancer Ther*. **2011**, *10*, 1533−1541.

37. Zhang, X.; Dong, Y.; Zeng, X.; Liang, X.; Li, X.; Tao, W.; Chen, H.; Jiang, Y.; Mei, L.; Feng, S. S. The Effect of Autophagy Inhibitors on Drug Delivery Using Biodegradable Polymer Nanoparticles in Cancer Treatment. *Biomaterials* **2014**, *35*, 1932−1943.

38. Wang, Y.; Kaur, G.; Chen, Y.; Santos, A.; Losic, D.; Evdokiou, A. Bioinert anodic alumina nanotubes for targeting of endoplasmic reticulum stress and autophagic signaling: a combinatorial nanotube-based drug delivery system for enhancing cancer therapy. *ACS Appl. Mater. Interfaces* **2015**, *7*, 27140-27151.

39. Maycotte, P.; Aryal, S.; Cummings, C. T.; Thorburn, J.; Morgan, M. J.; Thorburn, A. Chloroquine Sensitizes Breast Cancer Cells to Chemotherapy Independent of Autophagy. *Autophagy* **2012**, *8*, 200−212.

40. Mallick, A.; More, P.; Ghosh, S.; Chippalkatti, R.; Chopade, B. A.; Lahiri, M.; Basu. S. Dual Drug Conjugated Nanoparticle for Simultaneous Targeting of Mitochondria and Nucleus in Cancer Cells. *ACS Appl. Mater. Interfaces* **2015**, *7*, 7584-7598.